Shallow Vibrated Particulate Beds - Bed Dynamics and Heat Transfer

by

Benku Thomas

Dissertation submitted to the Faculty of the

Virginia Polytechnic Institute and State University

in partial fulfillment of the requirements for the degree of

Doctor of Philosophy

in

Chemical Engineering

APPROVED:

Arthur M. Squires, Co-Chairman

Y. A. Liu, Co-Chairman

Henry A. McGee, Jr.

Melvyn Pell

George B. Wills

February, 1988

Blacksburg, Virginia

Shallow Vibrated Particulate Beds - Bed Dynamics and Heat Transfer

by

Benku Thomas

Arthur M. Squires, Co-Chairman

Y.A. Liu, Co-Chairman

Chemical Engineering

(ABSTRACT)

Particulate beds which are mobilized and expanded by the application of mechanical vibrations are called vibrated beds. These beds are generally defined as shallow, if the depth-to-width ratio is less than unity. The dynamics of shallow vibrated beds and the heat transfer from immersed tubes to such beds are investigated using a vibrational frequency of 25 Hz.

The vibration equipment is designed to minimize distortions in the applied displacement waveform. Transducers used are of a sufficiently high frequency response to accurately follow the variation of bed properties over a vibrational cycle. An electronic circuit is designed to exactly phase-match data collected by a transducer with the vibrational displacement. The circuit may also be used to trigger a strobe lamp at any phase angle, thus permitting an accurate examination of the evolution of bed characteristics over a cycle.

Measurements of floor pressures beneath the bed, indicate cyclic characteristics, caused by the bed motion. Horizontal floor-pressure gradients cause the bed to pile up or bunker within the vessel. In bunkered beds, particle motion is determined by horizontal gas flows, and a compaction wave which propagates diagonally through the bed during the bed-vessel collision. In non-bunkered beds, particle motion is driven largely by wall friction.

The observed instant of bed-vessel separation lags the theoretical prediction by several degrees, most likely because of bed expansion associated with the bed lift-off.

Different "states" of shallow vibrated beds are identified, each with a unique set of characteristics. One state which exists in ultra-shallow beds of depths between 6 and 15 particle diameters is characterized by a high porosity and good gas-solid interaction, making it potentially useful for studies of reaction kinetics.

Surface-to-bed heat-transfer coefficients are measured for Master Beads and glass beads, and found to vary with particle size and vibrational intensity. Heat-transfer coefficients as high as 484 W/m^2-K are obtained. Heat transfer depends on particle circulation and the formation of air gaps which periodically surround the heater surface.

A simplified theoretical formulation for the heat-transfer coefficient appears to qualitatively predict observed trends in heat transfer.

Acknowledgements

The research presented in this study is supported under a university-industry cooperative research program by the National Science Foundation under grant No. CBT-8620244, and the Mobil Research and Development Corporation (MRDC). I would like to thank , , and of NSF, and and of MRDC for their interest in and support of this research. The U.S. Department of Energy supported the early development of vibrated -bed research facilities and laboratory instrumentation used in this study. Special appreciation is extended to , DOE Idaho operations office, and to , DOE Washington headquarters. Thanks are also due to the Norton-Alcoa company, Fort Smith, Arkansas, for supplies of their Master Beads for use as fluidizing solids in this research.

I would like to express my gratitude to my committee co-chairmen, Drs. Y.A. Liu and A.M. Squires for their friendship and personal help throughout my studies at Virginia Polytechnic Institute and State University. I am indebted to Dr. Squires for placing me here at VPI&SU, and for spending several hours every week discussing my research results. I am also deeply grateful to Dr. Liu who spent countless hours and several sleepless nights editing the manuscript of this dissertation, adjusting his busy schedule to fit my requirements.

Special thanks are due to , who designed, developed and interfaced the electronic instrumentation used in this study. I also value all the hours of discussion we had together regarding experimental techniques, and the useful advice he gave me regarding my experiments.

My colleague deserves special thanks for his time and help in collecting data, particularly heat-transfer coefficients for glass beads and the identification of vibrated-bed states. I am grateful to several undergraduate senior students, particularly , , and for helping me in collecting data for this study.

I gained much insight on vibrated-bed mechanics by the valuable and sometimes lively discussion I had with my colleague .

Thanks are due to and who machined and built the vibration system and associated hardware with extreme skill. Without their help, this research would have not been possible.

I would like to thank who spent several hours of her time producing the graphs in this dissertation.

I appreciate very much the assistance of , , , , and , staff of the Department of Chemical Engineering.

Other members of the vibrated-bed research team, both past and present, and my brother , merit thanks for their support and friendship.

Finally I would like to thank my parents who made great personal and financial sacrifices toward my education. Without their help and dedication, it would have been impossible to reach this stage of my educational career.

Table of Contents

List of Illustrations

List of Tables

1.0 Introduction and Review of Previous Work

The mobility and porosity of a particulate bed can be increased by subjecting the bed to low-frequency vertical vibrations. The frequencies most suitable are in the range of about 5 Hertz to over 100 Hertz. As the bed is subjected to increasing intensities of vibration, particles within the bed become mobile and a solid circulation pattern is developed within the bed. The bed porosity increases, and the bed becomes "fluid-like". The resulting bed behavior is similar, but not identical, to the behavior of a gas-fluidized bed. Beds that are mobilized and transformed into a fluid-like state through the use of mechanical vibrations are herein termed "vibrated beds".

Mechanical vibrations have been used for many years to induce mobility in granular material, for example, in vibratory conveyors. However, the primary purpose of vibratory conveying is to transport the material from one location to another, while expending the minimum amount of energy. Therefore, vibrations applied to the bed have a strong horizontal component that push the material along in the desired direction. The bed is thrown in the vertical direction as little as possible, so that the bed has an appearance of being shuffled along the conveyor [Hirt,1984]. Vibrated beds, on the other hand, use a much larger vertical component of vibration to induce bed fluidity. Vibrated beds are usually confined within a vessel, although it is possible to have a flowing vibrated bed in which a small horizontal component of vibration is introduced to create the flow of particles.

Vibrated beds have found wide commercial use within the last decade primarily for the drying of granular solids. Pakowski *et al.*. [1984], who reviewed the literature on vibrated beds, estimated that drying covers 90% of all applications, and cite 135 references pertaining to vibrated beds.

Terminology

There is confusion in the literature on the terminology surrounding vibrated beds. This originates because mechanical vibrations have been applied to gas-fluidized beds to reduce the occurrence of bubbles. In this study, a bed in which a fluid-like state is induced through the use of mechanical vibrations alone (that is, without a flow of fluidizing gas), will be referred to as a ***vibrated bed.*** Such beds have also been referred to as *vibrofluidized beds* in general [Chlenov and Mikhailov,1972], and as *vibroebullient beds* [Kapustin *et al.*,1980] depending on the nature of the bed. If an external flow of gas is maintained through the vibrated bed, it will here be referred to as an ***aerated vibrated bed*** when the gas flow is less than that the minimum fluidization velocity (u_{mf}) for the bed. If the gas flow is greater than u_{mf} for the bed, the bed is levitated primarily by the pressure drop in the gas, and not by the vibrations alone, in which case, the bed is called here a ***vibrated gas-fluidized bed.*** This classification will avoid the confusion in the literature caused by referring to all beds to which mechanical vibrations have been applied as vibrofluidized beds.

The term vibrofluidized beds is in wide use, but it is not preferred here, partly because it has often been used incorrectly as described previously, and partly because the vibrated bed has some differences in behavior from that normally associated with gas-fluidized beds as will be shown later. However, because of its to the wide usage, *vibrofluidization* will be used to describe the transformation of the vibrated bed into the fluid-like state.

1.1 Observation of Bed Dynamics

The displacement a at any instant t, of a vessel containing a vibrated bed that is subjected to vertical sinusoidal vibrations of frequency f and an amplitude of a_o is given by the equation for simple harmonic motion:

$$a = a_o \sin(2\pi f t) = a_o \sin(\omega t) = a_o \sin(\theta) \qquad [1.1]$$

where ω is the angular frequency, and θ is the phase angle. The vessel velocity ($\dot{a}$) and acceleration ($\ddot{a}$) may be obtained by successive differentiation of equation [1.1], which gives:

$$\dot{a} = a_o \omega \cos(\omega t) \qquad [1.2]$$

and

$$\ddot{a} = -a_o \omega^2 \sin(\omega t) \qquad [1.3]$$

It is useful to define a dimensionless vibrational intensity parameter K, which is the ratio of the peak vessel acceleration to gravitational acceleration (g):

$$K = \frac{\max\left|-a_o \omega^2 \sin(\omega t)\right|}{g} = \frac{a_o \omega^2}{g} \qquad [1.4]$$

Imagine a single particle of mass m, lying on a vibrating table. The force acting on the particle due to gravitational acceleration is $-mg$, and the force due to the vibrational acceleration is $ma_o\omega^2 \sin(\omega t)$. Therefore, the resultant normal reaction force N, acting on the particle due to the table is:

$$N = mg[1 + K \sin(\omega t)] \qquad [1.5]$$

Provided the acceleration of the table is greater than -1g, the normal force will be positive and the particle will remain in contact with the table. At the instant in the cycle of vibration at which the table acceleration just falls below -1g, (that is as $\sin(\omega t) \leq -1/K$), the normal force N, will equal zero as indicated by equation [1.5], and the particle will separate from the table, provided there are no other external forces acting on it; the particle will then move freely under gravity. It will remain in free flight, with its trajectory determined by simple Newtonian mechanics until some point later in the cycle, where it will collide with the table. If the collision is non-plastic (the particle rebounds after collision, or in other words, the coefficient of restitution of the particle is greater than zero), the particle will immediately rebound with its new trajectory determined by the mechanics of the collision. However, if the collision is completely plastic, that is, the particle's coefficient of restitution is zero, the energy of the collision is immediately dissipated, and the particle will remain in contact with the table until the point of separation in the next cycle. It is obvious from equation [1.5], that if the value of K is less than or equal to one, the particle can never lift off the table.

If one places just a few coarse particles in a vessel vibrating with K greater than 1, they bounce irregularly above the floor of the vessel, exhibiting predominantly vertical motion, and colliding at random times with the vessel floor [Sprung *et al.*,1986]. The behavior of the particles is dependent on the mechanics of free flight with the inclusion of air drag on each particle, and on the collision processes between particles and the vessel floor, and between each other. The nature of the bed will be dependent on the coefficient of restitution of the particles, their individual masses, shapes and surface characteristics, and vibration parameters. As more particles are added, the particles in the bed begin to move in concert, lifting off together at a point in the cycle and colliding with the floor at a later instant as shown in Figure 1 on page 5. Once the bed acts as a single mass, the collision with the vessel base is completely plastic, that is, the bed acts as if it had a net coefficient of restitution of zero. Bachmann [1940] observed that beds of lead and glass particles acted as a single mass if the bed depth exceeded about six particle diameters. This behavior of a bed which is more than a few particle diameters deep, has led several investigators [Bachmann,1940; Kroll,1954,1955; Yoshida and Kousaka,1967; Gutman,1974,1976a] to model the bed as if it were a

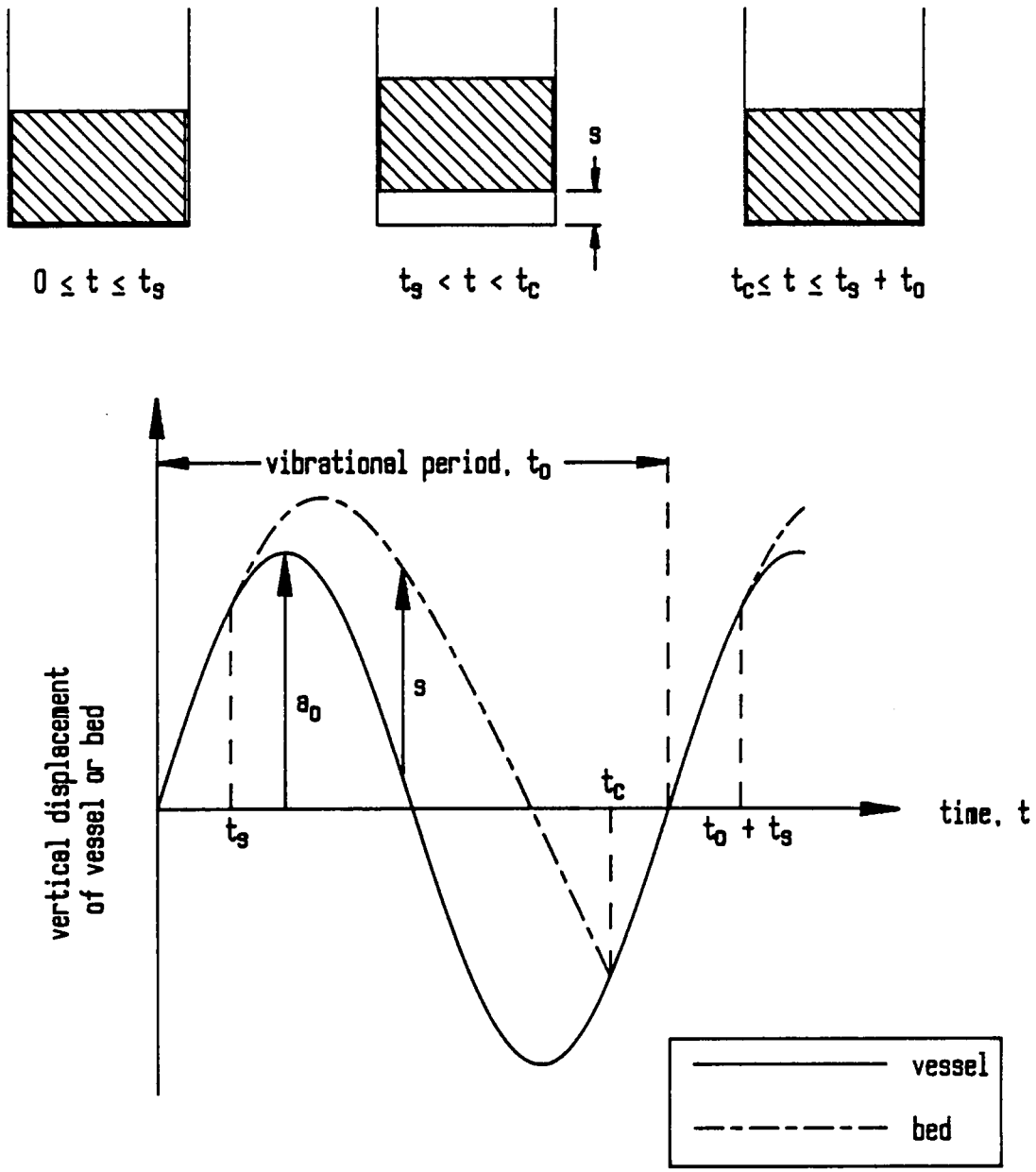

Figure 1. The bouncing motion of the vibrated bed: The bed is modeled as a porous plastic body, and the vibrational waveform is sinusoidal. The bed expands due to the vibration. Notation: t_s - the instant of bed-vessel separation; t_c - the instant of bed-vessel collision; t_o - the vibrational period.

single coherent plastic body. The plastic-body analogy assumes that the entire bed lifts off the vessel base uniformly without any significant bed expansion within each cycle.

Cinematographic studies of the vibrated bed [Bachmann,1940 Kroll,1954] have indicated that the bed does behave closely to the plastic mass assumption provided the particle size was large (>400 μm). The bed lifts off the vessel base at time t_l provided $K>1$, with a gap appearing at the bottom of the bed, causing a flow of air down across the bed into the gap. The bed later falls back toward the base, eventually driving air upward across the bed until an instant t_c when the bed collides with the vessel base and the gap is completely destroyed. The acceleration waveform will display a kink at the point of collision, and this has been used by Chlenov and Mikhailov [1972] to detect the instant of collision. The lift-off and collision points have also been located by using electrically conductive particles to detect the making and breaking of electrical contact at the base of the vessel [Gray and Rhodes,1972; Rippie *et al.*,1978].

Large-Particle Beds

Two distinct behaviors of large-particle vibrated beds have been reported for $K<1$ and $K>1$. In the former regime, there was no bulk motion of particles, but merely some bed compaction and a decrease in the apparent angle of friction brought about by the vibration. Chlenov and Mikhailov [1972] have described the bed as vibromobile in this region, a term that is rather misleading considering the nature of the bed. In fact, after the first few minutes of vibration when an initial period of particle rearrangement is over, there is no detectable movement of particles in the bed for $K<1$ [Thomas *et al.*,1986]. For $K>1$, the large-particle vibrated bed is similar in appearance to the gas-fluidized bed, which has led most investigators to refer to this regime as a vibrofluidization. It has a reasonably level top surface and the bed porosity increases with increasing vibrational intensity to a limiting value [Chlenov and Mikhailov,1965]. If large-diameter particles are loaded to different heights in the two arms of a U-tube and the tube vibrated, the levels in the two arms will

equilibriate when $K>1$ [Gutman,1976a]. There is a bulk circulation of the bed material, with particles moving down at the walls, and upward at the center.

Small-Particle Beds

As the particle size is reduced, a continuous change in bed behavior is noticed. The instant of bed lift-off becomes later in the cycle and the height of separation of the bed above the vessel floor also reduces with decreasing particle size [Gutman,1974], until a point is reached with very small particle sizes, when the bed cannot be observed to lift-off the vessel base during the entire cycle [Thomas *et al.*,1986].

The nature of the vibrofluidized bed itself is very different for small particles. The bed is observed not to have a level surface but rather to pile up or bunker at different locations within the vessel [Kroll,1955; Buevich *et al.*,1979; Sprung *et al.*, 1986]. The air that is being pumped first downward as the bed attempts to lift and later upward as the bed and vessel floor are pushed together has a noticeable effect on small-particle beds due to the reduced permeability of such beds to gas flows through them. As a result, the top of the bed is seen to expand significantly [Kroll,1955; Thomas *et al.*,1987] as the gas rushes out of the bed. For very fine powders like cement, bubbles are seen to form within the bed and erupt at the surface, leading to a description of such beds as vibroboiling beds by some authors [Chlenov and Mikhailov,1972]. Particle circulation is now determined by the shape of the bed and the locations of bunkers. In most regions of the bed with the exception of a relatively narrow layer on the top, particles move from the shallow regions of the bed toward the deeper sections, with a return flow from the top of the deeper section toward the shallower sections in the narrow region on the top of the bed [Kroll,1955; Thomas *et al.*,1986].

Even further changes in bed behavior are noticed as the particle size is reduced to below 100 μm. The bed no longer changes state at $K=1$, but rather at progressively higher values of K as the particle size is reduced. For 30 μm laundry detergent powder, the transition has been reported to occur between $K=3$ to $K=5$ depending on the vibrational frequency [Herber,1970]. Kapustin *et al.*

[1980], have measured the critical vibrational intensity K_{cr}, at which there is a transition to the vibrofluidized state as a function of particle size using beds of powdered nickel and iron, for bed depths varying from 10 mm to 100 mm. K_{cr} equals unity for all particle sizes greater than 100 μm, with an increase in K_{cr} to 1.5 for a particle size of 50 μm. The increase in K_{cr} is dramatic if the particle size is reduced further; increasing exponentially to 4 for a particle diameter of 25 μm, and beyond that for even smaller particle sizes. The transition point is delayed largely due to the cohesiveness of beds composed of particles less than 100 μm. In such cases, sufficient shear has to be applied to the bed to cause it to overcome the cohesiveness and bring about a fluid-like state. Even then, the bed mobility may be caused by the movement of air into and out of the large cavities produced in the bed as a result of the high shear. Vinogradov *et al.* [1980] studied the transition to vibrofluidization for ultra-fine powders, using 2-3 μm SiO_2 and sub-micron ($\simeq$0.7 μm) $CaCO_3$ particles. They hypothesize that, unlike for coarse systems, where the separation of particles in free-flight can be brought about by forces equal in magnitude to the weight of individual particles, the forces required to separate cohesive powders must be large enough to overcome the adhesive bonds that exist between such small particles. They suggest using the parameter $z_o^2\omega^3$ to characterize the transition instead of K_{cr} for such fine powders.

1.1.1 Models for the Vibrated Bed

The majority of models used to describe the mechanics of the vibrated bed have been based on the plastic body analogy. Attempts to model the bed as a viscoelastic mass [Gray and Rhodes,1972], have not proved to be of any advantage since several unknown factors are introduced which cannot be evaluated easily. As described earlier, this implies that particles lift off the vessel base as a single porous plug in flight; and on collision with the vessel later in the cycle, the bed immediately begins to move with the vessel again. Gray and Rhodes [1972] pointed out that the impact at collision, which takes a finite period of time to travel up to the top of the bed, must be small in comparison to the period of vibration, and must certainly be less than the time between the bed-vessel collision

and the point of lift-off in the next cycle. Therefore, they suggest an upper limit of 150 Hz and $K = 10$, or the onset of fluidization brought about by the gas flow induced by the bed vibration - whichever comes first - as the upper limit to the applicability of the plastic body analogy for a bed that is 15 cm deep. They based the limits on the vibrational parameters using a stress propagation velocity of 150 m/s in granular solids.

The simplest model is one which considers the bed as a single particle, neglecting the effect of the drag introduced by the gas flows [Takahashi *et al.*,1968]. The model is of limited use, since the effects of drag produces several effects in most beds. The lift-off of the bed will be delayed due to the drag. The bed acceleration relative to the vessel, and the rate of separation of the bed from the vessel will also be reduced. This will in turn restrict the amount of gas that flows into the bed during the lift period.

Yoshida and Kousaka [1967] have improved on the single-particle model by including an air drag term into the equations of motion. They assumed that the air flow into the bed was equal to the rate at which the bed separated from the vessel base, and so the drag force, which is proportional to the gas velocity relative to the bed, is also directly proportional to the rate of separation. The validity of this model has been examined using experimentally fitted values of the drag coefficient [Gray and Rhodes,1972], and the correlation between the predicted and experimentally observed flight times appeared to be reasonable within the range of conditions examined.

Kroll [1954,1955] attributed the gas flows to the pressure drops generated at the bottom of the bed as it attempted to lift off, and described a vibrated bed theoretically with the assumption that correlations for steady-state pressure drop in the gas flowing through a packed bed, such as Darcy's law, would provide a good approximation for the transient forces acting in the dynamic situation. He assumed that air was incompressible, so that the instantaneous linear pressure drop across the bed was proportional to the instantaneous gas velocity through the bed, which using the plastic mass assumption, is equal to the rate of separation of the bed from the vessel base. This allowed

Kroll to predict the bed projection and the air pressure variation in the gap below the bed through an entire cycle, as a function of bed properties and vibration conditions.

Measurements of the bed throw were made by cinematographic techniques, and satisfactory agreement with the Kroll model was found for the large-particle beds vibrated at relatively low frequencies; but as the particle size was decreased and vibration frequency increased, the accuracy of the model in predicting bed throw and pressure variations was poor [Gutman,1974]. To improve on this, Gutman [1974,1976a], suggested treating the air as a compressible fluid, since the bed resistance to air flow was now higher, and the time periods involved much smaller. This model showed a somewhat better agreement for both the pressure beneath the bed and the bed throw for smaller particles and higher frequencies. For large-particle beds and low frequencies, it was identical to the Kroll model. However, the model was increasingly in error with finer particle sizes and deep beds. The model was particularly in error as the particle size approached 100 μm.

Ryzhkov and Baskakov [1974] included the effect of wall friction in their model. They argued that for large-particle beds, the drag term was small compared to the wall friction, particularly in deep beds. This argument is dubious, since the resistance of the bed to gas flows also increases linearly with bed depth according to the Kroll model. In addition, the work of both Kroll [1955] and Gutman [1974] indicates that the wall friction was negligible in comparison with the drag for shallow vibrated beds. It is possible that the drag may be neglected in comparison with wall friction when one is dealing with very non-spherical particles in a tall and narrow bed.

All of the above models are based on the plastic body analogy, thus they do not take into account the variations of bed porosity in both space and time. Measurement of bed porosity by capacitance techniques [Gutman,1974; Rippie *et al.*,1978], clearly show a small cyclic variation in bed porosity with time during a cycle of vibration. This variation is small for large particles - only about 0.5% according to Gutman - but is reported to be larger for smaller particles [Chlenov and Mikhailov,1972], although no details are given of the measurement technique used or the actual variation in porosity. In any case, even a small increase in porosity in a fine-particle bed during the

period when the bed and vessel are attempting to move away from each other, will allow the bed to retain a considerable amount of the gas that is flowing into the bed as a result of the pressure drop at the bottom of the bed. This contradicts the plastic mass analogy, which assumes that any gas that flows into the top of the bed ends up flowing into the gap that is forming at the bottom. In fact, both the Kroll and Gutman theories predict that if no gaps form below the bed, then there is no gas flow into or out of the bed, and neither model can be solved in such cases.

An attempt was made by Buevich and Galontsev [1978] to include the effect of bed expansion during the flight fraction of the cycle, and bed compression at the instant of collision. They reasoned that the drag on the top-most layers caused by the down-flowing gas during the bed lift-off would be lower than for the rest of the bed, and so would allow these layers to lift off earlier and at a faster velocity than the lower regions of the bed. In addition, the lower surface also experienced a greater drag than the rest of the bed, so there would be an expansion into the gap that was forming at the bottom. The bed was assumed to expand uniformly, so that the center of gravity of the bed remained in the middle of the varying bed height at all times. They correlated the varying accelerations experienced by different layers due to delayed lift-off and different drag effects by introducing a term, which described the ratio of the drag on the top-most layers to that on the lower regions of the bed. However, it proved to be difficult to estimate this parameter, and later studies using this model have attempted to measure this ratio experimentally [Buevich and Kharisova,1978], and examine the effect of varying gas permeability caused by bed porosity variations during a cycle on forced gas flows through the bed [Erdesz and Halasz,1984]. The model treats the gas flowing through the bed as incompressible, whereas beds with significant periodic porosity variations, unfortunately, are tall small-particle beds in which, according to Gutman's analysis [Gutman,1974,1976a], compressibility effects become important.

A more detailed mathematical treatment of some of the models described above is given in Chapter 6.

1.2 *Heat Transfer*

Heat transfer from a surface immersed in a vibrated bed is several times higher than in a stationary packed bed, and measured heat transfer coefficients are comparable to those in gas-fluidized beds. The pressure drop of the gas flowing through vibrated beds is much lower than in gas-fluidized beds, since the gas no longer has to support the weight of the particles. It is apparent that the vibrated bed can be an attractive heat transfer device.

The experimental procedure generally used for measuring the surface-to-bed heat transfer coefficients has been to immerse a heated body (a heat-transfer probe) fixed relative to the vessel, within the bed. The surface temperature of the probe and the bed temperatures are monitored as the heat from the immersed body warms up the bed. Heat transfer from the side-walls and bottom of the containing vessel to the bed have also been studied. The temperature gradients within the bed have been found to be small at atmospheric pressure [Chlenov and Mikhailov,1972], so that an overall surface-to-bed heat transfer coefficient may be defined.

A variety of surface geometries have been studied including flat vertical surfaces, flat horizontal surfaces, horizontal cylindrical surfaces (tubes passing through the bed), and spherical (see for example, Table 1 on page 14). The heat transfer coefficients are influenced by several factors such as the vibrational parameters, vessel and heat-transfer surface geometries, particle size and type, and position of the heat transfer surface in the bed.

Influence of Particle Size

A compilation of some typical values of heat transfer coefficients is summarized in Figure 2 on page 13 and Table 1 on page 14 as a function of the particle size. Although these data represent many varying experimental conditions and different particle types, a trend of increasing heat transfer with

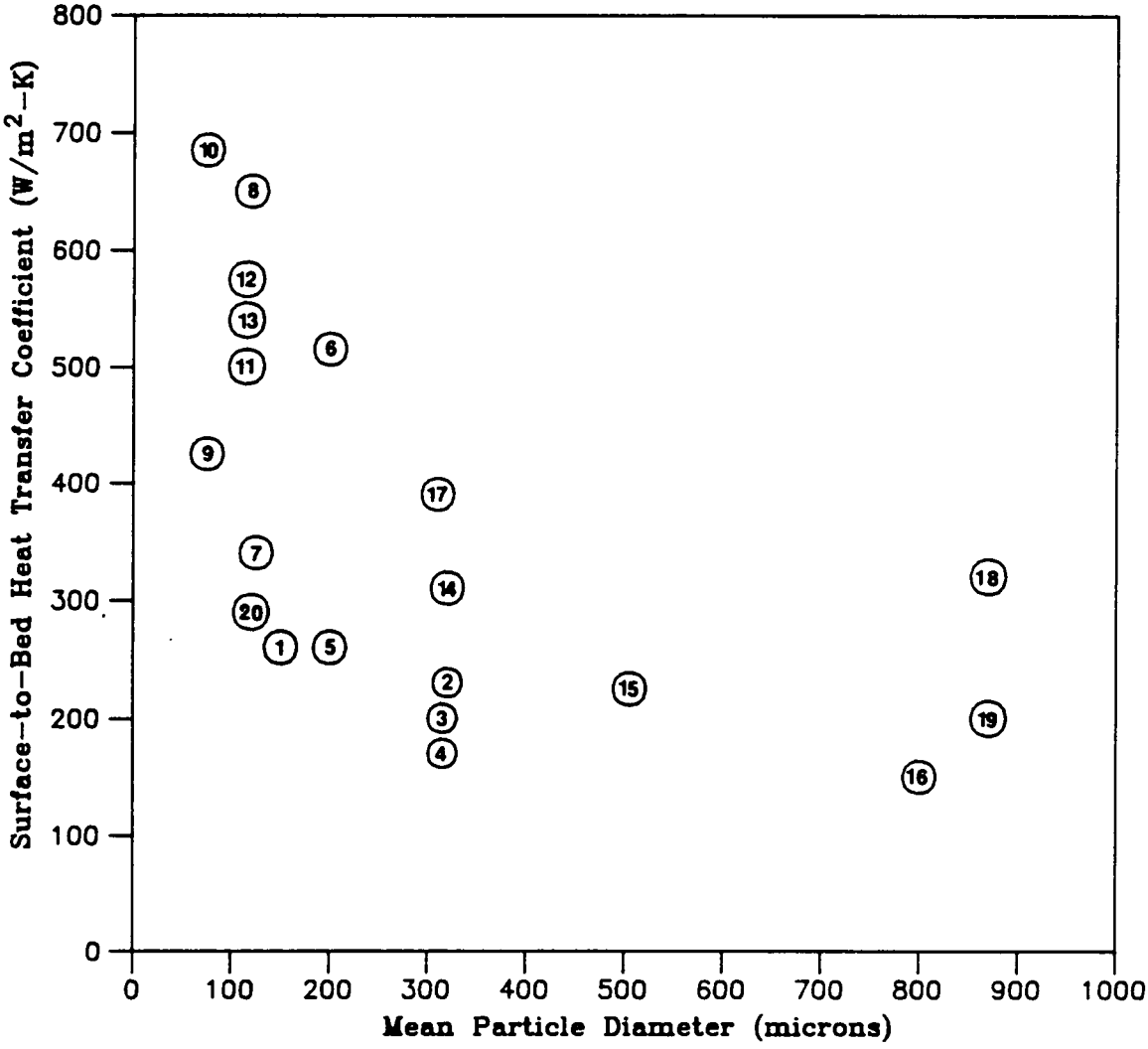

Figure 2. Surface-to-bed heat-transfer coefficients from previous studies: Heat-transfer coefficients obtained from selected previous studies, showing the effect of particle size. See also Table 1 on page 14.

Table 1. A summary of conditions used to measure surface-to-bed heat-transfer coefficients in previous vibrated-bed studies

Authors	Data Set	K	f(Hz)	Bed Depth (mm)	Particle Type and Shape	Type of Heater
Sapozhnikov and Syromyatnikov (1969)	1	3.6	52	45 to 50	synthetic corrundum (angular)	spherical heating probe
	2	3.6	52			
	3	6.0	57			
	4	2.5	41			
Ryzhkov *et al.* (1976)	5	2.5	15	100 to 500	aluminum oxide (spherical)	vertical heating surface
	6	9.9	30			
	7	2.5	15			
	8	9.9	30			
	9	2.5	15			
	10	9.9	30			
Kossenko *et al.* (1975)	11	2.7	20	120 to 140	fine electro-corrundum (angular)	horizontal tube bundles
	12	3.7	40			
	13	9.0	60			
	14	2.7	20			
	15	2.7	20			
		3.0	20			
	16	5.0	40			
		9.0	60			
Bukareva *et al.* (1970)	17	2.9	40	70	quartz sand (angular)	vertical heater
Gutman (1974)	18	3.0	20	65	glass beads (spherical)	flat vertical heater
	19	5.0	50			
	20	4.5	50			

decreasing particle size can be observed. The heat transfer coefficients have values between 150 and 700 W/m^2-K. Kal'tman and Tamarin [1969] and Zabrodsky *et al.* [1968] report values as high as 1200 to 1400 W/m^2-K, but these values must be treated with some suspicion since the immersed surface was at temperatures as high as 900°C, and it is not clear whether the high values reported could be as a consequence of radiation from the surface or due to the unsteady-state nature of the measurement method used. All investigators referenced in Table 1 on page 14 report a continuous increase in heat transfer coefficient with decreasing particle size, down to 100 μm. However, Zabrodsky *et al.* [1968], using a spherical heater located a maximum in the heat transfer coefficient for a particle size of 30 μm, whereas the maximum reported by Kal'tman and Tamarin [1969] occurred around 70 μm also using a spherical heat-transfer surface.

The Effect of Heat-Transfer Surface Geometry and Vibration Conditions

The geometry and orientation of the heat-transfer surface is important in determining the heat transfer coefficient. Bukareva *et al.* [1969] measured the coefficient using both flat, vertical and horizontal heating surfaces. The results for quartz sand (280 to 350 μm) are shown in Figure 3 on page 16, and clearly indicate that the coefficients for the vertical surface are much higher than those for the horizontal. This difference has been attributed to the air gap that forms between the horizontal surface and the bed during the flight period of the bed. The heat transfer coefficient was believed to have increased with increasing vibrational velocity, due to the increased particle circulation that was induced as a result. Maxima in the curves for horizontal surfaces occurred as the increase in the size of the gap offsets improvements produced by particle circulation.

One would expect a variation of heat transfer coefficients intermediate between these extremes if a horizontal cylindrical or spherical surface were used; and indeed, the results of Laikovskaya *et al.* [1968] using a spherical heater and 160-μm corrundum particles, confirm this. The heat-transfer coefficient increased rapidly with increasing values of the vibrational intensity parameter K, at low values of K, and reached a maximum at $K = 5.3$, then it gradually dropped with further increases in

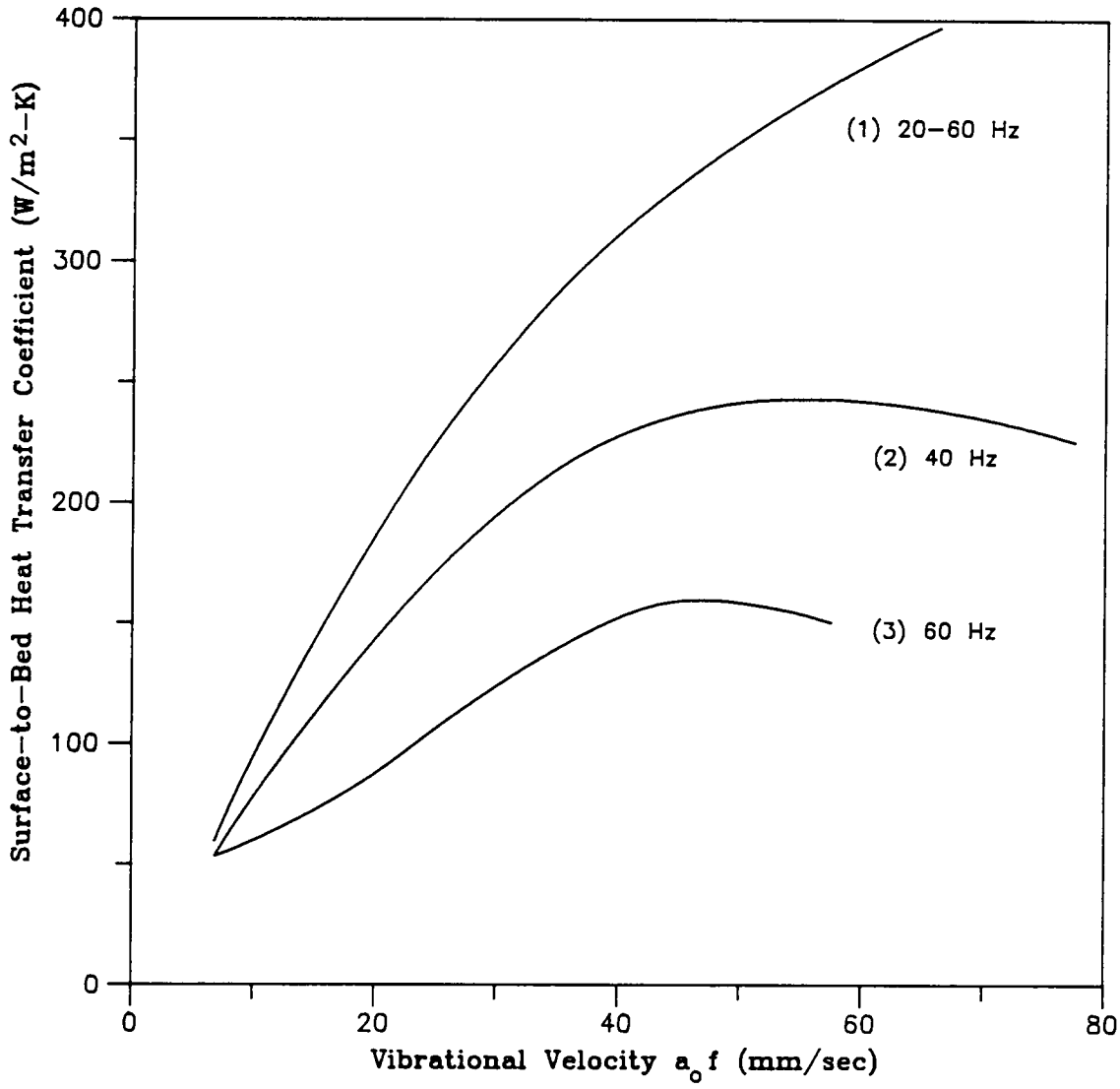

Figure 3. Effect of vibrational velocity on the surface-to-bed heat-transfer coefficient: Heat transfer from a vertical heater surface (1), and from a horizontal heating surface (2) and (3), to a vibrated bed of quartz sand (200 - 350 μm). [Bukareva *et al.*,1969].

K. Data for horizontal tube bundles obtained by Kossenko *et al.* [1975] also show similar trends. When using a single in-line row of tubes of 38-mm diameter in a vibrated bed of depth 160 mm, at a frequency of 20 Hz, they observed limiting values in the curves of heat transfer coefficient plotted against K (Figure 4 on page 18). Sapozhnikov *et al.* [1976] showed that the local heat transfer coefficient which varied with angular position around the tubular surface was always lowest at the bottom of the tubes, and highest at the lateral positions. However, this variation was attributed to observed differences in the particle circulation rates with angular position.

The results of Bukareva *et al.* [1969] (Figure 3 on page 16), would indicate that heat transfer from the horizontal heat-transfer surface is dependent on the frequency, with the heat-transfer coefficient dropping off as the frequency is increased. However, heat-transfer coefficients for the vertical surface fall onto a single curve for all frequencies if plotted against the vibrational velocity. Heat-transfer measurements by Strumillo and Pakowski [1980] from flat vertical surfaces immersed in beds of calcium carbonate spheres with diameters between 328 and 1730 μm show little dependence of the heat-transfer coefficients for a given particles size on the frequency (for a fixed amplitude of 0.125 mm) when $K > 1$. Kal'tman and Tamarin [1969], correlating their experimental results on the basis of a packet-type heat-transfer model (to be discussed later in Chapter 7), suggested that the optimum heat transfer coefficient would be located at the vibration parameter for which:

$$a_o\omega^{1.6} = 7.6 \quad \text{or} \quad K = 0.78\omega^{0.4} \qquad [1.6]$$

Here, a_o is the vibrational amplitude, and $\omega(= 2\pi f)$ is the vibrational velocity.

This relationship should be used with caution since it was based on data obtained from a narrow range of experimental conditions, and is therefore independent of experimental conditions such as particle size. Equation [1.6] obviously does not fit the data of Kossenko *et al.* [1975], (Figure 4 on page 18), which clearly indicate that the optimum value of the heat-transfer coefficient occurs at larger values of K as the particle size is decreased.

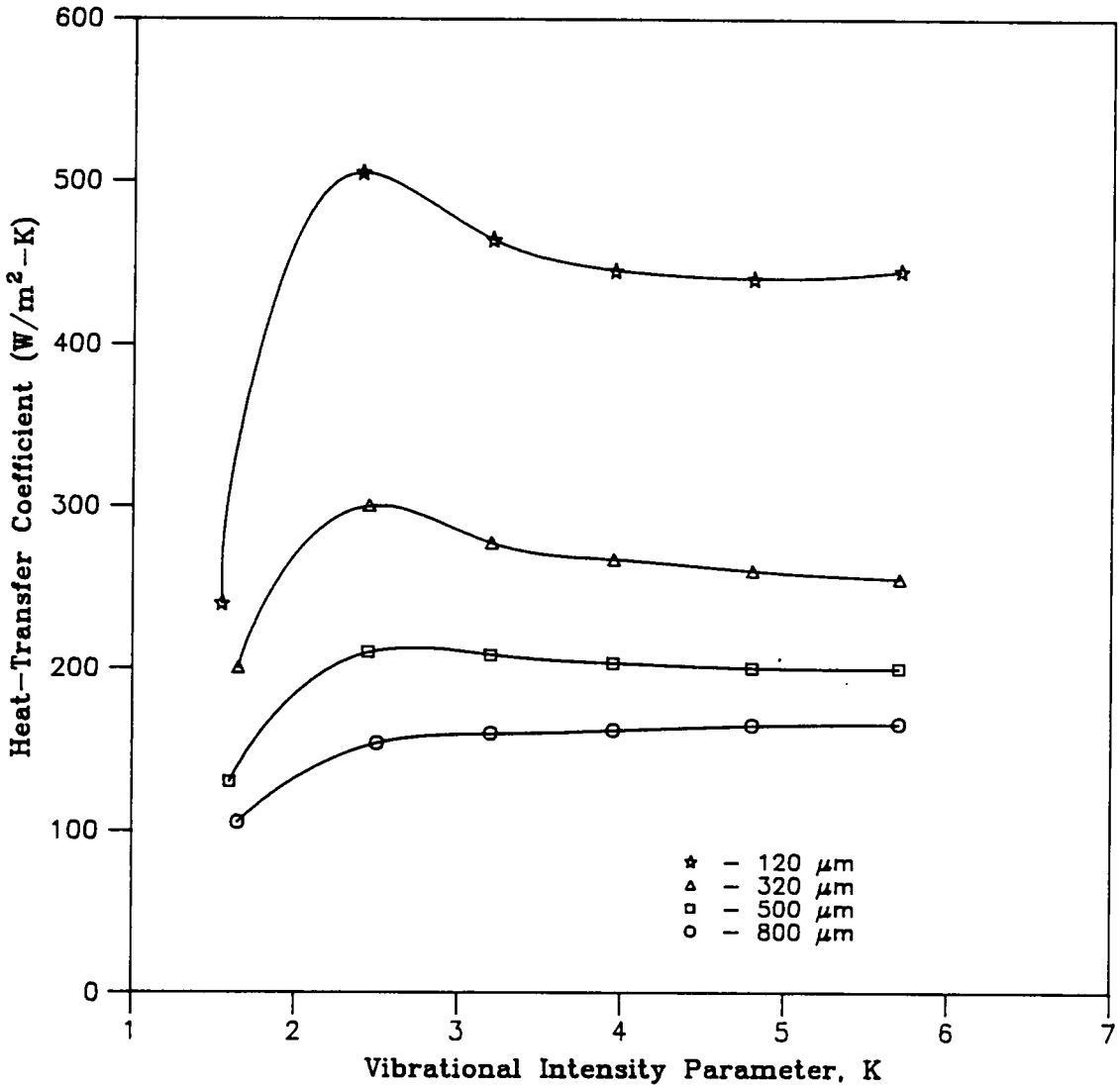

Figure 4. **Heat transfer from a single row of tubes to a vibrated bed:** Experimental conditions are as follows: vibrational frequency = 20 Hz; bed depth = 160 mm; tube diameter = 38 mm. [Kossenko *et al.*,1975].

Wall-to-bed heat transfer coefficients have been measured to be much higher than for immersed vertical surfaces. Values as high as 1200 W/m^2-K have been reported [Bukareva *et al.*,1970]. Plots in the reference were of the heat-transfer coefficient as a function of vibrational amplitude, and show an apparently strong frequency dependence. However, a given amplitude would then represent a range of values of K for different frequencies; if the data are replotted using K as the abscissa (Figure 5), it is seen that the frequency dependence is much less at low K, until a frequency of 50 Hz is reached. There is a large jump in heat transfer at 60 Hz and the heat transfer at high K appears to be quite high.

The heat transfer from the vessel base to the bed has been studied by Muchowski [1980]. The heat transfer coefficients increased from packed-bed values at $K=1$ to a limiting value of about 125 W/m^2-K at $K=3$ for 500-μm glass spheres. With 100-μm glass spheres, the heat transfer coefficient went through a maximum of 285 W/m^2-K.

Effect of Gas Pressure in the Bed

Decreasing the gas pressure within the vibrated bed has been found to decrease the surface-to-bed heat transfer coefficient. At a gas pressure of 40 Pa, the heat transfer coefficient was measured by Sapozhnikov and Syromyatnikov [1969,1970] to be about 40 W/m^2-K, which is close to packed-bed values. Coefficients for heat transfer from the bottom of the vessel to the bed were found to be between 15 to 20 W/m^2-K at a pressure of 13 kPa for glass beads of all sizes regardless of whether the bed was mechanically stirred or not [Muchowski and Mannchen,1980].

Effects of Particle Circulation and Mixing

The quantitative effects of particle circulation and mixing on heat transfer properties of vibrated beds have not been thoroughly investigated. Ryzhkov *et al.* [1976] have measured the bed-to-surface heat-transfer coefficient in a relatively deep bed. For values of K ranging from 1.2 to 1.4, the

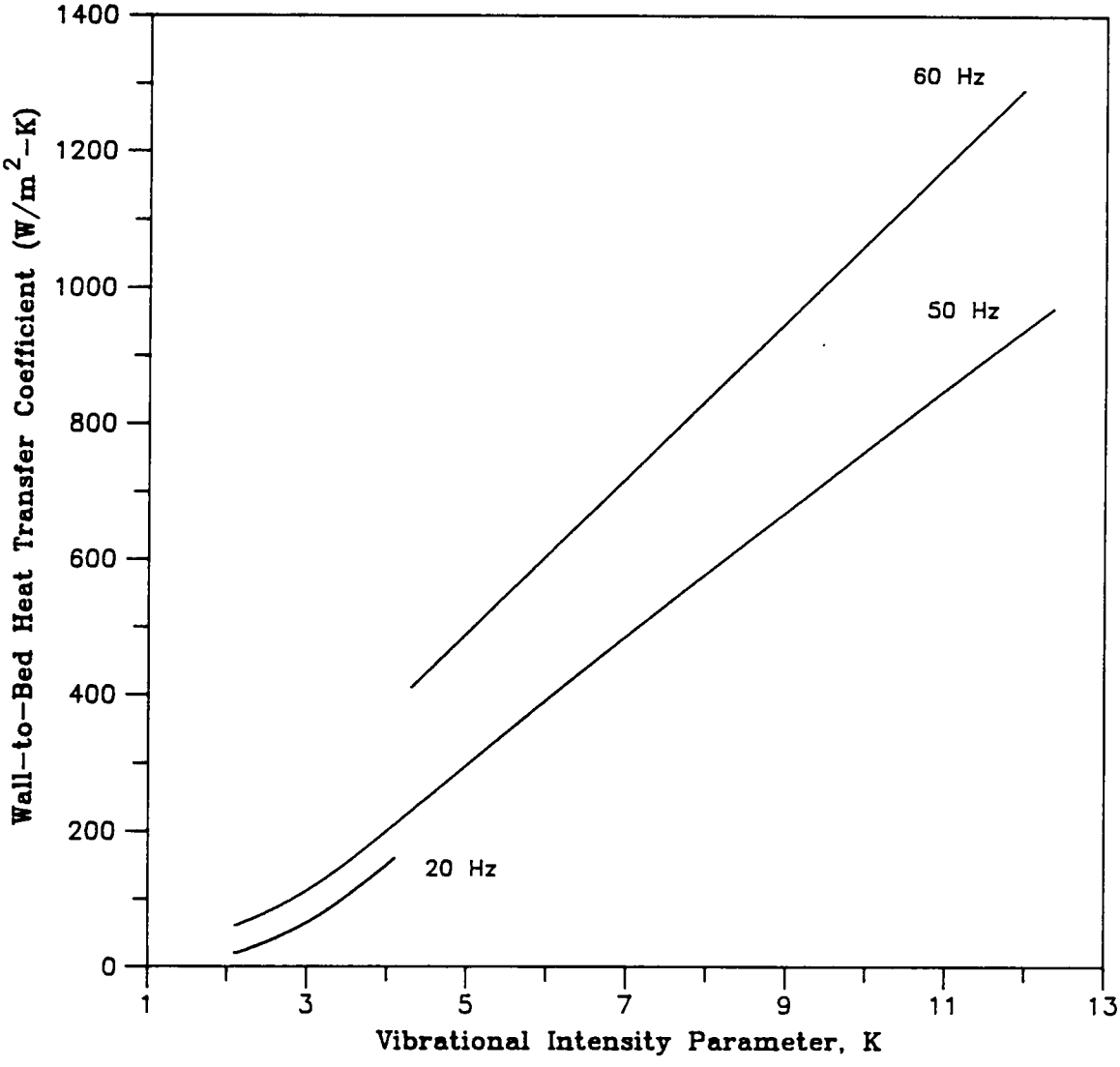

Figure 5. Wall-to-bed heat-transfer coefficients: Effect of the vibrational intensity parameter on the wall-to-bed heat-transfer coefficient at different vibrational frequencies. [Bukareva *et al.*,1970].

heat transfer coefficient was about 550 to 570 W/m^2-K at the top of the bed where a high particle circulation rate was observed; and the value of the coefficient was 80 to 100 W/m^2-K near the bottom of the bed where there was little particle circulation. As K was increased, the bed became less consolidated, and particle mixing appeared to extend from the top to the bottom of the bed, leading to an almost identical heat transfer coefficient over the entire height of the bed.

Muchowski and Mannchen [1980] induced additional particle circulation into the vibrated bed by mechanical stirring at different speeds. With additional mechanical stirring at 101 rpm, the heat transfer coefficients for 1000-μm glass spheres were as high as 200 W/m^2-K at $K=1$ (compared to 100 W/m^2-K at $K=3$ without stirring). However, as K was increased, the value dropped until at $K=4$, it was approximately equal to the heat-transfer coefficient without any stirring for that value of K (Figure 6 on page 22). When stirring 100-μm glass beads, the greatest improvement was again at $K=1$, with curves for different stirring speeds going through a single maximum, and then dropping off together. Increasing the stirring speed from 50 to 100 rpm always gave improved heat transfer coefficients, but this improvement decreased with increasing K. It is possible that the reduction in heat transfer to stirred packings with increasing K was due to the size and duration of the periodic gap that forms at the bottom of the bed. This gap could act as a resistance to heat transfer, but also the presence of the gap could reduce the friction between the bed and the vessel base leading to the bed simply rotating with the mechanical stirrer, rather than being mixed by it. However, Muchowski's plots of data are difficult to compare with those in the other literature, since they are lines of constant amplitude, and therefore represent varying frequencies across the range of K values on the abscissa.

The presence of an immersed heat-transfer surface in itself alters the particle circulation patterns in the locality of the surface. Thus the overall and local heat-transfer coefficients for tube bundles are a function of the number and arrangement of the tube-bundle rows in the bed [Kossenko *et al.*,1975 Sapozhnikov *et al.*,1976].

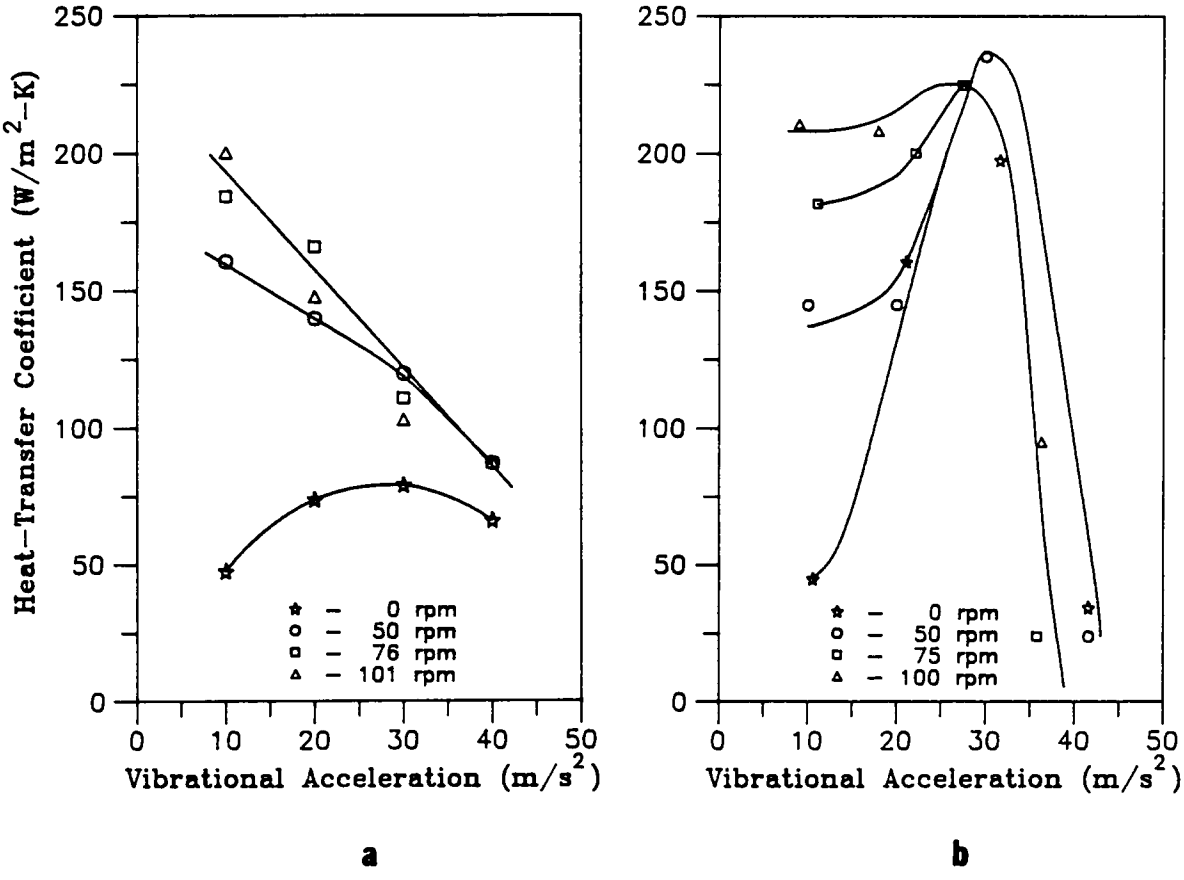

Figure 6. Heat transfer from the vessel floor to the vibrated bed: heat-transfer coefficients with and without additional mechanical stirring of the bed for (a) 1000-μm glass beads, and (b) 100-μm glass beads. [Muchowski and Mannchen,1980].

1.3 *Uses of the Vibrated Bed*

Although the phenomenon of vibrofluidization was described and studied by Bachmann in 1940, and subsequently modeled mathematically by Kroll in 1955, it was not until the work of Chlenov and Mikhailov [1964], nearly fifteen years after the first description of the phenomenon, that there was any commercial interest in the vibrated bed. Since then the number of commercial applications has grown steadily with most being in the drying of granular solids [Pakowski *et al.*,1984]. The majority of large-scale applications have been in the Soviet Union and Eastern Europe where the preponderance of literature originates. Chlenov and Mikhailov [1972] give several examples of commercial vibrated-bed applications using both non-moving and conveyed vibrated beds. A particularly interesting example of a commercial application which they cite is that of a French firm which uses a vibrated bed for drying 3000 kg/hr of material. A comparison of power usage with a gas-fluidized bed showed that the air flow rate through the bed was halved by using the vibrated bed. The pressure drop across the bed was reduced since the weight of solids no longer needed to be supported. As a result, the pumping requirement was reduced from 22 kW to 5 kW. The extra power required to vibrate the bed was just 2.2 kW if the unit was operated at the resonance frequency of the vibrating system.

A theoretical analysis of power usage for the vibrated bed by Gutman [1974] has shown that the power required to vibrofluidize coarse particles is less than for gas-fluidization. For fine particles, where the differences in power requirement are smaller, the vibrated bed has the advantage of having a reduced carry-over of fines. Studies of the segregation of granular material with a widely dispersed particle size under the action of vibration [Williams and Shields,1967; Ripple *et al.*,1973], show that finer fractions tend to move down to the bottom of the bed while large particles "float" to the top.

The vibrated bed is in wide use for drying various materials such as pharmaceutical preparations, foods, fertilizers, inorganic salts, and plastics. Most vibrated-bed dryers are of the conveying type. Where a short residence time is required, a straight horizontal trough is used, whereas a spiral up-flowing bed is used to achieve long residence times [Strumillo and Pakowski,1980]. Vibrated beds have found favor for use in drying for the following reasons:

- The vibrations produce an intensely mixed bed without requiring the flow of fluidizing gas through the bed, thus eliminating the elutriation of fines, while at the same time, considerably enhancing the heat and mass transfer, and giving higher rates of drying [Strumillo and Pakowski,1980]. This is particularly important to thermolabile materials which would be destroyed if large thermal gradients were to develop.
- It is possible to vibrofluidize wet, cohesive, and even paste-like substances with relative ease [Ginzburg and Syroedov,1965; Zaitsev *et al.*,1976] when compared to gas-fluidization.
- Mechanical action prevents beds of wet finely dispersed powders from consolidating and "seizing up" [Chlenov and Mikhailov,1967]; on the other hand, attrition of crystaline materials such as sugar is greatly diminished in the vibrated bed as compared to the gas-fluidized bed [Pakowski *et al.*,1984].
- Radiant *vacuum* drying of extremely thermally sensitive pharmaceuticals can be achieved, since no air flow is required for the vibrated bed [Volovik *et al.*,1975].
- The conveying vibrated-bed dryer has a narrow spread of residence time distributions of the product, which is desirable. This plug flow is achieved by having a large length-to-width ratio of 8 to 10, which is virtually impossible to achieve in a gas-fluidized bed [Pakowski *et al.*,1984].

Because of the high rates of heat transfer that can be achieved between heating surfaces and the vibrated bed, and between particles in the bed and a gas flowing through the bed, the vibrated bed makes an excellent heat-transfer device. A vibrated-bed heat exchanger has been proposed which exchanges heat between counter-current horizontally flowing streams of solids and hot air, or between a hot gas and a non-flowing vibrated bed of solids [Liu and Squires,1986]. Studies by Cheah

[1986] have shown that the pressure drop across the bed is small when compared to similar flows across gas-fluidized beds, and the heat recovery rate is high.

The vibrated bed is also in increasing use as a reactor because of the high mass- and heat-transfer rates that can be achieved, as well as the absence of bubbling. Studies of coal carbonization in a laboratory oven [Konyakhin *et al.*,1976] showed that the carbonization rate was almost doubled when the reactor was vibrated, and the coke quality indices were improved. More recently, the Fischer-Tropsch synthesis reaction has been studied in detail using a laboratory-scale vibrated-bed micro-reactor [Whiting,1985], which allowed a study of the reaction with a rapid switching of the feed gases using very low flow rates.

2.0 The Scope of This Study

The general overview of the current literature in the previous chapter indicates that the vibrated bed has several commercial uses. A vibrated bed is classified as being "deep" or "shallow", depending on the value of the ratio of the height-to-diameter ratio (L/D) of the bed. If this ratio is less than, say 0.5, the bed is usually defined as shallow; and if $(L/D) \ll 1$, the bed is described as ultra-shallow. Measurements of heat-transfer coefficients at various points along the height of the bed indicated that the heat transfer and particle circulation improved toward the top of the bed [Ryzhkov *et al.*,1976]. This indicates that shallow vibrated beds are probably preferable to deep beds for purposes of mass or heat transfer, since the particle circulation at the lower regions of the deep bed will be poor without any external aids.

This study is undertaken with the primary objective of gaining a better understanding of shallow vibrated beds, particularly in those areas pertaining to its use as a heat-exchange device and as a chemical reactor. This requires an extensive examination of bed dynamics, measurement of surface-to-bed heat-transfer coefficients, and an investigation of the heat-transfer mechanisms in the vibrated bed.

2.1 Limitations of Previous Studies

As will be illustrated in the following sections, the current literature in many instances either inadequately described and explained many phenomena, or results of different investigators were in conflict. Some of these differences arise from the varying conditions under which results were obtained — sometimes even within the same study.

2.1.1 Equipment Limitations

Previous studies have been conducted using many different types of equipment, some of which appear to have introduced some characteristic peculiarities into results obtained through their usage.

2.1.1.1 Vibration Equipment

Two types of vibrators have commonly been used for producing the mechanical vibrations required to induce vibrofluidization:

Electromagnetic vibrators use a coil assembly positioned axially within a strong hollow cylindrical permanent magnet. The coil assembly is directly attached by a shaft to a light-weight vibration table which is suspended from a set of weak leaf-springs. When the coil is energized by an alternating current, it responds by moving vertically within the magnet, with its position at any time determined by the polarity and magnitude of the applied voltage.

Mechanical vibrators basically consist of a massive vibration table that is vibrated by a mechanical method. The table is suspended from a set of stiff springs. The drive mechanism can be one of two basic designs. In one design, the vibration table is driven directly by an eccentric cam which is ro-

tated by an electric motor. The alternative design uses two motors that are attached onto the vibration table. Unbalanced weights are attached to the axes of the motors, so that when they rotate, a vibrational motion is induced in the table.

Gray and Rhodes [1972] have used both types of vibrators in their studies, and report that a difference in bed characteristics could be observed depending on the type of vibrator used. In particular, they conclude that when using the electromagnetic vibrator, the bed porosity is frequency-dependent, whereas when using the mechanical vibrator, no such dependence can be observed. They ascribe this difference to the different frequency responses of the two types of vibrator. The frequency response of the electromagnetic vibrator was measured to be nonlinear, because of the occurrence of resonance within the range of operational frequencies; whereas the response of the mechanical vibrator was measured to be linear. However, an examination of the technical specifications of many commercially available electromagnetic vibrators show that such vibrators exhibit essentially a flat response within the range of frequencies normally used for vibrofluidization (5 to 200 Hz). It is not clear why Gray and Rhodes observed a nonlinear response. It is possible that additional stiffer leaf-springs were used in their experiments to suspend the vibrating vessel. If this was done, the frequency response would have been determined by the stiffer leaf-spring assembly that was added to the system, and not by the electromagnetic vibrator itself.

There are also factors other than the frequency response of the vibrator that might have been responsible for the anomalies noted by Gray and Rhodes. It is clear from the waveforms of acceleration given in the reference [Gray and Rhodes,1972] that there is severe distortion of the sinusoidal displacement of the table when using an electromagnetic vibrator. This is caused by the collision between the heavy bed and the relatively less massive vibration table on the electromagnetic vibrator. The collision produces a change in the momentum of the vibrating table, and consequently a distortion in its acceleration and displacement. This distortion will alter the vibrational intensity, thereby causing changes in other factors such as the size and duration of the air gap that forms between the bottom of the bed and the vessel floor. Since the mass of the vibration table on a mechanical vibrator is large compared to the bed weight, the bed-vessel collision produces only a

slight change in the momentum of the table. Therefore, the distortion of the acceleration and displacement waveforms will be minimal when using a mechanical vibrator. The response of the electromagnetic vibrator to the bed-vessel collision can be made similar to that of the mechanical vibrator by increasing the weight of the table, so that it is several times more massive than the bed. This can be achieved by rigidly attaching additional weights to the table, and using stiff leaf-springs which support the additional weight added.

2.1.1.2 Phase-Correlation of Cyclic Phenomena

Many physical properties of the bed such as the gas pressure within the bed, the bed porosity, and the size of the air gap below the bed, vary cyclically usually with the same period as the applied vibration. If a number of cyclically varying properties are measured over the period of a cycle, it becomes necessary to correlate them to the phase of the displacement of the vibrating table. This will allow the interaction between the vibration and the properties to be established. For example, suppose that the displacement of the bed relative to the vessel base is observed. It is impossible to determine the exact point in the cycle where the bed lifts off or collides with the vessel base, unless the information on the relative bed displacement is matched with the phase of the vessel or table displacement.

Previous studies have usually achieved phase-correlation by simultaneously displaying both the output signal of the transducer used to measure the property being examined, and the vessel displacement on an oscilloscope; but the resolutions of most oscilloscopes are poor and the method can lead to errors. Moreover, if the displacement signal is distorted, further errors will be introduced into the phase-correlation. This is particularly true if the acceleration waveform is being used for phase-correlation [Gray and Rhodes,1972], since the acceleration signal will always contain small amounts of noise (see section 3.3.1.1 in the next chapter for a further discussion of the noise inherent in acceleration waveforms).

To obtain accurate phase-correlation of any property, it is also necessary to eliminate or calibrate any phase lags that are inherent in the transducers used to measure the property (see also the next section on pressure measurements).

A failure to correctly phase-correlate measured properties or eliminate transducer phase lags may have resulted in some ambiguous results in the literature. For instance, the variation of gas pressure beneath a 40-mm deep bed of 250—599-μm glass beads, as well as the thickness of the air gap below the bed were measured by Gutman [1974]. The data shown graphically in Figure 7 on page 31, were obtained at a frequency of 20 Hz with $K = 2.06$. The pressure below the bed was measured by a surface-mounted pressure transducer, and the thickness of the air gap was measured by a capacitance transducer [Gutman,1974,1976a]. As shown in Figure 7 on page 31, the gauge pressure in the gap increases above zero even though the gap is still expanding. This is physically impossible unless the bed undergoes compression during the flight period, forcing out air into the gap and thus causing the pressure in the gap to increase. Instantaneous measurements of bed porosity using a capacitance technique [Gutman,1974,1976a; Rippie *et al.*,1978] would suggest that the bed does not undergo any compression during flight, since the bed voidage remains approximately constant during the flight period. Another anomaly that may.;e noted in Figure 7 on page 31 is that the sharp positive peak in the pressure, that should occur at or after the instant when the bed collides with the vessel base, actually occurs prior to the collision while the bed the bed is still in flight. These anomalies may be due to one or more of the following reasons:

1. The measurement of the air-gap thickness was carried out in a 12.5-mm by 100-mm rectangular vessel, whereas the pressure measurements were made in a 63-mm-diameter cylindrical vessel.

2. Either one (or both) of the output signals from transducers used to measure the air gap thickness and pressure were incorrectly phase correlated with the vessel displacement.

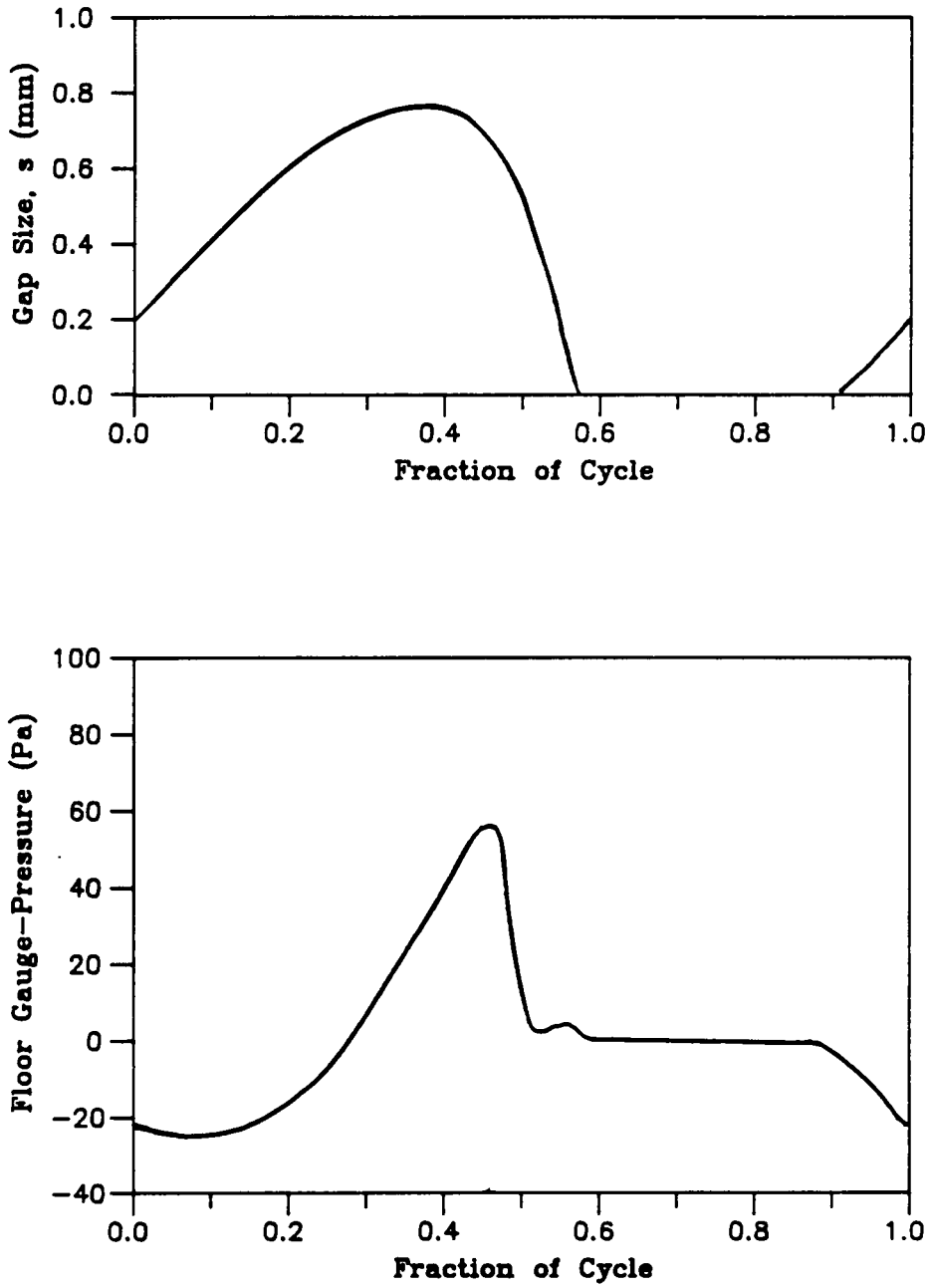

Figure 7. Gutman's measurements of air-gap and floor-pressure variation over a cycle: Experimental measurements of (a) air gap thickness, and (b) floor gauge-pressure beneath a vibrated bed of 250 to 599-μm glass beads. Bed depth = 40 mm; frequency = 20 Hz; K = 2.06. Note that the gauge pressure rises above zero while the gap is still expanding. [Gutman,1974].

3. There are inherent phase lags present in the system used to measure pressure and/or the transducer used to measure air-gap thickness.

It is likely that the difference in vessel sizes may account for some inconsistencies, but without eliminating causes (2) and (3), it is impossible to clearly establish this. It is also worth noting, however, that later attempts by Akiyama and Naito [1987] to measure the pressure beneath an identical bed showed that there were significant phase differences between their experimental results and those of Gutman.

2.1.1.3 Instantaneous Measurement of Cyclic Pressure Variations Below the Bed

All models of the vibrated bed predict that the time-averaged gauge pressure below the bed should be equal to zero provided that porosity variations are not significant over a cycle of vibration. Measurements of the pressure below the bed by Chlenov and Mikhailov [1965] were made using a differential manometer mounted remotely from the vibrating vessel and connected to the bottom of the bed by a narrow tube. The measurements indicated that the average pressure below the bed was always below atmospheric. They attributed this observation to voidage variations during the flight period. As described in the previous section, they argued that the "air-pumping" effect produced by this average negative pressure below the bed was responsible for particle circulation in the bed. Gutman [1974,1976a], however, argued that this was in fact a false result observed because of the presence of a large volume of air in the tube (comparable to the volume of air in the gap below the bed) between the sampling point at the vessel floor and the pressure transducer. Gutman [1974] showed that if pressure transducers were mounted directly below the bed without the presence of a dead volume, the average pressure below the bed was actually about 3% above atmospheric.

However, as outlined in the previous section, it is possible that Gutman's pressure measurements contained some phase-lag errors. Gutman [1974] did check the pressure transducers for possible

phase-lag errors, but did not include in the test, the additional resistance that could be introduced by the fine-mesh screen that was used to keep particles from falling into the transducer.

2.1.1.4 Heat-Transfer Probes

The most common method for experimentally determining surface-to-bed heat-transfer coefficients is to immerse a heated probe into the bed, which exchanges a known quantity of heat with the colder bed. By measuring the surface temperature of the probe and the bed temperature, the heat-transfer coefficient may be calculated. As outlined in the previous chapter, a number of different heat-transfer surface geometries have been used. Deficiencies exist with many of the probe designs used in some previous studies of vibrated-bed heat transfer. These are discussed fully in the next chapter, but are summarized briefly as follows:

- The surface of the probe may not be isothermal due to the variation of the local surface-to-bed heat-transfer coefficient around the surface of the probe. This will cause a transfer of heat along the periphery of the surface, leading to errors in the measurement of the heat-transfer coefficient.

- Heating elements used in many probes have dead zones at either end where no heat is generated. This produces distortions in the heat flow at the ends of the probe, and may lead to non-isothermal conditions at the ends of the probe.

- The manner in which thermocouples used to measure the surface temperature of the probe are placed could introduce distortions in the heat fluxes within the probe. Grooves cut into the probe to carry thermocouple leads distort heat fluxes, since they are filled after the leads are inserted, with a material of lower thermal conductivity than the material of construction of the probe. Instead, if the leads pass into the bed, they may act as fins, sinking heat directly into the bed.

- If the probe is held in place by vertical supports, solid circulation patterns at the ends of the probe could be altered, particularly for fine particles. This could lead to severe end effects in the process of heat transfer from the probe to the bed.

2.1.2 Bed Dynamics

Different aspects of the bed dynamics are investigated to obtain a better understanding of the physics of the bed.

2.1.2.1 Validity of the Plastic Body Analogy

The primary assumption of almost all models for the vibrated bed has been that the bed behaves as a single plastic porous body. The plastic mass analogy assumes that the bed will lift off the base as a coherent mass, that is, the position of the center of gravity of the bed is always midway between the top and bottom bed boundaries, and also that there is no significant expansion of the bed.

Limits on this assumption have been suggested by various investigators. Upper vibrational limits of 200 Hz at 10g have been suggested by Gray and Rhodes [1972] because of the requirement that the bed-vessel collision process must be complete before lift-off in the following cycle. Obviously, if the bed has not completely collapsed, lower particle layers will attempt to lift off when top layers are still falling downward. A process of inter-layer collisions will occur, possibly resulting in a break-up of the uniformity of the bed. The upper frequency limit was based on a velocity of propagation of a stress-wave in a packed bed of 150 m/s. However, it is not certain if this velocity will be the same in a loose or fluidized bed.

A bed depth of 6 particle diameters has been suggested by Bachmann [1940] as a lower limit at which the bed will still behave as a coherent mass, that is, all particles in the bed will lift off the

base in concert producing an air gap between the bottom of the bed and the vessel floor. Below this limit, it is assumed that particles will tend to follow individual trajectories dictated by simple Newtonian mechanics. There has been little investigation of ultra-shallow beds, even though the radiant drying of pastes has been found to be best suited to bed depths of 1 to 5 mm [Volovik *et al.*,1975]. It is not clear if once this lower limit is exceeded and coherent behavior is established, whether the bed will then immediately act as a single plastic mass, or whether large cyclic voidage variations will persist for all bed depths which can be described as ultra-shallow.

Gutman [1974] postulates that deep beds ($L/D \gg 1$) at high frequencies and vibrational intensities might break up during the flight period due to the occurrence of tensile stresses in the bed. Pakowski *et al.* [1984] suggest that such large voidage variations may be the reason for the discrepancies between the pressure measurements of Gutman [1974,1976a] and those of Chlenov and Mikhailov [1965]—but see also chapter 5 for a fuller discussion.

It has been suggested that the vibrated bed does not lift uniformly off the vessel base as the plastic body analogy would require [Buevich and Galontsev,1978]. Instead, top layers of millet grains have been observed to lift off prior to lower layers of the bed [Kapustin *et al.*,1980]. Buevich and Galontsev [1978] have attempted to extend the usefulness of the plastic body analogy by including bed expansion into the analogy. It is possible to do this as long as the center of gravity of the bed is always maintained midway between the top and bottom boundaries of the bed, so that it will always be at the same position as the center of gravity of a single plastic mass that is *equivalent* to the bed. This is because models based on the plastic body analogy attempt to predict the motion of the center of gravity of the plastic mass. The above constraint on the relative location of the bed's center of gravity makes it necessary to assume that both upper and lower boundaries of the bed expand uniformly during flight. However, there are no reports in the literature of any detectable expansion at lower boundaries of the vibrated bed.

To summarize, the plastic body analogy will possibly break down in the following circumstances:

1. the bed-vessel collision process is not completed before the instant of lift-off in the following vibrational cycle.

2. large voidage variations occur during the cycle, which may cause the bed to break up, or for cavities to be created within the bed.

3. the expansion of the bed is non-uniform, so that the center of gravity of the bed is not always located half-way between the upper and lower bed boundaries.

For the purpose of determining the applicability of current models to shallow beds, or to formulate new models, it is necessary to establish by experimentation, the practical conditions which would introduce one or more of the conditions listed above, thus establishing limits on the validity of using the plastic body analogy.

2.1.2.2 Bed Mobility and Particle Circulation

The lowest value of the vibrational intensity parameter at which bed mobility is induced is called the critical vibrational intensity (K_{cr}). In large-particle beds, $K_{cr} = 1$, but for fine particles, K_{cr} can be much higher. The particle size below which the value of K_{cr} increases above unity is usually quoted to be 100 μm [Gutman,1974]; but it has not been established why this should be the critical particle size, or whether in fact it might also depend on other particle characteristics such as solid density and particle cohesiveness. Ur'ev [1978] has found that K_{cr} for particles with diameters of 2 μm and less, can be as high as 8. The addition of a surfactant to the system which reduced the inter-particle cohesive forces had the effect of reducing K_{cr} to a value of about 2. If additional energy is required to provide the shear needed to initially break up a cohesive bed, the energy required to re-vibrofluidize the bed once it has been aerated might be lower. There have been no studies to examine if K_{cr} exhibits such a hysteresis, but it would seem more likely in light of the evidence

suggested by Ur'ev [1978], that the value of K_{cr} is determined by the cohesiveness of fine powders, rather than simply by their particle sizes.

Once bed mobility is induced particles begin to circulate within the bed. Several investigators [Kroll,1954; Takahashi *et al.*,1968; Buevich *et al.*,1979; Kapustin *et al.*,1980; Muchowski,1980] have investigated the particle circulation, but there is disagreement on the types of particle circulation patterns that have been observed. Kapustin *et al.* [1980] have examined the particle circulation in beds with depths varying from 10 to 100 mm, using frequencies of 10 to 40 Hz, and vibrational intensities of 2g to 4.5g. They found that overall circulation patterns did not exist in beds of particles with a diameter less than 100 μm. Mixing in such beds was caused entirely by the passage through the bed of gas bubbles created by the gas-pumping action of the vibrated bed. This was also confirmed by Muchowski [1980] who described beds of 100-μm particles as being turbulent in nature, with the mixing in the bed being of a totally random nature. For particle sizes in the range of 100 to 1000 μm, Kapustin *et al.* [1980] observed a downward flow of particles at vessel walls, accompanied by an upward flow in the center of the bed. The downward flow at the walls extended only a few particle diameters into the bed. Therefore, to maintain a continuity of solids flow, the downward flow at the walls would have to be several times faster than the upward flows within inner regions of the bed; and this was in fact observed.

On the other hand, studies by Kroll [1954], Buevich *et al.* [1979], and Muchowski [1980] seem to suggest that the type of circulation patterns described by Kapustin *et al.* described above, are restricted to large-particle beds. They observed a different type of circulation pattern in small-particle beds, particularly those which exhibited a tendency to form a top surface that was not flat. In this type of circulation, particles move within lower sections of the bed from a shallow region toward the deeper region of the bed. The return flow from the deep to the shallow regions is mainly in a narrow section at the top surface of the bed.

In addition to different types of particle circulation patterns observed by various investigators, a number of different mechanisms have been suggested for the circulation patterns observed. These include the following:

- Muchowski [1980] attributes particle circulation to the differential frictional drag experienced by various layers of particles in the bed. During the initial period of bed flight, when it is moving upward relative to the vessel, the friction at the vessel walls tends to slow down the lift of wall-adjoining particle layers, thus inducing a relative downward motion in these layers.

- According to Chlenov and Mikhailov [1972], the downward flow of particles at the walls is caused by an *average* negative gauge pressure below the bed - which they had measured earlier [Chlenov and Mikhailov,1965]. The average negative pressure induces a flow of gas downward at the walls where the bed porosity is highest. The down-flow of gas drags particles in this region along toward the bottom of the bed. To maintain solid continuity, particles would have to move upward at all other regions of the bed.

- Gutman [1974] theorizes that particle circulation is caused by average differences in the pressure between various *horizontal* locations within the bed. However, Gutman never experimentally measured any horizontal pressure distributions within the bed, and was therefore unable to offer any experimental evidence for this mechanism.

- Particle movement in the vibrated bed has been attributed by Buevich *et al.* [1979] to *instantaneous* variations in the horizontal pressure distribution across the bed, which occur for only a part of the vibrational cycle. Since their explanation of particle circulation is closely related to bed bunkering, a fuller discussion of their proposed mechanisms are given in the following section on bed bunkering.

It is possible that more than one type of particle circulation and mechanism may be applicable. The exact type may depend on bed conditions as well as vibrational parameters. However, since

particle circulation has not been examined over a wide range of particle and bed parameters by any one study, observations of particle circulation and mechanisms remain inconclusive.

There appears to be no literature on particle circulation in ultra-shallow beds. Although Volovik *et al.* [1975] have observed intense solid mixing in such beds, they do not describe any particle circulation patterns.

It is clear that any solid object such as a heat-transfer surface that is immersed in the bed and fixed to the vessel will interfere with particle circulation. Sapozhnikov *et al.* [1976] attributed lowered local heat-transfer coefficients at the bottom of tubes to reduced particle circulation below the tubes, which they observed using X-ray analysis of the bed. Despite this, there have been no systematic studies of alterations to particle circulation caused by the presence of a heat-transfer surface within the bed.

2.1.2.3 Shape of the Top Surface of the Bed

Gutman [1974] has alluded to the possibility that the top surface of a vibrated bed might not be horizontal, but has not reported beds with such surfaces in his study. Kroll's [1954] observations indicate that in general, large particle beds will have an approximately level surface if vibrations applied to the bed are completely vertical. Small-particle beds, however, often exhibit "bunkering", that is, they tend to pile up in certain sections of the vessel so that the top surface of the bed is far from level. The bunkering observed by Kroll was in some cases so severe that certain areas of the floor of the vessel became uncovered. Buevich *et al.* [1979] also observed this behavior in small-particle beds. However, Pakowski *et al.* [1984] state that bunkering is common only in large-particle beds contrary to the observations of other investigators.

Bunkering can have important consequences on both mass and heat transfer within the bed. If the bed were to bunker in one section of the vessel, heat-transfer surfaces in other sections of the vessel

might become exposed, leading to drastic reductions in heat transfer. An externally induced gas flow that passes vertically upward through the bed for the purpose of mass transfer with the bed, will now bypass the bed in sections of the vessel where the bed depth is very shallow. As a consequence, the gas will have different residence times in various sections of the bed. On the other hand, bed bunkering can also have positive effects. If, as described in the previous section, particle circulation is caused by the motion of particles between regions of the bed of different depths, then bunkering will serve to improve particle circulation. This will lead to improved heat transfer rates if the heat-transfer surfaces remain immersed within the bed.

Despite this, there have been no studies of what factors affect bed bunkering. Possible variables that might affect bunkering include: particle size, particle density, bed depth, bed geometry, and properties of the gas atmosphere within the vibrating vessel. Although a particle-size effect has been noted as described above, none of the previous studies has established a critical particle diameter below which bed bunkering will occur. Owing to the lack of experimental information, adequate mechanisms that explain bunkering do not exist. Gutman [1974] has compared bunkering to the results of the U-tube experiment described in the previous chapter. He attributes bunkering to the slow movement of particles from one section of the bed to another, driven by average horizontal differences in pressure as described in the previous section. As particles move from one section to another, bunkering is enhanced in regions of the bed that the particles move toward. However, as stated in the previous section, Gutman has no experimental evidence of such average pressure variations in the horizontal direction to support this hypothesis. Buevich *et al.* [1979] ascribe the occurrence of bunkering to micro-instabilities induced in the bed as a result of perturbations in the pressure field within the bed. The micro-instabilities manifest themselves as "humps" on the bed surface. As a result, circulating gas flows are said to develop, in which gas penetrates the bed through the valleys between humps and exit through the humps. Particles which are entrained by these gas flows move in the same direction, leading to a deepening of valleys and a growth of the humps. This eventually leads to large-scale bunkering within the bed. However, causes of perturbations in the pressure field are not clearly explained.

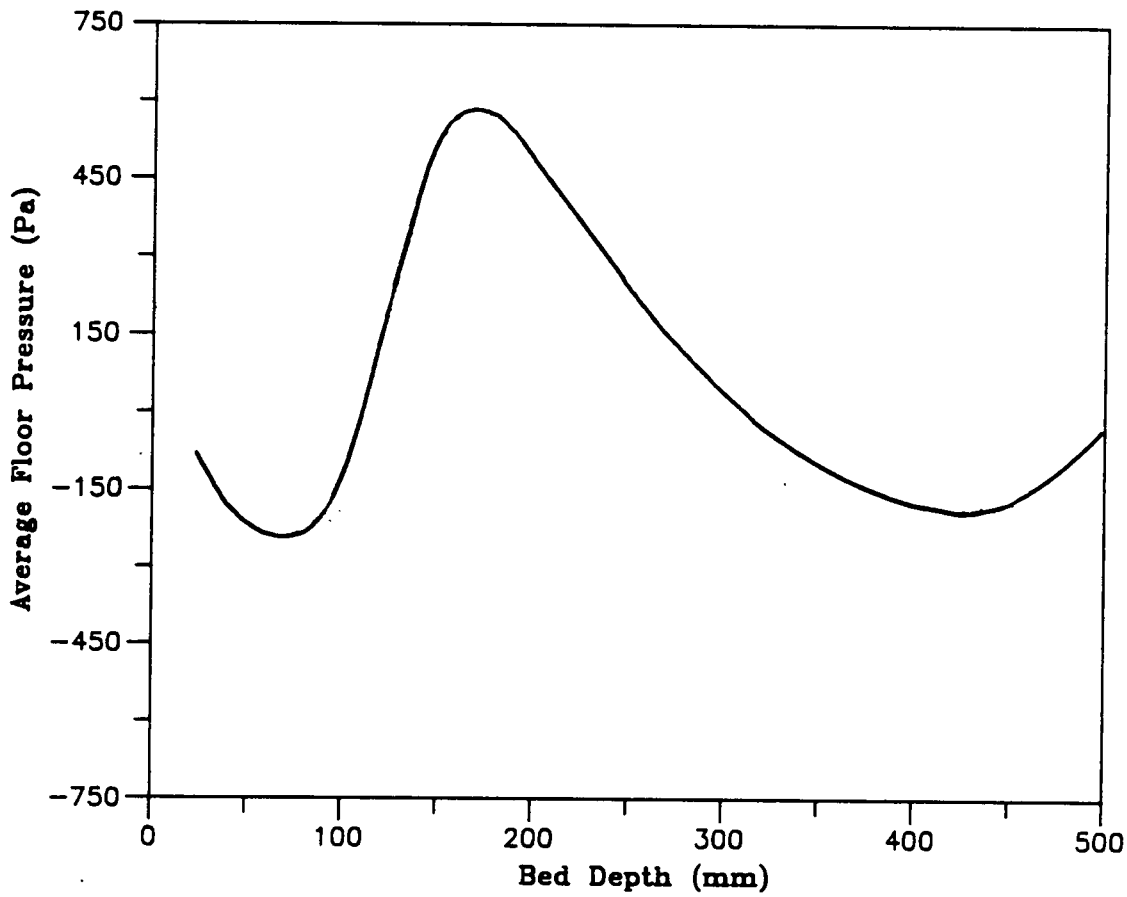

Figure 8. Dependence of average floor pressures during flight on bed depth: Bed of 80-μm corrundum particles vibrated at a frequency of 20 Hz, with $K = 4.35$. [Buevich *et al.*,1979].

Buevich *et al.* [1979] therefore correlate the limit in the growth of a bunker to the average floor pressure during bed flight. A plot of this variable as a function of bed height (as experimentally measured by them) is given in Figure 8 on page 41. The curve goes through a number of maxima and minima over a bed height of 0.5 m. Buevich *et al.* performed a series of experiments in which two beds of initially different depths were separated by a solid vertical barrier except for a narrow slit along the bottom. When the beds were vibrated together, final bed heights on either side of the barrier were determined by the value of the average floor pressure during flight, beneath each side. If the initial bed depths were L_1 and L_2 , such that $L_2 > L_1$, and the average pressures beneath the two beds during flight were $\overline{P}_f(L_1)$ and $\overline{P}_f(L_2)$, respectively, particles were found to move from the shallower bed to the deeper bed if $\overline{P}_f(L_1) > \overline{P}_f(L_2)$. According to Figure 8, this would be the case if for example, both beds were less than 60 mm deep. On the other hand, if both L_1 and L_2 were greater than 60 mm (but less than 180 mm), $\overline{P}_f(L_1) < \overline{P}_f(L_2)$. In this case, the two beds tended to equilibrate to a common average value, since the movement of particles was now from the deeper to the shallower bed. The situation again reversed beyond a bed depth of 180 mm. However, Buevich *et al.* caution against extrapolating this behavior of two one-dimensional beds that are interconnected only along the bottom, to the general case of bunkering in a two-dimensional bed. In the two-dimensional bed, horizontal pressure gradients can develop throughout the height of the bed, and not just at the bottom.

Pakowski *et al.* [1984] have described three final bed surface configurations that result as a consequence of bunkering - see Figure 9 on page 43. It is not known whether these are the total number of possible surface configurations, or if a particular surface configuration will result given a set of bed conditions.

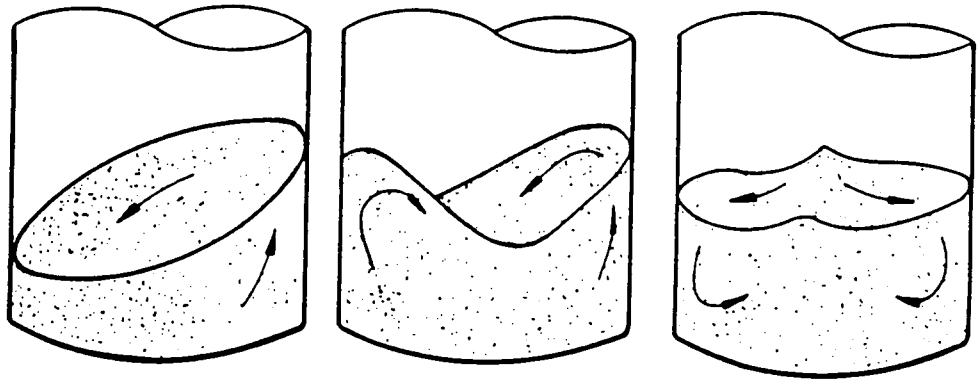

Figure 9. Possible configurations of the vibrated bed: The shape of the top surface of the vibrated bed as experimentally observed by Pakowski *et al.* [1984].

2.1.2.4 Appearance of the Vibrated Bed

As described in the previous chapter, different forms of vibrofluidization have been observed by various investigators. Each of these forms represent different physical appearances of the vibrated bed, and can be summarized as follows:

Vibromobility The slight mobility of the bed which occurs when $K < K_{cr}$, usually accompanied by some compaction of the bed caused by particle rearrangement [Chlenov and Mikhailov,1972].

Vibrofluidization When $K \geq K_{cr}$, the bed becomes very mobile, and overall particle circulation patterns are observed in the bed.

Vibroboiling At high values of K, the gas flows through the bed induced by bed vibrations (the so-called "air-pumping effect") can exceed the minimum fluidization velocity u_{mf} for the bed. At this point, the bed has an appearance of being gas-fluidized. If the velocity of the induced gas flow exceeds the minimum bubbling velocity u_{mb}, bubbles are created within the bed, giving an impression of a boiling bed.

These observations have been made over a wide range of bed depths ranging from 10 mm to over 1 m, a variety of particle sizes ranging from 2000 μm to sub-micron sizes, different particle densities, bed configurations, and vibrational conditions. However, it has not been established whether vibrofluidization characteristics are in any way affected by one or more of the factors listed above, with the exception of the vibrational intensity parameter for which a clear dependence has been established. It is also not certain if finer sub-divisions of bed behavior than those outlined above exist, nor is it known if all these forms of vibrated-bed behavior persist for ultra-shallow beds.

2.1.3 Heat Transfer

Botterill [1975] has observed that surface-to-bed heat-transfer coefficients in a gas-fluidized bed are strongly affected by several factors including the geometric design of the fluidizing vessel, and the heat-transfer surface. As the brief review in the previous chapter shows, this is certainly the case with vibrated beds as well. For that reason, it is important to obtain an understanding of factors influencing heat transfer from immersed surfaces. However, studies of the heat-transfer mechanisms must be undertaken in laboratory systems that are representative of commercial applications, since it is possible that the mechanisms might be altered by drastic changes in the design of the heat-exchange system.

2.1.3.1 Geometry of the Heat-Transfer Surfaces

It is clear from the results of various investigators reviewed in the previous chapter [Kal'tman and Tamarin,1969; Kossenko *et al.*,1975; Muchowski,1980; Bukareva *et al.*,1969; Gutman,1974] that the geometry and orientation of the heat-transfer surface within the bed strongly affects the measured heat-transfer coefficient. The heat-transfer coefficient is influenced by these factors because:

- Air gaps form around horizontal surfaces immersed in the vibrated bed. Thus, the heat transfer to the bed from the surface may be hindered by the additional resistance provided by the air gap.
- The presence of the heat-transfer surface within the bed interferes with the overall solid circulation patterns. This sets up different circulation patterns as well as dead zones - regions of little or no particle circulation - in the locality of the heat-transfer surface.

Therefore, the heat probes used must reflect the geometric design of heat-transfer surfaces that might be commercially used. This would include horizontally oriented cylinders (tubes), vertical

surfaces that might represent fins and container walls. Measurements of heat transfer from the floor [Muchowski,1980] and from flat horizontal surfaces [Gutman,1974; Bukareva *et al.*,1969] indicated that because of poor heat-transfer rates, there is little practical use for such surfaces, unless vertical fins are attached. In any case, spherical surfaces such as those used by Kal'tman and Tamarin [1969] are of limited practical use.

2.1.3.2 Mechanisms Controlling Heat Transfer

Previous studies have attributed observed trends in the data on heat-transfer coefficients to different factors. For example, Kal'tman and Tamarin [1969] using a packet-type model for the heat-transfer process, suggest that the contact time of particles with the heater surface is the controlling factor. The contact time is determined for a given length of the heater surface by the average particle velocity. Small-scale fast circulation loops were observed in the vicinity of the heater. These loops were smaller than the length of the heater. Therefore, Kal'tman and Tamarin [1969] argued that the contact time should be determined by the length of those circulation loops, and the average particle velocity within them.

In a study of the thermal diffusivity of vibrated beds, Tamarin and Kal'tman [1971] equated the dynamic vibrational energy input to the bed ($z_o^2\omega^3$) to the kinetic energy of particles in the bed. By doing this, the root-mean-square value of the particle velocity was shown to be proportional to $z_o\omega^{1.5}$. This group is similar to the group ($z_o\omega^{1.6}$) used in equation [1.6] to determine the locus of the maximum heat-transfer coefficient. Tamarin and Kal'tman argued that this clearly suggested that the heat-transfer process was controlled by the velocity of particles in the circulation loops.

However, Gutman [1974], using a flat vertical heater, did not observe any local circulation loops in the vicinity of the heater surface. As a result, he argued that the contact time should be determined by the length of the heater surface and the average overall particle circulation velocity. Using this definition of the contact time, the packet model of Kal'tman and Tamarin [1969] predicted heat-

transfer coefficients of 125 W/m^2-K that were much lower than the value of 400 W/m^2-K experimentally determined by Gutman [1974]. Gutman [1976b] suggested instead that the major resistance to heat transfer came from the presence of thin gas films between the heater surface and particle layers adjacent to the surface. Note that these films are formed as a consequence of the packing of spherical particles at the heater surface and are *not* the same as air gaps that form around horizontal heating surfaces. The scraping of these thin gas films at the vertical heater surface, caused by the vibrational motion of the particles next to the surface, was considered responsible for improving the heat transfer in a vibrated bed over those measured in a packed bed of identical particles. Gutman's model of heat transfer, therefore, assumes that the particle circulation - both overall and in the vicinity of the heater - makes no contribution whatsoever to the heat-transfer process. Although Gutman [1976b] got reasonable agreement between his experimental results and his mathematical model, it is worth noting that a number of constants in the model were experimentally fitted, and also that the model, which correlates heat-transfer coefficients indirectly with the vibrational intensity through the thickness of the air gap at the bottom of the bed, implicitly contains the particle circulation velocity which is a function of the vibrational intensity.

The formation of air gaps around flat horizontal heat-transfer surfaces have been assumed to be responsible for a reduction in the heat transfer from such surfaces [Gutman,1974; Muchowski,1980; Bukareva *et al.*,1969]; but Sapozhnikov *et al.* [1976] have attributed lower heat transfer coefficients measured at the bottom of horizontally placed tubes, to lower particle circulation velocities which they observed below the tubes. They do not appear to have noticed the formation of any air gaps around horizontal cylindrical surfaces, although more recent studies [Malhotra and Mujumdar,1985] show that such air gaps do appear to surround tubes placed horizontally within the bed.

2.2 *Objectives of This Study*

The review of the literature on past studies outlined in preceding sections of this chapter show that many vibrated-bed phenomena are currently inadequately explained. There are many ambiguities in the data of some studies; the observations and conclusions of different investigators are often in conflict. To remedy this situation and permit a better understanding of the dynamics of the vibrated bed as well as heat-transfer mechanisms, the objectives outlined below are undertaken in this study.

2.2.1 Development of Equipment to Yield Unambiguous Results

The specifications on the equipment and instrumentation designed to meet this requirement include:

1. Construction of a vibration system that will easily allow examination of the bed at different frequencies and over a practical range of vibrational intensities. This suggests the use of an electromagnetic vibrator.

2. Design of the vibrating system so that distortions in the displacement waveform that occur during the bed-vessel collision (for example as observed by Gray and Rhodes [1972]) are avoided.

3. Design of an electronic circuit that would be capable of producing a trigger pulse that could be correlated with the phase of the vessel displacement. This would permit easy and accurate phase correlation of the output signals of transducers used to measure various properties of the vibrated bed. The design of the circuit would also allow for the trigger pulse to be output at

any phase angle, so that the bed could be observed at any given phase angle, as will be explained further in the next chapter.

4. Eliminate all sources of phase-lag and amplitude-modulation errors in the systems used to measure various properties of the bed. This is particularly true of pressure transducers in view of the controversy surrounding the average pressures below the bed. If the phase lags cannot be eliminated by design—for instance, if they are inherent in the design of the transducers—then, they must be measured accurately at the frequency of vibration, so that they can be computationally eliminated during data acquisition.

5. Design of a heat-transfer probe that is representative of surfaces that may be used in commercial applications. This suggests a horizontally placed cylindrical surface, since tubes are most commonly used in practical heat exchangers. The probe should be designed so that the heating element does not produce any end effects, and the manner in which thermocouples are placed in the probe must not interfere with heat fluxes. The supports that hold the probe within the bed should not interfere with particle circulation patterns at the ends of the probe.

The equipment and instrumentation designed for use in this study to the specifications listed above are described in Chapter 3.

2.2.2 Study of Vibrated-Bed Dynamics

The dynamics of the vibrated bed must be carefully observed and possible mechanisms formulated to explain the observations. This covers the following:

1. Examination of bed behavior under varying conditions, as a function of the phase angle. This will show how the bed dynamics change through a vibrational cycle, that is, on a micro-time scale.

2. Examine the behavior of shallow and ultra-shallow beds as a function of particle properties, bed depth, pressure of the gas in the vibrating vessel. Such a study will indicate if different "states" of the vibrated bed exist, and if they do, whether they can be correlated to dimensionless groups of the factors influencing bed behavior. The dependence of the critical value of the vibrational intensity parameter (K_{cr}), at which there is a transition from the packed bed state to a state of vibrofluidization, on various parameters needs to be determined.

3. Measurement of the cyclic pressure variations below the bed at various locations along the width of the bed, to determine if there are horizontal gradients in the pressure field within the bed. This information could be used to explain the particle circulation patterns and bed bunkering.

4. As described previously, bed bunkering might affect the heat- and mass-transfer characteristics of the bed in many ways. It is therefore necessary to determine the combination of factors that might cause bed bunkering, and be able to predict the nature of the bunkering in light of the measurements of cyclic pressure variations in the bed.

5. Obtain particle circulation patterns in the bed under different conditions. Suggest possible mechanisms that cause particle circulation and by identifying factors that influence the circulation. This hopefully, will allow particle circulation patterns to be predicted in other vibrated-bed geometries.

6. Determine if there are any limits on the applicability of the plastic body analogy as far as shallow and ultra-shallow vibrated beds are concerned.

Experimental procedures to study the dynamics of the bed are outlined in Chapter 4. Observations of the bed dynamics and suggested mechanisms, as well as mathematical formulations of the mechanisms are given in Chapter 5. Recommendations for further experimental work and theore-

tical analysis to extend the understanding of vibrated-bed dynamics beyond this study are given in Chapter 7.

2.2.3 Heat Transfer from Heated Tubes to Shallow Vibrated Beds

A study of the heat transfer from horizontally placed cylindrical heat-transfer surfaces to shallow vibrated beds must include the following:

1. Repeatable measurements of heat-transfer coefficients from the immersed tubular surface to beds of different particle types and sizes as a function of vibrational parameters.

2. Examine the size and coverage of the heat-transfer surface by air gaps; and also if these properties of the air gaps vary with phase angle during a vibrational cycle.

3. Determine the possible effects of particle circulation on heat transfer. To do this, the overall particle circulation must be mapped as described in the previous section, but also the variation of particle circulation in the locality of the heat-transfer surface must be examined. The occurrences of any "dead zones" of particle circulation in the vicinity of the heat-transfer surface must be mapped since they are detrimental to heat transfer.

4. Observe the contact time of particles at the heat-transfer surface, and how particles mix into the rest of the bed after contacting the heating surface. This will identify the paths of heat transfer from the surface into the bed.

Details of the experimental procedures used to measure the surface-to-bed heat transfer coefficients and also to determine the effects on heat transfer of the factors outlined above, are given in Chapter 4. A discussion of the manner in which the factors given above affect heat transfer is given in

Chapter 6. Work that would further enhance the understanding of vibrated-bed heat-transfer is suggested in chapter 7.

3.0 Equipment and Instrumentation

The equipment used in this study may be divided into three broad categories:

(i) Vibration Equipment: The equipment used to create the mechanical vibrations applied to the bed, as well as the mechanical structure used to support the bed and containing vessels.

(ii) Vibrated-Bed Containers: The solids to be vibrated are placed into these containers, which are then mounted onto the vibrating assembly and subjected to mechanical vibrations in order to levitate the particles.

(iii) Instrumentation: Several instruments of varying types are used to extract information about the nature of the bed, its behavior during a cycle of vibration, as well as to measure physical quantities such as the pressure drop across the bed and heat-transfer coefficients for various surfaces immersed within the vibrated bed, among others.

3.1 The Vibration System

The vibration system consists of the equipment used to generate mechanical vibrations, and the support structure for the vibrated bed and container. The support structure is designed to guarantee that the motion of the containing vessel is absolutely vertical, and to allow for the system to be adjusted so that it will be close to resonance at the forcing frequency.

The waveform is electronically generated on a WAVETEK function generator, capable of generating frequencies up to 4 MHz. The signal is then amplified by a CROWN DC-300 series power amplifier. The amplifier is capable of generating 300 Watts of output power; although full power was never used in practice during this study. The amplified signal is used to drive a Vibration Test Systems VG-100 electromagnetic vibrator which provides the mechanical vibrations required to create the vibrated bed.

As indicated in Figure 10 on page 55, the vessel containing the vibrated bed is mounted on a circular titanium plate which in turn is suspended by up to eight leaf springs. The leaf springs are attached at one end by quarter-inch bolts to specially designed L-shaped mounting bracket assemblies onto the massive outer steel cylinder surrounding the electromagnetic vibrator. As shown in Figure 11 on page 56, the L-shaped mounting brackets allow both radial and circumferential movements of the leaf springs. This permits precise alignment of the leaf springs relative to the steel cylinder. This allows for the titanium plate to be correctly centered within the cylinder, and also for the leaf springs to be angled normal to the circumference of the titanium plate. The other end of the leaf springs are attached by quarter-inch bolts to the titanium plate. Fine adjustments can be made to the tension of a leaf spring by slightly varying the torque on the No.8 screw at the end of the spring which is attached to the titanium plate (Figure 10 on page 55). After the springs and the plate are aligned, a symmetric arrangement of the springs around the titanium plate ensures that its motion is restricted to the vertical direction because of the evenly and symmetrically distributed

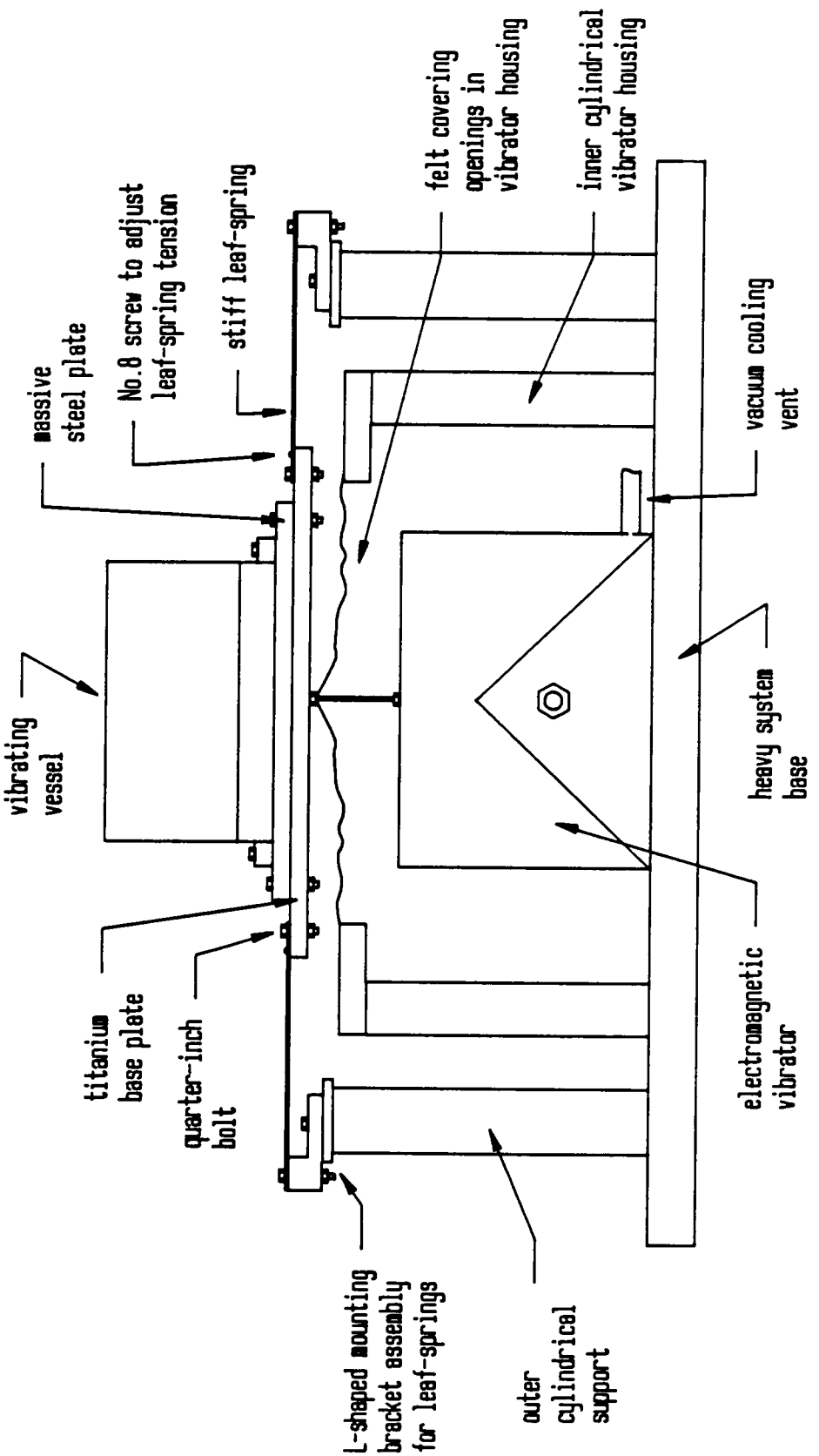

Figure 10. Schematic drawing of the vibrated-bed system: The drawing shows the details of the vibrating system, with a cylindrical vessel attached to the vibrating table

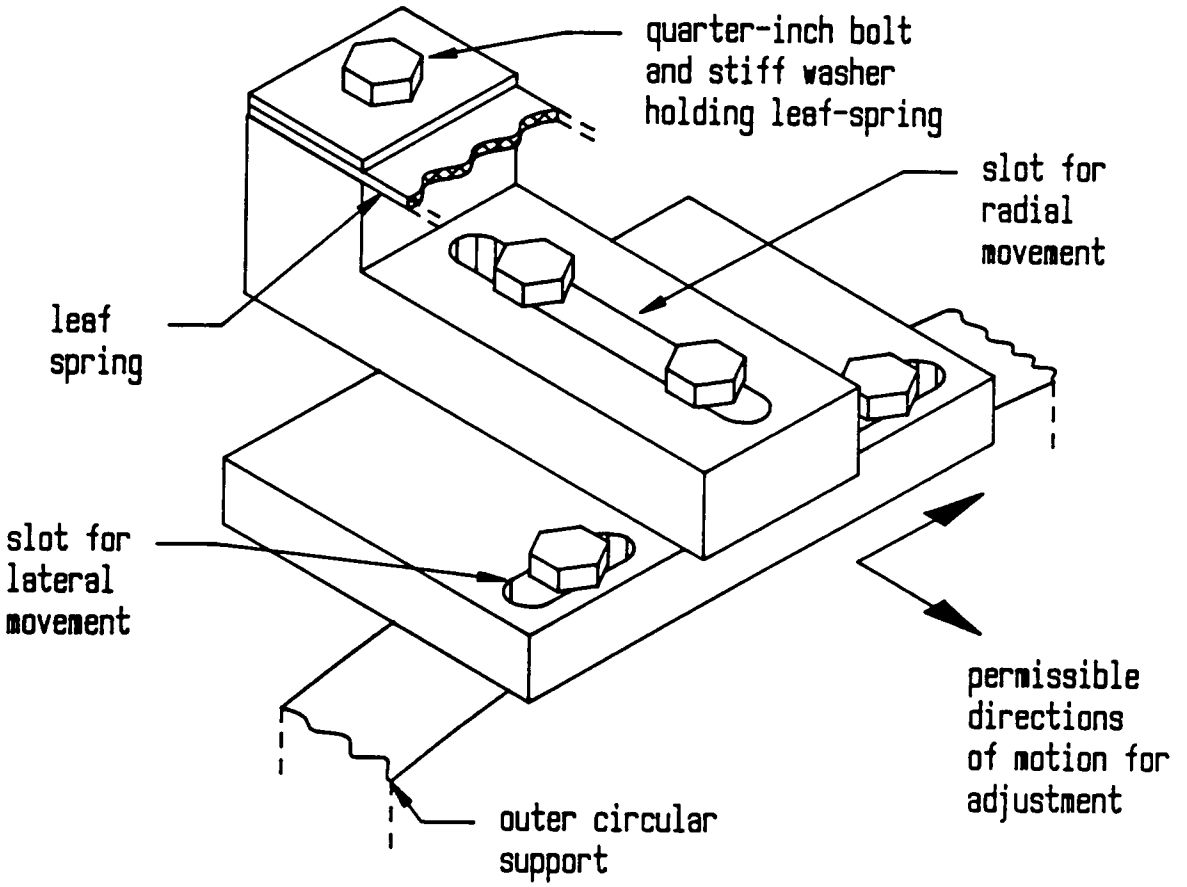

Figure 11. Leaf-spring mounting bracket assembly: The L-shaped mounting bracket assembly allows precise alignment of the leaf-spring in all directions.

spring constant, and the high stiffness of the leaf springs in the horizontal direction. In addition, if the springs are not skewed (that is, they are set normal to the circumference of the titanium plate), a turning moment on the plate is avoided during vibration.

The first design for the system used linear bearings in an attempt to restrict the vibrations to the vertical direction. The bearings were placed on the circumference of the titanium plate, and rode on vertical shafts attached to the inner steel cylinder However, the bearings were susceptible to mechanical wear at a high rate due to the vibration, and would soon start to "chatter" introducing minor secondary vibrations into the system. It was also found that the centering of the titanium plate and the precise alignment of the leaf springs were more important in reducing non-vertical vibrations in the system, and therefore the bearings were removed.

The titanium plate is mechanically coupled to the vibrator, but the weights of the plate and bed are not supported by the vibrator since the plate is suspended by the leaf springs. Initially, a stiff coupler was used, but this required precise alignment of the vibrator and the titanium plate because the motion of the plate must be restricted to the vertical direction. However, such accurate alignment is impossible mainly because the vibrator is extremely unwieldy. A lack of alignment induces a lateral stress onto the vibrator coils and will eventually result in their damage. To prevent this, a flexible coupler made of a piece of thin steel rod, 60 mm in length and 1.54 mm in diameter, is now used. This permits sufficient flexibility that the center of the titanium plate could be up to a quarter inch off the center of the vibrator without any detrimental effects to the vibrator coils. However, it is stiff enough in the vertical direction, that the vertical motion of the vibrator is efficiently transmitted to the vibrating table.

If the resonance frequency of a vibrating system is close to that of the forcing frequency, the amount of power required to drive the system is greatly reduced. In addition, effects of secondary vibrations (or mechanical "noise") of another frequency are reduced if the system is at resonance. Since the vibrating assembly is a spring-mass system, its resonance frequency is fixed by the mass of the assembly (titanium plate, bed, etc.) and the combined spring constant of the leaf springs. The mass

of the system can be increased by adding weights to the vibrating assembly in the form of heavy circular steel plates that are attached onto the top of the titanium plate as shown in Figure 10 on page 55. The added mass must have a symmetric weight distribution about the center of the titanium plate in order to prevent a turning moment on the vibrating system in the vertical plane. The stiffness of the system (the combined spring constant) may be adjusted by using leaf springs of a different stiffness, or by varying the number of springs as long as the symmetry of the system is maintained. Thus, eight, six, or four springs could be used. Since much of this study is done primarily at 25 Hz, the system is always maintained at this resonance frequency.

If the mass of the vibrated bed is significant compared to that of the vibrating table, the cyclic collision of the bed and vessel will cause a distortion of the displacement waveform of the table. To prevent this, the initial mass that is added onto the titanium plate is as large as necessary to eliminate any waveform distortion for a particular bed - usually several times the total weight of the particles in the bed. Using that mass as a starting point, either more mass is added to the system, or the stiffness of the springs and the number of springs used are varied to achieve resonance at 25 Hz.

The entire vibrating system is fixed onto a heavy rectangular steel plate. There are four leveling screws located at the corners of the plate, which are used to keep the vibrating system level. The steel plate in turn rests on a massive concrete block (0.91 m × 0.91 m × 1.22 m) placed on a wooden skid. The concrete block acts as an infinite mass to absorb vibrations from the vibrator that propagate downward, and the wooden skid further dampens this vibration, so that vibrations are not transmitted to the building.

In order to keep the coils of the vibrator cool, at least 35 cfm of cooling air must be drawn down through the vibrator casing across the coils. This air is drawn through by a venturi-type device attached to the end of the vacuum cooling line shown in Figure 10 on page 55. To prevent small particles from being drawn into the vibrator, all openings to the vibrator are covered with felt.

3.2 Vibrated Bed Containers.

A number of different bed containers have been used in this study, but essentially two geometries are employed — a three dimensional cylindrical geometry, and a "two-dimensional" rectangular geometry in which the depth of the bed is very small compared to other dimensions.

3.2.1 The Cylindrical Vessel

The three-dimensional bed container is shown schematically in Figure 12 on page 60, together with some of the auxiliary instrumentation for measuring heat-transfer coefficients for which it is primarily used. The vessel is made of a 170-mm open plexiglas cylinder attached onto a thin steel base. The base is raised within the inner circumference of the cylinder, so that it provides an elevated floor, and it has a lip that extends beyond the outer circumference of the cylinder by 13 mm. The lip has eight equally spaced holes drilled on it to attach the vessel to the vibrating table assembly as indicated in Figure 10 on page 55.

A quarter-inch thick plexiglas lid with several large holes in it is placed over the top of the cylindrical bed. Thermocouples for measuring the bed temperature are hung down from this roof at various locations into the bed. The thermocouples are strengthened, so that they do not move around due to the vibrations and the particle motion in the bed, by sheathing them with small-diameter thin-walled aluminum tubes that are attached to the plexiglas lid. The sheaths do not extend into the bed since, they would sink heat from the bed in the locality of the thermocouple and thus give false (lowered) bed-temperature readings.

As indicated in Figure 12 on page 60, the heater tube and supports extend through the diameter of the vessel, with the center of the heat-transfer tube being 20 mm above the floor of the vessel.

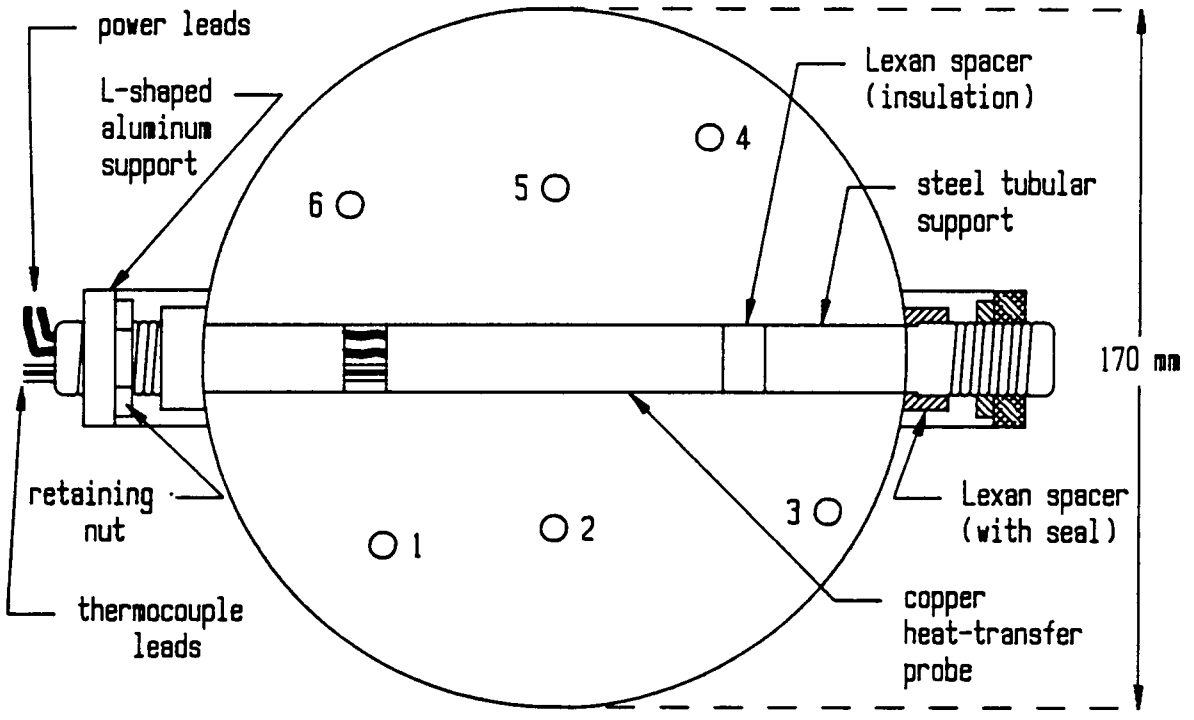

Figure 12. The cylindrical vibrated-bed vessel: A top view of the cylindrical vessel showing the heater tube and supports. The approximate locations of thermocouples in the bed are shown as black circles: Thermocouples 2 through 5 are level with the center line of the heat-transfer tube; thermocouples 1 and 6 are in line with the upper and lower edges of the tube respectively.

The tube is supported at either end by L-shaped aluminum supports which are attached to the lip of the steel floor of the cylindrical vessel.

3.2.2 Two-Dimensional Vessels

Three types of two-dimensional vessels are used for the following purposes:

- General observation of the bed behavior as a function of various parameters.
- Measurement of the floor pressures below the vibrated bed.
- Observation of solid circulation patterns.
- Observation of the bed under lowered pressures and in different gas atmospheres.

All the vessels have the same basic dimensions shown in Figure 13 on page 62. As the depth of the vessel (25.4 mm) is small compared to its other dimensions, the two-dimensional vessel is intended to represent a "slice" across a three-dimensional bed. Reducing the bed depth further would make the bed even more "two-dimensional", but there is a danger that wall effects caused by the large front and back walls could induce unrepresentative bed behavior. The depth used is chosen as a compromise between these two conflicting requirements. However, as will be shown later, the presence of any containing walls around large-particle beds causes a wall-effect on the circulation patterns that extends a few particle diameters into the bed. Therefore, true two-dimensional bed behavior cannot be attained in such beds - at least as far as the solid circulation is concerned.

As shown in Figure 13 on page 62, a dummy heat-transfer tube could be placed across the bed by attaching it to the front and back walls. This dummy tube simulates the effect of the actual heat-transfer tube on bed behavior in the three-dimensional beds. Experiments are performed in all three types of two-dimensional beds both with and without the dummy tube in place.

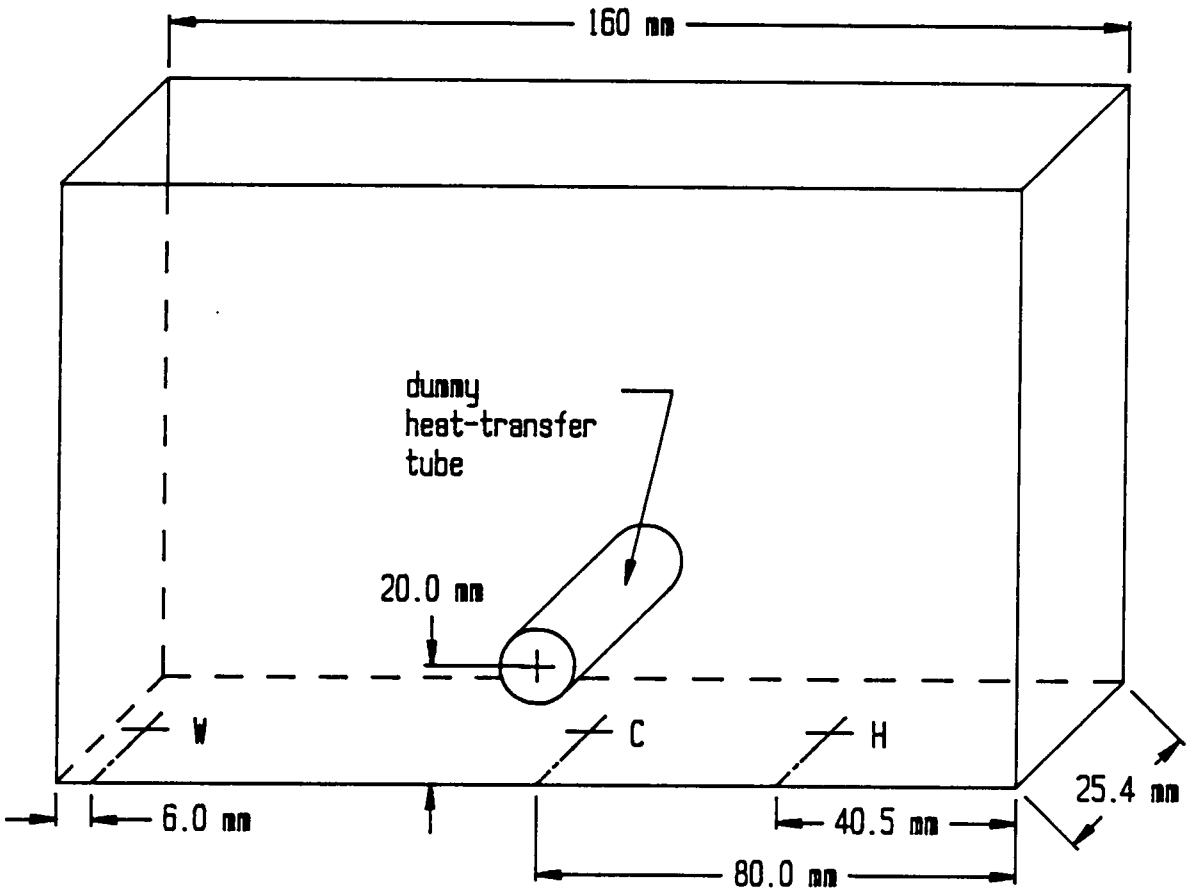

Figure 13. Schematic drawing of the two-dimensional vibrated-bed vessel: The locations of the pressure sampling ports on the floor are indicated by a '+'. A dummy heat-transfer tube is placed across the vessel, but may be removed if desired.

3.2.2.1 Vessel for Floor Pressure Measurements

This vessel shown schematically in Figure 13 on page 62, has quarter-inch plexiglas walls on the front and back to permit general observation of the bed. The side walls and bottom are aluminum, and the top is open. There are three ports for measuring pressures beneath the bed, located on the floor at the points marked with a "+" in the drawing. The three ports allow the floor pressures to be sampled at a location close to the wall (position W), at the center of the vessel (position C), and half-way between the wall and the center (position H).

The ports are made by drilling small holes 0.8 mm in diameter through the base of the vessel which is 12.5 mm thick. However, the lower 9.3 mm of the hole are enlarged to a diameter of 5 mm to accommodate the sampling ports of the pressure transducers used. Therefore, the actual pressure sampling points are located 3.2 mm below the floor of the vessel. Previous work [Gutman,1974] has indicated that the volume of gas in the sampling port must be kept to an absolute minimum, since the presence of a large volume will introduce a capacitance into the measurement that is sufficient to produce an error in the sampling of floor pressures which are varying cyclically with frequencies of 20 Hz or greater.

The top 3.2 mm of the ports are stuffed with loosely packed steel wool to prevent particles form falling into the pressure transducers. It is found that covering the top of the port with a mesh fine enough to keep out the smallest particles used (20 μm in diameter), would introduce a resistance into the measurement capable of causing a few degrees of phase lag in the output. The steel wool, on the other hand, keeps the particles out because of the tortuosity of the passages within it, but is open enough not to cause any phase-lag errors. Details of the transducers used for pressure measurements and techniques used to determine the presence of any phase lags are discussed later in Section 3.3.2.

3.2.2.2 Vessel for Circulation and Ultra-Shallow Bed Studies

The plexiglas vessel described above is sufficient for the examination of most particle beds. However, for ultra-shallow beds with a depth of up to 500 microns, and for light particles such as fluid cracking catalyst (FCC), the static induced on the wall by the rubbing of the bed material with the wall, causes particles to stick to the wall, greatly reducing the visibility of the bed. To overcome this problem, another vessel with plate glass is used. This is found to reduce the static problem to negligible levels, thus permitting the observation of bed behavior as a function of bed height, even for heights as small as a mono-layer of particles.

The vessel consists of a four-sided rectangular shell made of half-inch thick aluminum that provides the base, the two narrow side walls, and a roof with a large opening (12.7 mm wide and 152 mm long) cut through it to permit access to the bed. The front and back of the shell are open, and an O-ring is located in a groove running along the width and height of the bed on both the front and back of the shell (see Figure 14 on page 65). The front and back walls are inserted into frames that are screwed down onto the shell, thus pressing the walls flush against the shell.

This vessel also allows a technique (described in detail in the next chapter) for mapping bed circulation and inactive zones in the bed using fluorescent tracers illuminated by ultra-violet light. The quarter-inch plexiglas walls absorb so much of the UV light that practically none of it reached the bed to illuminate the tracers; but with this vessel, quartz-glass walls which are essentially transparent to UV light may be used instead.

3.2.2.3 The Vacuum Bed Container

The "vacuum" container is essentially of the same design as the glass-walled vessel described above, except that the top of the aluminum shell is closed other than for a pipe fitting that allows a vacuum hose to be connected to the vessel to evacuate the air within it. The O-ring seals are also designed

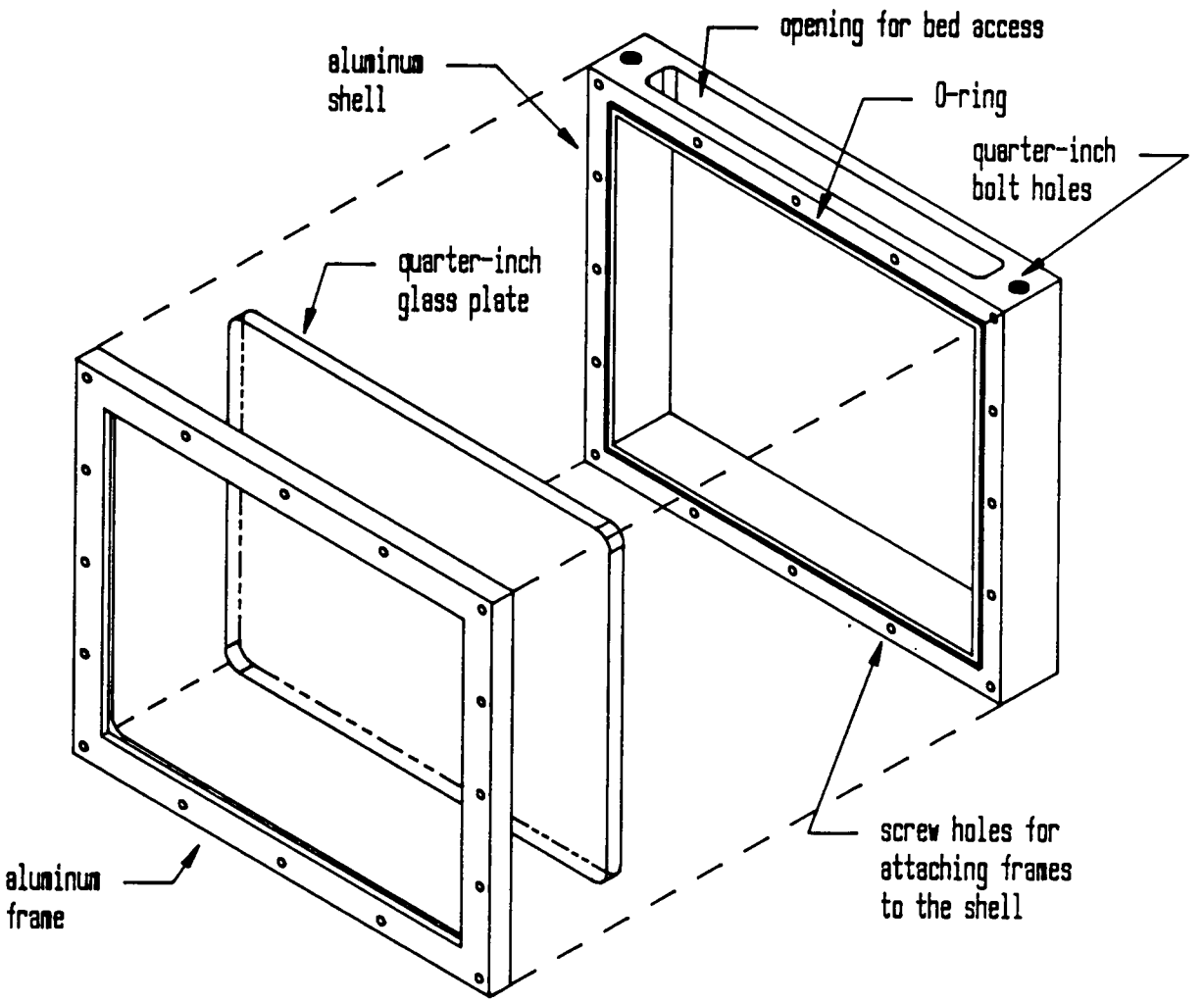

Figure 14. The two-dimensional glass-walled vessel: The components of the two-dimensional glass-walled vessel. The rear wall (not shown) is symmetric to the front wall.

to a greater tolerance and smeared with high-vacuum grease to prevent any leaks of air into the system. Particles are loaded into the bed by first removing the connecting hose and dropping them into the vessel through the pipe fitting.

Although this vessel has been described as a vacuum vessel, the hose connected to the vessel passes into a two-way valve which permits air to be drawn out in one position, and readmitted into the vessel in the other. It is therefore, possible to change gas atmospheres within the vessel by first evacuating the air from within the vessel, and then reintroducing another gas into the vessel. This allows examination of the bed at various pressures below atmospheric, as well as under different gas atmospheres.

3.3 Instrumentation

Several instruments are used in this study, both to measure physical quantities such as the pressure within the bed, bed properties such as heat transfer coefficients, as well as to aid in a detailed examination of phenomena occurring within the bed. Most of the physical quantities and observed phenomena are cyclic in nature and change rapidly within a small time interval. At 25 Hz, a resolution of one degree within a cycle corresponds to approximately 0.1 millisecond, so that the instruments used are required to have a fast response relative to the frequency of vibration.

3.3.1 Measurement of Vibrational Parameters

The bed acceleration and vertical displacement are measured independently of each other. The vibrational frequency is set on the waveform generator, but a check on the frequency is made by measuring the period of either the acceleration or vertical displacement signal on an oscilloscope.

3.3.1.1 Measurement of Vessel Acceleration

The vessel acceleration is measured by means of an accelerometer. A typical accelerometer consists of a quartz crystal placed in-between a base and a mass. When the device is subjected to an acceleration, the force applied on the crystal by the mass varies with the acceleration. The quartz crystal generates a voltage or charge that is proportional to the applied force and thereby to the acceleration. Usually, the output from the crystal is very small and needs to be amplified.

A Scientific Atlanta DYMAC M90 accelerometer is used in this work. This accelerometer has an internal amplifier, so that a high-level voltage signal can be monitored. This makes the measurement less susceptible to noise than if external amplification were used. The accelerometer has a sensitivity of 100 mV/g, and is linear in the frequency range of 2 to 5000 Hz.

It is important to note that since the output from the accelerometer results from the force applied on the quartz crystal by the mass, an impulse force will appear as a large acceleration pulse in the output. For example, if a few particles are dropped onto a static plate, the accelerometer output will show large sharp peaks corresponding to the collision between a particle and the plate. Therefore, the accelerometer's output signal is almost always noisy because of the constant collisions between the particles and the vessel during vibration. The noise manifests itself as a higher frequency with an amplitude usually smaller than that of the vibrational frequency superimposed onto the vibrational waveform (see Figure 15 on page 68). This noise is not the same as the distortion of the waveform of the vibrating table that results from a collision between a heavy bed and a light-weight table as described earlier. In that case, the displacement also deviates from the applied sinusoidal waveform, and the output from the accelerometer is far from sinusoidal in form.

The accelerometer is mounted directly onto the vibrating table if two-dimensional beds are used, or onto the lid of the three-dimensional bed. The accelerometer is powered from an 18-volt battery power supply thus eliminating 60 Hz A.C. power-line noise. The output from the accelerometer

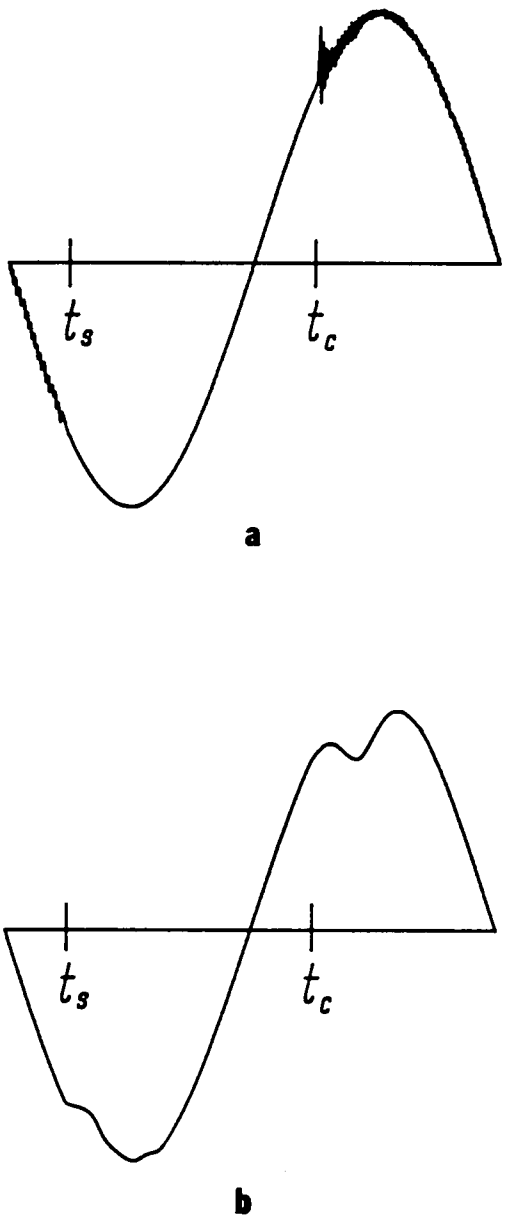

Figure 15. Distortion and noise on the acceleration waveforms: Acceleration oscillographs showing: (a) noise imposed on the signal due to particle impact without waveform distortion, and (b) distortion of the sinusoidal waveform caused by a heavy bed colliding with a light vibrating table. Notation: t_s - instant of lift off; t_c - instant of collision.

is normally monitored on an oscilloscope, but can also be sampled by an analog-to-digital (A/D) converter, so that it may be read by a digital computer.

3.3.1.2 Measurement of Vessel Displacement

Two devices are used for measuring the vessel displacement: a linear variable-differential transformer (LVDT) displacement transducer, and a photoelectric proximity sensor. The LVDT transducer is a contact device, that is, a part of the transducer moves with the vibrating table relative to the rest of the transducer which is stationary. The photoelectric sensor, on the other hand, is a non-contact device that uses a beam of light to measure the distance to the table, rather than using a mechanical contact.

The LVDT Displacement Transducer

An LVDT transducer consists of a primary coil and two secondary coils symmetrically spaced above and below the primary coil on a cylindrical form. A free-moving rod-shaped magnetic core inside the coil assembly provides a path for the magnetic flux linking the coils. When the primary coil is energized by an AC source, voltages are induced in both secondary coils. These coils are connected in such a manner, that the two induced voltages are of opposite polarity. The output is the difference between these voltages, and it is zero at the center or null position. As the core is moved from the null position, the voltage induced in the coil toward which the core moves increases, while the voltage on the coil it is moving away from decreases. This produces a differential output voltage that is directly proportional to the position of the core. The polarity of the output changes as the core is moved form one side of the null position to the other. The inherent symmetry of the LVDT construction produces excellent null repeatability (the null point of the measured displacement is easy to detect), a feature that is required for phase correlation (see later in Section 3.3.3).

A Trans-Tek Model 0243 DC LVDT is used which utilizes a DC power source, providing the AC excitation for the primary coil by means of an internal oscillator. The output of the transducer is linear up to frequencies of 110 Hz, with a practically infinite resolution. The rod-like core which threaded at one end, is attached to the vibrating table assembly. The coil assembly is held stationary by means of an aluminum holder which is attached onto the non-moving inner steel cylinder of the vibration system. The top end of the core is sheathed in teflon to prevent it from mechanically damaging the inside of the coil assembly.

The Optical Displacement Transducer

Despite the sheathing of the core in teflon and the careful alignment of the core and coil assembly, long usage of the LVDT will result in mechanical damage because of the repeated high-speed motion of the core within a tight-fitting coil several times per second. The mechanical wear can be avoided by using a non-contacting device. Three basic types are available: a capacitance measurement which is non-linear, a Hall-effect probe which would be unsuitable for this study because of the stray magnetic fields in the vicinity of the vibrator, and an optical system which is chosen.

The optical system used is a Keyence PA-1801U photoelectric proximity sensor. The sensor unit focuses a narrow beam of light generated from a light emitting diode (LED), through a lens to make the beam convergent on a spot 40 mm from the lens. The beam is reflected off a white surface (on the table) and is focused by another lens assembly onto a photo-detector placed at an angle with respect to the emitted light beam. The (reflected) spot position on the photo-detector, which will move with the proximity of the white target, is converted into a corresponding output voltage.

Although the optical transducer has the advantage of being a non-contact device, it is not as accurate as the LVDT. It has a resolution of 10 microns, compared to the infinite resolution of the LVDT. It is also noisier than the LVDT, making accurate phase detection to a resolution less than $\pm 2°$ impossible. However, it is adequate for general observation of the bed, whereas the LVDT is used when critical measurements are required.

Unlike the accelerometer which reads zero at rest, both displacement transducers have to be zeroed to give an output voltage of zero at the null or rest position of the vessel. As will shown later, an accurate zeroing is required for phase correlation. However, since they directly measure displacement, they do not record noise due to the impact of particles on the vessel floor as is the case with the accelerometer; and the absence of noise makes them more suitable for phase correlation.

3.3.2 Pressure Transducers for Measurement of Floor Pressures

As described previously, the cyclic separation of the bed and vessel followed by a collision of the bed with the vessel base later in the cycle results in a variation of pressure throughout the bed. The pressures below the bed establish a boundary condition at the bottom of the bed, and can be measured directly without interfering with the bed.

Measurements of the floor pressures are made using the two-dimensional bed described earlier and shown in Figure 13 on page 62. The transducers used are Honeywell 143PC01D solid-state differential pressure sensors. They have a full range of $\pm$ 1 psi., and have a flat frequency response at frequencies below 1000 Hz. The transducers produce an output voltage signal that varies linearly with the pressure measured. The transducers measure a differential pressure between two ports. For these experiments, one port is always vented to the atmosphere, so that a gauge pressure is always read. The transducers are mounted onto the bottom of the two-dimensional vessel as shown in Figure 16 on page 72.

A number of tests are performed on the transducers to check that they do not introduce any error into the floor-pressure measurements. The effect of subjecting the sensing elements, in particular the minute silicon wafer diaphragm within the transducer to high accelerations, is examined. The transducers are mounted below an empty bed which is then vibrated with a peak acceleration of 10g. The output of the transducers never deviate from zero, indicating that the sensing elements

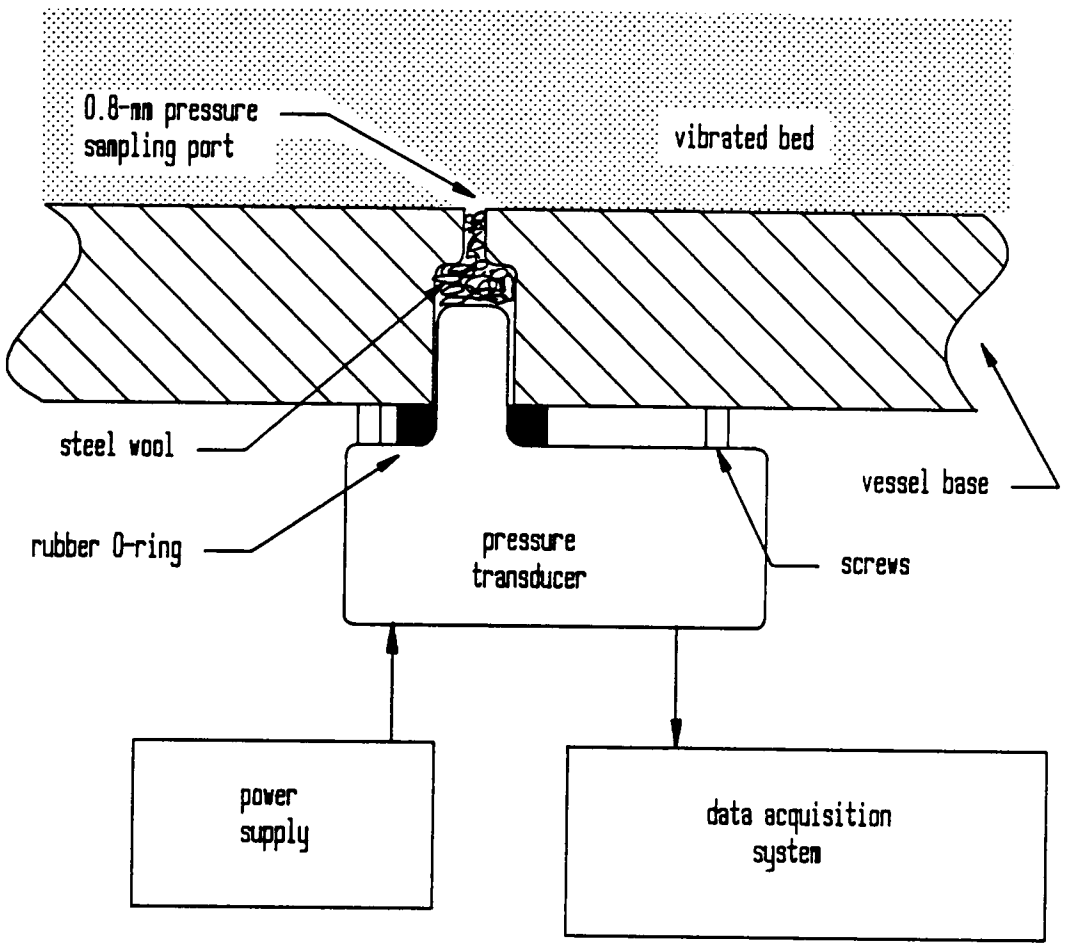

Figure 16. Mounting of the pressure transducer beneath the two-dimensional vessel: The pressure transducer is held to the bottom of the vibrating vessel by two screws as shown

are not affected by an accelerative force. This is to be expected since sensing elements within the transducer are mounted at right angles to the sampling port, and therefore are also normal to the direction of vibration, so that the component of the acceleration acting on the elements is zero.

To check for the presence of any phase errors introduced by the transducers, a piece of stiff nylon tubing is placed under the lower surface of the vibrating table so that a central section of the tubing is squeezed under the table when it is in the null position. Two pressure transducers are then attached to either end of the tube. The tube is compressed as the table moved downward, and expands as it moved upward. Since the pressure in the tube is atmospheric at the null position of the table, the pressure varies cyclically above and below atmospheric as the table is vibrated. The outputs of both transducers are compared on an oscilloscope against the acceleration waveform of the table for frequencies up to 60 Hz. The signals are completely in phase with the acceleration signal, indicating that the pressure transducers themselves do not introduce any phase errors into measurements of the floor pressure.

To detect any phase-lag errors caused by the construction of the sampling ports in the two-dimensional vessel, a test is used similar to that described above, except that a cylindrical piece of metal with a diameter equal to the inner diameter of the nylon tubing and equal in length to the sampling ports in the vessel is placed into one end of the tube before the pressure transducer is inserted into that end of the tube - see Figure 17 on page 74. The cylindrical piece has a hole 0.8 mm in diameter drilled through it which is loosely stuffed with steel wool, so that it exactly simulates the sampling ports on the two-dimensional vessel. The other pressure transducer is inserted directly into the other end of the nylon tubing with no blockage in its path. The signals from both transducers are compared with the displacement waveform on an oscilloscope. No phase lags or differences in amplitude are observed between the outputs of the pressure transducers, nor are there any phase lags between the outputs of either transducer and the displacement signal. This indicates that no errors are introduced at 25 Hz due to the sampling ports. However, if the steel wool is replaced by a single 20-micron mesh, a small but noticeable phase lag is introduced.

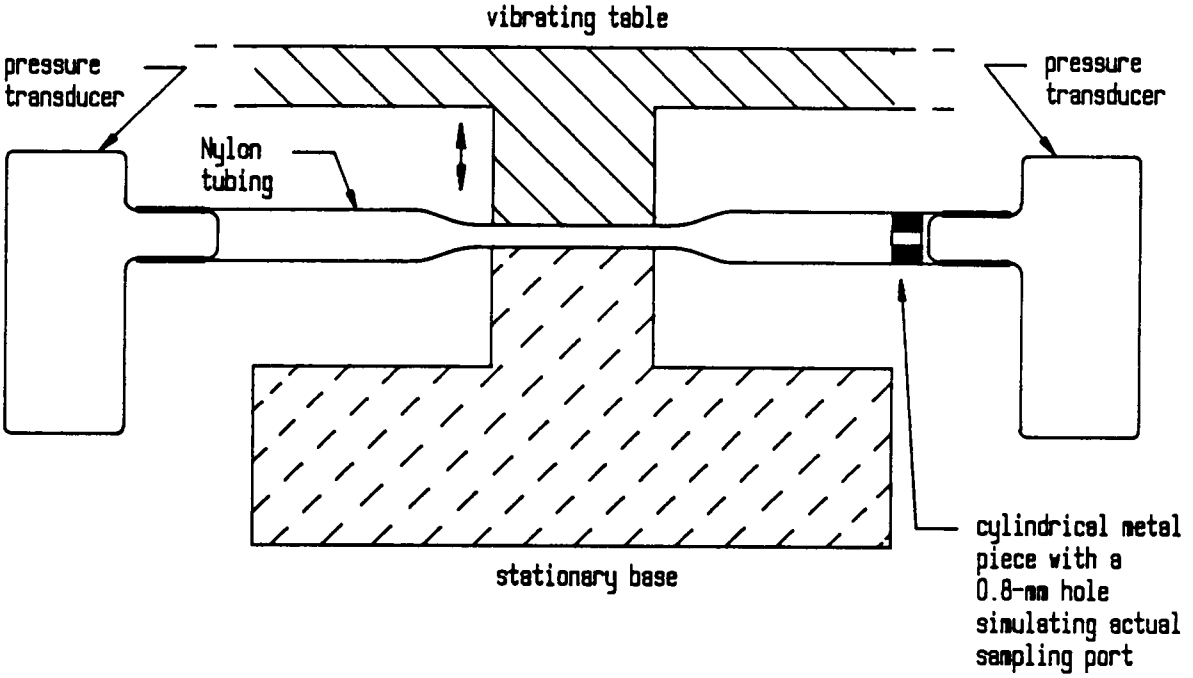

Figure 17. Set-up to determine the presence of phase lags in pressure measurements: Schematic of the apparatus to simulate floor-pressure measurements in the two-dimensional vessel and check for phase lags in the measurement.

Calibration of the Pressure Transducers

The pressure transducers are calibrated against a light-oil manometer in their full operating range. The output voltage is recorded as a function of the gauge pressure. The fit of the data to first-, second-, and third order polynomial, and logarithmic equations is tested using a least squares technique. It is found that the linear fit describes the data best - that is, it gives the correlation coefficients closest to one. The linear fits obtained for the three transducers located at positions W, C, and H (see Figure 13 on page 62) and corresponding correlation coefficients are given in appendix A.

The calibration of the pressure transducers vary with temperature since the output voltage of the piezoresistive sensing elements within them are temperature dependent. Both the sensitivity (unit change in output voltage per unit change in pressure) and the null point (output voltage at zero pressure) vary with temperature, and must be compensated for, since the temperature within the laboratory is not constant. Additional circuitry within the transducer compensates for some of this error, reducing the final combined error due to null point and sensitivity shifts, to approximately $\pm 1\%$ of maximum full scale output (FSO). This error in calibration can be further reduced externally by computational compensation techniques to less than $\pm 0.1\%$ FSO. It is experimentally determined that the null shift is far greater than the shift in sensitivity, which is essentially constant within the range of room temperatures experienced in the laboratory. This is probably because the shift in sensitivity with temperature is predictable, unlike the null shift which varies from one transducer to another; therefore the shift in sensitivity is easier to correct internally within the transducer.

Figure 18 on page 76 shows the shift in the null point with temperature, assuming no shift in sensitivity. At both the calibration and operating temperature, a straight-line fit is used to describe the correlation as shown. The equation of the fit between the measured pressure P_m and the output voltage V_t may be written as:

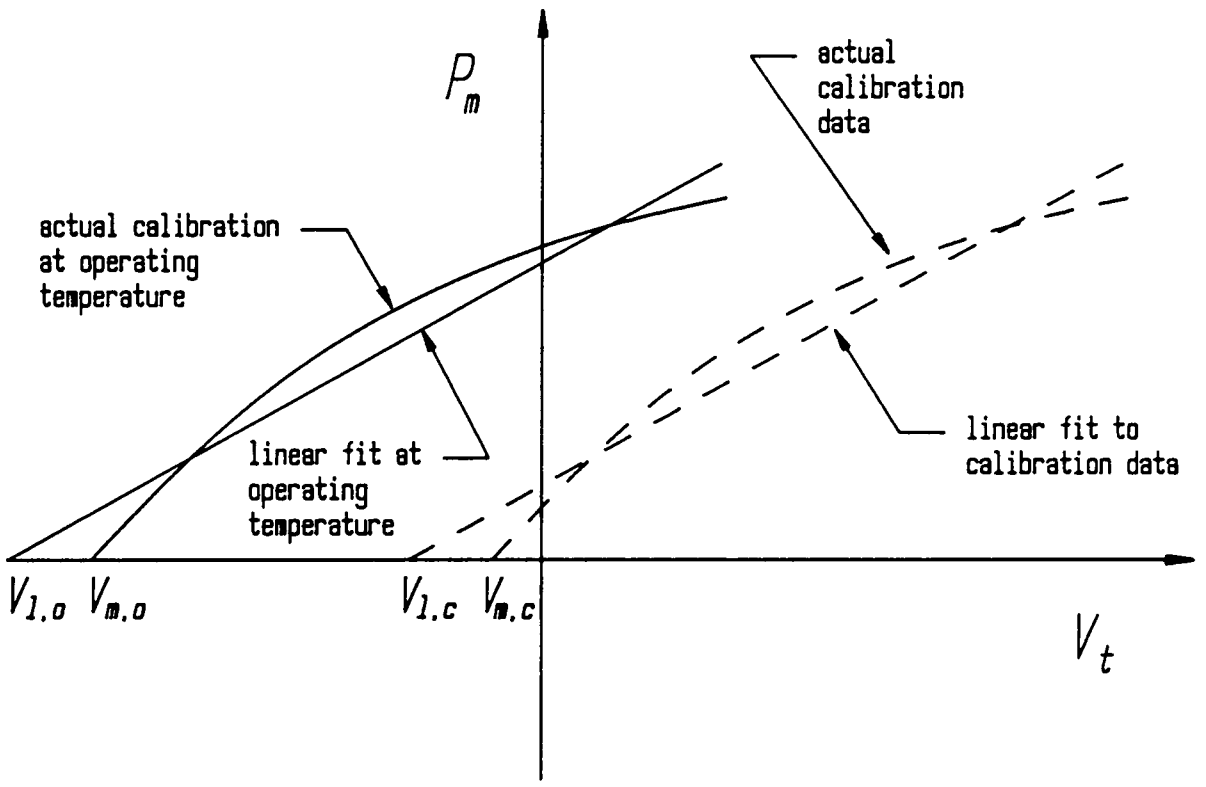

Figure 18. The shift in pressure-transducer calibration curves with temperature: Illustration of actual and linear fits to the pressure-transducer response at calibration and operating temperatures. It is assumed that the only shift is in the null point, and that the gradient is unaffected by temperature. Notation: P_m - measured pressure; V_t - output voltage; $V_{m,c}$ - the measured zero-pressure output voltage at the calibration temperature; $V_{l,c}$ - the zero-pressure output voltage predicted by the linear fit at the calibration temperature; $V_{m,o}$ - the actual zero-pressure output voltage at the operating temperature; $V_{l,o}$ - the zero-pressure output voltage predicted by the linear fit at the operating temperature.

$$P_m = A\,V_t + B \qquad [3.1]$$

where A is the inverse of sensitivity, and B is the pressure that produces an output of zero volts. The voltage output at zero pressure that is predicted by the straight line fit is different from the actual voltage output at zero pressure. Suppose that as shown in Figure 18 on page 76, the measured output voltage at zero pressure at the calibration temperature is $V_{m,c}$, and that the output voltage at zero pressure predicted by the linear fit is $V_{l,c}$. Then if the actual output voltage at zero pressure is measured at the operating temperature to be $V_{m,o}$, the output voltage at zero pressure predicted by a linear fit at the operating temperature (assuming no change in sensitivity with temperature) is given by

$$V_{l,o} = V_{m,o} + (V_{l,c} - V_{m,c}) \qquad [3.2]$$

Since the pressure that will give an output voltage of zero at the operating temperature is

$$B_{oper} = -A\,V_{l,o}$$

the equation of the fit at the operating temperature is given by

$$P_m = A\,(V_t - V_{l,o}) \qquad [3.3]$$

where $V_{l,o}$ is obtained from equation [3.2].

3.3.3 Phase-Delayed Triggering.

Typical vibrated-bed characteristics such as the bed expansion ratio, solid circulation rate and surface-to-bed heat-transfer coefficients are time averaged quantities, since they are commonly measured over a period of time that is long compared to the period of vibration. However, due to the cyclic nature of the vibration process, such quantities are influenced by phase-dependent phe-

nomena that occur within each cycle of vibration. For example, the pressure beneath the bed varies cyclically as the bed first lifts off the vessel base and later lands back on it. Thus, an objective of this study is to develop a method to permit viewing, photographing and measuring of phase-dependent phenomena in the vibrated bed.

In the past, observations of such phase-dependent phenomena have been made through the use of high-speed cinematography [Kroll,1954; Gutman,1974]. However, this method suffers from several disadvantages. It has poor resolution, is expensive and tedious, and it is difficult to analyze several hundred frames of the film even with the aid of a computer. It is not easy to synchronize the frequencies of the high-speed movie camera and the mechanical vibrations imposed on the bed, thus requiring the use of timing lights with the camera. In addition, such analysis gives information on only a few vibrational cycles, and so it is impossible for the investigator to choose a particular range of phase angles of interest and carry out a detailed investigation within them.

Non-visual phase-dependent information, such as the bed voidage or the pressures at the bottom of the bed, are obtained by the use of the appropriate sensors or transducers. Although the transducers give the variation of the measured quantity through a cycle, they do not yield any information to correlate the output with the phase of the applied vibrations. Previously, investigators [Kroll,1954; Gutman,1974; Gray and Rhodes,1972] have phase-matched the output of the transducers with the vessel displacement by displaying both simultaneously on a dual-trace oscilloscope. Quantitative information is then obtained from the oscilloscope display when the signals are matched; but this is not an accurate method, since the resolutions of most oscilloscopes are poor.

An alternative method used in this study utilizes an electronic circuit that detects the positive zero-crossover point of the vessel displacement in each cycle of vibration. This point corresponds to the instant in the cyclic motion of the table at which it moves upward past its rest or null position, and represents a phase angle of zero degrees. The circuit may be configured to issue a trigger pulse that is delayed by a previously specified number of degrees past the zero-crossover point. By

using this electronic pulse that has a given phase lag with respect to the zero-crossover position of the sinusoidal motion of the vessel to continuously trigger a strobe light every cycle, it is possible to observe any visual phenomenon within the bed at that particular phase angle. If the phenomenon being observed has reached a steady state, and varies cyclically with the same period as the applied vibration, it will appear "frozen" at the observed phase angle provided that the triggered strobe light is the only source of illumination.

Phase-delayed triggers capable of resolving down to 10^{-4} of a degree have been devised for use with turbomachinery [Powell *et al.*,1984], but such systems are very expensive requiring the use of a digital computer; whereas triggers for vibrated beds do not require more than one degree of phase resolution. A related circuit for use at low frequencies (below 5 Hz) as a shaft encoder has been proposed for obtaining angular positional information on antenna [Franke *et al.*,1985], but the frequency range required for the vibrated bed is both higher and wider.

Rippie *et al.* [1978], when measuring the bed porosity, used an electronic gate trigger with the capacitance circuit they used to measure the porosity. The gate trigger was capable of issuing a pulse that corresponded to the zero-degree phase-angle position of the vessel displacement. This trigger was used to initiate the acquisition of bed porosity data, thus matching the phases of the bed-porosity and vessel-displacement waveforms. However, this trigger uses a reference point on the flywheel of the mechanical shaker to obtain the zero-degree position. The flywheel was calibrated so that positioning the reference point at different locations around the flywheel would give a trigger pulse at different phase angles. Therefore, this trigger arrangement can only be used with a mechanical vibrator which uses a cam driver.

Details of the electronic phase-delayed trigger circuit developed for this study have been reported elsewhere [Thomas *et al.*,1987]. However, since the input signal conditioning and the zero-crossover detection of the circuit have been improved, details of the new circuit are summarized in appendix B. The phase-delayed pulse may also be used to trigger or initiate a data-acquisition procedure which samples the output of a transducer used to measure a phase-dependent property

of the vibrated bed such as the floor pressures. The collected phase-dependent data can then be referenced to the zero-degree phase angle of the vibratory motion, thus permitting the cyclic data to be easily phase-matched with the periodic displacement of the vibrated bed.

The circuit uses the output signal of either displacement transducer to detect the zero-crossover point, and issues a trigger pulse that is delayed by the number of degrees programmed into it. A typical set-up using the phase-delayed triggering circuit to permit the back-lit phase-delayed photography of the bed is shown in Figure 19 on page 81. Since the phase delay of the triggering is referenced to the zero-crossover point, it is important that the displacement transducers be capable of being accurately set at the null position when the vibrating table is at rest, and also have excellent null point repeatability. Both displacement transducers used here easily meet these criteria.

Measurement of Inherent System Phase-Lags

There are a number of sources of inherent phase lags in the system, the main source being the displacement transducer, but smaller lags are present in the strobe light or electronic flash. The phase lag of the triggered lighting unit is determined by comparing the trigger pulse sent to the unit with the response of the unit as picked up by a photo diode. For the strobe light used (General Radio Strobotac 1531-A), the delay is approximately 0.2 milliseconds or about 2 of degrees lag at 25 Hz, and the delay in the electronic flash (Vivitar Model 285) is approximately 0.1 milliseconds or about 1 degree of lag at 25 Hz. The lag in the phase-delayed trigger circuit is measured by comparing an input signal with the output trigger pulse, and is found to be less than 5 microseconds, or 0.05 degrees at 25 Hz.

Once the phase lags in the strobe light and trigger circuitry are known, the phase lag in the displacement transducers can be measured for a given frequency - say, 25 Hz. A knife-edge mounted on a stationary part of the vibration system (for example, on the inner steel cylinder - Figure 10 on page 55) is aligned with a mark on the vibrating table, when the system is at rest. The system is vibrated at 25 Hz and illuminated solely by a triggered strobe lamp with an inherent phase lag

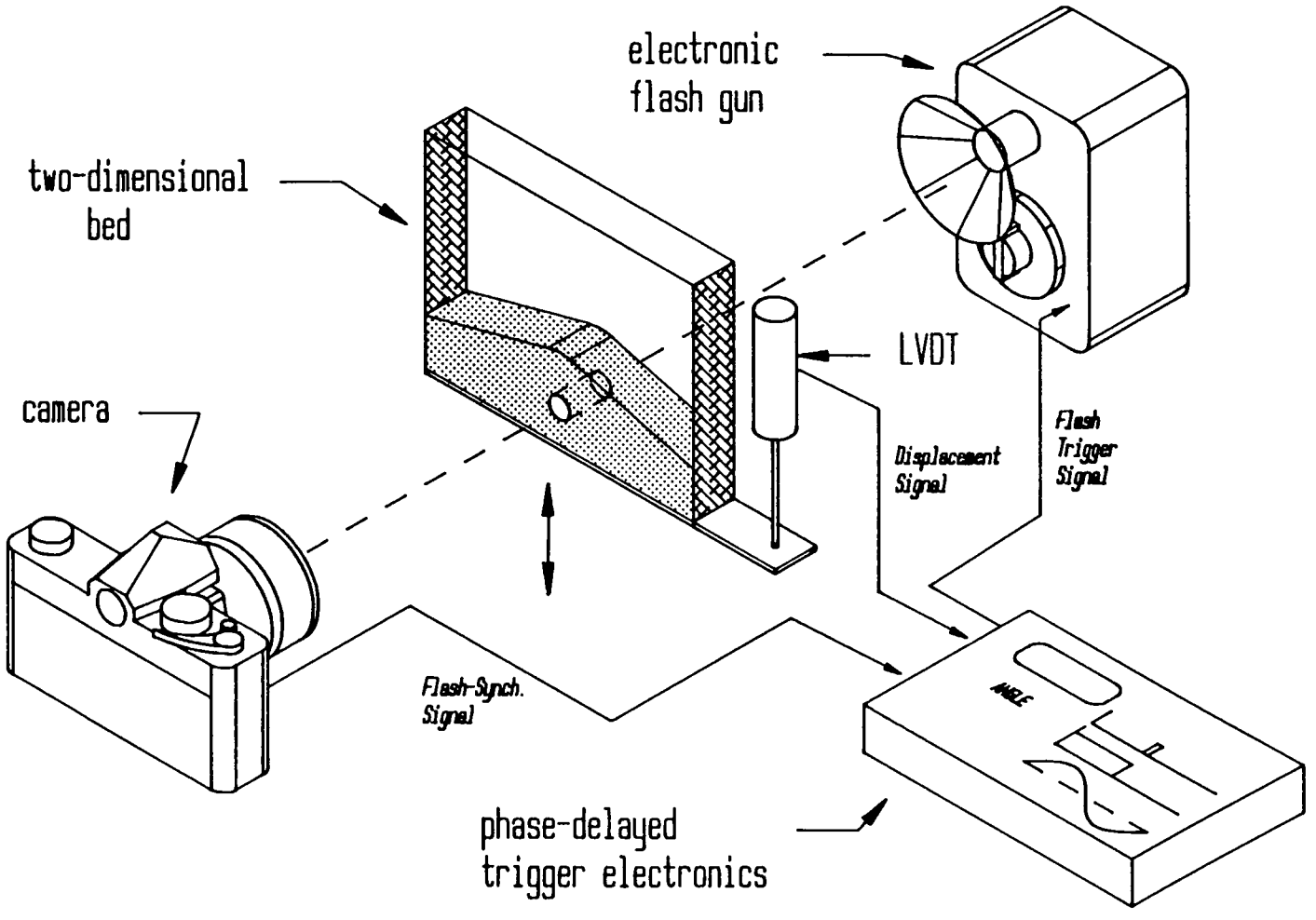

Figure 19. Typical set-up for back-lit phase-delayed photography: Experimental set-up to obtain back-lit photographs at any phase angle using the phase-delayed trigger electronics [Thomas *et al.*,1987]

of 2° at 25 Hz. If the lag in the displacement transducer were zero, the mark on the table would appear to be aligned with the stationary knife-edge when the lamp is triggered with a phase delay of 358° or 178°, since the mark and knife-edge should be aligned at the 0° and 180° positions in the cycle. However, if the lag in the transducer is non-zero, the phase delay set in the triggering circuit must be changed until the mark is seen (with the aid of a close-up lens) to align with the knife-edge. The difference between the theoretical trigger phase-delay for alignment and the actual trigger phase-delay, gives the phase lag inherent to the transducer. At 25 Hz, the phase lag in the LVDT and photoelectric displacement transducers is 18 degrees. As indicated by equations [1.1] and [1.3], the vessel acceleration is 180° out of phase with its displacement. Therefore, the phase lag of the accelerometer can be measured by the same technique used for the displacement transducers, if the inverted output of the accelerometer is used in place of the displacement signal. Using this method, the inherent phase lag of the accelerometer is found to be less than one degree at 25 Hz. The output of the accelerometer can therefore be used as a standard against which the phase lags inherent in other transducers at 25 Hz may be calibrated.

The actual phase-delay of the trigger signal is the sum of the angle set into the triggering circuit and any phase-lags inherent in the system, therefore some compensation must be made for the inherent system phase lags when setting the desired phase angle for triggering into the circuit. For example, suppose it is desired to trigger the strobe lamp at a phase angle of 90° at a vibrational frequency of 25 Hz. If the LVDT displacement transducer is being used to obtain the displacement waveform, the total phase lag inherent in the system, obtained by summing the individual inherent phase lags given above, is 20° Therefore, an angle of 70° must be set in the phase-delayed trigger circuit to obtain the trigger at the desired angle of 90°.

3.3.4 A Cylindrical Probe for Heat-Transfer Measurements

If local surface-to-bed heat transfer coefficients vary with position around an immersed heating surface, a probe for measuring the heat-transfer coefficients that maintains a constant surface temperature is preferable to one which maintains a constant heat flux over the surface. A constant-flux probe will have surface temperatures that vary with the local heat-transfer coefficient. This will introduce errors into the measurements since particles flowing around the surface could transfer heat from a region of the surface at a higher temperature to one at a lower temperature.

A theoretical analysis of the heat conduction process within the probe given in appendix C, is used as the basis for the design of a cylindrical heat-transfer probe that would maintain a constant surface temperature even if the local heat transfer coefficients varied considerably with angular position. The analysis shows that the factors having a major influence on the surface temperature distribution are the thermal conductivity and the thickness of the metal surrounding the heating coil. Copper is chosen as the primary material of construction due to its high thermal conductivity.

The design of the probe is shown in Figure 20 on page 84. The heating element consists of a nichrome wire that is 0.508-mm thick, wound onto an electrically insulated thin-walled aluminum tube. The wire is bonded onto the aluminum by filling the spaces between the coils with a high-temperature high-conductivity ceramic cement. A coiled-wire heating element is used in preference to a commercially available cartridge heater, since cartridge heaters often have a "dead zone" on either side of the heating element where the heating element is connected to the power supply leads. The presence of these dead zones causes severe distortions in the temperature distribution at the ends of the probe. The heating element is inserted into an outer copper annular cylinder with a wall thickness of 3.27 mm and an outer diameter of 12.7 mm. Note that the mathematical analysis in appendix C indicates that a thickness of 3 mm or greater will give surface temperature variations of less than 1°C. The space between the outer surface of the heating element and the inside of the

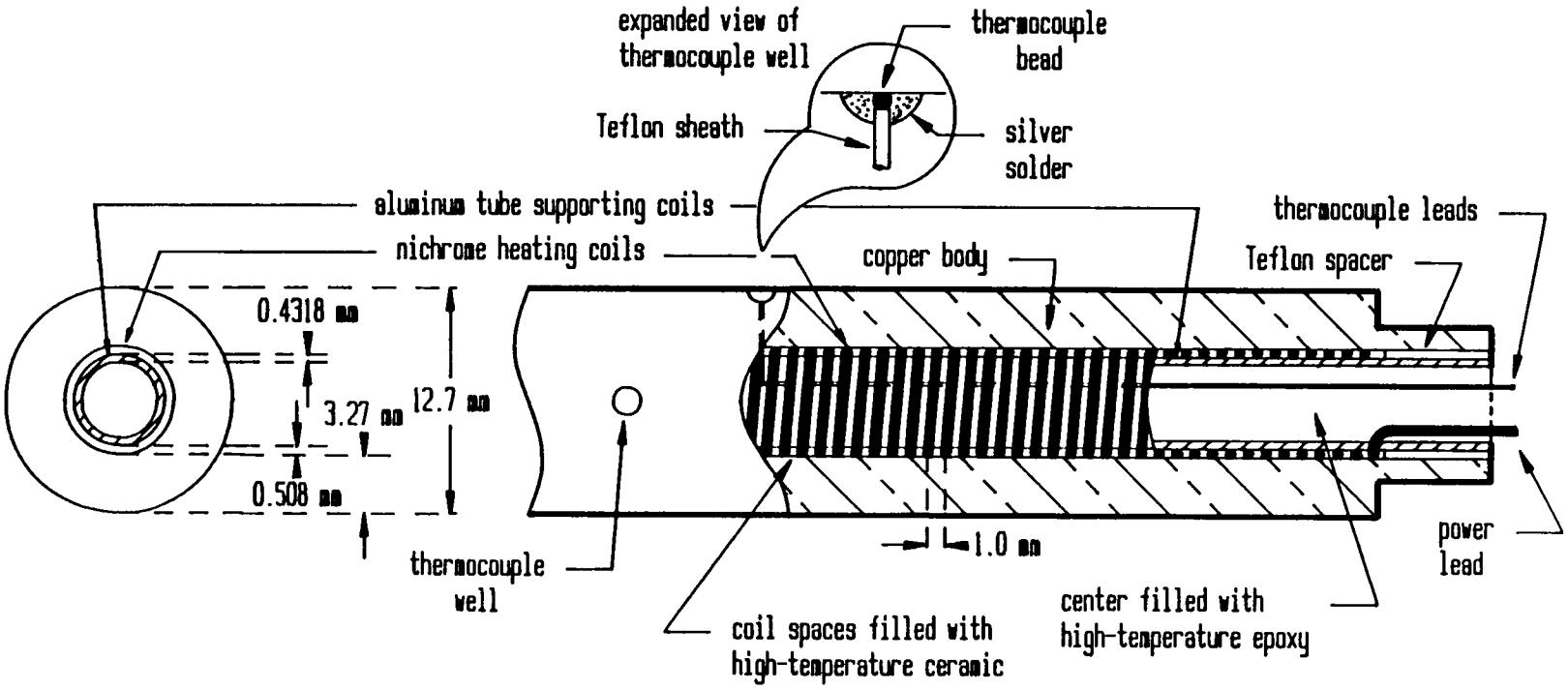

Figure 20. Schematic drawing of the heat-transfer probe: Details of the cylindrical heat-transfer probe used to measure the average (overall) surface-to-bed heat-transfer coefficient. The inset drawing shows details of a typical thermocouple well located on the surface of the probe

copper cylinder is filled with a high thermally-conductive, but electrically-insulating epoxy, that bonds the heating element into place within the outer tube, and also ensures good thermal contact.

To obtain an accurate heat transfer coefficient, the surface temperature of the probe must be accurately measured. Previous designs have placed the thermocouples at the surface by different means. One method [Chen and Withers,1978] has grooves cut into the surface of the tube. After the thermocouples are laid into the grooves, they are filled up with a solder or an epoxy. The disadvantage of this method is that the grooves running along the surface produce distortions in the heat flux, since the material filling them has a different thermal conductivity from the rest of the probe surface. Another technique that has been used [Genetti *et al.*,1971] is to directly solder the thermocouple leads onto the surface of the probe from outside, with their leads immersed in the bed. The thermocouples may therefore act like fins, sinking heat directly into the bed, and may also alter the particle flow patterns around the probe. Probably the best method of placing the thermocouples is to run them radially downward within the tube and through the coils as used by Abu-Baker [1981]. This arrangement produces only a minimal distortion of the heat flux.

To allow the thermocouples to pass radially down through the coil, holes are drilled in the 1-mm spaces between the coils at four points along the length of the coil. Small holes 0.51 mm in diameter are drilled in the outer copper annulus so that they exactly align with the holes in the heating element when it is inserted into the annulus. After the heating element is fixed inside the copper annulus, thermocouple wires are passed radially down through these holes in the copper and the coil, into the hollow center of the heating element. The thermocouple leads then pass axially out of the tube as shown in Figure 20 on page 84. After the thermocouples are put into place, the center of the aluminum tube is filled with a high-conductivity epoxy. Copper-constantan (T-type) thermocouples are used, since they have a large variation of output voltage with measured temperature in the range of interest, and are relatively easy to solder. Teflon-coated thermocouples with a total thickness of 0.508 mm are used; each wire in the thermocouple pair is 0.0762 mm in diameter. The thermal mass of the wire is so low that virtually no heat is conducted away from the surface by the thermocouples. The thermocouple junction is formed by mechanically twisting the

wire pair together to form a bead about 90 microns in diameter, and then filling the hole around the bead with silver solder as shown in the inset in Figure 20 on page 84. This allows a true local surface temperature to be measured.

Four thermocouple junctions are positioned along the length of the probe at various angular positions so that when the probe is positioned in the bed, one thermocouple faces upward; one downward; and two horizontally on either side of the probe.

Placement of the Probe Within the Bed.

The probe is placed horizontally across the three-dimensional cylindrical bed as shown in Figure 12 on page 60, with its center located 20 mm above the floor of the vessel. The probe is held by two cylindrical supports of the same diameter as the probe. The supports pass through the walls of the vessel and are held in place by retaining nuts against L-shaped aluminum supports that are attached to the outer section of the vessel base (see Figure 12 on page 60). A rubber sealing ring positioned at the points at which the supports penetrate the vessel walls, prevents particles from leaking out of the bed. This method of supporting the heat probe is preferable to suspending the probe in the bed by vertical rods, since vertical rods at the ends of the probe produce disturbances in the solid circulation at the probe ends by providing a preferential path for air flow into and out of the bed. Also, the horizontal configuration better simulates a tube with a heating fluid, such as steam, passing through the bed.

The support itself consists of two sections, a 12.7-mm Lexan "insulating" section and a 50.8-mm stainless-steel section. One end of the Lexan section is machined to fit over the 6.35 mm protrusions at each end of the copper probe (Figure 20 on page 84), and the other end is threaded to fit into the stainless-steel section. The end fitting over the probe protrusions is coated on the inside with a rubber compound to provide thermal insulation and a rubber ring is used between the copper and Lexan sections as additional insulation. A thermocouple is implanted within the Lexan section right at the end of the copper protrusion to permit an analysis of the heat losses from the

supports. Both the Lexan and stainless-steel sections have a 6-mm hole through their centers to allow the passage of thermocouple and power leads from the copper probe to the outside.

3.3.4.1 A Thermocouple Switching Circuit

A high-accuracy thermocouple amplifier (DORIC Model 400A) is used to indicate temperatures read by thermocouples on the probe surface, as well as those placed within the bed. The amplifier contains a linearizing circuit for the T-type thermocouples used so that the error within the amplifier is less than 0.1°C and the total error in reading the thermocouple is approximately ± 0.5°C.

There are several thermocouples to be read, and since the cost of the amplifier is high, a switching circuit is used to allow a single amplifier to read up to sixteen thermocouples. The thermocouples are connected to an array of sixteen dual-pole five-volt silver reed relays. Closing a particular relay completes the circuit between the thermocouple junction connected to that relay and the amplifier, allowing the amplifier to read that thermocouple. Each relay in the array is assigned an address code, and a de-multiplexer selects a particular relay for each code that it receives.

Dissimilar-metal thermocouple junctions occur within each relay, since the reeds within the relays are made of silver. There are two copper-silver junctions and two constantan-silver junctions when the relay is closed. Dissimilar-metal junctions introduce an error into the thermocouple reading since a voltage is generated at the junction (the Seebeck effect). However, if all dissimilar-metal junctions in the relay are maintained at an identical temperature, the net error will equal zero. Differences in the temperatures of each junction in the relay can occur due to local variations in the ambient temperature, and more importantly, due to the heating effect of the electromagnetic coil in the relay that closes the switches. To maintain isothermality, the array of relays is sandwiched between two quarter-inch aluminum plates which act as large thermal sinks. The lower plate which is in contact with the connector pins of the relay is coated with an epoxy paint to prevent short-circuiting the relays. With this arrangement, isothermality can be maintained, for any one closed

relay, over approximately one minute, after which the heat generated by the internal coil produces temperature variations in the junctions within the relay, causing errors in the thermocouple reading of greater than 0.1°C.

4.0 Experimental

4.1 Range of Experimental Conditions

The experiments in this study are conducted under a variety of conditions, which include different particles types and sizes, a range of vibrational intensities, and varying bed depths. The ranges over which these factors are varied are summarized below.

4.1.1 Particle Types and Sizes

The majority of experimental observations are made using three types of particles:

Master Beads: These particles are commercially used in grinding and as a packing in deep oil and gas wells. Substantially spherical, the solid is non-dusting in a fluid bed. It contains mainly alumina (about 86%), and other constituents, including 2-4% silica, 6-8% iron oxide, and 4-5% titania in a solid solution. The presence of minor constituents gives the solid a dark, almost black color, instead of the white color that is normally associated with pure alumina. The density of the solid is

approximately 3600 kg/m^3. Its thermal conductivity and specific heat (as quoted by the manufacturer) are approximately 36 W/m-K and 765 J/kg-K respectively. However Cheah [1986] reports a measured specific heat capacity of 670 J/kg-K for this solid. Master Beads are manufactured by the Norton-Alcoa company.

Low-density glass beads: These technical-quality beads are made of ordinary soda-lime silicate glass and are extremely spherical. The beads have a solid density of 2500 kg/m^3. The specific heat and thermal conductivity for this glass are 750 J/kg-K and 1.4 W/m-K respectively [Incropera and DeWitt,1981] Low-density glass beads are manufactured by Potters' Industries (P-series glass beads).

High-density glass beads: High-density glass is a barium-titanate glass that is highly retro-refractive, and is commonly used as a reflective coating for road signs. Beads of this material used in the study are of technical quality, and are extremely spherical. The solid density of the beads is 4490 kg/m^3. The specific heat and thermal conductivity for this glass are not readily available. However, the thermal conductivity for most barium glasses is approximately 1 W/m-K. These glass beads are also manufactured by Potters' Industries (H-series glass beads).

Particles of each of the three solid types listed above are sized into seven size ranges. These size ranges are reported in Table 2 on page 91, in U.S. Standard Mesh numbers, as well as equivalent sizes in microns. For each size range, a geometric mean $\bar{d}_p$, is also reported which is calculated from:

$$\bar{d}_p = \sqrt{d_{p,u}\, d_{p,l}} \qquad [4.1]$$

Here, $d_{p,u}$ and $d_{p,l}$ represent the upper and lower limits, respectively, of the size range in microns.

In addition to these solids, other particle types with more restrictive size ranges are also occasionally used. These include:

Table 2. Size ranges for Master Beads and glass beads used in this study

U.S.Standard Mesh Size	Size Range in microns	Geometric Mean Size (microns)
-140 +200	74 – 105	88
-100 +140	105 – 149	125
-70 +100	149 – 210	177
-60 +70	210 – 250	229
-40 +50	297 – 420	353
-30 +40	420 – 595	500
-20 +30	595 – 841	707

1. Spent fluid cracking catalyst (FCC) powder with a size range of: 40—120 μm. ($\rho_s \simeq 1006$ kg/m^3).
2. Spherical copper powder with an average particle diameter of 10 μm. ($\rho_s = 8930$ kg/m^3).
3. Fine aluminum powder with a size range of: 40—105 μm. ($\rho_s = 2702$ kg/m^3) .
4. Fine-ground white wheat flour with a size range of: 20—105 μm. ($\rho_s \simeq 700$ kg/m^3).
5. Fine Teflon micropowder with a size range of 10—25 μm. ($\rho_s = 2200$ kg/m^3) .

4.1.2 Vibrational Conditions

It is clear from equation [1.3] that the frequency, amplitude and acceleration of the vibrating vessel are inter-related. Therefore, the choice of any one of these vibrational parameters will set limits on ranges of the remaining parameters.

Vibrational Frequency

The choice of vibrational frequency for this study is based on certain practical considerations. Frequencies below 15 Hz are not practical, mainly because the amplitude that would be required to produce a significant vibrational intensity would be large. For example, since the maximum peak-to-peak amplitude permitted by the electromagnetic vibrator used is 12.7 mm, a limiting value of 2.6 is imposed on the vibrational intensity parameter K at a frequency of 10 Hz. In addition, at very low frequencies (less than 10 Hz), the period during which the bed remains in contact with the vessel base becomes sufficiently long, that the bed returns to the packed state during that part of the cycle. The degree of bed expansion reduces at frequencies above 40 Hz [Chlenov and Mikhailov,1972], an observation also noted in initial tests in this study. Because of the lower bed expansions they produce, higher frequencies are probably less desirable.

Most commercial mechanical vibrators, that are designed to operate at resonance and are based on the rotation of electric motors, have an upper frequency limit of 30 to 40 Hz. This limits the range of frequencies of practical interest to 15 — 35 Hz. A frequency of 25 Hz is chosen for this study since it is half-way between the limits of practical interest.

Vibrational Intensity

In this study, the vibrational intensity parameter K is generally maintained at a value between 1 and 7. In the majority of cases, bed mobility starts at $K = 1$. However, the rate of particle motion is too slight to be of practical interest until $K = 2$. Values of K below 2, are only examined to detect the value of K at which bed mobility is first induced.

Increasing the vibrational intensity produces greater stresses on the mechanical components of the vibration system. A K-value of 7 is probably the safe upper limit at which the system used in this study can be operated for a long period of time without the risk of catastrophic mechanical failure. Some experiments of short duration are conducted at higher values of K.

Using equation [1.4], the equivalent range of vibrational (half-wave) amplitudes at 25 Hz is calculated to be 0.396 to 2.783 mm for $K = 1$ to 7. The amplitudes corresponding to values of K greater than 7 are reported in the appropriate sections.

4.1.3 Bed Depth

Since the expansion of the vibrated bed is dependent upon several factors, including most importantly the vibrational intensity, bed depths reported in this study are always those of equivalent (flat-surface) static beds—that is, with $K < 1$. In the majority of experiments, the static bed depth is 30 mm. Since major horizontal dimensions of the containing vessels are between 162 and

170 mm, the depth-to-width ratio (L/D) is between 0.176 and 0.185. Thus, this vibrated bed can truly be regarded as "shallow". For some heat-transfer studies, bed depths of 60 mm are used; and in some experiments to study the bed dynamics, the bed is only a few particle layers deep. In such cases, the bed depth is noted in the relevant section.

4.1.4 Low Pressures

Most of the experiments carried out in this study are at atmospheric pressure. However, some aspects of the bed dynamics are also examined at low pressures. These include: particle circulation patterns, degree of bed bunkering, and the formation of air gaps beneath the bed. The dynamics of the vibrated bed are strongly affected by the viscous drag exerted by the flow of gas through it. Therefore, to make a significant difference to bed behavior, the pressure of the gas must be such that the gas viscosity is small. From the result of the simple kinetic theory of gases, the viscosity of the gas is independent of pressure when the mean-free path of the gas λ_m, is smaller than the conduit in which the gas flow is taking place [O'Hanlon,1980]. If the mean-free path becomes much larger than the size of the conduit, the viscosity of the gas drops off sharply and disappears, and gas flow takes place by molecular flow, rather than by viscous flow. In the molecular flow regime, flow properties are determined by gas-wall collisions. As a result, the gas does not exert a drag on the walls of the conduit. If the diameter of the conduit is d, molecular flow takes place if $\lambda_m \gg d$. The mean-free path according to kinetic theory is [O'Hanlon,1980]:

$$\lambda_m = \frac{1}{\pi\sqrt{2}\, d_o^2 \rho} \qquad [4.2]$$

where d_o is the molecular diameter and ρ, the gas density. For air at room temperature, equation [4.2] can be written for λ_m in meters as:

$$\lambda_m = \frac{6.6 \times 10^{-3}}{P} \qquad [4.3]$$

where P is the absolute pressure in pascals. Thus, to eliminate viscous drag effects in the vibrated bed, the pressure must be reduced to a value at which the mean-free path of the gas is equal to some characteristic dimension that describes the flow of gas within the bed. The most common choice of this characteristic dimension is the particle diameter d_p. Combining the condition that $\lambda_m \gg d_p$ with equation [4.3] gives the requirement on the pressure to eliminate viscous drag:

$$\frac{6.6 \times 10^{-3}}{P} \gg d_p$$

The largest particle size used in this study is 707 μm. For this particle size, the pressure must be lower than 9 pascals for the mean-free path to be just greater than the particle size. In practice, the vacuum vessel used can be evacuated to an absolute pressure of 8 pascals. This barely meets the criterion for the elimination of the viscous drag for 707-μm particles, but it easily meets the criterion for smaller particle sizes, where viscous drag effects are most important at atmospheric pressure. Allen [1980] suggests that the characteristic dimension for flow properties in a packed bed is the mean interstitial gap size which is approximately equal to $0.1\, d_p$. If this dimension is used, the pressure of 8 pascals used in the vacuum work in this study meets the requirement for the elimination of viscous effects for even the largest particle size.

In this study the word "vacuum" will mean a pressure within the bed of 8 pascals. At this pressure, effects of viscous drag are eliminated. From the point of view of gas-solid interactions within the bed, operating the bed at 8 pascals does in fact represent a vacuum.

4.2 *Measurement of the Transition to the Vibrofluidized State*

As noted earlier, the transition from the packed state to the mobile (vibrofluidized) state in the vibrated bed occurs when K is equal to unity in large-particle beds. Previous investigators [Herber,1970; Kapustin *et al.*,1980] have observed that the critical vibrational intensity K_{cr} at which there is a transition to the vibrofluidized state increases as the particle size is reduced, particularly below 100 μm.

The critical value of the vibrational intensity parameter (K_{cr}) at which there is a transition to a mobile bed has been measured for a variety of solids. The solids are chosen to reflect types A, B, and C according to the Geldart classification [Geldart,1973] and include:

- Soda-lime glass beads, barium-titanate glass beads, and Master Beads with particle size ranges of:
  1. 74 - 105 μm (geometric mean = 88 μm)
  2. 149 - 210 μm (geometric mean = 177 μm)
  3. 595 - 841 μm (geometric mean = 707 μm)
- Spent fluid cracking catalyst (FCC)
- Spherical copper powder
- Fine aluminum powder
- Fine-ground white wheat flour

Sizes and densities of these particles are given in section 4.1.1. Initially, the bed is packed by tapping the vessel and by vibrating the vessel at high frequencies of about 1000 Hz which produces additional bed compaction above that possible by mechanical tapping alone. The critical vibrational intensity parameter is obtained by slowly increasing the vibrational acceleration of the

vessel from zero, and visually observing the point where the bed just becomes mobile. Once the bed has been mobilized from this packed state, K_{cr} is measured for the uncompacted bed, both by increasing the vessel acceleration until vibrofluidization is observed, and by decreasing the acceleration while the bed is in the mobile state until no further signs of bed mobility can be observed. The critical vibrational intensity parameter for each transition from a static to a vibrofluidized bed is measured several times. The values are found to be repeatable to within two decimal places of accuracy between experiments.

4.3 Phase-Delayed Observation and Photography of the Vibrated Bed

As described in the previous chapter (§3.3.3), it is possible to observe visual bed characteristics that are varying cyclically with the same period as the applied mechanical vibrations at any given phase angle with the aid of the electronic phase-delayed trigger circuit, provided that the bed is at steady-state. If the phase-delayed output pulse of the circuit is used to externally trigger a strobe light that provides the sole source of illumination for the vibrated bed, the bed will appear to be frozen at the phase angle set into the circuit.

The phase-delayed trigger circuit can be configured to produce a continuous stream of output pulses, one in each cycle of vibration, as would be required for visual observation of the bed with a strobe light. Alternatively, it is possible to issue a single trigger pulse on demand (see the circuit diagram in appendix A). With this configuration, phase-delayed photography of the bed is possible. A typical arrangement to obtain phase-delayed photographs using a 35-mm camera and an electronic flash-gun is shown in Figure 19. The flash-synchronization signal from the camera, which is produced every time the camera shutter is opened, is used to demand an output trigger pulse from

the phase-delayed trigger circuit. The single phase-delayed output pulse fires an electronic flash-gun. Since the trigger pulse can be delayed by up to 359°, the camera shutter must remain open at least as long as the period of vibration. In this study, a shutter speed of ¼ second is used at a vibrational frequency of 25 Hz. The duration of the flash is approximately 0.1 msec, so that the actual exposure of the film to light is extremely short, giving true "instantaneous" photographs of the bed. If the photography is done in a darkened environment, this technique is capable of producing phase-delayed photographs of very high resolution of the vibrated bed, showing extremely fine detail as will be illustrated in the next chapter.

Placing the light source behind the vibrated bed as shown in Figure 19 produces a back-lit image of the bed. The bed appears as a dark shadow silhouetted against a light background. This will give information on the formation of air gaps within and below the bed as well as on the overall shape of the bed.

Placing the strobe directly over the bed and pointing downward provides top-lighting. As will be shown later, a bed of glass beads illuminated in this manner will refract the light toward the front and back of the bed provided the bed is in a highly expanded state. Such a bed will then appear very bright against the dark background. As the porosity of the bed is reduced, less light will be refracted forward. The bed will appear progressively darker as the porosity is reduced until finally it will be as dark as the surroundings.

Front-lighting the bed is useful in determining the presence of any large porosity variations within a bed of opaque material such as Master Beads. Also, since it gives the appearance of eliminating the vertical sinusoidal motion of the bed, it is useful in examining the movement of colored tracers at the front face of the bed.

4.3.1 Observation of Air-Gap Formation Below the Bed

By viewing from the front, a back-lit two-dimensional vibrated bed, air gaps that form below the bed are clearly observed. When a gap forms below the bed, the rays of light come through the gap, clearly demarking the bottom surface of the bed. Use of a stroboscopic light source externally triggered by a phase-delayed pulse determines the variation of the gaps through the whole cycle of vibration. If a gap is present for a bed under a certain set of vibrational conditions, the entire cycle of vibration is scanned by continuously stepping up the phase-delay angle of the output pulse from the phase-delayed trigger circuit at a frequency (2 Hz) far lower than the frequency of vibration. This gives a visual indication of how the gap varies through the cycle. The instants at which the bed lifts off the vessel floor and later collides with it are determined by noting the phase angles at which the light can first be seen beneath the bed, and when it finally disappears.

Phase-delayed photographs of the gap are used to determine the manner in which the gaps form and collapse for different beds under varying vibrational conditions.

Beds with average particle sizes of 707 μm (a large particle size), 177 μm (a medium particle size), and 88 μm (a small particle size), of Master Beads,and high- and low-density glass beads are examined. K is varied between 1 and 7 for all beds. Visual observations of the gaps below the bed are also made under varying degrees of vacuum.

4.3.2 Observation of Air Gaps Surrounding Heating Surfaces

The formation of gaps around flat horizontal heat-transfer surfaces immersed in a vibrated bed has been noted by previous investigators [Bukareva *et al.*,1969; Gutman,1974; Muchowski,1980; Ringer,1980]. The presence of air gaps has also been observed around cylindrical heat-transfer tubes immersed horizontally in a vibrated gas-fluidized bed [Malhotra and Mujumdar,1985]. It would be

expected that similar gaps form around cylindrical heaters in a vibrated bed. However, the time-averaged techniques used previously by other investigators to observe these gaps, fail to yield phase-dependent information on them.

In this study, visual observations of the air gaps surrounding a cylindrical heat-transfer surface immersed in a vibrated bed are made by using the two-dimensional vessel, and by simulating the effect of a cylindrical heater surface with a dummy heat-transfer tube placed across the vessel as shown in Figure 13 on page 62. The bed is back-lit by a strobe lamp, triggered by a phase-delayed pulse. In addition, photographs are taken at regularly spaced phase angles within a cycle of vibration using transparency film. The photographs give accurate quantitative information on the size of the air gaps and the fraction of the heat-transfer surface blanketed by them at any point in the vibrational cycle.

Visual observations of the gaps are made using all sizes of Master Beads and glass beads of both densities. However, quantitative information using phase-delayed photography is obtained only with Master Beads with average particle sizes of 88, 177, and 707 μm. The edges of the air gaps are not clearly defined when using glass beads, because glass particles that line the edge of a gap refract light into the gap. The vibrational intensity parameter K, is varied from 2 to 6.

4.3.3 Investigation of the Rarefied Zone on the Top Surface of a Vibrated Bed

The existence of a region of high porosity on the top surface of a vibrated bed has been alluded to previously [Buevich and Galontsev,1978]. High-speed cinematography by Kroll [1955] also shows a region that resembles a spray or cloud above the bed apparently in that part of the cycle when gas is forced out of the bed.

The nature of the top surface of the vibrated bed has been investigated in this study using phase-delayed stroboscopic top-lighting over the two-dimensional vessel. If glass beads are used, the rarefied zone—if it exists—can be seen clearly as a brightly lit region on the top surface of the bed as described above. Phase-delayed photographs are also taken at various phase angles, so that the formation and variation of the expanded region may be correlated to the trajectory of the vibrated bed, and also to the cyclically varying pressures beneath the bed.

At any phase angle, as the intensity of the top lighting is increased, a point is reached when increasing the intensity any further does not show an increase in the depth of the brightly-lit zone on top, although the overall brightness of the image improves. This limiting depth is taken to be the depth of the rarefied zone at that phase angle. For an opaque particle, such as Master Beads, a view with reduced resolution of the rarefied zone may be obtained by front-lighting the bed.

The existence of an expanded region at the bottom of the bed (but above the gap) is investigated by illuminating the bottom of the bed in a similar fashion. The aluminum base of the vessel is replaced by a transparent plexiglas base. Light is directed from the strobe lamp or other phase-delayed light source, up onto the lower bed surface via a mirror placed below the vessel base, and angled at 45° to the horizontal.

4.4 Measurement of Cyclically Varying Pressures Beneath the Vibrated Bed

As described in the previous chapter (§3.3.2), the floor pressures beneath the bed can be measured directly with the aid of solid-state pressure transducers. The pressure is sampled at three locations

below the two-dimensional bed as indicated in Figure 13 on page 62, through small sampling ports drilled through the floor of the vessel.

The output signals from the three pressure transducers and the accelerometer are simultaneously sampled using an analog-to-digital converter (Data Translation Series DT2801). Each channel is sampled at 3000 Hz, and the digital data are collected by a micro-computer. The high sampling rates are achieved by using a direct memory access (DMA) scheme to transfer digital data directly into the memory of the computer without the intervention of the central processing unit (CPU) of the computer.

Output voltages from the transducers are sampled over two cycles. The data acquisition is initiated by a pulse from the phase-delayed trigger circuit. The trigger pulse is delayed by zero degrees, so that sampling is always started at the beginning of a vibrational cycle. Since there is an uncertainty of $\pm 1°$ in the phase delay of the trigger pulse (see §3.3.2), the first sample point of the accelerometer output is also checked after data are collected. If the magnitude of this point is greater than 0.05g, the data are rejected, and the phase delay of the trigger pulse is adjusted within the range of uncertainty until the condition is met. Using this technique, the pressure data that are finally accepted are accurately phase-matched with the displacement of the vibrating vessel to less than one degree of phase lag.

After the acceptable data are in the memory of the computer, they are converted to equivalent accelerations and pressures using calibrations of the accelerometer (§3.3.1.1) and the pressure transducers (appendix A), respectively. They are also processed to compensate for the temperature drift in the transducer circuitry caused by the difference in temperatures during data collection and calibration, as described in section 3.3.2 of the previous chapter.

In this study, floor pressures are measured beneath beds of Master Beads of all sizes, and glass beads with average particle sizes of 88, 177, and 707 μm. Pressures below beds with depths of 43 and 60 mm are also measured for some sizes of Master Beads.

4.5 *Identifying the "States" of the Vibrated Bed.*

As noted by Bachmann [1940], the nature of the bed changes from a freely-bouncing state to a coherent state as the bed depth is increased above about six particle diameters. Initial observation of the bed shows that although the bed does start to act as a coherent mass with a bed depth beyond a few particle diameters, it remains in a highly expanded state until a greater depth is reached where the degree of bed expansion is much less. Further experiments are carried out to identify the characteristic associated with each "state" of the vibrated bed, as well as to obtain preliminary quantitative information on the transitions between different states.

To obtain repeatable results, an accurate and reproducible measure of bed depth is necessary. The reported bed depth, L , is an equivalent, static, packed-bed height. It is determined by dividing the volume of packed solids by the cross-sectional area of the bed. This method of defining the bed depth allows for equivalent bed depths of less than a single particle diameter. A bed depth where $L/d_p < 1$ can perhaps best be thought of as a fractional coverage of the vessel floor by a monolayer of particles.

Since transitions occur at equivalent bed depths corresponding to volumes of a few tenths of a milliliter for several of the particles studied, volume itself cannot be measured accurately or repeatably. Instead, the packed-bed density of each particle type is determined by measuring the weight of a packed volume of ten milliliters of particles on a chemical balance accurate to a tenth of a milligram. The average of six measured packed-bed densities is used. For each particle type, the measured packed densities do not vary from the average by more than two percent. The volume required to obtain a given equivalent bed height is then measured as an equivalent weight to the nearest tenth of a milligram, which in most cases, represents an accuracy to within a few particles for the entire bed volume.

Initial experiments also indicate that transitions from one state to another are best observed by a combination of back and top lighting of the bed. Also, glass particles show the transitions more critically than do other solids. As observed above, this is because glass particles refract light from the lighting source above the bed toward the front if the bed is in an expanded state, but not if it is in a packed state. Therefore, although the existence of different states is confirmed for Master Beads (with the same size ranges as for glass beads) and FCC, critical conditions for transitions from one state to another are determined only for two types of glass beads.

Experiments to determine the transitions are performed with the aid of a pair of synchronized strobe lamps which run slightly slower than 25 Hz. This has an apparent effect of slowing down the motion of the bed which facilitates observation of phase-dependent phenomena through the cycle of vibration. One of the strobe lamps is placed behind the bed, providing back-lighting to determine the presence of bunkering in the bed, and also to observe the gap below the bed. The other strobe lamp is placed above the bed to observe the state of expansion of the bed by top-lighting.

Average particle sizes of 88, 177, and 707 μm are used for glass beads and Master Beads. The equivalent bed depth is increased from 24 μm up to 2.82 cm, as given in Table 3. For each bed depth, the behavior of the bed is observed and recorded for values of K of 2.5, 3, 4, 5, and 6.

Phase-delayed photographs which illustrate the different states observed in the bed are taken with either top- or back-lighting, depending on the bed characteristic that the photograph is intended to bring out. The camera is placed in front of the bed for the majority of photographs. In some cases, the structure of the bed is best observed by placing the camera on top of the bed, looking directly down at the bed, with lighting through the front wall of the vessel.

Table 3. Particle sizes and bed depths used in the study of vibrated-bed states

Particle Size (Microns)	Equivalent Bed Depths Examined (Microns)
88	24,48,72,96,120,168,240,360,480, 600,720,840,960,1080,1200,1440, 1680,1920,2160,2400,2640,2880, 3120,3360,3600,4080,4800,6000, 7200,8400,9600,12000,14400, 19200,28800
177	24,48,72,96,120,168,240,360,480, 600,720,840,960,1080,1200,1440, 1680,1920,2160,2400,2640,2880, 3120,3360,3600,4800,6000,7200, 9600,12000,14400,16800,19200, 28800
707	48,72,120,168,240,360,480,720, 960,1200,1680,2400,2880,3600, 4800,6000,7200,9600,19200, 28800

4.6 Examination of Particle Circulation in the Vibrated Bed

Particle circulation in the vibrated bed affects the heat transfer and solid mixing characteristics of the bed. The circulation patterns that can be easily observed are time-averaged over several cycles. Some investigators [Gutman,1974; Buevich *et al.*,1979] have suggested that the movement of particles is caused by the cyclically-varying pressure gradients that exist in the bed. If this is the case, the time-averaged particle motion is the result of minute displacements of particles during each cycle. It is therefore necessary to examine both the overall time-averaged particle circulation as well as the movement of particles within each cycle of vibration.

4.6.1 Overall Time-Averaged Particle Circulation

The circulation patterns of particles in shallow vibrated beds has already been examined in work connected with this study [Sprung *et al.*,1986]. Sprung [1987] has extended the work to include a measure of the relative circulation rates in vibrated beds under varying conditions. The previous work used colored tracers to examine the circulation patterns at the transparent walls of the two-dimensional vessel. By using fluorescent-dyed glass particles and an ultra-violet (UV) light source to illuminate the bed, the movement of particles located a few particle diameters into the bed can also be examined. Since the background (the undyed particles) will appear dark, fluorescent tracers which appear as bright spots of light are easier to follow than colored tracers used with white light.

Preparation of Tracer Particles

Fluorescent dye is used to mark the tracer particles. Any dye that is used must meet certain criteria. The dye must be able to adhere to glass and continue to fluoresce after it is dried. It must also have sufficient wear-resistance that it does not rub off the glass particles which it coats, as it is scoured by other particles in the vibrated bed. Acetone-soluble dyes have been found to meet the first condition. Two types of dye are particularly suitable:

- A blue fluorescent dye (A-946 Blue) manufactured by the Volk Corporation
- The "permanent" non water-soluble dye of various colors, used in Sakura SG7 fluorescent markers.

Both dyes are diluted with a large quantity of acetone, so that dye coats on the tracers will be extremely thin, and will not significantly affect particle properties. Adding a few drops of cyanoacrylate to the solution produces a tough wear-resistant dry coat on the tracer particles. In initial tests, the dye coat did not wear or rub off even after several hours in a vibrated bed with $K = 5$. After the dye coating is dry, the dyed particles are sized through screens so that tracer particles are of the same size as other particles in the bed.

Observation of the Circulation Patterns

The two-dimensional vessel with glass walls (see Figure 14 on page 65) is used for observing and recording the solid circulation in the vibrated bed. Quartz glass walls are used, since this material is very transparent to UV light. To observe the effect of an immersed heat-transfer surface on the circulation patterns, a dummy heater tube is placed across the bed between the front and back walls.

The bed is prepared for filming by placing small quantities of blue, yellow and orange tracers in specific locations within a bed of un-dyed particles. A packet of one color is placed at each lower corner of the bed. Two packets of different colors are placed one above and one below the dummy heater tube. Since tracers of different colors which stand out against a dark background are used, it is possible to use a larger volume percentage of tracers than is normally possible. Also, the use

of different colors at various locations within the bed allows the degree of mixing between different regions of the bed to be estimated.

The bed is illuminated by a 100-watt long-wave UV light source. This causes tracer particles to glow brightly and un-dyed particles to appear black. The UV light penetrates about 3—6 mm into the bed of glass particles depending on the particle size. A larger particle size allows greater penetration. Thus, tracers within the bed can also be observed. The proximity of the tracer to the wall can be approximately judged from the brightness of the glow; tracers appear fainter as they move away from the wall into the bed. The movement of the tracers are recorded on video-tape.

Bed circulation patterns are studied using 707-μm glass particles of both densities, with bed depths of 30 and 60 mm, and also using 177-μm low-density glass particles [Johnson, 1987].

4.6.2 Particle Motion Within a Cycle of Vibration

Particle motion within a cycle of vibration is studied using high-speed cinematography. Colored tracer particles are used in a two-dimensional bed. The bed is illuminated by three 1000-watt white-light lamps. Filming is done with a HYCAM-II high-speed camera at 1250 frames per second (fps), giving 50 frames per cycle of vibration, and at 2500 fps, giving 100 frames per cycle.

A K-value of 4 is used in all experiments. Once the bed has reached a steady state, the camera is turned on, and run until the 400 feet of film in the camera runs out. A stationary knife-edge placed against a scale mounted on the vessel, gives an approximate indication of the vessel displacement relative to its rest position. After the film is developed, it is viewed on a cine projector.

4.7 *Measurement of Surface-to-Bed Heat Transfer Coefficients*

The surface-to-bed heat-transfer coefficient for a cylindrical surface immersed horizontally in a shallow vibrated bed is measured. The heat-transfer probe described in section 3.3.4 of the previous chapter is used as the heater (see Figure 20 on page 84). The heater tube and its supports extend through the diameter of the cylindrical three-dimensional vessel as shown in Figure 12 on page 60. Power is supplied to the electrical heating coils within the cylindrical heater probe from a stable DC-voltage supply. The power supplied to the heater coils can be varied between 3 and 150 watts, although in practice, 40 watts of power is never exceeded at steady-state.

The power input to the heater coil is measured by reading the voltage across a power resistor of known value that is connected in series with the heater coil as shown in Figure 21. By measuring the voltage V_r across the 0.1-ohm resistor, and the voltage across the heater coil V_h, the power input Q may be calculated from:

$$Q = \frac{V_h V_r}{0.1} \qquad [4.4]$$

The surface temperature of the heater tube is measured by four thermocouples placed at various locations along the surface of the tube, as described in Section 3.3.4. The heat probe is placed in the bed so that one thermocouple faces upward; one, downward; and two horizontally, facing forward and backward.

Initial experiments in which the bed is mapped at steady-state with a hand-held mobile thermocouple indicate that the bed can be divided by temperature into six regions. Each region is roughly isothermal. The bed temperature is read by T-type thermocouples at six locations indicated

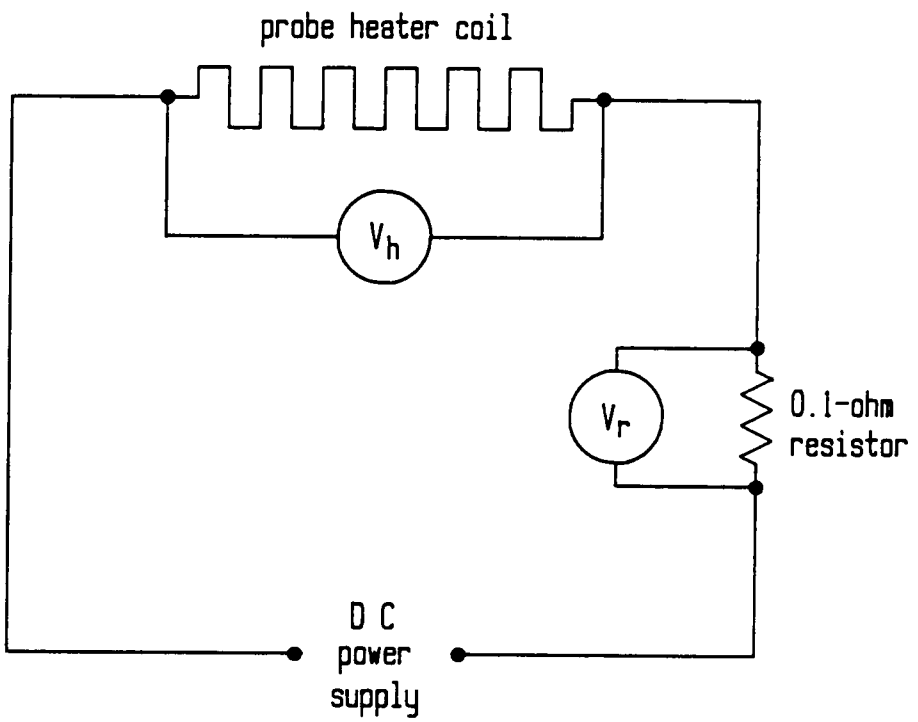

Figure 21. Circuit for measuring the power input to the heat-transfer probe: Voltages V_h and V_r are measured across the heater coils and the 0.1-ohm resistor respectively.

by dark circles in Figure 12 on page 60. There is one thermocouple in each of the six isothermal regions. Mixing of the solid appears to be more intense perpendicularly to the axis of the probe than longitudinally. The two bed thermocouples labelled 2 and 5, closest to the probe usually read a few degrees higher than the other four bed thermocouples. Thermocouples 1, 3, 4, and 6 reflect solid mixing parallel to the probe, and heat does not reach them as efficiently as it reaches 2 and 5. The bed temperature is an average of temperatures read at these six locations.

In addition to the six temperatures that are used to calculate the average bed temperature, three additional thermocouples read temperatures within the bed at locations close to the probe and at the bottom of the bed, to obtain additional information on the flow of heat in the bed, but are not used in the calculation of the heat-transfer coefficient. One the thermocouples is placed 6 mm directly below the bottom surface of the heater—that is, 7.65 mm above the floor of the vessel. This thermocouple reads the temperature within any "dead" zones that may exist below the probe as identified by Sprung *et al.* [1986]. Dead zones are regions in the vicinity of the heat-transfer surface, of reduced particle activity or mixing, and are therefore detrimental to heat transfer. Another compares the effect of the proximity to the probe, and is located in the horizontal plane passing through the axis of the heater and 6 mm to one side of the heat-transfer surface. It is located in a region of high particle mixing. The third thermocouple which is located 7.65 mm above the floor, but away from the probe, gives an indication of temperatures at the bottom of the bed. By comparing readings of these three thermocouples, the effect of the dead zone below the probe on heat transfer may be determined.

Heat-transfer data are collected by a digital computer. Thermocouples in the probe, the probe support, and bed are sampled sequentially. The thermocouples are switched to a common amplifier using the switching circuit described in section 3.3.4.1. Each amplified thermocouple output is digitized and read by a computer. Thermocouples are sampled every 45 seconds. The heat-transfer surface temperature is the average reading of the four probe thermocouples, and the bed temperature is taken as the average reading of the six major bed thermocouples. The voltage V_t across the

0.1-ohm resistor and the voltage across the heater V_h are digitized and read by the computer, and are used to calculate the power supplied to the heater using equation [4.4].

Temperatures of the bed and probe usually reach a steady state in 60 to 90 minutes. The power is varied so that the steady-state temperature of the heater surface is between 80° to 90°C for every experiment. Once this condition is reached, the computer fixes the value of the power supply, and regulates it to less than 0.5% of this value.

After a steady state is reached, all temperatures in the probe and bed, as well as the power input to the heater are recorded once every five minutes over a period of 30 to 40 minutes. From these data, an average value of the heat-transfer coefficient is calculated.

Measurements of heat-transfer coefficients are made for Master Beads over the entire array of size ranges given in Table 2 on page 91. K is varied from 2 to 7; however, with the smallest particle sizes (125 and 88 μm), the bed becomes unstable, bunkering off to one side and exposing the heater when $K > 5$, so no measurements are made for those beds beyond $K = 5$. With glass beads, heat-transfer coefficients are measured for particle sizes of 88, 177, and 707 μm.

5.0 Bed Dynamics - Results and Discussion

5.1 Theoretical Background

All existing physical models for the vibrated bed are based on the assumption that the bed can be modeled as a *single coherent plastic mass*. This means that the bed can be treated as a single homogeneous entity, which does not rebound after colliding with the vessel floor. Models for vibrated beds are largely based on the following assumptions:

1. The bed moves as a single porous piston. This means that the center of gravity of the bed always remains midway between the top and bottom surfaces of the bed. This requirement may be achieved by assuming that:

    a. the voidage of the bed remains constant, or
    b. any change in voidage occurs uniformly over the entire bed, or
    c. the voidage changes are symmetric — for example, if the expansions of the top and bottom regions of the bed were uniform at any given instant.

2. The collision between the bed and the vessel floor takes place instantaneously, and is completely inelastic (there is no rebound).

3. The percolation of air across the bed caused by the formation and closure of the air gap at the bottom of the bed, is entirely in the laminar flow regime, and obeys Darcy's law. This assumption is valid, at least up to frequencies of 100 Hz, according to the results of Gutman and Davidson [1975].

4. The vibrated bed can be treated as a one-dimensional system. This assumption is based on the reasoning that variations in gas pressure and velocity in the vertical direction are much larger than those in any of the horizontal planes, since applied vibrations are in the vertical plane.

In addition to the above, it may also be assumed that wall-friction effects on shallow vibrated beds are negligible. Experimental analysis by Gutman [1974] shows that wall friction is negligible if the bed is relatively shallow ($L/D < 1.$) .

The single-particle model of Takahashi *et al.* [1968] will not be considered here as it has been found to be in serious error, particularly in neglecting the effects of air drag on the bed [Gray and Rhodes,1972]. Apart from the single-particle model, there are four major models for the vibrated bed.

The Kroll model [Kroll,1954,1955] assumes in addition to the assumptions listed above, that the air within the bed can be treated as an incompressible fluid. The Gutman model [Gutman,1974,1976a] is really an extension of the Kroll model, in that it eliminates the assumption of incompressibility, and treats the gas as a compressible fluid.

The wall-friction model of Ryzhkov and Baskakov [1974] considers the influence of wall friction in relatively deep beds ($L/D > 1$). The model neglects drag effects since wall friction has been found to be of importance only in large-particle beds, where drag forces are small. However, as will be shown later, drag effects are not negligible even in large-particle beds. Therefore, the validity of this

model is questionable until drag effects are included. In any case, the model will not be discussed any further since this study deals exclusively with shallow vibrated beds.

The expanding-bed model of Buevich and Galontsev [1978] attempts to address the expansion of the bed during the flight period. In order that the center of gravity of the bed remain midway between the top and bottom surfaces, the expansion is assumed to be uniform, and only to take place at the top and bottom regions of the bed. Expansions of the extreme regions of the bed are assumed to be caused by differences in drag forces on the particles in these regions as compared to particles inside the bed.

5.1.1 Force Balance on the Vibrated Bed

The forces acting on a vibrated bed are shown schematically in Figure 22. If frictional forces in the bed can be considered to be negligible, the balance of forces on the bed can be written as:

$$M_b \frac{d^2(s+a)}{dt^2} + M_b g - A_b(P_L - P_o) - N_b = 0 \qquad [5.1]$$

In the force balance, N_b is the normal force acting on the bed, M_b is the mass of the bed, A_b is the cross-sectional area of the bed, P_L is the pressure at the bottom of the vibrated bed, P_o is atmospheric pressure, a is the displacement of the vessel, and s is the displacement of the bed relative to the vessel. When the bed is in flight, the normal force on the bed disappears, and $N_b = 0$. The mass of the bed M_b, is equal to $A_b L \rho_b$, where ρ_b is the bulk density of the bed. Substituting for the vessel acceleration and bed mass, the equation of motion for the bed during the flight period can be written as:

$$\frac{d^2 s}{dt^2} = \frac{P_L - P_o}{\rho_b L} + a_o \omega^2 \sin(\omega t) - g \qquad [5.2]$$

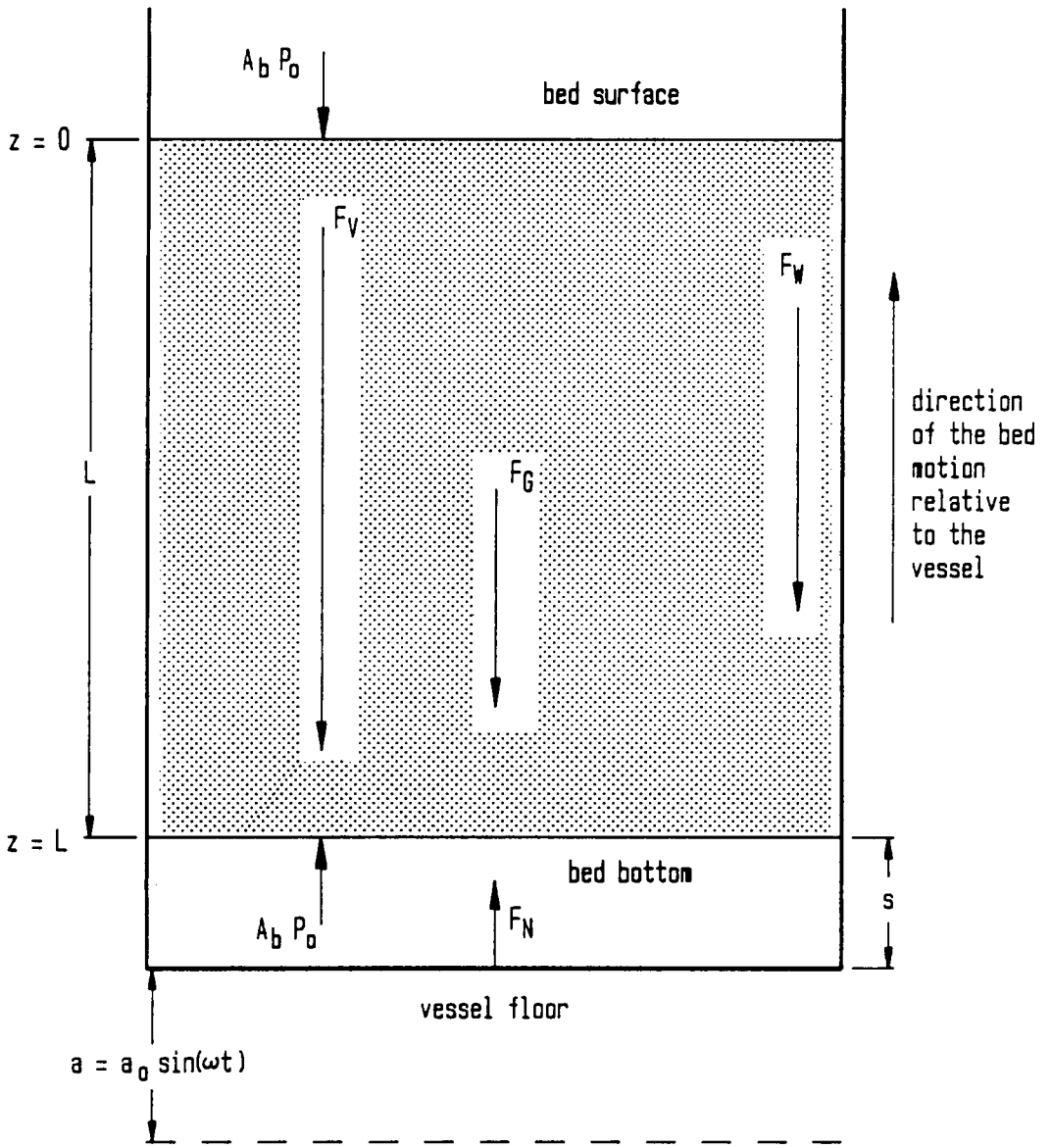

Figure 22. Force balance diagram for a vibrated bed: Schematic representation of the forces acting on a vibrated bed modeled as a single plastic mass. Notation: L - bed depth; A_b - cross-sectional area of the bed; P_o - atmospheric pressure; P_L - pressure at the bottom of the bed; s - air gap thickness; z - vertical ordinate; a - vessel displacement at time t ; a_o - vibrational amplitude; F_g - gravitational force on the bed; F_v - viscous drag force due to the gas flow; F_w - wall friction force; F_N - normal force (only during bed-vessel contact).

While the bed is in contact with the vessel floor, there is no gap at the bottom of the base ($s = 0$). Also, the rate of change of the gap thickness equals zero. As a result $(d^2s/dt^2) = 0$. For the fraction of the cycle in which the bed is in contact with the vessel floor, the force balance for the bed is given by:

$$\frac{N_b}{A_b \rho_b L} = g - a_o \omega^2 \sin(\omega t) - \frac{P_L - P_o}{\rho_b L} \qquad [5.3]$$

The instant at which the net force is equal to zero while the bed is still in contact with the vessel floor, represents the instant of bed lift-off, provided the bed is considered to be rigid and there are no time-dependent variations in bed porosity. At the instant of separation, the normal force on the bed will just equal zero; and since the bed has not yet started moving relative to the vessel, $(d^2s/dt^2) = 0$. Thus the instant of bed-vessel separation t_s is obtained from:

$$\left.\frac{P_L - P_o}{\rho_b L}\right|_{t_s} + a_o \omega^2 \sin(\omega t_s) - g = 0 \qquad [5.4]$$

5.1.2 The Kroll Model

The Kroll model [Kroll,1954,1955] assumes that the air flowing through the bed can be treated as an incompressible gas. The superficial velocity of the air is related to the vertical pressure gradient in the bed through Darcy's law:

$$u_o = -\frac{\kappa}{\mu} \frac{dP_z}{dz} \qquad [5.5]$$

where P_z is the pressure of the gas at any depth z within the bed. The permeability κ of the porous medium is given in m^2 by the Kozeny-Carman correlation [Bird *et al.*,1960]:

$$\kappa = \frac{1}{180} \frac{d_p^2 \varepsilon^3}{(1-\varepsilon)^2} \qquad [5.6]$$

The assumption of gas incompressibility implies that the pressure gradient across the bed will be linear. Since the bed porosity is assumed constant, the flux of air through the bed must accumulate in the gap below the bed. Therefore, the velocity of gas flow through the bed must equal the rate of change of gap thickness. Thus:

$$\frac{ds}{dt} = u_o = -\frac{\kappa}{\mu} \frac{P_L - P_o}{L} \qquad [5.7]$$

Substituting this into the equation of motion for the flight period [5.2] gives:

$$\frac{\kappa}{\mu L} \frac{d}{dt}(P_L - P_o) + \frac{1}{\rho_b L}(P_L - P_o) = g - a_o \omega^2 \sin(\omega t) \qquad [5.8]$$

In addition, the assumption of incompressibility means that the pressure in the bed must equal zero when the bed is in contact with the vessel floor:

$$\left. \frac{P_L - P_o}{\rho_b L} \right|_{t_s} = 0 \qquad [5.9]$$

The phase angle θ_s ($= \omega t_s$) of bed-vessel separation can be obtained by substituting this into equation [5.4] and solving the resulting equation to give:

$$\theta_s = \sin^{-1}(g/a_o \omega^2) \qquad [5.10]$$

If the superficial velocity of the gas (which equals the relative velocity of the bed) is substituted in the equation of motion during the flight period, the model of Yoshida and Kousaka [1967] is obtained. Therefore, the models of Kroll and of Yoshida and Kousaka are mathematically identical.

The equation of motion can be put into a dimensionless form by introducing the following dimensionless variables:

$$\Phi = \frac{(P_z - P_o)}{P_o}; \quad Z = z/L; \quad T = (\omega t)$$

Since the equation of motion is valid only for the flight period, the time axis can be shifted so that $T = 0$ corresponds to the instant of lift-off. The Kroll model may now be written as:

$$\Psi \frac{d\Phi_L}{dT} + \Lambda\Phi_L = \frac{1}{K} - \sin(T + \theta_s) \qquad [5.11]$$

where Φ_L is Φ evaluated at $z = L$. The dimensionless groups Ψ and Λ are given by:

$$\Psi = \frac{\kappa P_o}{\mu L a_o \omega} \qquad [5.12]$$

$$\Lambda = \frac{P_o}{\rho_b L a_o \omega^2} \qquad [5.13]$$

The equation of motion of the vibrated bed, [5.11], is an initial-value ordinary differential equation that can be solved subject to the following initial conditions:

$$\Phi_L = 0; \quad S = 0 \quad \text{at} \quad T = 0 \qquad [5.14]$$

The analytic solution to this equation is:

$$K\Lambda\Phi_L = 1 - \frac{R_h}{R_h^2 + 1}\left[\left(R_h\sqrt{K^2 - 1} + 1\right)\sin T + \left(R_h - \sqrt{K^2 - 1}\right)\cos T - \frac{R_h\sqrt{K^2 - 1} + 1}{R_h}\exp(-R_h T)\right] \qquad [5.15]$$

In this equation, R_h is the ratio of the dimensionless groups Λ and Ψ, and is given by:

$$R_h = \frac{\Lambda}{\Psi} = \frac{\mu}{\rho_b \omega \kappa} \qquad [5.16]$$

Since the inverse of permeability ($1/\kappa$) is a measure of the resistance of the bed, the factor R_h is proportional to the resistance of the bed per unit bed weight at a given frequency. Obviously, as the viscosity of the gas increases, this resistance would be expected to increase. However, it is interesting to note that the value of the resistance per unit bed weight would tend to *decrease* as the vibrational frequency were increased.

Expanding the group of dimensionless parameters on the left-hand side of equation [5.15] gives:

$$K\Lambda\Phi_L = \frac{P_L - P_o}{\rho_b L g} \qquad [5.17]$$

This represents the ratio of the pressure force acting on the bed to the weight of the bed or the drag force per unit bed weight. In the absence of any external forces other than gravity acting on the bed, gas fluidization of the bed due to the upward flow of gas would take place if this ratio exceeds unity. In practice, the drag force per unit bed weight exceeds unity for a fraction of each cycle, therefore the bed does not have sufficient time enter a fully fluidized state. Note that equation [5.15] suggests this ratio should depend only on the vibrational intensity parameter K and R_h, which is independent of bed depth.

Using dimensionless variables, a dimensionless gas velocity may be defined as:

$$U_o = \frac{dS}{dT} = \frac{u_o}{a_o \omega} \qquad [5.18]$$

The dimensionless velocity is related to Φ_L by:

$$U_o = -\Psi \Phi_L \qquad [5.19]$$

Therefore, the dimensionless air-gap size S can be obtained by integrating equation [5.15] for Φ_L, with the initial condition that $S = 0$ at $T = 0$. This gives:

$$S = \frac{1}{R_h K}\left[T - \frac{R_h}{R_h^2 + 1}\left[\left(R_h - \sqrt{K^2 - 1} \right) \sin T - \left(R_h \sqrt{K^2 - 1} + 1 \right) \cos T \right.\right.$$

$$\left.\left. - \frac{R_h \sqrt{K^2 - 1} + 1}{R_h^2} \exp(-R_h T) \right] - \frac{R_h \sqrt{K^2 - 1} + 1}{R_h} \right] \qquad [5.20]$$

The factor $(1/R_h K)$ does not contain the bed depth. This means that the gap size predicted by the Kroll model is also independent of the bed depth.

Plots of the group $K\Lambda\Phi_L$ and the gap size as a function of the phase angle of vibration are given in Figure 23 on page 122 with $K = 2$, and in Figure 24 on page 123 with $K = 4$. The three values of R_h used in the plots are equivalent to beds with particle diameters of 707, 177, and 88 μm, with a bed porosity of 0.41, and a solid density of 3600 kg/m^3. The value of R_h decrease with increasing particle size. The vibrational frequency is 25 Hz. The plots indicate that particularly at $K = 4$, the pressure drop across the bed exceeds the bed weight for a part of the vibrational cycle for the two smaller particle sizes. Also, at $K = 4$, the bed of 707-μm particles undergoes unstable cyclic throws. That is, it collides with the bed later than the instant at which it should lift-off.

Equation [5.19] is a dimensionless form of Darcy's equation since it relates the dimensionless velocity through the bed to the dimensionless linear pressure drop across the bed. Therefore, the dimensionless group Ψ, may be described as a "dimensionless bed permeability parameter". Alternatively, it may be considered as a dimensionless group that describes the effect of viscous drag caused by an oscillatory flow of gas through a porous bed. The dimensionless group Λ, contains the bed density and vibrational acceleration, and therefore, describes the apparent weight of the bed under the action of vibrational acceleration.

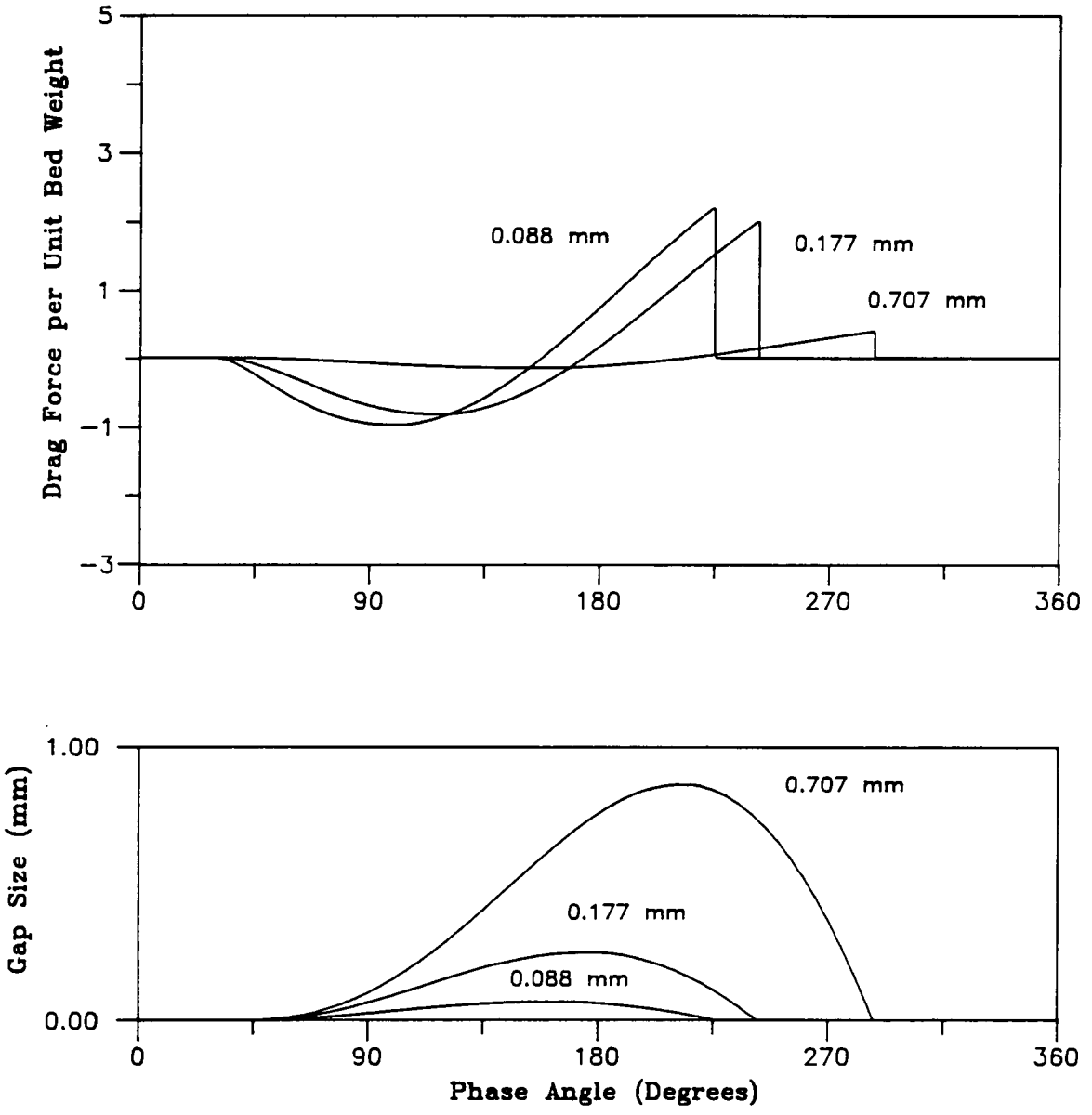

Figure 23. Predictions of the Kroll model at K = 2: Drag force per unit bed weight and size of the gap beneath the bed as predicted by the Kroll model, for a vibrational intensity parameter, $K = 2$, and with particle sizes of 707, 177, and 88 μm.

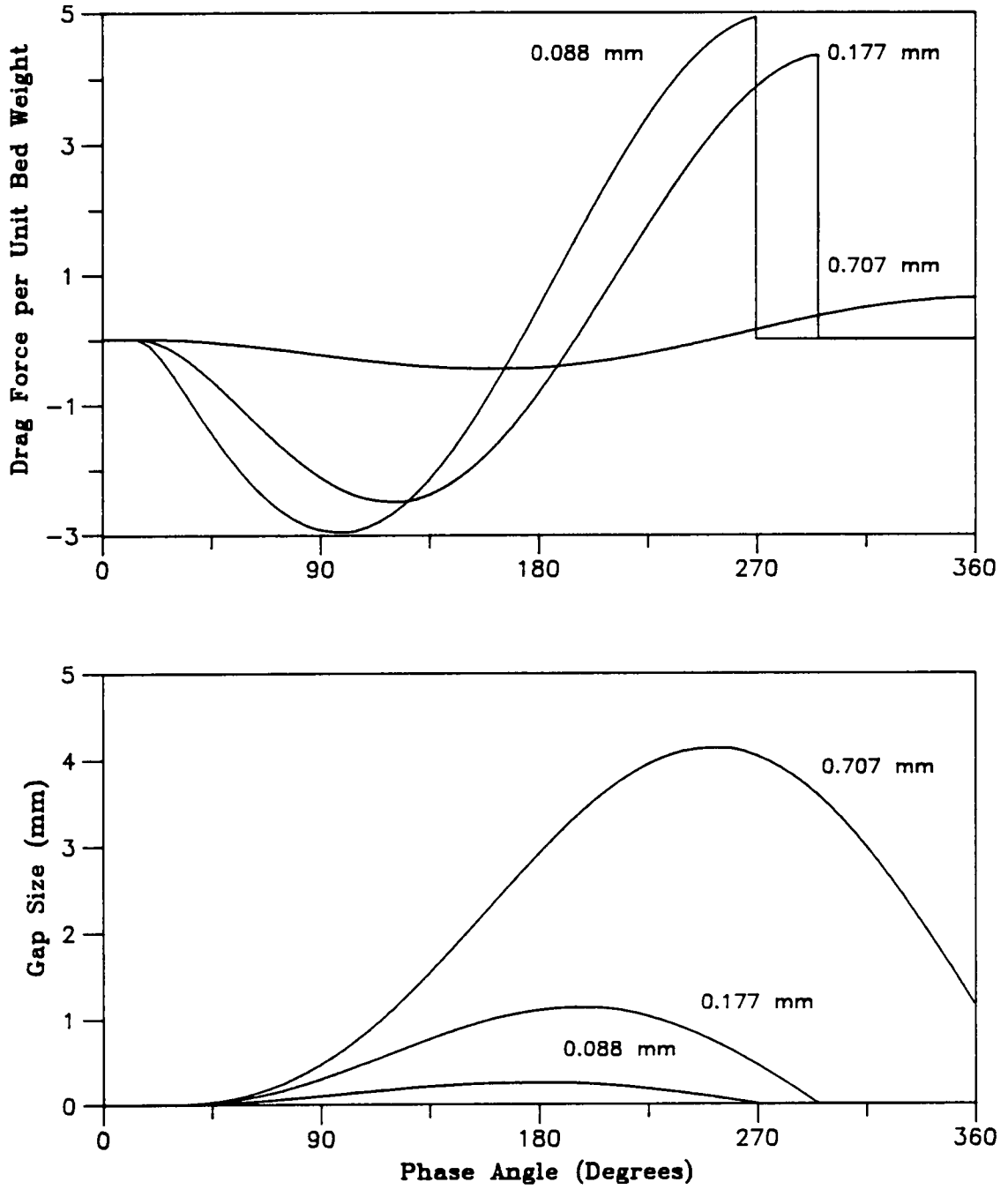

Figure 24. Predictions of the Kroll model at K = 4: Drag force per unit bed weight and size of the gap beneath the bed as predicted by the Kroll model, for a vibrational intensity parameter, $K = 4$, and with particle sizes of 707, 177, and 88 μm.

5.1.3 The Gutman Compressible-Gas Model

The only difference between formulations of the Gutman and Kroll models is the elimination of the assumption of incompressibility in the Gutman model. In addition, it is assumed that the compression of the gas in the bed will be isothermal. This is a reasonable assumption since the gas is in close contact with a large mass of particles that have a large heat capacity in comparison to the gas, and therefore the particles act as an infinite heat sink.

With the assumption of constant bed porosity, the one-dimensional equation of continuity for the flow of gas through the bed can be written as:

$$\varepsilon \frac{\partial \rho}{\partial t} = -\frac{\partial}{\partial z}(\rho u_o) \qquad [5.21]$$

Here, ρ_z is the density of the gas at a depth z within the bed at any time t. Substituting Darcy's equation, [5.5], for the superficial gas velocity into the above equation, and expanding gives:

$$\frac{\partial \rho}{\partial t} = \frac{\kappa}{\varepsilon \mu}\left[\frac{\partial \rho}{\partial z}\frac{\partial P_z}{\partial z} + \rho \frac{\partial^2 P_z}{\partial z^2}\right] \qquad [5.22]$$

Using the equation of state for a compressible gas, the change in density of the gas can be related to the change in pressure (for isothermal compression of the gas) by: $\partial \rho = \rho_o \partial P$, where ρ_o is the gas density at atmospheric pressure. Substituting for ρ in equation [5.22] gives:

$$\frac{\varepsilon \mu}{\kappa P_z}\frac{\partial P_z}{\partial t} = \left[\frac{1}{P_z}\left(\frac{\partial P_z}{\partial z}\right)^2 + \frac{\partial^2 P_z}{\partial z^2}\right] \qquad [5.23]$$

If pressure variations in the bed are small in magnitude, and vary about a mean pressure, say atmospheric, then $P_z \simeq P_o$, and

$$\frac{\partial^2 P_z}{\partial z^2} \gg \frac{1}{P_o}\left(\frac{\partial P_z}{\partial z}\right)^2$$

Using these approximations, the equation of continuity now becomes:

$$\frac{\partial P_z}{\partial t} = \frac{\kappa P_o}{\varepsilon \mu} \frac{\partial^2 P_z}{\partial z^2} \qquad [5.24]$$

This is identical in form to the one-dimensional diffusion equation. Using the dimensionless variables defined above, the equation can be written in a dimensionless form

$$\frac{\partial \Phi}{\partial T} = \Gamma \frac{\partial^2 \Phi}{\partial Z^2} \qquad [5.25]$$

The dimensionless group Γ is defined as

$$\Gamma = \frac{\kappa P_o}{\varepsilon \mu \omega L^2} \qquad [5.26]$$

Note that Γ is similar to the dimensionless group $(\varepsilon\mu\omega/2\kappa P_o)^{0.5}L = (2\Gamma)^{-0.5}$ that Gutman [1976a] obtains in his solution to the equation.

The dimensionless initial condition is:

$$\Phi = 0 \quad \text{at} \quad T = 0 \qquad [5.27]$$

The pressure on the top of the bed is always atmospheric, so the upper boundary condition is

$$\Phi = 0 \quad \text{at} \quad Z = 0 \qquad [5.28]$$

The mass flow rate of gas across the lower boundary obeys Darcy's law, and it must equal the rate of accumulation of air in the gap below the bed if the porosity of the bed is invariant. Therefore,

$$\rho_o u_o = \frac{d(\rho s)}{dt} = -\rho_o \frac{\kappa}{\mu} \frac{dP_z}{dz}\bigg|_{z=L} \qquad [5.29]$$

where ρ_o is the average density of the gas in the gap. Assuming that pressure variations are small, $\rho \simeq \rho_o$. Then, the gas density can be taken out of the differential in the equation above. In dimensionless form, the lower boundary equation of continuity is:

$$\frac{dS}{dT} = -\Psi \left. \frac{d\Phi}{dZ} \right|_{Z=1} \qquad [5.30]$$

This equation can be combined with the equation of motion for the bed during flight, [5.2], to give a single lower boundary condition during the period of flight. In dimensionless form it is:

$$\Phi_L = \frac{1}{\Lambda}\left[\frac{1}{K} - \sin(T) - \Psi \frac{d}{dT}\left(\left. \frac{d\Phi}{dZ} \right|_{Z=1} \right) \right] \qquad [5.31]$$

When the bed is in contact with the vessel floor,

$$\left. \frac{d\Phi}{dZ} \right|_{Z=1} = 0 \qquad [5.32]$$

Equation [5.31] is an unusual boundary condition in that it contains a double derivative of the dependent variable with respect to both time and space, but this does not pose a problem to the solution of the governing equations. A semi-analytical solution was obtained by Gutman [1974,1976a] by assuming that the pressure P_L of the air in the gap could be expressed as a Fourier series, and then solving for the Fourier coefficients. However, Akiyama and Naito [1987] have shown that a more reliable result can be obtained if the model is solved by a numerical technique such as orthogonal collocation, rather than by pre-supposing the form of the solution.

A numerical solution technique would start off from the first cycle of vibration. At this point, as the initial condition states, the pressure is atmospheric everywhere in the bed. Therefore, the instant of bed lift-off is given simply as $\sin^{-1}(1/K)$. The solution is then carried out over several cycles until the steady-state criterion, that the pressure at any instant t in one cycle must equal the pressure at $t + 2\pi$ in the following cycle, is met.

5.1.3.1 The Effect of Gas Compressibility

Kroll [1955] has shown that the ratio of the pressure at any depth z in the bed to the pressure below the bed at the instant when the pressure beneath the bed is most negative can be obtained in the form of an analytic expression from equation [5.24]. The solution assumes the fluctuation of the pressure beneath the bed to be a simplified sinusoidal function of the form $P_L = P_o + C_p \sin(\omega t)$, where C_p is a constant. Using dimensionless variables, the ratio can be expressed as:

$$\frac{\Phi}{\Phi_L} = Z - \frac{2}{\pi} \sum_{n=1}^{\infty} \frac{(-1)^{n+1}}{n\left[(n\pi)^4 \Gamma^2 + 1\right]} \sin(n\pi Z) \qquad [5.33]$$

A graph of the ratio (Φ/Φ_L) as a function of the dimensionless bed height ordinate, $1 - z/L$, is given in Figure 25 using values of Γ between 5 and 0.09. This clearly establishes Γ as a measure of the effect of gas compressibility in the bed. The smaller the value of Γ, the larger the effect of gas compressibility in the bed. The effect of compressibility is determined only by the frequency of vibration and *not* by the vibrational intensity. It is strongly affected by the particle size and bed depth. As shown in Figure 25, when $\Gamma = 0.09$, approximately 50% of the pressure drop across the bed takes place in the bottom 20% of the bed. Obviously, as the pressure beneath the bed reaches a maximum positive value, the greater part of the pressure drop across the bed will still be in the bottom part of the bed, but the actual gauge pressure will now be positive. Therefore, the bottom section of a bed that is strongly influenced by gas compressibility will be subjected to extremely large swings in the pressure gradient over a single cycle of vibration.

As a comparison, Table 4 on page 129 gives values of Γ for various bed conditions, and at vibrational frequencies of 25 and 50 Hz.

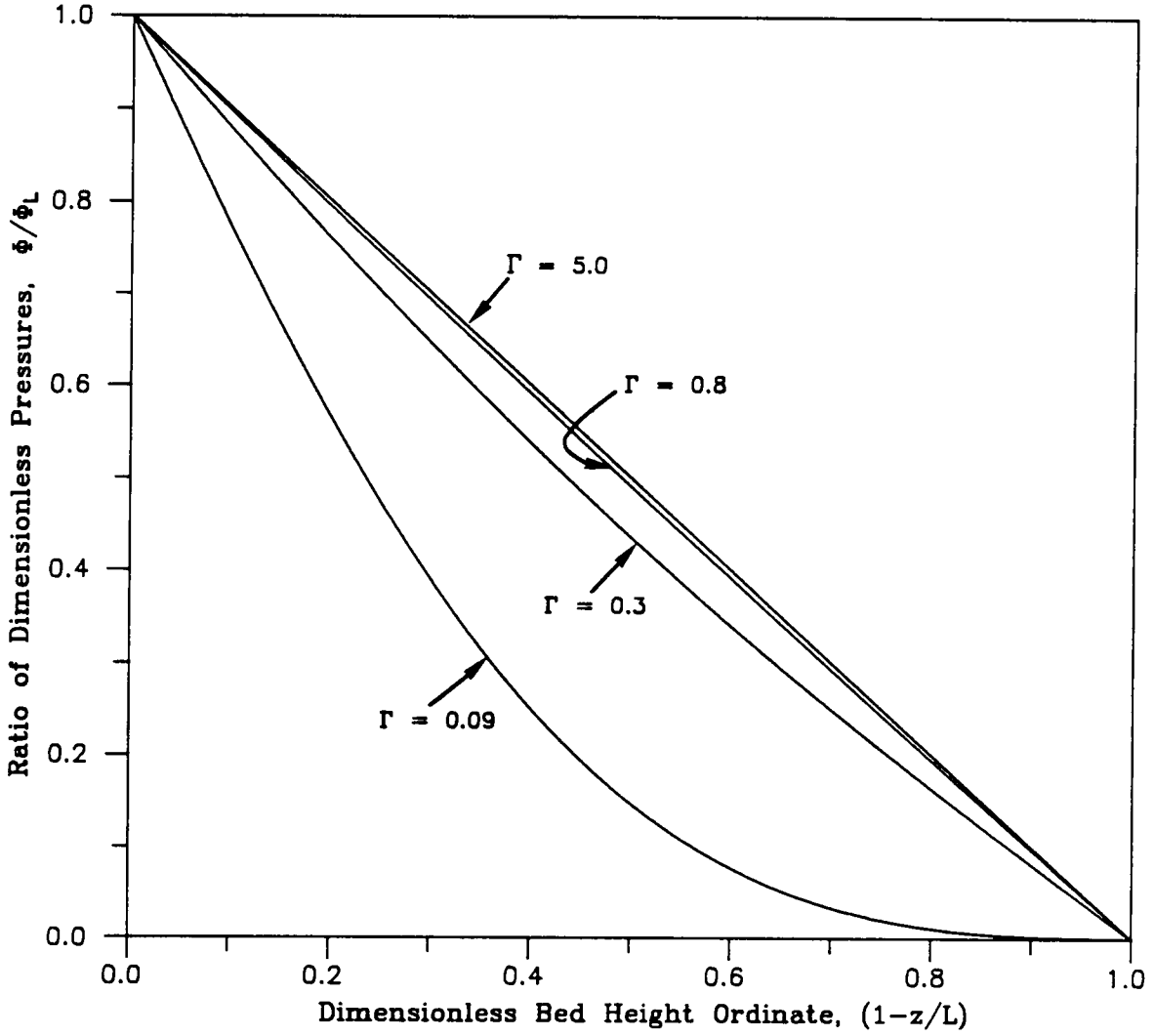

Figure 25. Effect of gas compressibility on the vertical pressure gradient: The dependence of the ratio of the dimensionless pressure Φ, at depth z, to the dimensionless pressure Φ_L, at the bottom of the bed (at depth L), on Γ, the dimensionless group describing the effect of gas compressibility.

Table 4. Values of the compressibility parameter Γ, for various bed and vibrational conditions

Particle Size (microns)	Frequency (Hz)	Bed Depth (mm)	Γ
800	50	40	18.749
707	25	30	52.066
177	25	30	3.263
100	50	40	0.293
88	25	30	0.807
20	25	30	0.017

It can be seen by comparing Table 4 with Figure 25 that even with a 30-mm deep bed of 88-μm particles vibrated at 25 Hz, the pressure drop across the bed is close to linear. However, Gutman has noted by comparing the variation in the pressure beneath the bed over an entire cycle, that compressibility effects can be neglected if:

$$\left(\frac{\varepsilon\mu\omega}{2\kappa P_o}\right)^{0.5} L < 0.5$$

This is equivalent to the condition: $\Gamma > 2$.. It is also important to note that the dependence of Γ on the bed depth is so strong that if the bed is bunkered, it is possible for compressibility effects to be important in the deeper section of the bed even though they may be inconsequential if the average bed depth were considered.

A comparison of cyclic pressures beneath the bed and gap sizes as predicted by the Kroll and Gutman models (as solved by Gutman [1974,1976a]) for a 40-mm deep bed of 800-μm particles vibrated at 20 Hz with $K = 2.06$ is given in Figure 26 on page 131; and for 100-μm particles vibrated at 50 Hz with $K = 5.03$ is given in Figure 27 on page 132. As expected, differences between the predictions of the two models are small with larger particles and lower frequencies. With smaller particle sizes and higher frequencies, the differences are more apparent. The primary difference is that after the bed collides with the vessel base, the incompressible-gas model predicts an instantaneous drop to zero in the pressure beneath the bed, whereas the inclusion of gas compressibility means that this pressure will decay more slowly after the collision. Also, if the effect of compressibility is noticeable, both positive and negative limiting values of the pressure fluctuation are greater in magnitude for the compressible-gas model. However, Akiyama and Naito [1987], have suggested the possibility of some error in Gutman's solutions. Their solutions tend to give smaller magnitudes for the limiting values of the pressure fluctuation. As shown in Figure 27 on page 132, the gap size predicted by the compressible-gas model is larger than that obtained from the incompressible-gas model.

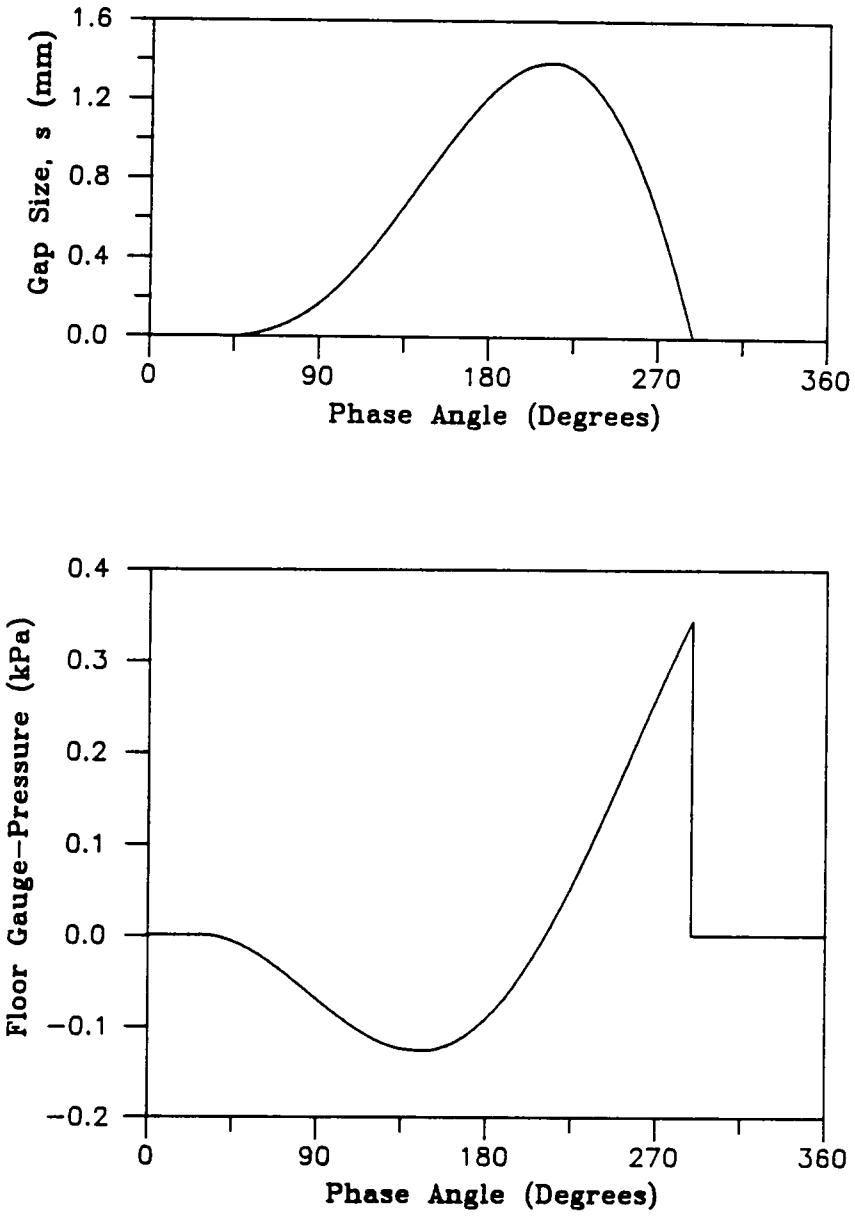

Figure 26. Comparison between Kroll and Gutman models when compressibility effects are negligible: The predictions of the Kroll and Gutman models of the air gap thickness and floor pressures for a 40-mm deep bed of 800-μm particles. The frequency of vibration is 20 Hz, and $K=2.06$ [Gutman,1974]. Note that the predictions of both models are identical in this case.

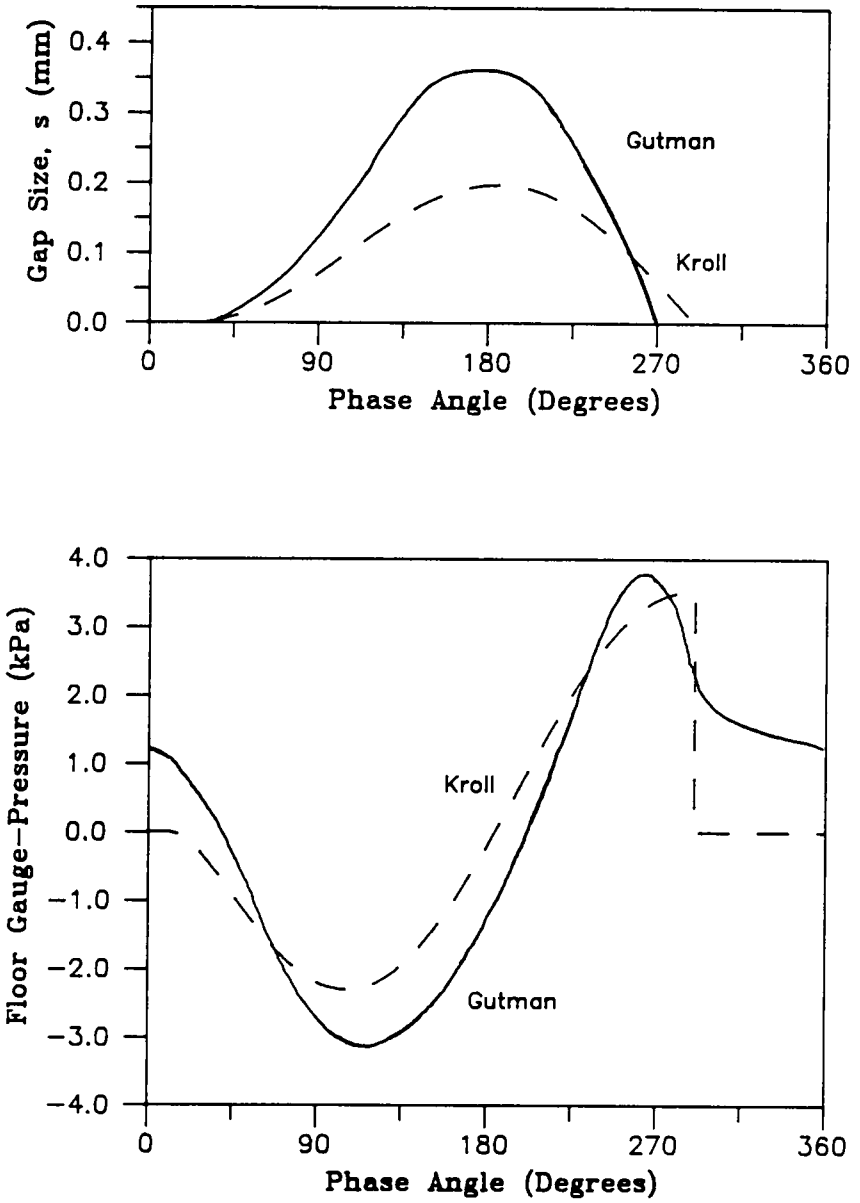

Figure 27. Comparison between Kroll and Gutman models when compressibility effects are important: The predictions of the Kroll and Gutman models of the air gap thickness and floor pressures for a 40-mm deep bed of 100-μm particles. The frequency of vibration is 50 Hz, and $K = 5.03$ [Gutman,1976a]. The predictions of the Gutman model is different from that of the Kroll model in this case.

5.1.3.2 Limitations of the Compressible-Gas Model

The incompressible-gas model predicts that both maximum and minimum floor pressures continuously increase with bed depth. With the inclusion of compressibility, the maximum and minimum values increase to a limit, and then there is no further increase in the extreme values. In practice, Gutman [1974] found that although this was the trend in larger particles, the maximum pressure beneath the bed reached a limiting value with fine particles at a bed depth of 60 mm, after which it started to decrease. This is consistent with the findings of Buevich *et al.* [1979], as reported in Chapter 2. There is no definite explanation for this phenomenon. Gutman [1974] has suggested that it might be due to the generation of tensile forces within the bed caused by the extreme nonlinearity of the pressure gradient. These tensile forces cause a break-up of the bed structure creating large porosity variations within the bed and invalidating the assumption of constant bed porosity. Solution of equation [5.33] with very small values of Γ will give negative values of the pressure ratio Φ/Φ_L in some regions of the bed. Gutman has suggested that the compressible-gas model breaks down when $\Gamma < 0.125$.

Gutman and Davidson [1975] have shown that for oscillatory gas flows at frequencies above 100 Hz, Darcy's law is no longer valid. Above 100 Hz, the dissipation of energy from the gas is increasingly caused by rapid changes in the momentum of the gas flow. However, for most practical purposes, frequencies higher than 100 Hz are not used since the bed is only very slightly mobile.

As will be shown later, the assumption of constant bed porosity may not be valid even in beds where the effects of compressibility are not large enough to cause break-up of the bed structure. Expansion of the bed as the pressure beneath the bed goes negative will cause some of the air flowing down into the bed to be retained by the bed, rather than appearing in the gap below the bed.

If the bed bunkers, then the bed depth will vary, causing horizontal variations in pressures below the bed. This will create horizontal flows of gas from one region of the bed to another, thus invalidating the assumption of one-dimensionality in the model.

5.1.4 The Expanding-Bed Model

Buevich and Galontsev [1978] have attempted to extend the Kroll model to include the effects of bed expansion. The expansion is assumed to be uniform, and also is assumed to take place only at the top and bottom sections of the bed. The model was originally developed for vibrated beds with additionally imposed gas flows, so that the vessel floor is permeable to gas flow. However, it is possible to adapt it for a non-permeable vessel floor.

The greatest problem with any model that attempts to include porosity variations is to describe the trajectory of the center of gravity of the bed, since it will shift between the upper and lower boundaries of the bed as the porosity varies. However, if the bed expansion is uniform over the entire bed, the center of gravity will remain midway between the upper and lower surfaces of the bed as shown in Figure 28. This means that the trajectory of the center of gravity during the flight period will be exactly the same whether the bed expands or not. Since air is assumed to be compressible, the equation of motion of the center of gravity will be exactly the same as for the Kroll model. That is:

$$\frac{d^2 z_c}{dt^2} + \frac{\mu}{\rho_b \kappa} \frac{dz_c}{dt} = a_o \omega^2 \sin(\omega t) - g \qquad [5.34]$$

where z_c is the vertical position of the center of gravity of the bed relative to the vessel floor. Obviously, substituting $s = z_c$ in this equation would make it identical to the Kroll model. As shown in Figure 28, the distance between the center of gravity and either the top or bottom surface of the bed at any instant is $H = f(t)$. The distance between the top of the bed and the vessel floor at any

instant is $z_c + H$. If the ratio of the drag force on the top of the bed to that inside the bed is σ, the equation of motion of the top of the bed can be written as:

$$\frac{d^2(z_c + H)}{dt^2} + \sigma \frac{\mu}{\rho_b \kappa} \frac{d(z_c + H)}{dt} = a_o \omega^2 \sin(\omega t) - g \qquad [5.35]$$

Expanding and substituting for the equation of motion of the center of gravity gives:

$$\frac{d^2H}{dt^2} + \sigma \frac{\mu}{\rho_b \kappa} \frac{dH}{dt} = (1 - \sigma) \frac{\mu}{\rho_b \kappa} \frac{dz_c}{dt} \qquad [5.36]$$

A similar analysis on the bottom surface gives:

$$\frac{d^2H}{dt^2} + \sigma \frac{\mu}{\rho_b \kappa} \frac{dH}{dt} = (\sigma - 1) \frac{\mu}{\rho_b \kappa} \frac{dz_c}{dt} \qquad [5.37]$$

Note that the permeability in the equation of motion for the center of gravity is time-dependent. The porosity of the bed at any instant can be determined by solving for the trajectories of the top and bottom surfaces of the bed. Thus using the three equations of motion, the bed expansion can be taken into account. The initial conditions for solving the model are:

$$H = H_o; \; z_c = H_o \quad \text{at} \quad t = \theta_s \qquad [5.38]$$

Here, H_o is half the static height of the bed, and θ_s is the phase angle of lift-off given by $\sin^{-1}(1/K)$.

However, this model suffers from a number of drawbacks:

- The expansion of the bed is unlikely to be uniform at all times. Particularly as the bed is lifting off the vessel floor, it is more likely that the top of the bed will expand earlier than the bottom of the bed.

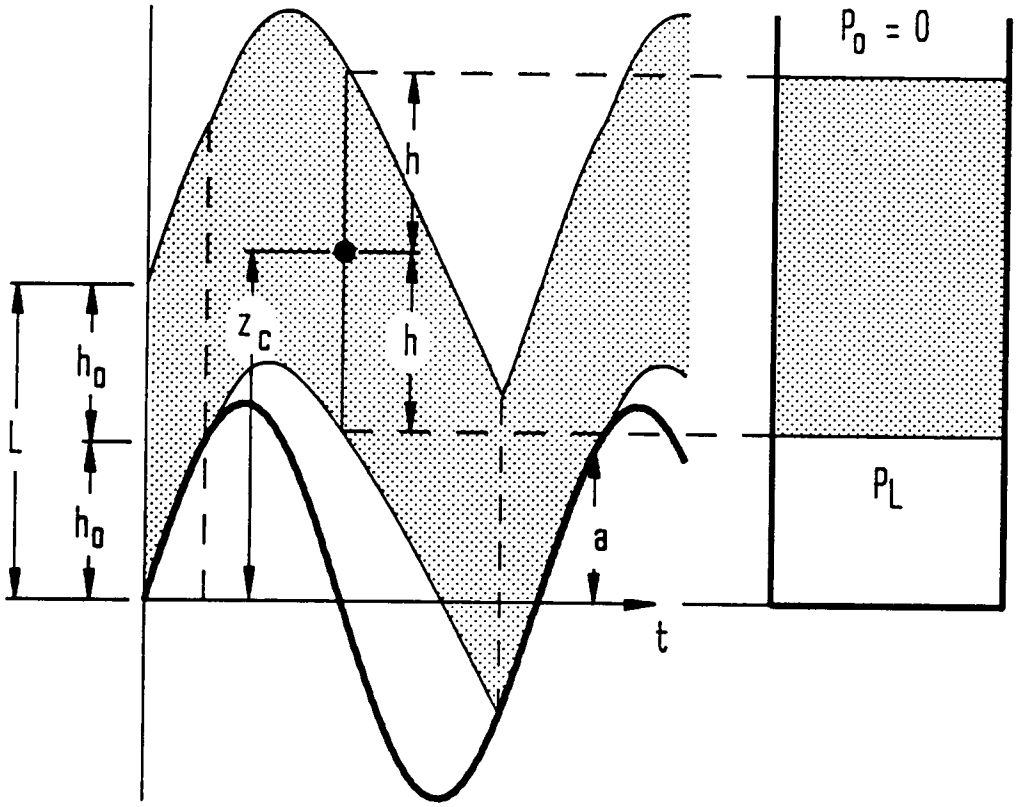

Figure 28. Schematic representation of the expanded-bed model: The one-dimensional expanded-bed model according to Buevich and Galontsev [1978]. Notation: L - Bed depth; z_c - vertical ordinate of the center of gravity of the bed relative to the vessel floor; H - half-bed height; H_o - half-bed height at lift-off; a - vertical displacement of the vessel; P_o - atmospheric pressure; P_L - pressure at the bottom of the bed; t - time.

- The drag ratio σ cannot be theoretically evaluated. No empirical correlations for σ exist. As a result, this model has been solved only for "typical" values of σ by Buevich and Galontsev [1978].
- The variation in bed porosity is more likely to be of greater importance in small-particle beds. However, in such beds, the assumption of gas incompressibility will be increasingly in error.

5.2 Mechanics of the Shallow Vibrated Bed

This section will deal with observation and discussion of the overall mechanics of the shallow vibrated bed. Floor pressure fluctuations and their effects on bed motion and expansion will be discussed. Later sections will deal with particle circulation and localized phenomena in the vibrated bed.

5.2.1 Observation of the Bed Trajectory

By using a strobe lamp, which is continuously triggered by a phase-delayed pulse, to back-light a "two-dimensional" vibrated bed, it is possible to observe the instant of lift-off of the bed from the vessel floor, and later in the cycle, the instant of bed-vessel collision. More critical values can be obtained by taking back-lit phase-delayed photographs of the gap. The lift-off and collision points observed in beds of 707- and 177-μm Master Beads with K ranging from 3 to 7 are summarized in Table 5 on page 138. The gap size at $K = 2$ is very small, and reliable values of the lift-off and collision are not possible. With the two smallest particle sizes (125 and 88 μm), no gap can be observed beneath a 3-cm deep bed even with $K = 5$ at atmospheric pressure.

Table 5. Observed phase angles of lift off and collision for 707 and 177 μm Master Beads

Particle Size (μm)	Phase Angle of:	Vibrational Intensity Parameter, K				
		3	4	5	6	7
707	lift-off	52/36	52/36	(a)	(a)	(a)
	collision	318	354	(a)	(a)	(a)
177	lift-off	112	93	68	58	47
	collision	270	293	314	320	33[illegible]

(a) - unstable bed throw

5.2.1.1 Bed Lift-off

Two phase-angles are quoted for the lift-off of 707-μm particles. The larger value corresponds to the phase angle at which a very narrow (often broken) strip of light appears at the bottom of the bed. The thin strip of light can be observed consistently at every cycle at the given phase angle. The lower value represents the instant at which occasional "flashes" of light can be seen beneath the bed. Obviously, these flashes of light can only be seen if there is a particle-free pathway for the light to travel across the bed. However, the flashes are small — approximately equal in diameter to the particles — and do not appear in every cycle. The significance of these values will be discussed later.

The lift-off of the bed is very gradual (relative to other cyclic phenomena) and is therefore difficult to observe accurately. It is particularly difficult with small particle sizes and low vibrational intensities.

The results summarized in Table 5 on page 138, show that as the particle size is reduced, the bed lifts off the vessel floor at larger phase angles. Eventually, when the particle size is reduced to 125 μm, the bed cannot be observed to lift-off the vessel base any longer.

With small particle sizes, the phase angle of lift-off is reduced as the vibrational intensity is increased. As the particle size is increased, the phase angle of lift-off increasingly becomes less K-dependent for $K \geq 3$. A rough measurement of the phase angle of lift-off at $K = 2.5$ with a particle size of 707 μm gives a value of 43°, indicating that there is possible K-dependence at lower values of K.

When the bed is vibrated in a vacuum, all particle sizes are observed to lift off the vessel base. This is true even of FCC powder and 10-μm copper powder. As the pressure in the vessel is slowly increased, the gaps below these fine-particle beds suddenly disappear.

5.2.1.2 Bed Trajectory and Bed-Vessel Collision

The size of the air gap is observed to increase with increasing vibrational intensity and particle size. In a vacuum, the differences in the air gap thickness between different beds tends to diminish.

Unlike the lift-off, the instant of bed-vessel collision is relatively easy to detect because in most cases, it is sudden. None of the beds show any tendency to rebound off the vessel floor after the collision. Therefore, the assumption that the bed-vessel collision can be modeled as being completely plastic appears to be valid (but see also the later discussion about the "states" in ultra-shallow beds).

The results in Table 5 on page 138 show that as the particle size is increased, the duration of the flight period also increases. The instant of collisions also appears later in the cycle as K is increased. For 707-μm Master Beads, the cyclic throw of the bed becomes unstable for values of K greater than 4, because the period of flight becomes longer than the period of vibration. This means that the bed collides with the vessel floor later than the instant of lift-off. Thus, the collision process does not have sufficient time to decay before the bed is in flight again. The result is an unstable behavior of the vibrated bed, where the bed begins to rock in the (major) horizontal direction about a central axis. One half of the bed is in flight during one cycle, while the other half remains in contact through the entire cycle. In the following cycle, the bed rocks in the opposite direction, so that the half that was in flight in the first cycle now remains in contact with the floor throughout the cycle. This unstable rocking motion is observed in beds of 500-μm particles when $K > 5$, and also in small-particle beds under vacuum at values of K greater than about 4.

The collision between large-particle beds and the vessel floor can also be observed on an oscilloscope trace of the accelerometer output. A "kink" appears in the waveform as shown in Figure 15 on page 68. The kink is caused by the collision which sends an impulse through the vessel floor that is picked up by the accelerometer. The displacement of the vessel is not affected

by this collision if the mass of the vibrating table is large compared to that of the bed. If either the leaf springs are not sufficiently stiff or the mass of the vibrating table is low, the output of the displacement transducers will also show severe distortion at the instant of collision. The collision is also audible. With small-particle beds (335 μm and below), there is no distortion of either the acceleration or displacement waveforms. This difference will de discussed further in later sections on bed bunkering.

The entire bed does not fall back onto the floor at one instant. Instead, the gap closes first at the side walls, and closes from either wall toward the center of the floor. As shown in Figure 29 on page 142 and Figure 30 on page 143, this difference in the phase angle of gap closure at the side walls and at the center is more noticeable in smaller particles (177 μm) than in larger particles (707 μm).

Compaction of the Bed During the Bed-Vessel Collision

High-speed cinematography at 2500 frames per second (fps) of a bed of 177-μm Master Beads at $K=4$ also clearly shows the closure of the gap from the side walls toward the center. In addition, the film played back at 25 fps — slowing down the action 100 times — shows a "compaction" wave that travels through the bed during the collision process as illustrated in Figure 31 on page 144. The film clearly shows that the section of the bed behind the wave-front is in a compacted or tightly packed state. Ahead of the wave-front, the bed is still loose and mobile. At any instant during the collision process, the leading edge of the wave is coincident with the point at which the bed has just collided with the vessel floor as shown in Figure 31 on page 144.

The wave front slopes back toward the side wall from this point. The angle of the wave-front represents the resultant of the horizontal and vertical propagation velocities of the compaction wave as shown in Figure 32 on page 146. The horizontal component represents the rate at which the bottom gap closes toward the center. The vertical component represents the speed at which the compaction wave will propagate upward through the vibrated bed for the bed and vibrational

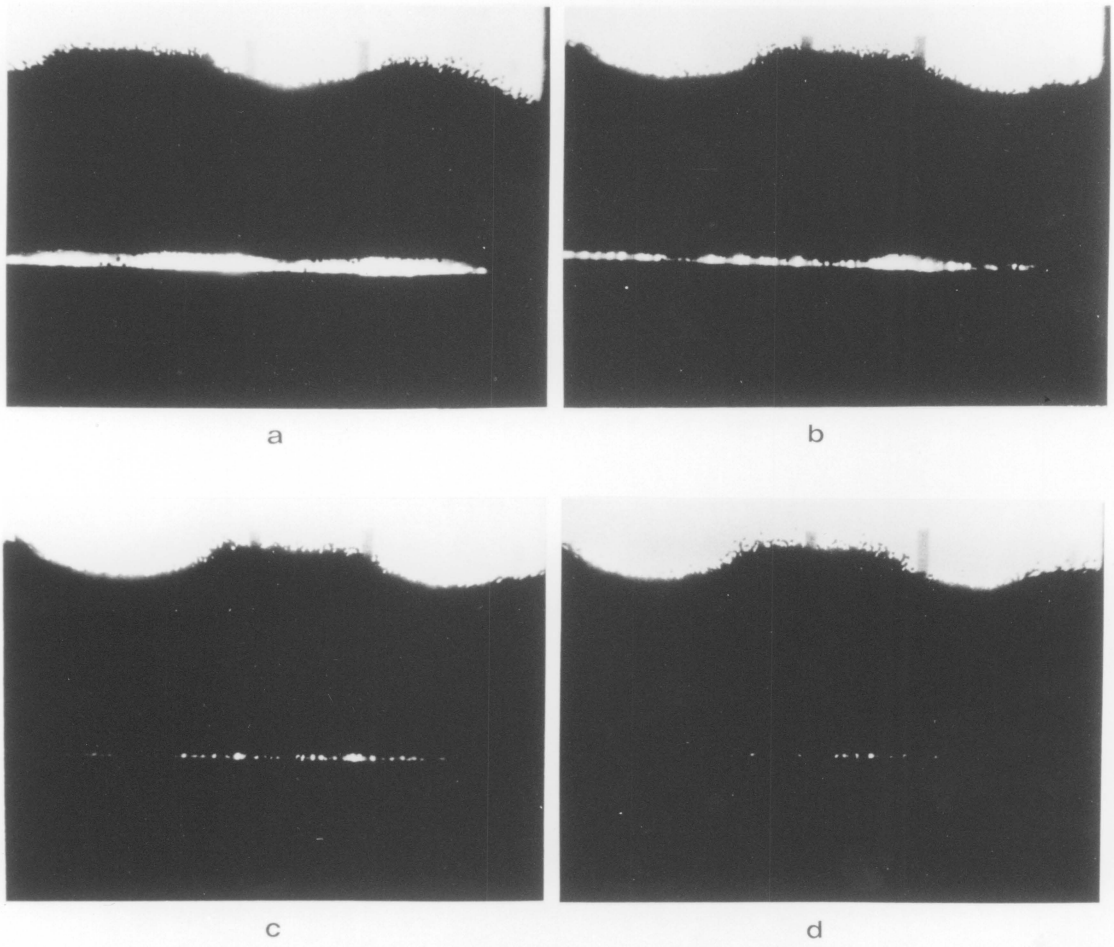

Figure 29. Closure of the floor gap below a large-particle bed: Phase-delayed photographs showing the closure of the gap beneath a bed of 707-μm Master Beads at $K = 4$. (a) At 305°, the gap is still fully formed, except at the wall where it is almost closed. (b) At 314°, the gap is smaller and parts of it are narrower than others. (c) At 323°, the gap is only visible in some places. (d) At 332°, the gap is only barely visible and only at some spots. The gap finally disappears at 354° Note that only one half of the bed is shown.

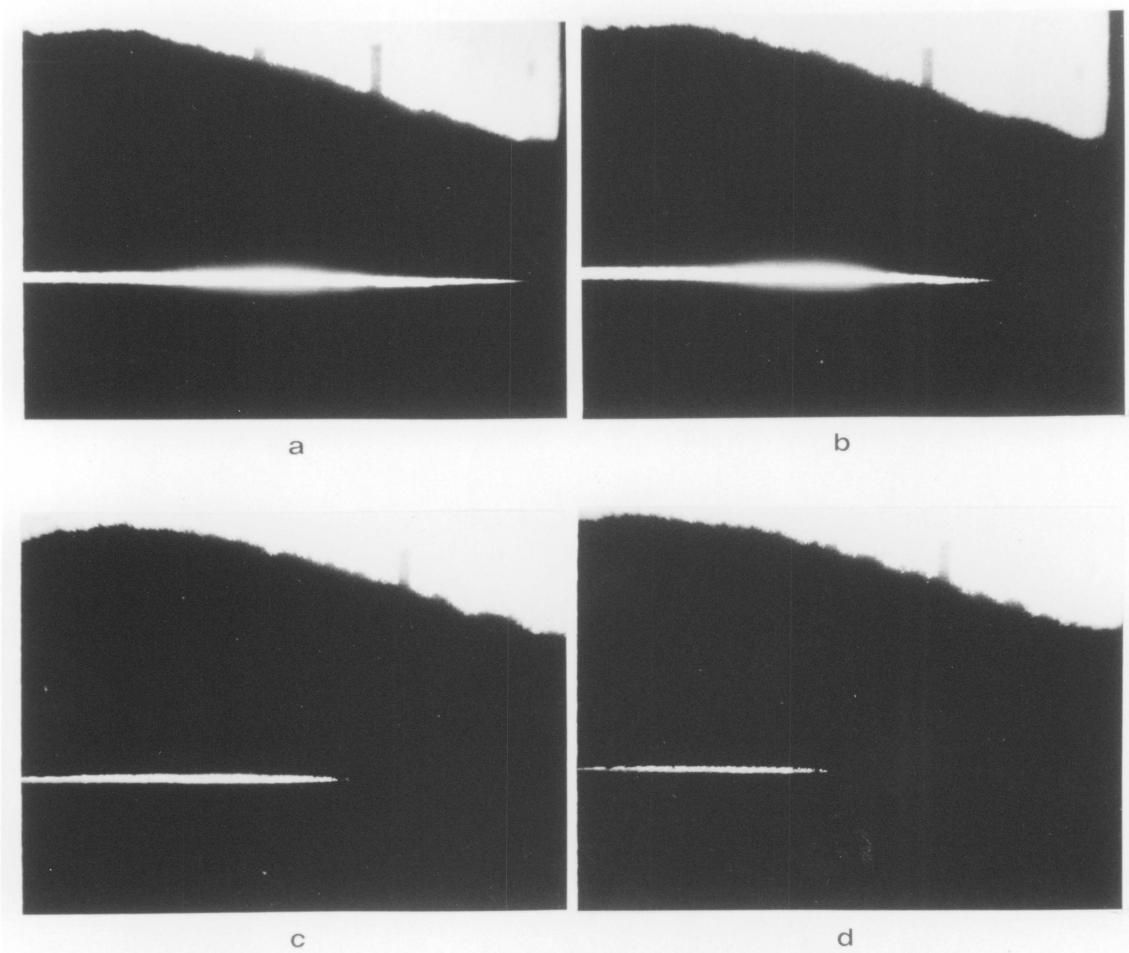

Figure 30. Closure of the floor gap below a small-particle bed: Phase-delayed photographs showing the closure of the gap beneath a bed of 177-μm Master Beads at $K = 4$. (a) At 178°, the gap is fully open. (b) At 228°, the gap has closed at the wall. (c) At 268°, the gap has closed almost halfway to the bed center. (d) At 278°, the gap is quite small. The gap is fully closed at 298° Note that only one half of the bed is shown.

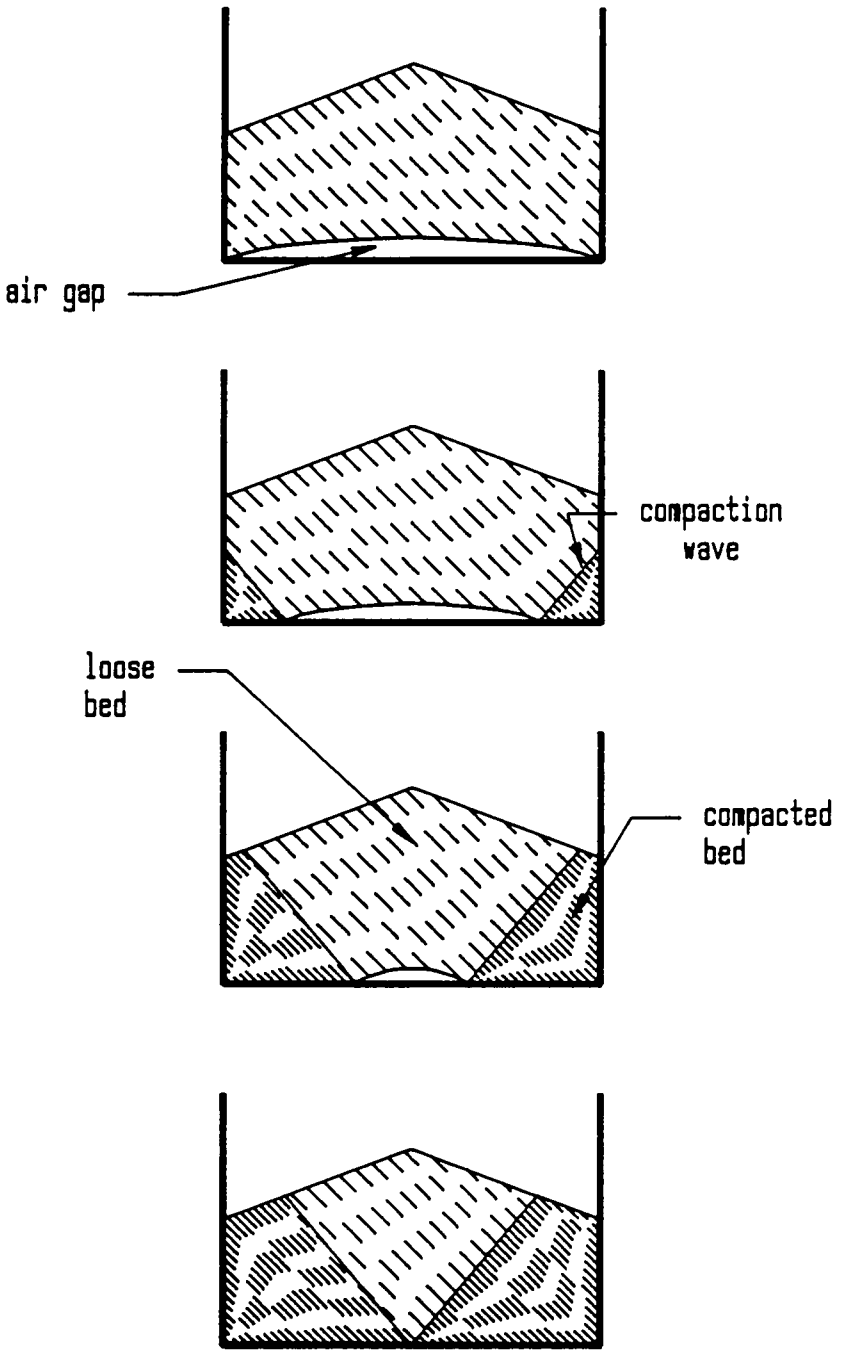

Figure 31. Propagation of the compaction wave through the bed during the bed-vessel collision: The region behind the wave is compacted, and the bed is loose in front of the wave. The wave propagates diagonally across the bed as the bed collides with the vessel floor from the side walls toward the center

conditions used. From Figure 32 on page 146, it is clear that the vertical propagation velocity may be

determined by:

$$V_v = V_h \cot \zeta \qquad [5.39]$$

V_v and V_h are the vertical and horizontal wave propagation velocities, respectively; and ζ is the angle of the wave-front to the horizontal axis. The vertical propagation velocity will be determined by the rate at which gas can be expelled from the bed. This will depend on a number of factors, including the permeability of the bed and the relative accelerations of the bed and vessel at the instant of collision. It would be expected that the vertical propagation velocity will be higher in large-particle beds and will become smaller as the particle size is reduced.

Graphs of floor pressure and phase-delayed photographs of the gap closure show that the horizontal rate at which the gap closes toward the center (the horizontal propagation velocity of the compaction wave) is not constant in a bed of 177-μm particles. When $K=4$, the peak in the floor pressure at the wall position (6 mm from the wall) is at 239°; at the position half-way between the wall and center, the peak is at 298°; and at the center, the peak occurs at 325.5° The horizontal rate of gap closure therefore appears to speed up as it approaches the center of the bed.

The compaction wave can easily be detected when the film is viewed at 25 fps, because of the motion of the wave through the frame of view. However, it is difficult to detect the position of the wave front when viewing single (stationary) frames of the film. This problem can possibly be overcome by digitally enhancing the individual frames of the film to make the wave front clearer. This will permit accurate determination of the propagation velocities of the compaction wave. However, such techniques are beyond the scope of this study, and further analysis will not be attempted here.

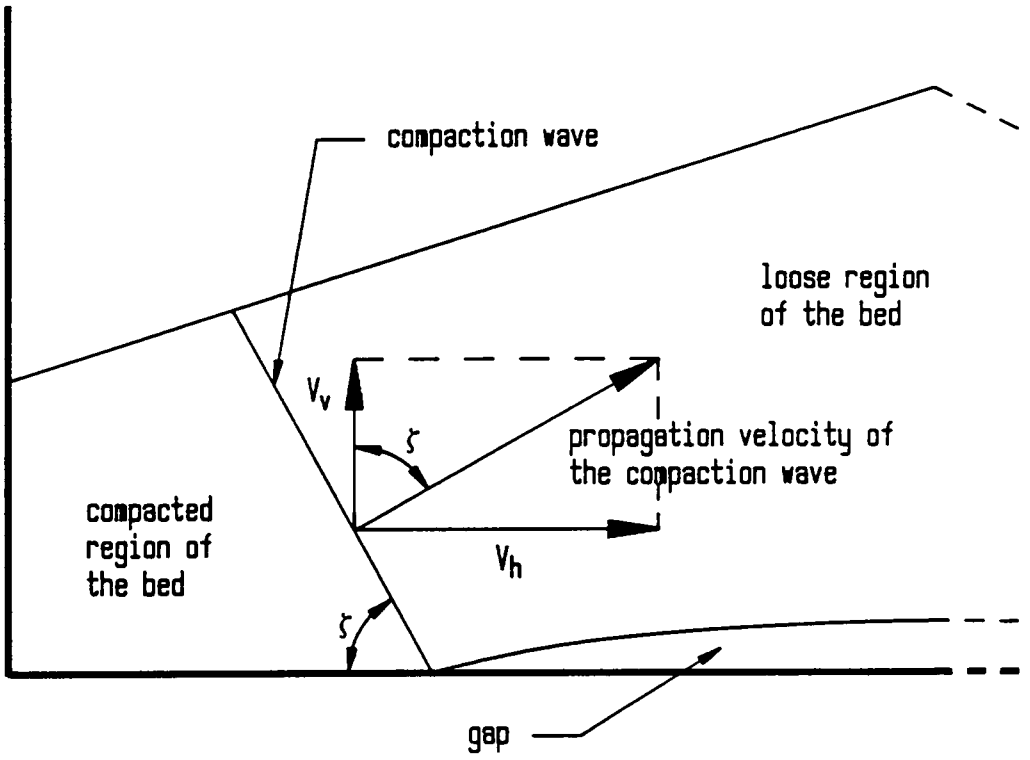

Figure 32. Propagation velocity of the compaction wave: The diagonal propagation velocity of the compaction wave is the resultant of the horizontal velocity component V_h, and the vertical velocity component, V_v. The angle that the compaction wave makes with the negative x-axis is ζ.

It is worth noting that previous investigators [Gray and Rhodes,1972; Gutman,1974; Buevich and Galontsev,1978] have postulated the existence of a compaction wave, but the present investigation is the first instance in the published vibrated-bed research that the compaction wave has been directly observed. The wave has previously been assumed to propagate directly upward through the bed. This investigation clearly shows that the wave propagates diagonally across the bed for small particles. Gutman [1974] has argued that the compaction wave might be reflected off the top surface of the bed as a tensile (expansion) wave that would be dampened by inter-particle friction to virtually nil by the time it reaches the bottom of the bed. Careful and repeated examination of the film shows *no* evidence that the compaction wave is reflected back downward — at least in small-particle beds. With larger particles, the oscilloscope trace of the accelerometer output indicates the bed-vessel collision might not be instantaneously dampened since "spikes" are seen several degrees after the instant of collision. In large-particle beds, it is possible that the collision process results in the rebound of successive colliding layers of particles.

5.2.2 Correlation of Floor Pressures with the Vertical Bed Motion

The variation of floor gauge-pressures beneath a 3-cm deep vibrated bed at the three horizontal locations described in Chapters 3 and 4, is shown for values of the vibrational intensity parameter K of 2 and 4 Figure 33 on page 148 for 707-μm Master Beads, in Figure 34 on page 149 for 177-μm Master Beads, and in Figure 35 on page 150 for 88-μm Master Beads. These three particle sizes represent three broad ranges of particle sizes — fine, small (or medium), and large which exhibit different characteristic floor-pressure variations. A complete set of data of floor-pressure variations beneath vibrated beds of Master Beads, at K-values ranging from 2 to 5, and in some cases for bed depths greater than 3 cm is given in appendix D. Data on floor-pressure variations beneath vibrated beds of glass beads of both high and low densities are given in appendix E.

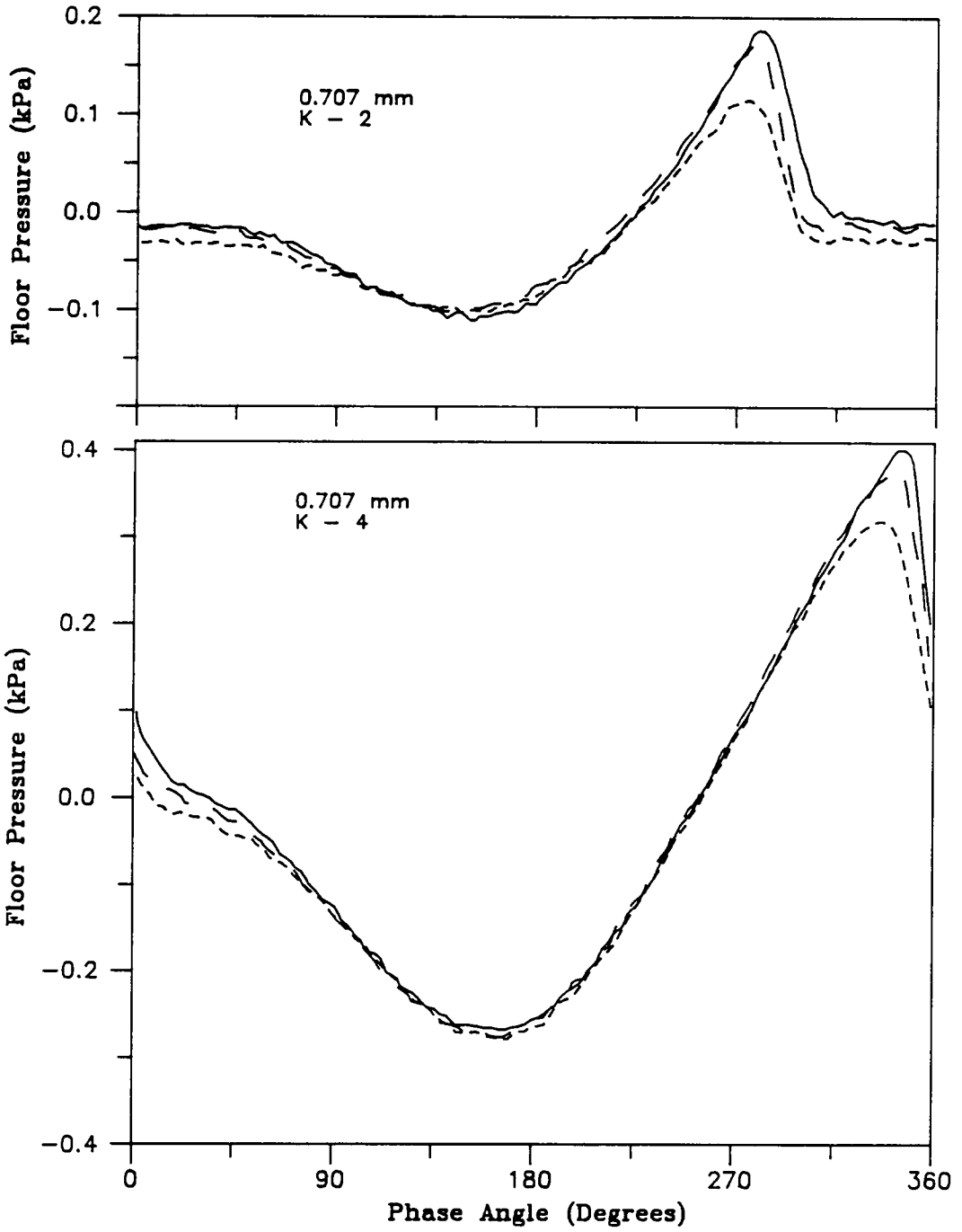

Figure 33. Cyclic variation of floor pressures beneath a bed of 707-μm Master Beads: The cyclic variation of floor gauge-pressures beneath a bed of 707-μm Master Beads at $K = 2$ and 4. The pressures are measured at three locations: ———— at the center of the bed; — — — — halfway between the wall and the center; ——— at the wall.

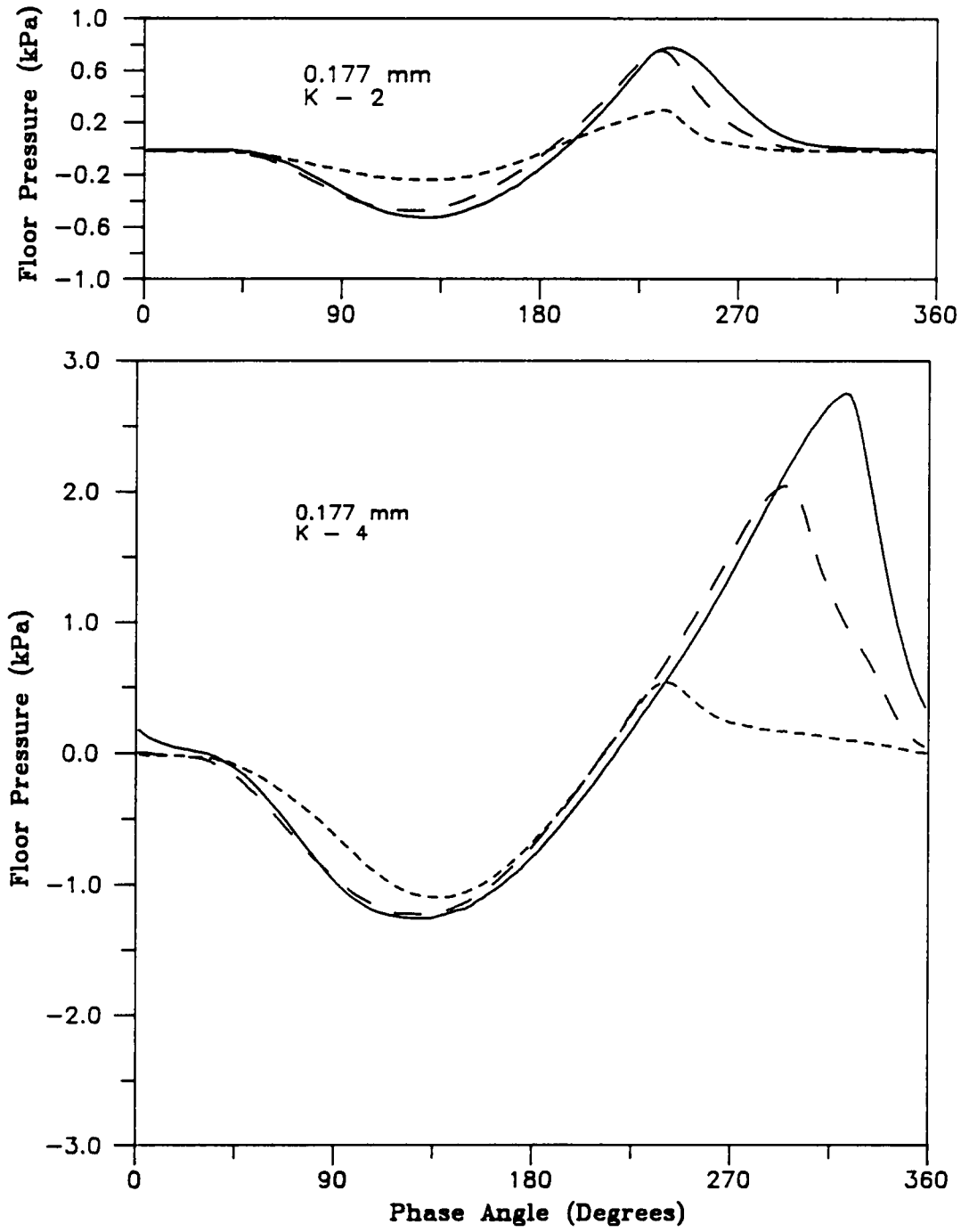

Figure 34. Cyclic variation of floor pressures beneath a bed of 177-μm Master Beads: The cyclic variation of floor gauge-pressures beneath a bed of 177-μm Master Beads at $K = 2$ and 4. The pressures are measured at three locations: ———— at the center of the bed; — — — — halfway between the wall and the center; ———— at the wall.

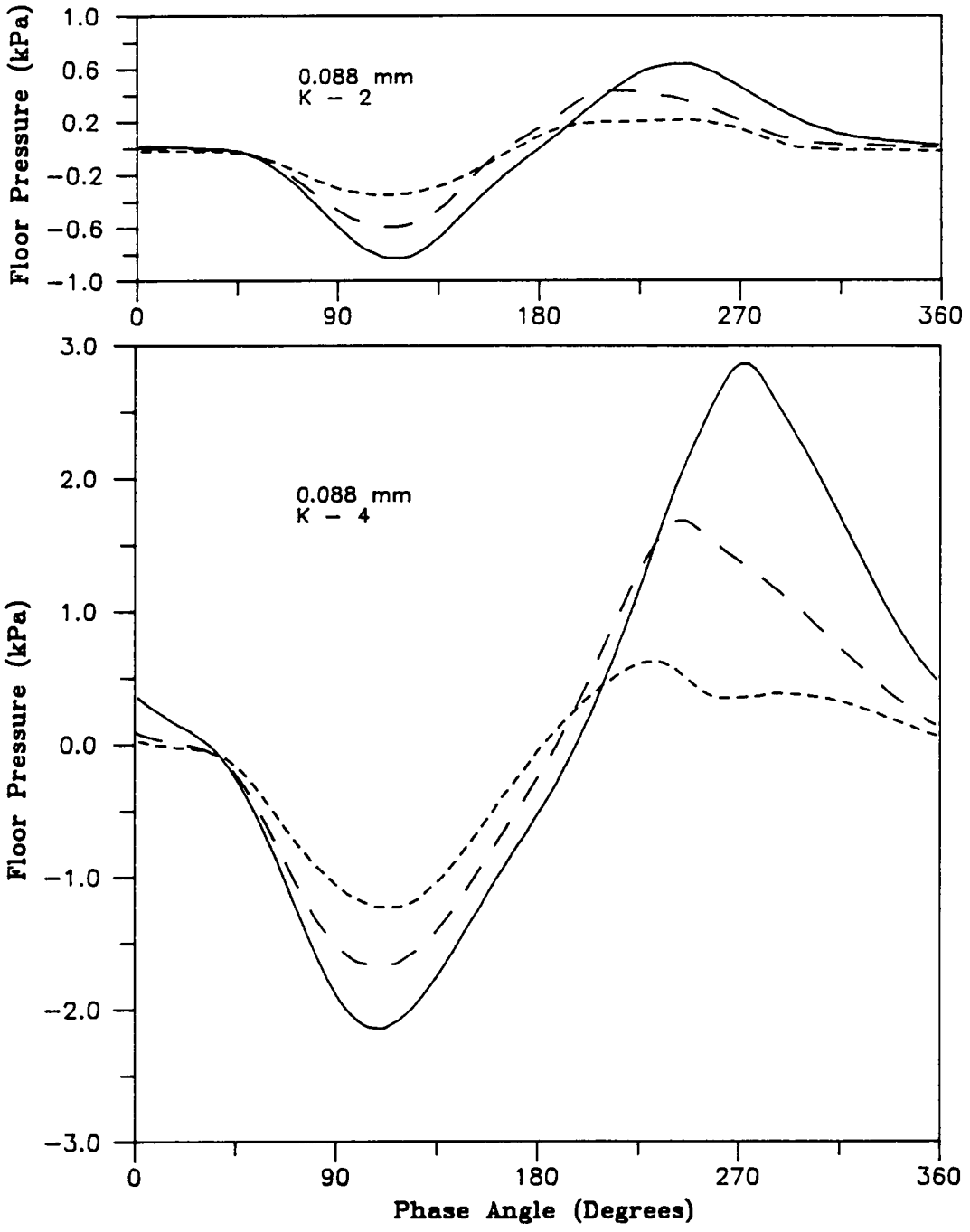

Figure 35. Cyclic variation of floor pressures beneath a bed of 88-μm Master Beads: The cyclic variation of floor gauge-pressures beneath a bed of 88-μm Master Beads at $K = 2$ and 4. The pressures are measured at three locations: ———— at the center of the bed; — — — — halfway between the wall and the center; ····· at the wall.

Basic Sequence of Events in a Vibrational Cycle

The simplified correlation between floor-pressure variations and gap formation or bed trajectory that is common in the vibrated-bed literature, is immediately obvious from the graphs of floor-pressure variation.

1. As accelerations of the bed and vessel differ after the vessel acceleration drops below -1g, the bed attempts to separate from the vessel floor, causing the pressure beneath the bed to fall below atmospheric. The negative vertical pressure gradient produces a downward flow of gas that tends to retard the upward lift of the bed due to viscous drag. Eventually a point is reached when the net force on the bed equals zero — the null force point predicted by equation [5.4] — and the bed, if modeled as a coherent mass, separates from the vessel floor.

2. The gap grows in size causing the floor pressure to further decrease. The down-flowing gas retards the growth of the gap. In a small-particle bed, which is less permeable to gas flow, the drag force will be larger, so the retardation of gap growth will be greater than in a large-particle bed.

3. Eventually the gap reaches a maximum thickness, at which time the gauge-pressure beneath the bed is most negative. As the bed starts to fall back toward the vessel base, the pressure beneath the bed starts to increase, but remains below atmospheric. The down-flowing gas accelerates the bed toward the vessel floor.

4. The floor pressure rises above atmospheric, causing the expulsion of air from the gap. The bed collides with the vessel floor causing a sharp peak in the floor pressure, after which the pressure decays toward atmospheric pressure.

5.2.3 Magnitude of the Floor-Pressure Fluctuations

Dependence on Particle Size

Both Kroll and Gutman models predict that the magnitude of the pressure fluctuations will be greater for small-particle beds which have the greatest resistance to gas flows. The maximum and minimum floor gauge-pressures measured at the center position in beds of Master Beads are summarized in Figure 36 on page 153 and Figure 37 on page 154, respectively, as a function of particle size for values of K ranging from 2 to 5.

The largest pressure fluctuations are in beds of 88-μm particles where no gaps are observed. Thus, pressure fluctuations must be a result of the difference in accelerations between the bed and vessel, after the vessel acceleration has dropped below -1g, and the bed continues to accelerate at -1g. This can perhaps be visualized best by considering the gas present at the bottom of the bed before lift-off (the gas in the interstitial spaces) as a "spring" which connects the bed to the vessel floor. As the vessel acceleration falls below -1g, it attempts to drag down the bed with it. The force caused by these unequal accelerations manifests itself as a negative gauge-pressure in the air beneath the bed. Gas that rushes down across the bed relieves the negative gauge-pressure beneath the bed. More extreme pressure fluctuations would be expected in less permeable beds and where compressibility effects are important.

The Effect of Bed Depth and Solid Density

Equation [5.15] shows that the pressures predicted by the Kroll model are linearly dependent on the bed depth. The compressible-gas model also predicts a linear relationship between bed depth and peak floor pressures for shallow beds, where it is identical to the Kroll model. For deeper beds (for example, deeper than 60 mm at 30 Hz and $K = 2.5$ and a particle diameter of 200 μm), the

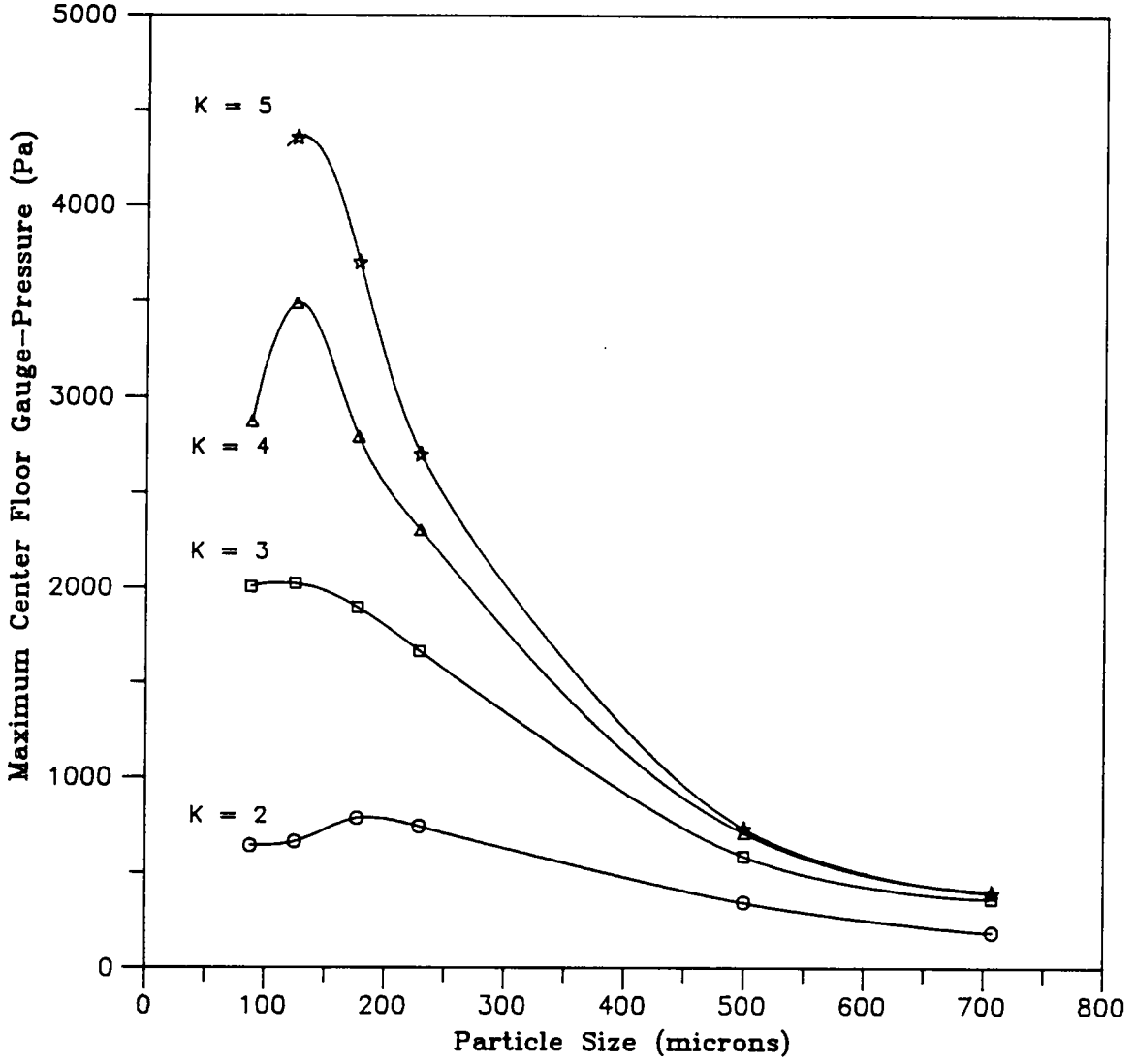

Figure 36. Maximum floor gauge-pressures beneath the bed center: Peak positive floor gauge-pressures beneath the center of vibrated beds of Master Beads, as a function of particle size for different values of the vibrational intensity parameter, *K*.

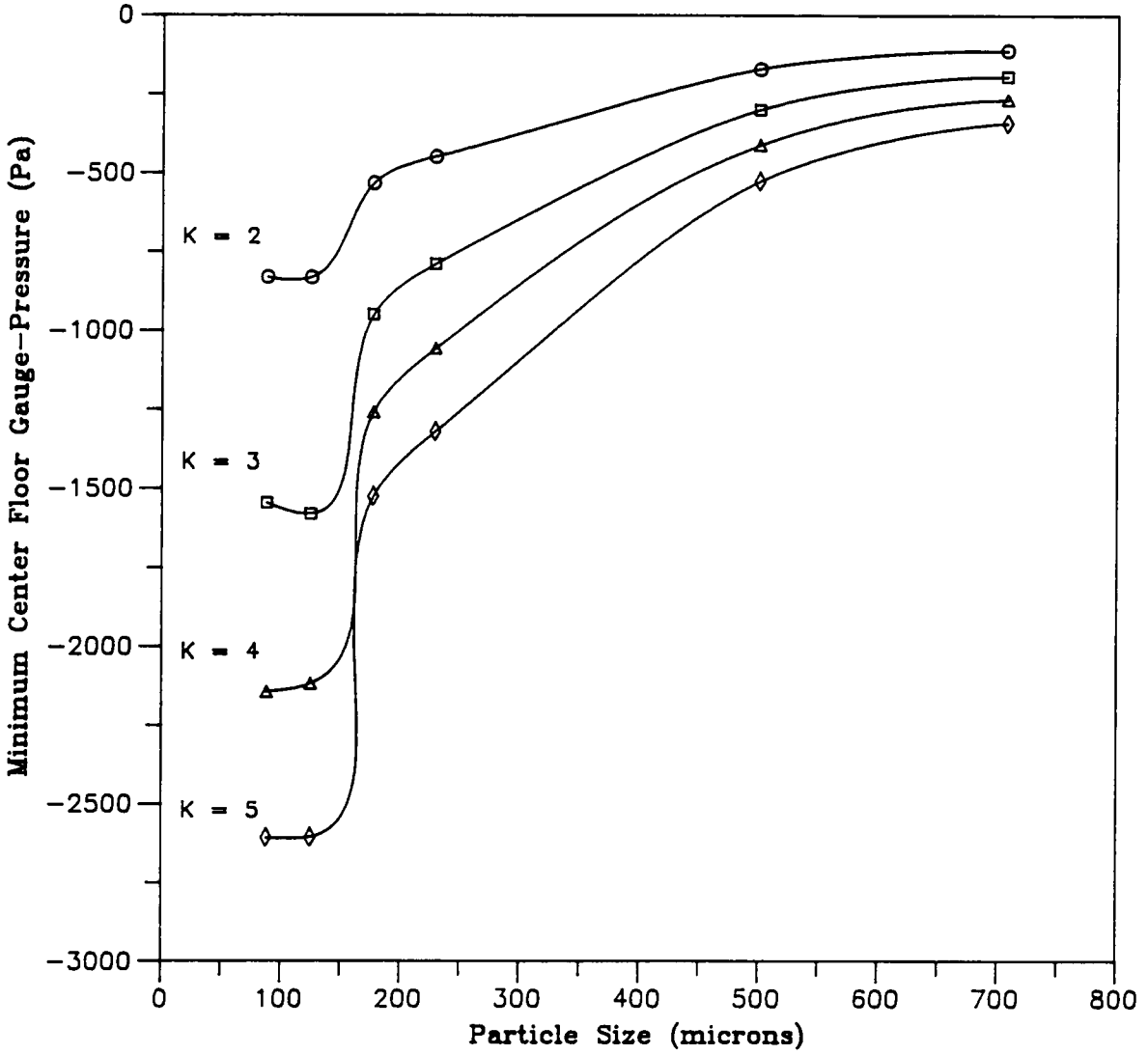

Figure 37. Minimum floor gauge-pressures beneath the bed center: Peak negative floor gauge-pressures beneath the center of vibrated beds of Master Beads, as a function of particle size for different values of the vibrational intensity parameter, *K*.

Gutman model predicts that the peak positive pressure grows at less than a linear rate with bed depth, and reaches a limiting value for very deep beds.

The negative and positive peak floor gauge-pressures measured at the center of beds of 177-μm and 125-μm Master Beads with depths of 30 to 60 mm are given in Figure 38 on page 156, and Figure 39 on page 157respectively. The results indicate a linear increase of both negative and positive peak pressures with bed depth over the range examined even at $K = 4$.

The effect of bed density on the peak floor pressures is studied using low-density glass beads ($\rho_s = 2500\ \mathrm{kg/m^3}$) and high-density glass beads ($\rho_s = 4490\ \mathrm{kg/m^3}$) in 30-mm deep beds. The results are shown in Figure 40 on page 158 for the peak positive floor pressure, and in Figure 41 on page 159 for the peak negative floor pressure, for particle sizes of 707, 177, and 88 μm. The peak positive pressures appear to show a logarithmic dependence on K (shown by the lines in the graph), whereas the peak negative pressures show a strong linear dependence on K. It is not immediately obvious from equation [5.15] describing the Kroll model why this should be so.

There is little effect of solid density or vibrational intensity on the positive or negative peaks for 707-μm particles. This is because the drag per unit mass in such beds is small; but it also implies that the drag per unit mass is greater for low-density beads than it is for high-density beads. If very light particles (a light plastic for example) were used, the effect of solid density would be more noticeable with this particle size.

With smaller particle sizes, the K-dependence is stronger. As expected, peak pressures are greater in magnitude for a smaller particle size because of the greater resistance to gas flow. However, both positive and negative peak pressures are more dependent on solid density than on particle size. The ratio of particle sizes is 2 (177 μm/88 μm), but the ratio of densities of the two types of glass is 1.8. Both the negative and positive peak pressures are larger in magnitude for 177-μm high-density glass beads than for 88-μm low-density beads. This is not an intuitive result, considering the strong de-

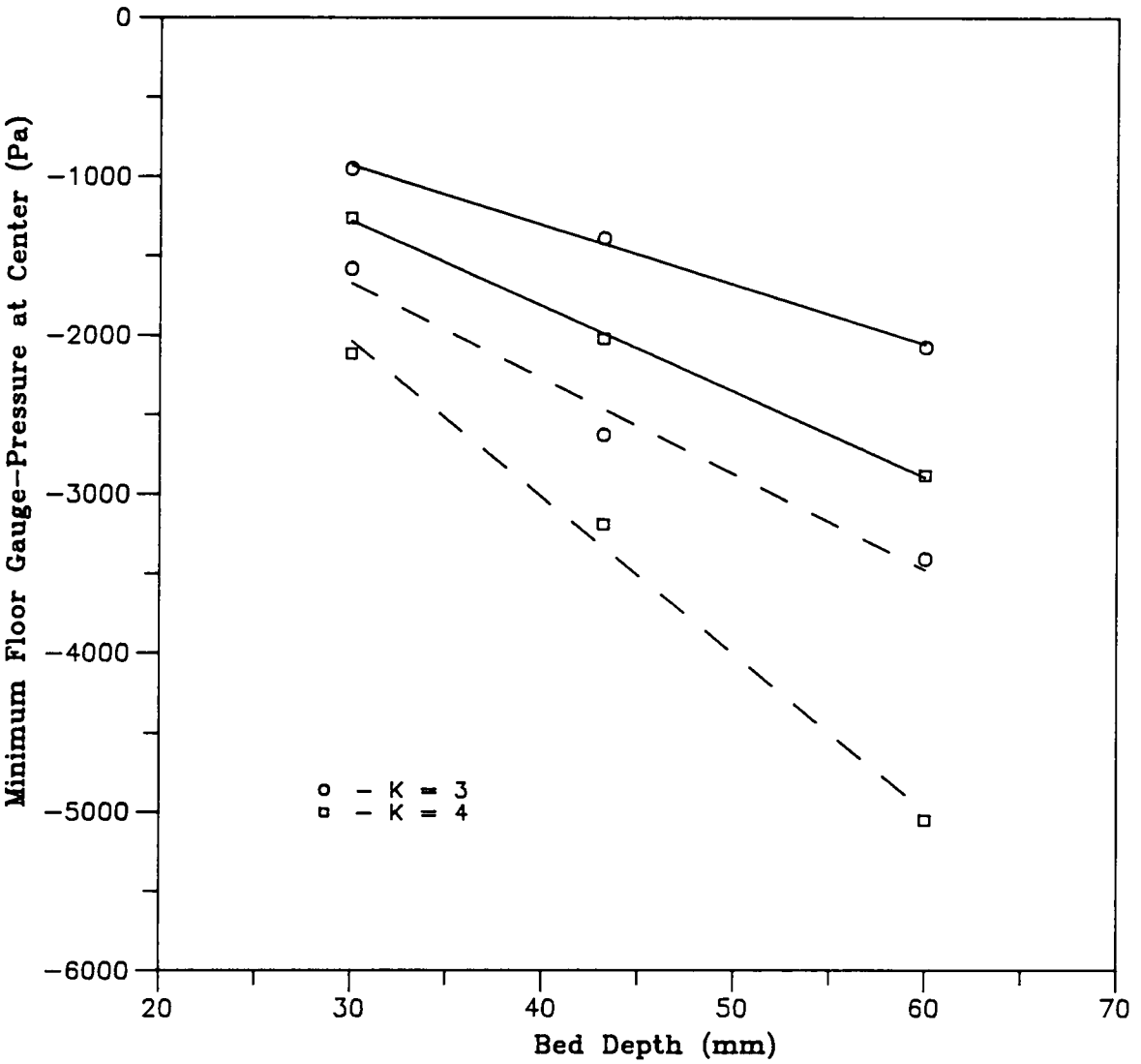

Figure 38. The effect of bed depth on the minimum floor pressure: Measured peak negative floor gauge-pressure beneath the center of the bed as a function of the bed depth (up to 60 mm), for $K = 3$ and 4. ———— 177-μm Master Beads; — — — — 125-μm Master Beads.

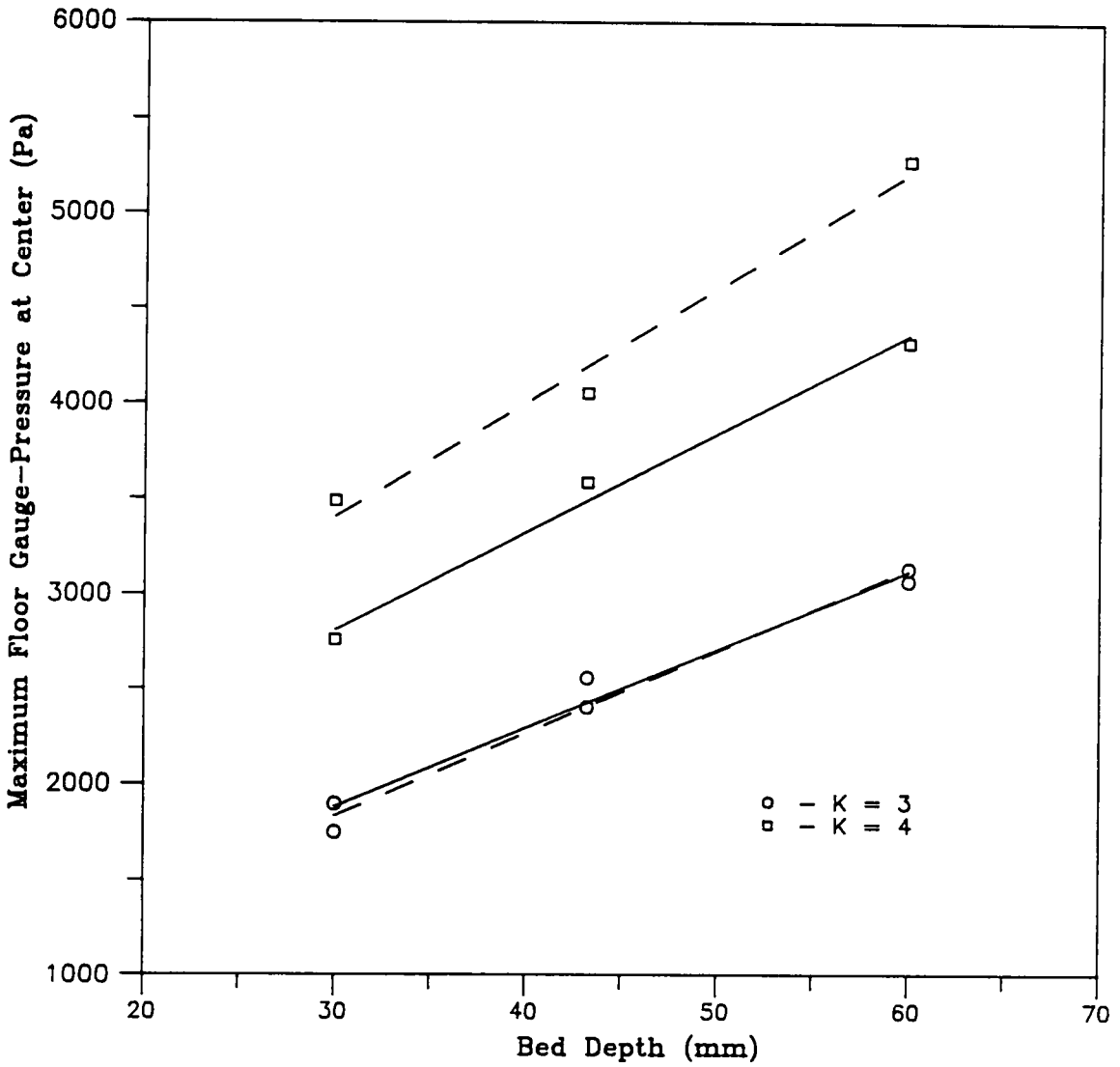

Figure 39. The effect of bed depth on the maximum floor pressure: Measured peak positive floor gauge-pressure beneath the center of the bed as a function of the bed depth (up to 60 mm), for $K=3$ and 4. ———— 177-μm Master Beads; — — — — 125-μm Master Beads.

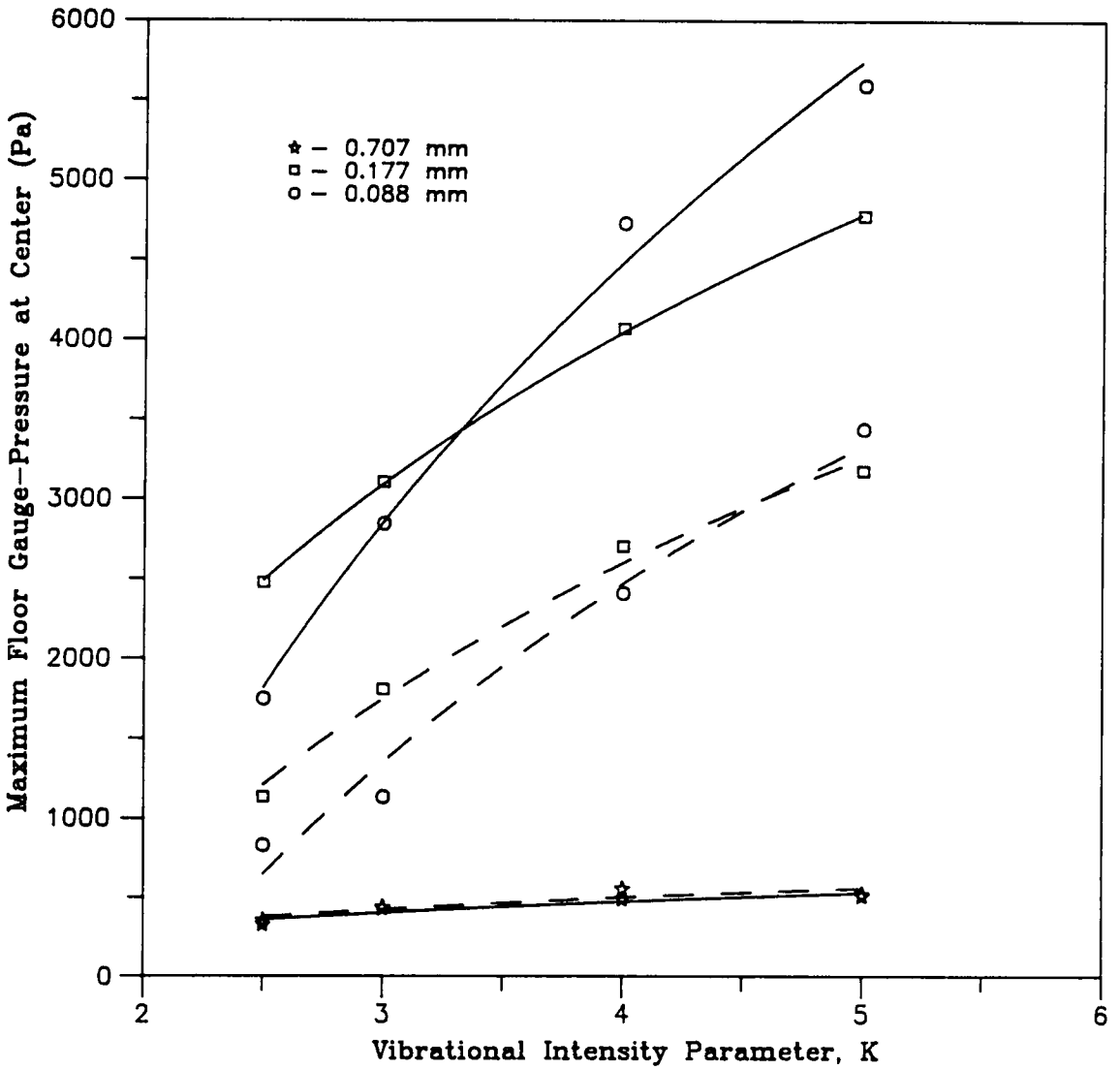

Figure 40. Dependence of the peak positive floor pressure on solid density: Peak positive floor gauge-pressure beneath the center of the bed as a function of K, for high- and low-density glass beads with particle sizes of 707, 177, and 88 μm. ———— high-density glass (ρ_s = 4490 Kg/m^3); — — — — low-density glass (ρ_s = 2500 Kg/m^3).

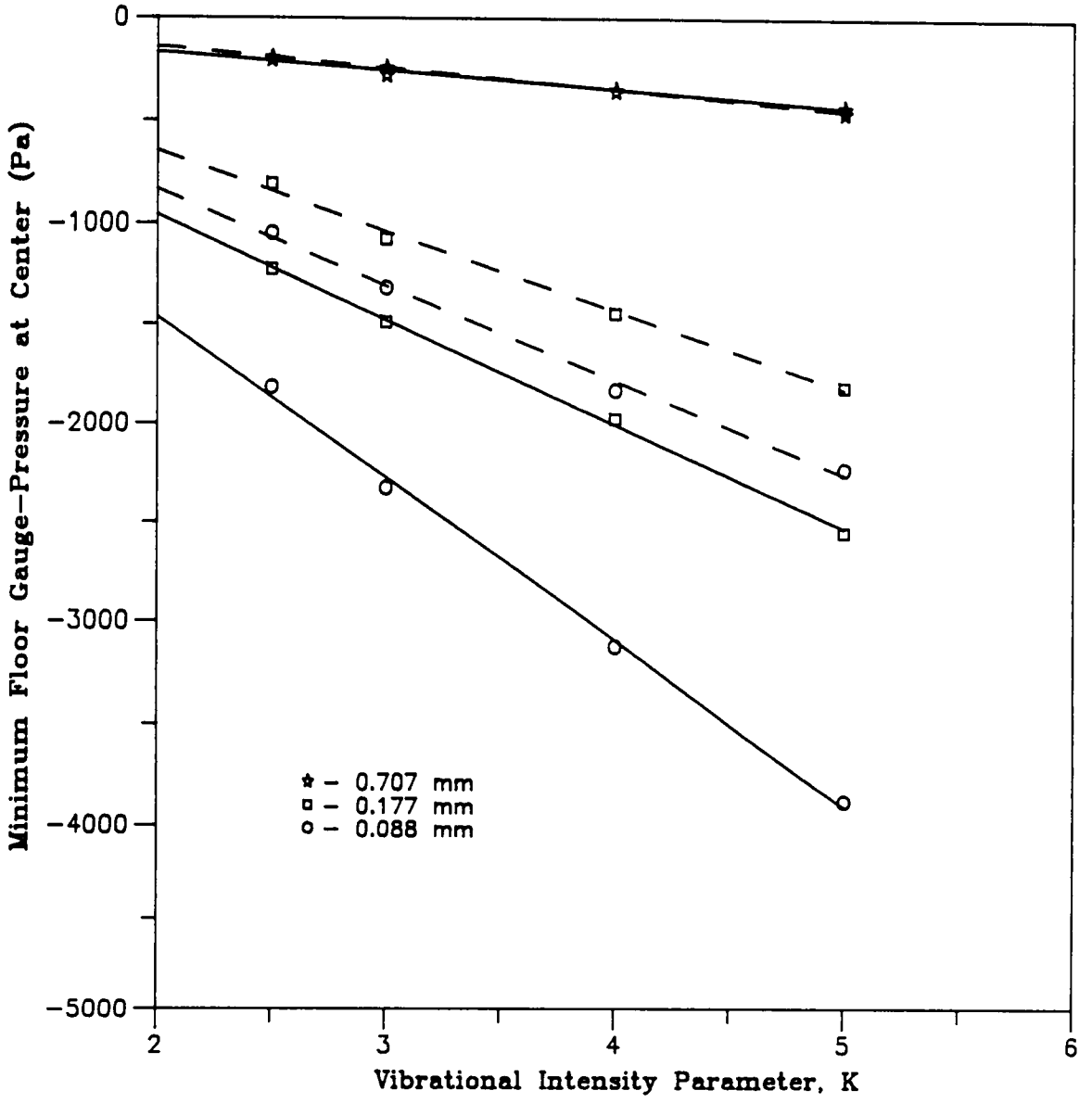

Figure 41. Dependence of the peak negative floor pressure on solid density: Peak negative floor gauge-pressure beneath the center of the bed as a function of K, for high- and low-density glass beads with particle sizes of 707, 177, and 88 μm. ———— high-density glass (ρ_s = 4490 Kg/m^3); — — — — low-density glass (ρ_s = 2500 Kg/m^3).

pendence of drag forces on particle size — the bed permeability is a function of the square of particle diameter.

The effect of the gas flow on the bed may be quantified by considering the ratio of the maximum drag force acting on the bed to the total bed weight. Assuming that the pressure drop is due to the drag force (that is, the flow of gas in the bed is laminar), the drag force per unit bed weight is given by $[(P_L - P_o)/\rho_b Lg]$. This is identical to the group $K\Lambda\Phi_L$ in equation [5.15]. Values of this ratio using measured values of peak positive pressures with $K = 2.5$ and 4 for 707-μm particles, and $K = 2.5$ and 5 for 177-μm particles, together with values of the ratio predicted by the Kroll model are given in Table 6 on page 161.

With 707-μm particles, the Kroll model predicts that the maximum drag force per unit bed weight should be lowest for high-density glass beads and highest for low-density glass beads, with an intermediate value for Master Beads. This trend is observed with measured values of the ratio both at $K = 2.5$ and 4, although some deviation from predicted values is observed. Actual values deviate from predicted values by 10 — 20%. For 707-μm Master Beads at $K = 2.5$, the deviation is 30%. It is not clear why the error is so large in this case, particularly in view of the small error (1.5%) for this solid at $K = 4$. It is possible that due to noise on the accelerometer output close to the signal peaks at $K = 2.5$, the vessel acceleration was incorrectly set during the experiment.

Predictions of the Kroll model indicate (as shown in Table 6) that the drag force per unit bed weight for small particle sizes is not greatly influenced by solid density. This is also observed with measured values of the ratio at $K = 2.5$. However, at $K = 5$, the measured ratios are higher for both types of glass beads than for Master Beads as well as the predictions of the Kroll model for each solid. A smaller expansion of glass-particle beds would explain this result. A bed porosity of 0.41 is used in solving the Kroll model at $K = 5$ for all solids. If the expansion of glass-particle beds is limited at higher accelerations, the resulting lower permeability to gas flows compared to beds of equivalently sized Master Beads will result in higher pressure drops and consequently, larger drag forces per unit bed weight for glass beads.

Table 6. Maximum drag force per unit bed weight calculated from measured pressures compared to the prediction of the Kroll model

Particle Size (microns)	K	High Density Glass Beads		Low Density Glass Beads		Master Beads	
		actual	Kroll	actual	Kroll	actual	Kroll
707	2.5	0.40	0.50	0.78	0.84	0.42	0.60
	4	0.63	0.55	1.28	1.01	0.64	0.65
177	2.5	3.02	2.80	2.48	2.83	2.21	2.77
	5	6.12	5.00	7.30	5.59	5.07	5.22

Despite the higher values of this ratio for 177-μm glass-particle beds at $K = 5$, the particle-circulation velocities are lower in these beds than in beds of equivalently sized Master Beads (see section 5.4.2.1). This clearly suggests the presence of inter-particle forces (most probably electrostatic) which prevent glass particles from readily moving apart from, or relative to one another. As a result, a lower degree of bed expansion than would be expected in the absence of such forces is also observed.

5.2.4 Horizontal Scale-Effects on the Cyclic Floor Pressures

Graphs of floor pressures show a feature which has not been published in the vibrated-bed literature by previous investigators — the differences in pressure fluctuations at the three horizontal locations along the bottom of the bed. As seen by comparing Figure 33 on page 148 with Figure 34 on page 149, the horizontal pressure differences are much greater in fine-particle beds than in large-particle beds.

In small-particle beds, as pressures in the bed fall below zero (the bed is attempting to separate from the vessel floor), the floor pressure at the wall does not fall as much as the floor pressure at the center. Small-particle beds tend to bunker, and it should be noted that floor pressures obtained in this study for small particles, are for beds that are highest in the center and lowest at the side walls. Since the magnitude of pressure fluctuations are dependent on the bed depth, smaller negative fluctuations at the walls would be expected.

For a bed of 88-μm Master Beads at $K = 4$, the depth of the bed at the side walls is measured to be 1.7 cm, and at the center is 4.3 cm. From Figure 35 on page 150, the most negative pressure at the wall is about -1.25 kPa, and at the center is -2.2 kPa. Therefore, the vertical pressure drop (and consequently the drag force) per unit bed depth is larger at the wall than it is at the center, even though the overall vertical pressure drop is larger at the center. This result can be explained by

considering the horizontal flows of gas in the bed. Since the pressure at the wall is higher (less negative) than at the center, gas will flow from the walls toward the center. As a result gas reaches the center of the floor from three different directions: directly down from the top, and from each side wall. By contrast, gas reaches the bottom of the bed at the wall only from the top of the bed. Thus the quantity of gas flowing down the bed at the walls per unit time is larger than at the center, and results in larger drag forces per unit bed height at the walls

As gauge-pressures below the bed rise above zero, the direction of the horizontal pressure gradient is maintained, so that gas continues to flow from the wall toward the center. Because of the higher drag force per unit bed height at the wall, this section of bed does not lift off the vessel floor as high as the rest of the bed. This causes the section of bed close to the walls to collide with the floor before other regions of the bed as seen in Figure 30 on page 143. The graphs of the floor pressures show a positive peak at each of the horizontal locations. Each peak corresponds closely to the instant at which the bed collides with the vessel floor at the location of that pressure sampling port. As stated previously, the graphs of floor pressures (particularly for smaller particles) show that the gap closes first at the wall and last at the center as observed in the phase-delayed photographs in Figure 30 on page 143. With the largest particle size (707 μm), the phase difference between the three peaks is small, and this also agrees with the phase-delayed photographs of gap closure in such beds shown in Figure 29 on page 142.

As can be seen from the graphs of floor pressures, particularly Figure 35 on page 150, the direction of the horizontal pressure gradient in the bed reverses as the gap closes, so that when the gap is completely closed, gas flows horizontally from the center toward the wall. The sequence in which the general shape of the horizontal pressure gradient at the bottom of the bed changes through the vibrational cycle is represented in Figure 42 on page 164. By consideration of continuity at the wall (there is no flux of gas into or out of the side walls), one can write:

$$\left.\frac{\partial P_x}{\partial x}\right|_{wall} = 0 \qquad [5.40]$$

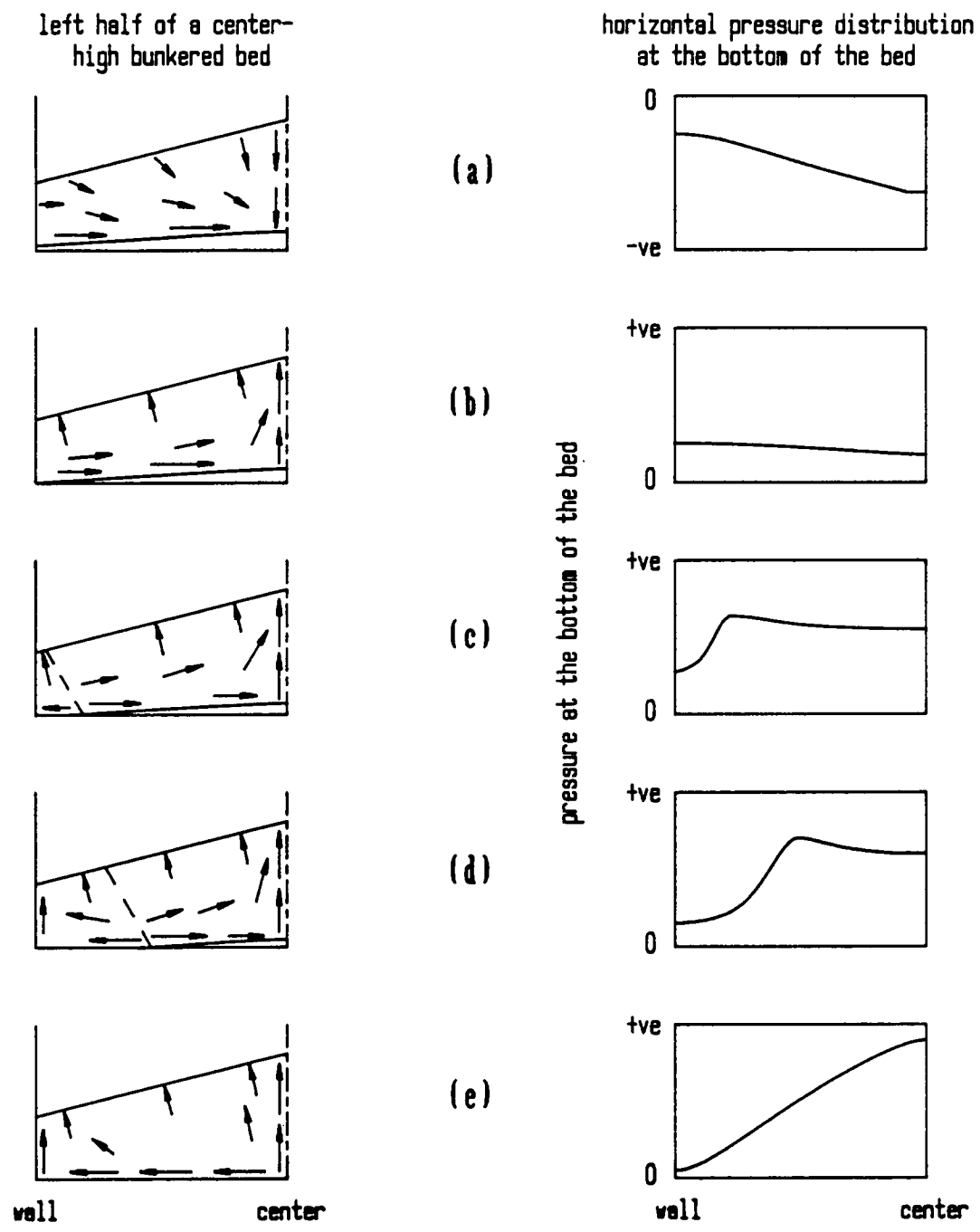

Figure 42. Variation of the horizontal pressure gradient as the floor gap closes: The horizontal pressure gradient at the bottom of the bed reverses direction as the gap closes and the bed collides with the vessel floor. The reversal of the gradient moves with the compaction wave from the wall toward the center of the bed. The pressure gradients are shown on the right, and half of the bed on the left. The dashed line through the bed in (c) and (d) indicate the compaction wave. The arrows show the direction of gas flows in the bed.

where P_x is the horizontal component of the pressure at any horizontal location x within the bed. Because of the symmetry of the bed, there is no flux of gas across the center-line of the bed. Therefore:

$$\left.\frac{\partial P_x}{\partial x}\right|_{center} = 0 \qquad [5.41]$$

The shapes of pressure gradients shown in Figure 42 on page 164 are approximated from relative values of the floor pressures for 88-μm Master Beads at $K = 4$, and the values of the horizontal pressure gradient at the wall and center given by the two equations above.

The gradients indicate that as the gap is closing, the horizontal pressure gradient behind the compaction wave reverses so that the gas flows backward toward the wall in the section of the bed behind the compaction wave. In front of the compaction wave, the horizontal pressure gradient still slopes down toward the center. Gas therefore flows in opposite horizontal directions from each side of the compaction wave. It will be shown later in this discussion by comparing the observed phase angle of the bed-vessel collision with the phase angle of the floor-pressure peaks, that the peaks possibly lag the collision by a few degrees. In that case, the moving maximum in the horizontal pressure gradient might not be located at the compaction wave front as shown in Figure 42 on page 164, but instead lags slightly behind the compaction wave.

While the compaction wave is in-between the wall and the center, the gas at the center can only flow directly upwards down the vertical pressure gradient. The net result of the sequence of events described above is that the small-particle bunkered vibrated bed acts as a sort of "gas circulation pump", drawing in gas at the walls and expelling it upwards at the center.

Once the whole bed is in contact with the vessel floor and compacted, gas now flows down the horizontal pressure gradient toward the wall of the vessel. As a result, the pressure at the wall decays more slowly than predicted by theory, whereas the rate of pressure decay at the center after the bed-vessel collision is faster and closer to theoretical predictions.

5.2.5 Time-Averaged Pressure Beneath the Vibrated Bed

As discussed in Chapter 2, the vibrated-bed literature contains widely varying values of the average pressure beneath the bed even with shallow vibrated beds. Two techniques have been used to obtain average pressures. A remotely mounted sluggish manometer gives average pressures that are very negative [Chlenov and Mikhailov,1972]. Values as low as -6000 Pa have been quoted for a 30-mm deep bed. This is close to the *maximum* pressures obtained beneath 30-mm beds in this study. A time-averaged pressure has been obtained by electrically integrating the output of a fast-response pressure transducer [Gutman,1974]. This method gives average floor pressures that are slightly above atmospheric, and only about 3-4% of the maximum floor pressures obtained by Gutman. Both the Kroll and Gutman models predict that the time-averaged floor pressure over one vibrational cycle should be equal to zero, since there is no net accumulation of gas beneath the bed, and the bed does not expand.

In this study, floor pressures are obtained by fast-response pressure transducers mounted close to the floor of the vessel with little or no phase-lag errors (see §3.3.2 in Chapter 3). Outputs of the transducers are digitized and collected over two cycles. A reading in one cycle is averaged with the corresponding reading at the same phase angle in the second cycle (ensemble averaging) to reduce errors due to the random noise in the measuring system. Cubic spline interpolation is used to fit the data. This defines a cubic spline interpolating function $\Phi_L^{(3)}(\theta)$ which exactly fits all collected data points. The average pressure is calculated from:

$$\overline{\Phi}_L = \frac{1}{2\pi} \int_0^{2\pi} \Phi_L^{(3)}(\theta)\, d\theta \qquad [5.42]$$

Average floor pressures at the wall and at the center obtained by this method are given in Figure 43 on page 168 and Figure 44 on page 169 respectively. It should be noted that if the

pressure transducers are assumed to be accurate to 1% FSO (Full Scale Output) due to drifts in the power supply, measured pressures will have an error of about ± 70 Pa.

It is observed that average floor pressures are close to zero, but slightly negative for large-particle bed ($d_p > 500\,\mu$m) , whether at the wall or at the center. This result is close to that predicted by theory. On the other hand, average floor pressures at the wall and center increasingly deviate from zero as the particle size is reduced. As indicated in Figure 44 on page 169, average floor pressures at the center become increasingly positive with decreasing particle size until a maximum is reached with 125-μm Master Beads, after which it falls as the particle size is reduced to 88 μm. At the wall, average floor pressures become increasingly negative with decreasing particle size, until a minimum is reached at a particle size of 177 μm (Figure 43 on page 168). Below this size, the average floor pressure at the wall increases.

Reasons for these trends and the apparent deviation from theory for small-particle beds may be explained in light of the horizontal scale-effects on the floor pressure, discussed in the previous section. In large-particle beds, there is little or no horizontal variation in floor pressures. Pressure gradients in such beds are mainly restricted to the vertical dimension as required by existing one-dimensional theories. As a result, average floor pressures at all horizontal locations remain close to zero. As the particle size is reduced to 177 μm, horizontal pressure differences become more noticeable. When the floor pressures are all negative, there is only a small difference between the floor pressure at the wall and at the center when compared to horizontal differences later in the cycle, when the floor pressures become positive. The gap at the wall closes first, causing the floor pressure at the wall to reach only a small peak, after which it decays to zero. The pressure at the center goes through a large positive peak. The pressure at the center does not decay to zero by the start of the next cycle, and is drawn down to zero only by the relative accelerations of the bed and vessel in the next cycle. Thus, the floor pressure at the wall is negative for a longer period of time and to a greater magnitude than it is positive, whereas the floor pressure at the center remains positive for a longer period of time and at a greater magnitude than it is negative. Indeed, by comparing the trend in average floor pressures at the center (Figure 44 on page 169) with maximum floor pressures be-

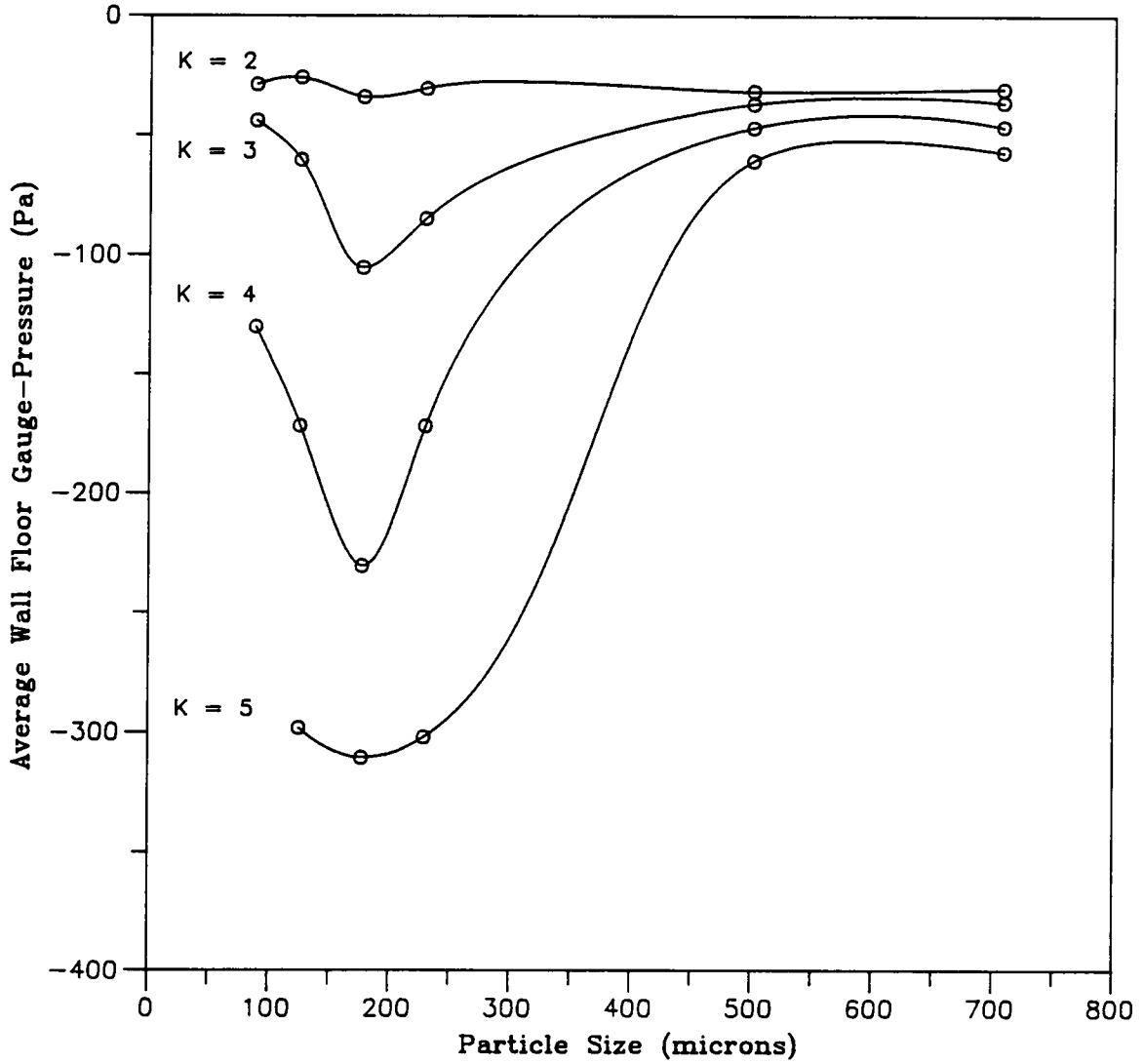

Figure 43. Average floor gauge-pressures at the wall: Average floor gauge-pressures at the wall as a function of particle size, for various values of *K*. Mean pressures are obtained by averaging measured floor pressures at the wall over one vibrational cycle.

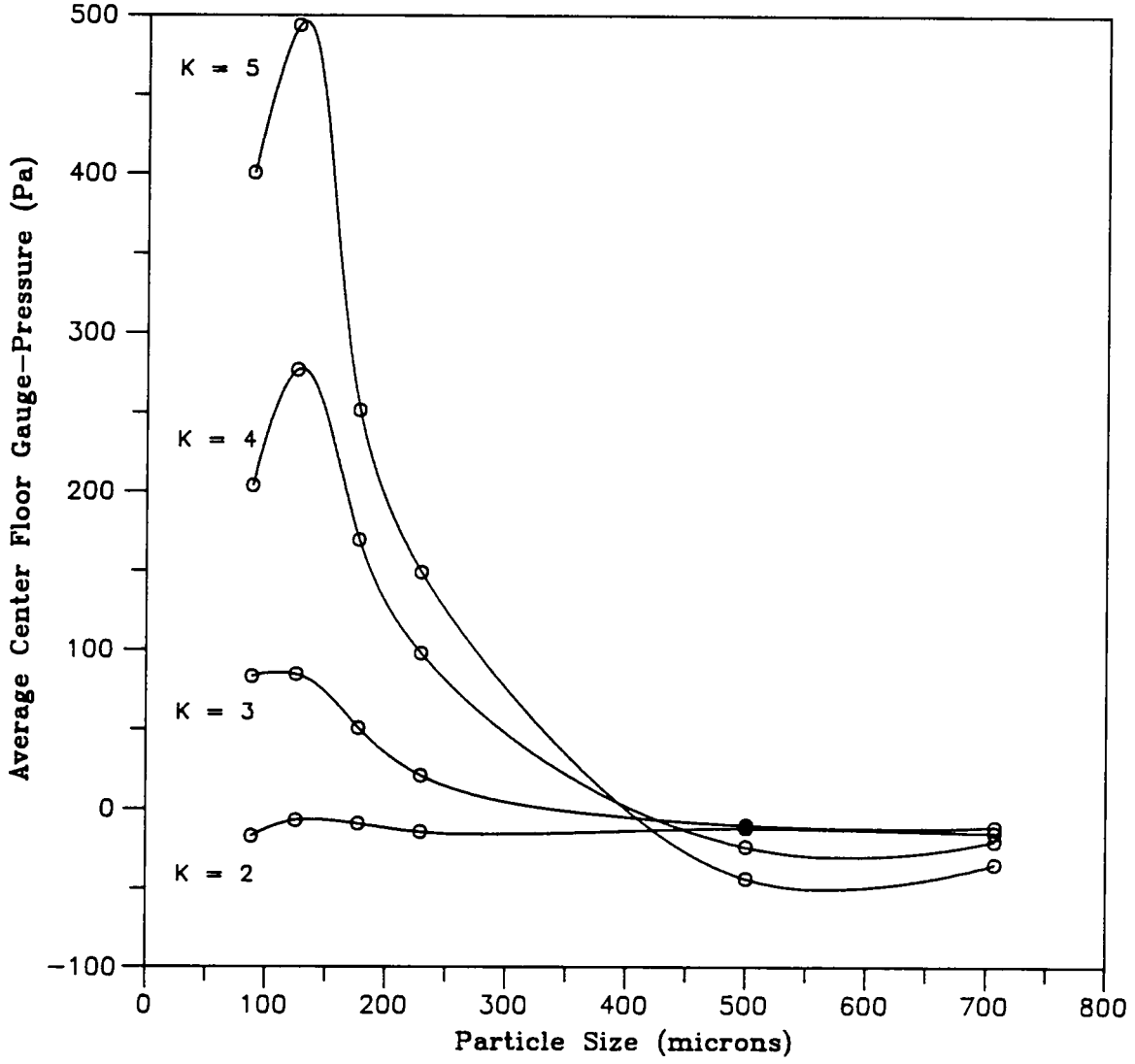

Figure 44. Average floor gauge-pressures at the center of the bed: Average floor gauge-pressures at the bed center as a function of particle size, for various values of *K*. Mean pressures are obtained by averaging measured floor pressures at the center over one vibrational cycle.

neath the bed (Figure 36 on page 153), it can be seen that the average of the floor pressure at the center is largely dominated by its maximum values. Comparing the trend in average floor pressures at the wall (Figure 43 on page 168) to the minimum floor pressure (Figure 37 on page 154) shows — although not as obviously as the similarity in trends between the center floor pressure and peak positive pressures — that the average wall floor pressure is dominated by the minimum floor pressure.

Continuity of mass (of the gas within the bed) is not violated because the gas does not move only in the vertical direction as predicted by the one-dimensional theories, but also in the horizontal directions as explained in the previous section.

It is not always correct to predict the net direction of gas flows using average floor pressures below the bed, as has been done previously in the vibrated bed literature (for example the explanation for bed bunkering by Gutman [1974]). Based on average floor pressures, the net flow of gas should be downward at the wall and upward at the center — which is correct. However, the *average* difference in horizontal pressures would predict that the horizontal flow of gas should be from the center to the wall, which is obviously not correct if the directions of flow in the vertical direction are correct.

5.2.6 Comparison of Results with Theory

A theoretical evaluation of the dimensionless group Γ, in Section 5.1.3.1, shows that the effect of gas compressibility can be neglected at a vibrational frequency of 25 Hz for particle sizes of 125 μm and larger if the bed depth is 30 mm.

5.2.6.1 Calculation of Gap Sizes from Measured Floor Pressures

The measured (dimensionless) floor pressures can be accurately described by a cubic spline function $\Phi_L^{(3)}(\theta)$, as described in Section 5.2.5. Using this function, the gap size predicted by the compressible-gas (Gutman) model can be calculated by using the equation of motion of the bed during the flight period — equation [5.2]. This equation is valid even if gas-compressibility effects are important, since it explicitly contains the floor pressure which is dependent on the compressibility. It is identical to equation [5.31], which is the lower boundary equation during the flight period for Gutman's model. Writing equation [5.2] in dimensionless form, and substituting for the floor pressure Φ_L with the cubic spline function describing the measured floor pressures gives:

$$\frac{d^2S}{dT^2} = \Lambda\Phi_L^{(3)}(\theta) - \frac{1}{K} + \sin(T) \qquad [5.43]$$

This equation allows the gap-size to be predicted without having to solve the Gutman model, but including the effect of compressibility. It can be considered as a semi-empirical solution to the bed trajectory equation, since it uses experimentally measured pressures.

The instant of lift-off can be obtained by solving equation [5.4] iteratively using the cubic spline interpolating function for the pressure. Then equation [5.43], which is an initial-value ordinary differential equation, is solved using a fifth-order Runge-Kutta variable-step method. The numerical method continues to solve the equation of motion until the dimensionless gap size S, becomes negative. The instant at which the gap closes ($S = 0$), is determined iteratively from the solution of the differential equation. Using the floor pressures measured at the location half-way between the center and wall of the bed, gap sizes have been calculated for beds of Master Beads with particle sizes of 707, 177, and 88 μm.

The calculated gap sizes for $K = 2$, 3, and 4 are shown in Figure 45 on page 173 for 707-μm Master Beads. At $K = 4$, the gap is predicted to persist into the next cycle, but actually closes prior

to the instant of lift-off, so that the throw of the bed is still stable. The gap sizes decrease with decreasing K. A bed porosity of 0.4 and bed depth of 30 mm is used in the calculation of gap sizes. Changing the bed porosity to 0.43 has little effect on the solutions.

Gap sizes calculated by the semi-empirical method for 177-μm Master Beads are shown in Figure 46 on page 174 at values of K from 2 to 5. For this particle size, the bed-floor collision is within one cycle even at $K = 5$. The maximum gap sizes are also much smaller than for 707-μm particles. The bed porosity and bed depth used for this particle size are the same as used for the 707-μm particles. However, for this particle size, the assumption of a bed depth of 30 mm will be in greater error because of the bunkering of the bed.

With a particle size of 88 μm, gap sizes obtained from the measured pressures are even smaller as shown in Figure 47 on page 175. Values of the vibrational intensity parameter K corresponding to the curves are 2, 2.5, 3, and 4. With this particle size, the bed porosity is more critical. The dashed line in Figure 47 shows the effect of using a bed porosity of 0.43 (assuming identical floor pressures), as opposed to the bed porosity of 0.40 used to calculate the trajectories shown as solid lines.

The effect of increasing porosity is to decrease the gap size rather than increase it as might be expected. This is because the only dimensionless group that is used to calculate bed trajectories is Λ, which contains the bed density. The bed density ρ_b can be written as $\rho_s(1-\varepsilon)$, where ρ_s is the density of the solid. If the bed density is reduced, the drag per unit bed mass increases, so that the bed will be retarded while it is moving away from the bed. This will result in a smaller gap size for a lighter bed. If a fully analytical solution of the bed trajectory was considered, decreasing the porosity would have the effect of increasing the drag on the bed, resulting in larger calculated floor pressures, and consequently, smaller gap sizes. However, with the semi-empirical solution used here, the floor pressures are fixed and altering the value of the porosity only has the effect of making the bed lighter.

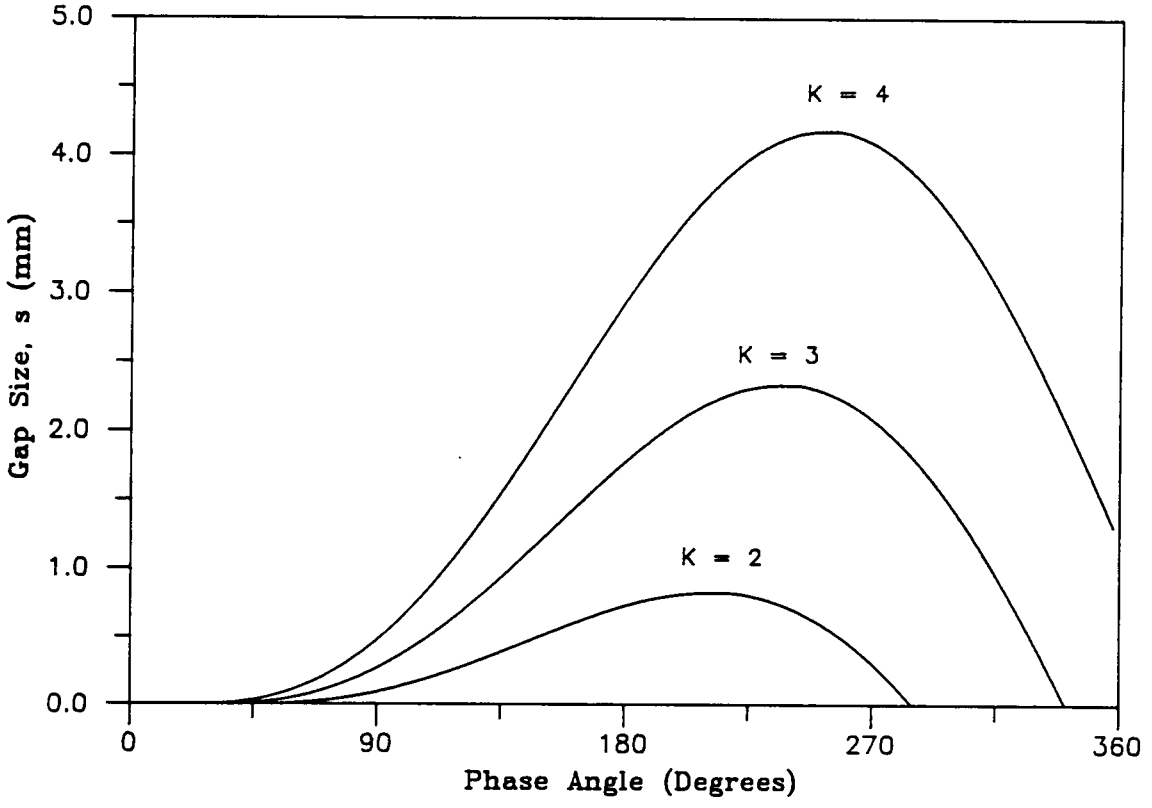

Figure 45. Gap sizes below beds of 707-μm Master Beads: Thickness of the air gap below a 30-mm deep bed of 707-μm Master Beads, calculated from measured floor pressures by the semi-empirical method, for $K = 2$, 3, and 4. Note that at $K = 4$, the gap only closes in the following cycle.

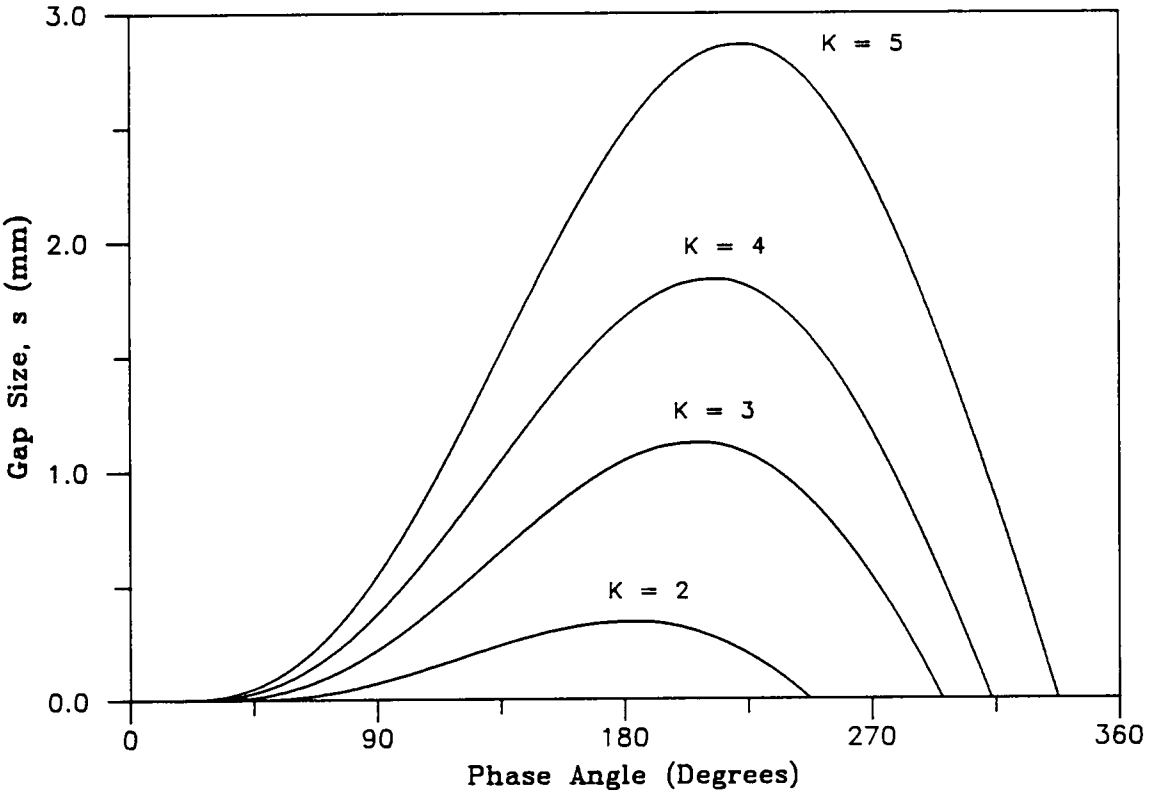

Figure 46. Gap sizes below beds of 177-μm Master Beads: Thickness of the air gap below a 30-mm deep bed of 177-μm Master Beads, calculated from measured floor pressures by the semi-empirical method, for $K = 2$, 3, 4, and 5.

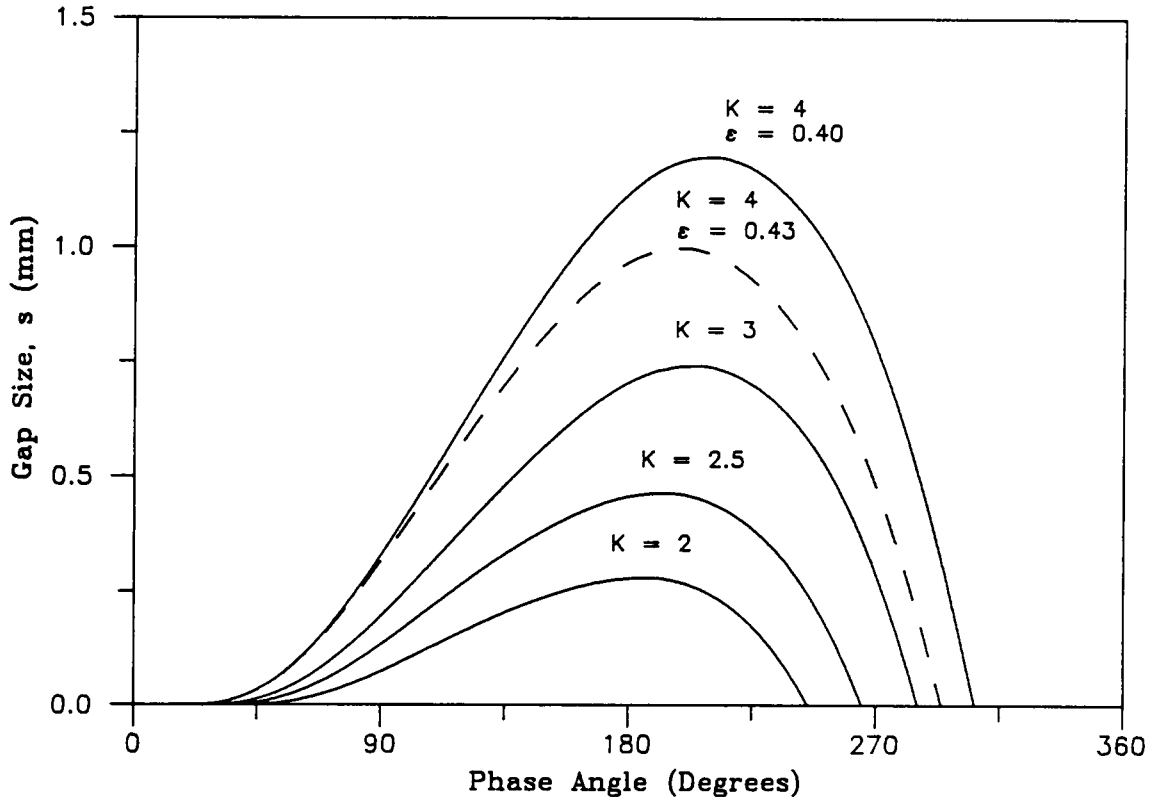

Figure 47. Gap sizes below beds of 88-μm Master Beads: Thickness of the air gap below a 30-mm deep bed of 88-μm Master Beads, calculated from measured floor pressures by the semi-empirical method, for $K = 2$, 2.5, 3, and 4. The dashed line shows the effect of using a bed porosity, ε, of 0.43 (instead of 0.4 as for the solid lines).

5.2.6.2 Comparison of Results with the Kroll Model

The analysis of compressibility effects in 30-mm deep beds in Section 5.1.3.1 shows that even if the vertical pressure gradient deviates from linearity for 125- and 88-μm particles, the deviations are small. The Kroll (incompressible-gas) model is easier to solve than the Gutman (compressible-gas) model, and it would be preferable to use the assumption of incompressibility for extensions of current models to include bed expansion and three-dimensional effects. To check on the validity of this assumption, the predictions of the Kroll model are compared with experimentally measured pressures at the center of the bed with $K = 4$ for Master Beads with particle sizes of 707, 177, and 88 μm in Figure 48 on page 177, Figure 49 on page 178, and Figure 50 on page 179 respectively. Results of the Kroll model are shown as dashed curves and measured pressures are shown as solid curves in the figures. Gap sizes, obtained by the semi-empirical method from measured pressures as outlined in the previous section, are also compared with those obtained from the Kroll model for each particle size in the figures.

707-μm Master Beads

The floor-pressure graphs are not all drawn to the same scale. Keeping this in mind, it is observed as expected, that the deviation of experimentally measured floor pressures from the Kroll model is smallest for 707-μm particles. The location of the positive peak is earlier for measured values than for the theoretical curve. This could possibly be due to an inaccuracy in measuring the vessel acceleration in the experiment. It is difficult to set the vessel acceleration accurately when using large particles because of the "spikes" that are present on the output of the accelerometer as discussed in Chapter 3 (§3.3.1.1).

Despite discrepancies in the locations of the peaks, the gap size predicted by the Kroll model is virtually identical to that obtained by the semi-empirical method. The reason for this is clear if relative magnitudes of the variables in equation [5.43] for the gap size are examined. In the

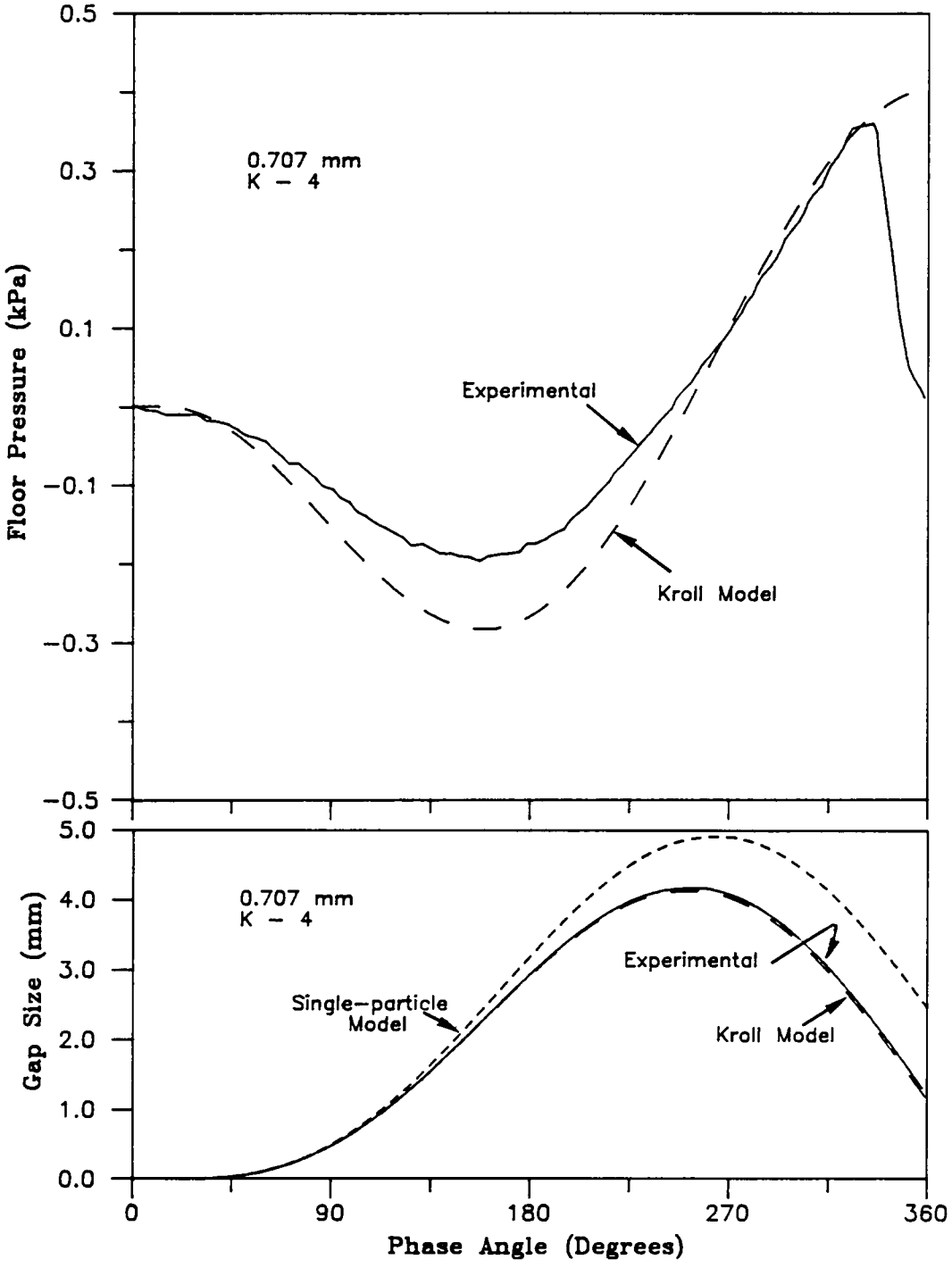

Figure 48. Comparison of the Kroll model with experimentally measured pressures for 707-μm Master Beads: (a) Floor gauge-pressures; (b) Gap size. The gap size predicted by the single-particle model, which represents the trajectory that would be obtained in the absence of drag forces is also shown.

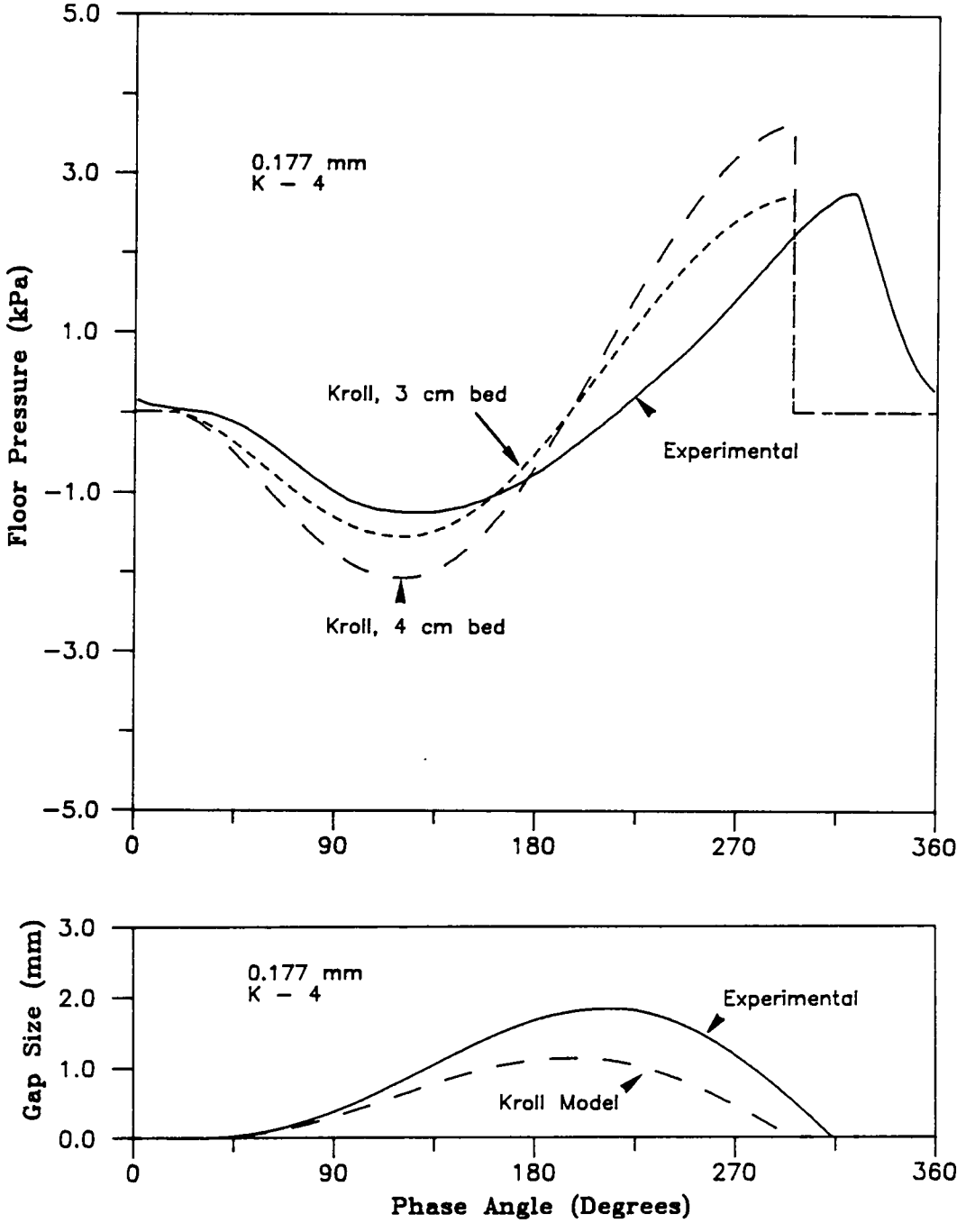

Figure 49. Comparison of the Kroll model with experimentally measured pressures for 177-μm Master Beads: (a) Floor gauge-pressures; (b) Gap size. Note: For the Kroll model, gap sizes are independent of bed depth.

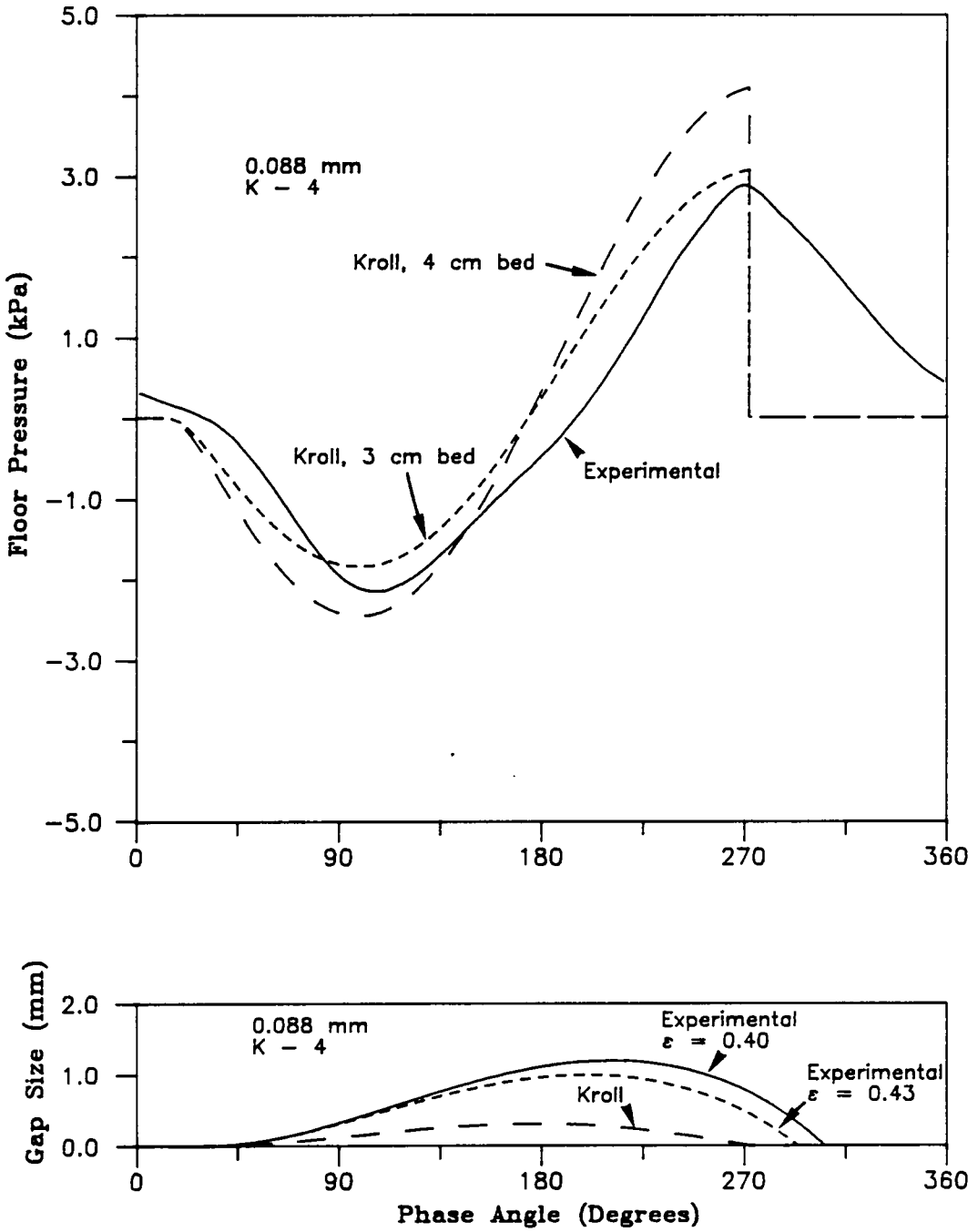

Figure 50. Comparison of the Kroll model with experimentally measured pressures for 88-μm Master Beads: (a) Floor gauge-pressures; (b) Gap size. ε is the bed porosity. Note that the gap sizes predicted by the Kroll model are independent of bed depth.

707-μm particle bed, magnitudes of the floor pressure (drag force) are small ($\Lambda\Phi_L \simeq 0.004$ at the positive peak) in comparison with $1/K$ ($=0.25$) and $\sin T$ (≤ 1.0). The trajectory for the single-particle model can be obtained by solving equation [5.43] with $\Phi_L = 0$ (no drag force). This trajectory is shown as a dotted line in Figure 48 on page 177, and can be seen to deviate from the other trajectories. Thus the effect of drag force is small but not negligible in 707-μm particle beds even if they are shallow.

177-μm Master Beads

With 177-μm particles, absolute discrepancies between measured floor pressures at the center and the predictions of the Kroll model are larger as shown in Figure 49 on page 178. Since the bed is bunkered, and the bed depth is no longer constant through the entire bed, the solution of the Kroll model for bed depths of 30 mm (the dashed curve) 40 mm (the dotted curve) are shown. The Kroll model using a 30-mm deep bed predicts pressures that are reasonably close — relative to the peak values — to measured pressures. The main difference appears to be in the location of the positive peak, which is later for the experimentally measured pressures. This is possibly because the gap does not close uniformly in this bed. Magnitudes of the negative and positive peaks predicted by the Kroll model are comparable to measured values; but the pressure does not decay instantaneously after the collision, indicating that compressibility effects in this bed are only important in determining this feature of the floor-pressure fluctuation.

The gap sizes obtained by the Kroll and semi-empirical method are different. As with the fully analytical solution of the Gutman model, gap sizes predicted by the semi-empirical method are larger than those obtained by the Kroll model. Since the pressures predicted by the Kroll model are reasonably close to measured values, differences in gap sizes obtained by the two methods imply that the gas compressibility has the greatest effect in predicting the bed trajectory. However, this argument supposes that the bed porosity remains constant. If the bed porosity were to increase during the flight period, the Kroll model would tend to predict larger gap sizes.

88-μm Master Beads

Floor pressures measured at the center of the 30-mm deep bed are compared with predictions of the Kroll model for beds with depths of 30 and 40 mm in Figure 50 on page 179. Even for this particle size, the deviation of the Kroll model with a bed depth of 30 mm from measured values does not appear to be great relative to the magnitude of the peaks. The negative peak lies in-between the curves obtained from the Kroll model for 30- and 40-mm deep beds. The effect of gas compressibility again appears to be most important in determining the rate of decay of the floor pressure after the positive peak.

The difference in gap size predicted by the two methods is even greater for this particle size. The dotted curve shows the gap size obtained by the semi-empirical method using a porosity of 0.43 instead of 0.4 as used for the trajectory represented by the solid curve. This still deviates considerably from the Kroll model. Since gas compressibility is far more important in this bed ($\Gamma = 0.807$) than in the other particle sizes discussed above, the difference in gap sizes would appear to be caused by compressibility effects.

5.2.7 Discrepancies Between Predicted and Observed Bed Trajectories

Phase angles for lift-off and collision obtained from the semi-empirical method using experimentally measured floor pressures, are listed in Table 7 on page 182, and Table 8 on page 183 respectively for 707-, 177-, and 88-μm Master Beads at $K = 2$, 3, 4, and 5. The phase angles of lift-off are based on pressures measured at the location half-way between the center and wall of the bed. All sections of the bed separate from the vessel floor at approximately the same instant, but as discussed previously, the bed collides with the floor first at the side walls and last at the center. The phase angles of collision given in Table 8 therefore represent "average" values for the bed.

Table 7. Phase angles of lift-off calculated from measured floor pressures using the semi-empirical method.

Particle Size (microns)	Vibrational Intensity Parameter, K			
	2	3	4	5
707	31.2	20.2	14.3	(a)
177	31.4	20.5	15.1	12.1
88	30.7	19.8	14.3	(b)
Kroll model	30.0	19.5	14.5	11.5

(a) - unstable bed throw

(b) - center-high configuration is too unstable for accurate measurement

Table 8. Phase angles of collision calculated from measured floor pressures using the semi-empirical method.

Particle Size (microns)	Vibrational Intensity Parameter, K			
	2	3	4	5
707	284.5	340.3	14.1	(a)
177	247.4	295.6	313.5	337.6
88	245.3	285.2	305.9	(b)

(a) - unstable bed throw

(b) - center-high configuration is too unstable for accurate measurement

Bed Lift-Off

The phase angle of lift-off is obtained by solving equation [5.4] in its dimensionless form iteratively, and using the cubic spline interpolating function for measured pressures. Phase angles of lift-off calculated by this semi-empirical method are close to those predicted by the Kroll or single-particle model given by $\sin^{-1}(1/K)$, as shown in Table 7 on page 182. At the instant of lift-off, floor gauge-pressures are usually close to zero. Therefore, the magnitude of the term $A\Phi_L$ is small in comparison with other factors in the equation. This implies that drag forces have little effect on the predicted instant of lift-off. Some of the phase angles of lift-off obtained by Gutman [1974,1976a] from theory, occur later in the cycle than obtained by the semi-empirical method (see Figure 26 on page 131). However, Akiyama and Naito [1987] have suggested that these values may be in error, caused probably by inaccuracies in Gutman's solution technique.

A comparison of calculated phase-angles of lift-off with observed phase-angles (given in Table 5 on page 138) indicates large discrepancies in all cases. The largest discrepancy is with 88-μm particles, which can never be observed to lift off the vessel floor, although calculated gap sizes indicate the presence of a gap, albeit a small one, even at $K = 2$. Even with a bed of 707-μm Master Beads with $K = 4$, the observed lift-off is either 38° or 22° later than the calculated value, depending on how the phase-angle of lift-off is measured (see §5.2.1.1) There are three possible causes for these discrepancies, and these are discussed below.

1. Error in Determining the Bed Lift-Off: As the bed lifts off the vessel floor, the bottom of the bed is not perfectly flat. For light to pass under the bed from one wall of the vessel to the other, the space below the bed must be free of particles. If the gap does not form uniformly, but instead some particles lift off sooner than others, the bed will have to lift to some height, probably $0.5d_p$, before a gap can be seen. This cause of phase-lag in the observed lift-off will be more noticeable in large-particle beds since the bottom of such beds will be more irregular, and the height to which they will have to lift to form a visible gap much greater.

2. Delays Caused by Wall Friction: The friction at the wall might tend to hold down particles adjacent to the front and rear walls, delaying their lift-off. In this case, the center of the bed (the section midway between the front and back walls) will lift off first. However, as long as particles at the wall are held down to the floor, no gap can be seen. It will be shown later that fictional forces might be of significance in large-particle beds ($\geq 500\ \mu m$) .

3. Expansion of the Bed During Lift-Off: As accelerations of the bed and vessel differ, pressures below the bed drop below atmospheric, thus drawing gas into the bed. An expansion of the bed during the process of lift-off could delay the separation of the bed and vessel, since the volume of gas is drawn into the bed during the time of bed expansion would not appear below the bed, but instead would fill up the growing voids within the bed. This means that the solution to equation [5.4] predicts not the instant of lift-off, but the instant at which the net forces on the bed equal zero — a null-force point. No gap will be seen at the bottom of the bed as long as the rate at which the void volume in the bed increases is greater than or equal to the rate at which gas is flowing into the bed. The increase in bed porosity can be calculated from the gap size, if it is assumed that the rate at which the bed porosity increases is equal to the rate of gas flow into the bed. In that case, the increase in bed height at any instant will equal the predicted increase in gap size (assuming a fixed cross-sectional area for the bed).

When the vibrational intensity parameter $K = 4$, the increase in porosity of a bed of 707-μm particles that would result in a 22° phase lag in the bed-vessel separation is calculated (by equating the predicted gap size at 36° from Figure 45 on page 173 to the increase in bed height) to be approximately 0.06%, assuming a bed porosity of 0.41 at lift-off and a bed depth of 30 mm. Even a phase lag of 38° between the observed and measured lift-off, which would place the observed lift-off at 52°, would only require a porosity increase of 0.33%. With 177-μm Master Beads, a porosity increase of about 1.9% would be required after the instant of null force on the bed to result in bed-vessel separation at 93° as observed in Table 5 on page 138. For 88-μm particles, a porosity increase of about 5% at $K = 4$ would result in the bed never lifting off the vessel floor during the cycle.

A compaction of the bed is observed during the bed-vessel collision process, which obviously implies that the bed must expand at some point in the cycle. Observation of the high-speed movie film does not clearly indicate a transition from a compacted bed to a looser bed. This might be because the expansion of the bed is more gradual than the compaction process. Porosity variations within a cycle have also been reported by Gutman [1974] and Rippie *et al.* [1978]. Both studies used a capacitance method to estimate the bed porosity, based on the principle that the dielectric constant of the bed depends on its porosity. Results from both studies contain some degree of error due to inadequate calibration of the method. However, their results do indicate an increase in bed porosity associated with "lift-off".

Porosity increases can occur for a number of reasons. All regions in the bed might not be experiencing the same extent of drag as the gas starts to flow down into the bed. It will be shown later (section 5.3) that there is considerable expansion of the top layers of small-particle beds because of a lesser drag on these layers than on the rest of the bed. Also, since particles move relative to each other both horizontally and vertically, adjacent layers of particles within the bed are sheared relative to each other. This will result in the particles moving apart, since that is the only way in which they can move over one-another if the bed is initially in a close-packed state — the Bagnold effect [Bagnold,1954].

Bed-Vessel Collision

There are discrepancies between phase angles of collision calculated from measured floor pressures, and those obtained by direct observation of the gap using phase-delayed strobed back-lighting of the bed. Comparing Table 5 on page 138 with Table 8 on page 183 shows that the observed instant of collision always occurs earlier in the vibrational cycle than the calculated value, usually by about 20° These phase lags could be due to the one or more of the following reasons:

1. There could be difficulty in detecting gaps by the experimental method used, when gap sizes are smaller than the particle diameter, as discussed earlier. However, it is much easier to detect

the instant of collision than the instant of lift-off since it is sudden. Also, the lower bed surface is much flatter as the bed approaches the floor. Therefore, the lag due to this cause of error would probably be much smaller than that for the lift-off.

2. The bed density used in the calculation of the gap size from measured floor pressures is far more critical in determining the phase angle of collision than for the phase angle of separation. As shown in Figure 47 on page 175, an increase in bed porosity from 0.4 to 0.43 (this reduces the bed density if the same bed height is assumed) can result in phase angles of collision that are further apart than the 20°-difference between measured and observed phase angles.

3. If the bed compacts after it makes contact with the vessel floor due to the compaction wave that passes through it, the pressure of the gas within it will continue to increase. This will cause the peak in the measured floor pressure to occur later than the instant at which the bed and floor make contact. Since calculated gap sizes are based on measured pressures, this would result in a calculated phase angle of collision that would be later than the instant at which the gap below the bed is observed to close. The effect of changes in the bed density at the instant of collision are more difficult to analyze than at lift-off, since all horizontal sections of the bed do not collide with the floor at the same instant, so that additional horizontal scale-effects are also present.

Because of the difficulty in determining the bed porosity and hence the bed density accurately, it is impossible to tell which of the reasons listed above is the most probable cause of the discrepancies observed.

5.2.8 The Behavior of Fine-Particle (A-C) Beds

Fine particles that may be classified as group A-C by the Geldart classification [Geldart,1973] exhibit a behavior that is different from other particle types. In this study, such powders include FCC

powder and the fine aluminum powder with a size range of 40-105 μm. Beds of A-C powders with a depth greater than 20 mm, vibrated at 25 Hz, do not draw in gas and expel it at the same frequency as the applied vibration as do other beds. Instead, the bed draws in gas over several cycles, the bed remaining in a mobile state throughout that period. The bed continues to expand, until suddenly the air is expelled from the bed within one cycle. This cyclic phenomenon, which occurs with a period of approximately one second, has never been reported previously in the vibrated bed literature. It may be termed "breathing", since at 25 Hz, it occurs on a slightly shorter time scale than human breathing. Also, by continuously expanding and contracting on such a time scale, the bed has the appearance of a lung. The time scale implies that air is being drawn in over 23 or 24 cycles of vibration, and expelled in one or two cycles. Once the air is expelled, the bed remains immobile (no particle circulation) for a brief period of time until more air is drawn into the bed.

While the major portion of the bed is "breathing" in this manner, the top few layers of the bed behave as a non-breathing vibrated bed. These layers lift off the rest of the bed during the flight period. A gap forms between these layers and the lower part of the bed. The layers undergo a very large degree of expansion while in flight (see also the later sections on the expanded zones in the bed and on vibrated bed "states"). Later in the vibrational cycle, the top layers collide with the lower part of the bed and partially collapse onto it, until the next vibrational cycle. Phenomena in the top few layers of the bed occur at the same frequency as the vibrational frequency, whereas in the lower part of the bed, all phenomena occur with the same period as the "breathing".

The phenomenon of "breathing" is only present with fine particles that are aeratable, namely the Geldart group A or A-C powders. It is absent in group C (fine cohesive) powders, such as the fine-ground white wheat flour and fine Teflon powder used in this study. At 25 Hz, it is absent in very shallow beds of fine aeratable powders with depths of less than about 1 cm.

A qualitative explanation for the phenomenon of "breathing" can be postulated in terms of the compaction wave that passes through the bed during the bed-vessel collision process. Although fine-particle beds do not lift off the vessel floor, the semi-empirical method of solving the force

balance on the bed using floor pressures measured beneath such beds, shows that there is an instant at which the net force on the bed equals zero. A fine-particle bed will, at this instant, become loose and start to expand. The vertical pressure gradient draws air into the bed to fill up the voids. Finally, the vessel accelerates upward and pushes on this expanded bed (equivalent to the collision of a bed in flight with the vessel floor). Because of the horizontal scale-effects, the bed will be compacted from the wall toward the center. As stated previously, the vertical propagation velocity of the compaction wave will depend on the rate at which gas can be expelled from the bed. With an aeratable powder, the gas cannot be expelled from the bed before the start of the next cycle. Thus, the bed never completely compacts onto the vessel floor. At the start of the next cycle, more air is drawn in, which cannot all be expelled by the end of that cycle and so on. The bed continues to expand as air is drawn into it. Finally, the amount of air in the bed reaches a critical amount at which time, it is suddenly expelled from the bed.

It is not certain what determines this critical volume of gas. It is possible that the bed expands to a point at which the gas can be completely expelled from the bed during one cycle. Alternatively, the quantity of air in the bed might reach the volume at which bubbling will occur in the aeratable powder. Micro-bubbles are formed within the bed which rush out of the bed. The later mechanism is supported by studies of bubbling gas-fluidized beds. For fine aeratable powders in a gas-fluidized, bed there is a bed porosity associated with the initiation of bubbling, which is greater than the minimum fluidization porosity. If the air velocity into the bed is increased further, the dense-phase porosity actually decreases since most of the air within the bed passes into the form of bubbles [Tung and Kwauk,1982]. These investigators have also found that if the air supply to such a bubbling bed suddenly turned off, the escape of residual gas from the bed in the form of bubbles is very rapid. This finding tends to support the argument that the gas might rush out of the "breathing" vibrated bed in the form of micro-bubbles. In the vibrated bed, the added forces created by the vibration aid in forcing out the bubbles from the bed.

The behavior of the top-most layers is the same as the expanded zones found on the top surfaces of all small-particle bunkered beds; this will be dealt with in the following section.

5.3 *The Expanded Zone*

A phase-dependent feature of the vibrated bed which is examined herein is the presence of an expanded zone on the top surface of the bed. The existence of such a zone has previously been postulated by Buevich and Galontsev [1978], who also suggest the existence of a expanded zone along the bottom surface of the bed. A expanded zone has been observed in part of the vibrational cycle in previous work connected with this study [Sprung *et al.*,1986]. The existence of a region of increased porosity can clearly be seen above a bed of 177-μm Master Beads as shown in Figure 51 on page 191, if the bed is front-lit by a stroboscopic light source, triggered by a phase-delayed pulse.

In this study, the mechanics of the expanded layer on the top surface are examined by observing a bed of glass-beads that is directly illuminated from above by a strobe lamp triggered by a phase-delayed pulse as described in Chapter 4 (§4.3.3) The refraction of light by the glass beads in the expanded zone makes it appear as a brightly lit band above the bed. Top-lit phase-delayed photographs of the expanded zone allow its characteristics to be related to the cyclic pressure variations within the bed.

The existence of an expanded zone along the bottom surface of the bed is checked by directing the strobed light up through a transparent base of the vessel with the aid of a mirror as described in Chapter 4. Particles with sizes from 707 to 88 μm of both high- and low-density glass are examined. The vibrational intensity parameter K, is varied between 2 and 6 for all beds. However, no expanded zone or region of increased porosity can be observed beneath the bed (but above the expanded zone) under any conditions.

On the other hand, the expanded zone on the top of the bed can be clearly seen along the top surface of the vibrated bed as shown in the phase-delayed photographs presented in Figure 52 on page 193, of a top-lit bed of 177-μm high-density glass beads, vibrated at $K=4$. The photographs show that an expanded zone is present on top of the bed during most of the cycle, even as the bed

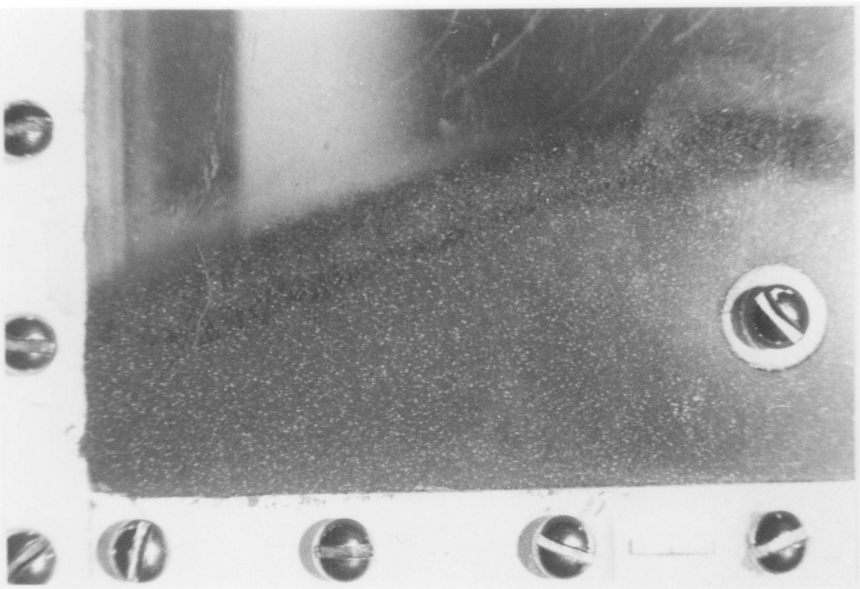

Figure 51. An expanded zone on top of a bed of 177-μm Master Beads: A front-lit phase-delayed photograph of a bed of 177-μm Master Beads at $K = 4$, showing the existence of an expanded zone along the top surface. The photograph is taken at a phase angle of 270°, when gas is rushing out of the bed.

lifts off the vessel floor. No expanded zone can be observed above or below a bed of either high- or low-density glass beads with a particle size of 707 μm

The formation of the expanded or rarefied zone and its evolution through a vibrational cycle may be explained by considering the flow of air through the bed during one cycle, which is driven by pressure gradients within the bed. The variation of floor pressures for this bed is given in Figure 53 on page 194.

As the acceleration of the vessel falls below -1g, negative pressures develop at the floor, causing a down-flow of gas through the bed, and producing a downward drag that retards the motion of the bed which is upward relative to the vessel. This behavior of the top layers can be understood to be the result of a lower drag force acting downward upon these layers in comparison with the drag on the more compacted particles below. Earlier, the closure of the gap in the previous cycle caused gas to escape from the bed, dilating the surface layers. This is confirmed by viewing the high-speed film shot at 2500 frames per second of a bed of Master Beads of the same size. In the film, the expanded zone is seen to grow most rapidly as the bed collides with the floor. The film also shows that the compaction wave that travels through the bed as described earlier does not penetrate the expanded zone. In the film, particles are observed to move down the slope of the top surface within the expanded zone. Partly because of the continued motion of particles within this layer (thus producing a lateral shear), and partly due to the degree of expansion in the previous cycle, there is insufficient time for these layers to settle into the compacted condition before the acceleration reaches -1g in the current cycle. Experiencing less drag than the rest of the bed, the top layers are free to move upward faster than the center of gravity of the bed.

Buevich and Galontsev [1978] have postulated that the expanded layer forms during the lift-off of the bed, based on the argument that there is a lesser drag on these layers than on the rest of the bed. However, the reason they have suggested for the lowered drag is derived from a misinterpretation of the results of Rowe and Henwood [1961], who measured the drag force exerted on individual layers of an assembly of spheres by a flow of gas. The results of Rowe and Henwood state

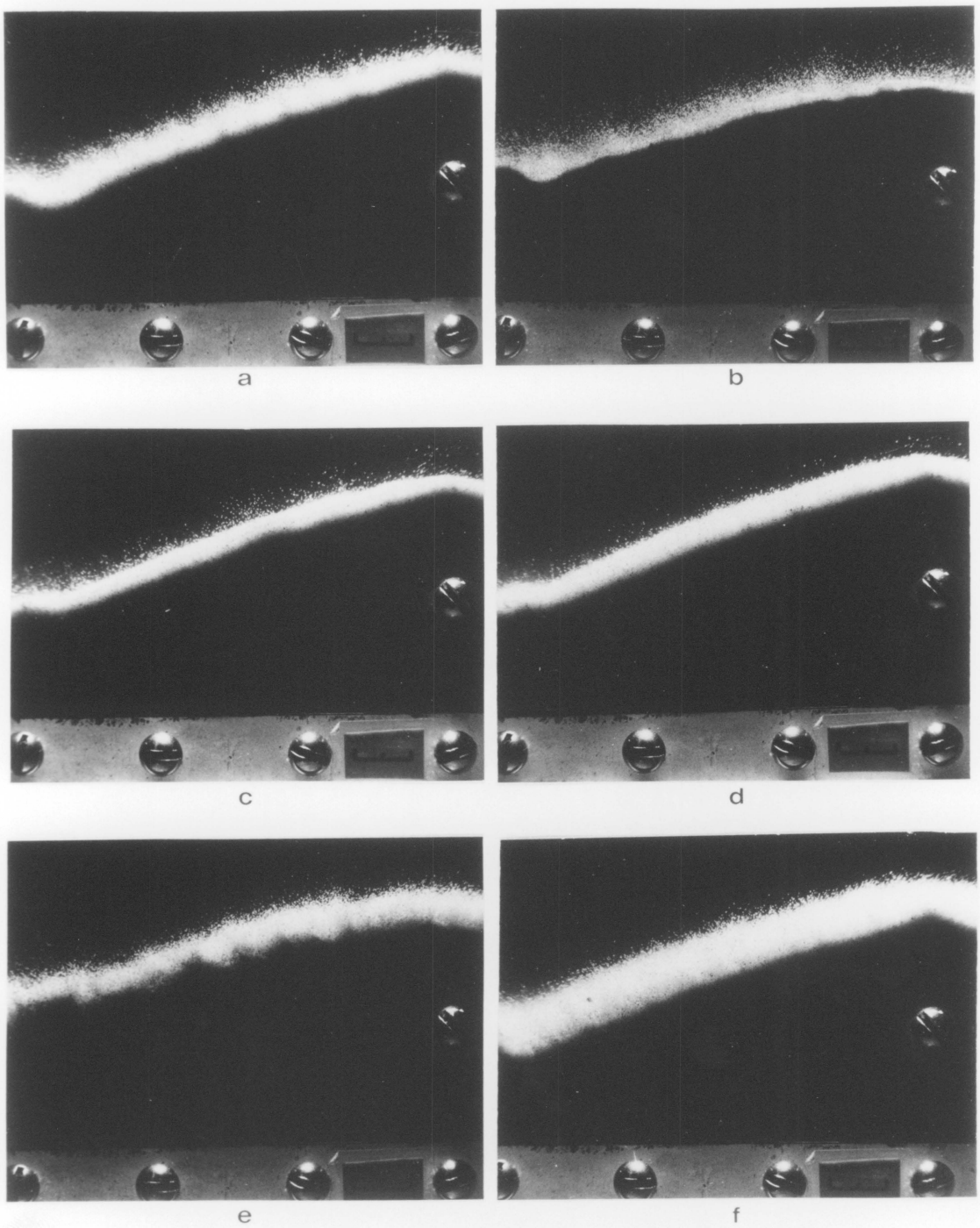

Figure 52. **Evolution of the expanded zone over a vibrational cycle:** Top-lit phase-delayed photographs showing the evolution of the expanded zone on the top surface of a vibrated bed of 177-μm glass beads (-70 +100 mesh), at a frequency of 25 Hz and $K = 4$. (a) phase angle = 15°; (b) phase angle = 42°; (c) phase angle = 82°; (d) phase angle = 150°; (e) phase angle = 270°; (f) phase angle = 280°.

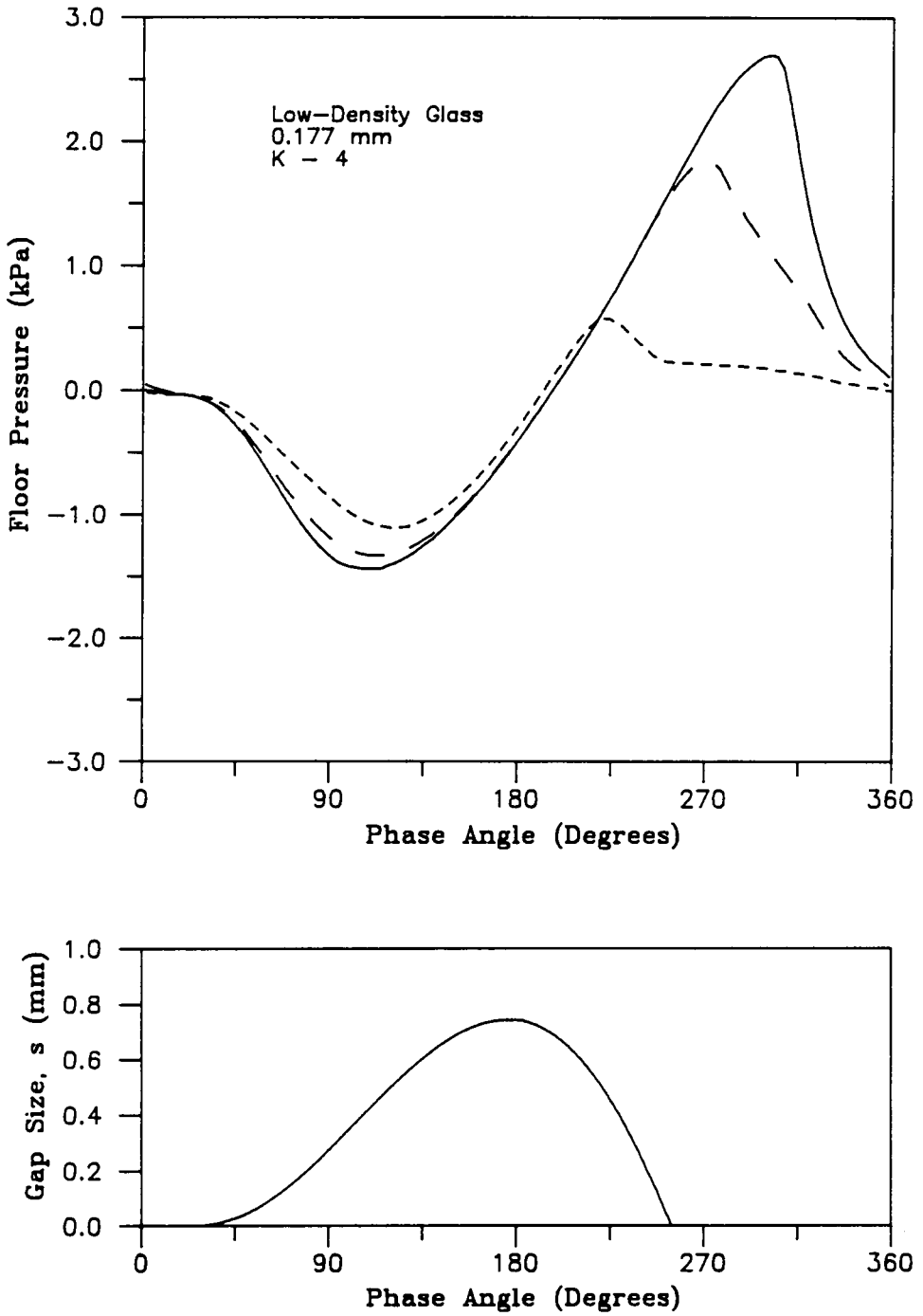

Figure 53. Floor pressures and gap thickness beneath a bed of 177-μm glass beads: The cyclic variation of the floor gauge-pressure and the gap thickness beneath a bed of 177-μm low-density glass beads. The pressures are measured at three locations: ———— beneath the center of the bed; — — — — halfway between the center and the wall; ---------- at the wall. The gap size is obtained by the semi-empirical method from pressures measured at the location halfway between the center and the wall.

clearly that the drag on an upstream-facing layer is typical of the drag in the interior, but that the drag on the downstream-facing layer is higher than on the rest of the bed. This would suggest that the expansion during lift-off would occur on the lower surface of the bed (the downstream-facing layer as gas rushes downward) rather than on the top surface (the upstream-facing layer). However, experimental observation in this study shows that there is no expanded zone formation along the bottom surface of the bed. The results of Rowe and Henwood [1961] also indicate that the drag on an open-packed assembly is much smaller than on a close-packed assembly, and that this difference in drag far exceeds the difference in drag between the downstream-facing layer and the rest of the bed. Thus, the results of Rowe and Henwood tend to support the argument that the lesser drag is caused by the looser packing of particles at the top of the bed during lift-off.

Furthermore, soon after the gas begins to flow downward, particles in a "spray" above the bed fall quickly downward. The surface of the expanded zone becomes more sharply defined, probably because of an effect noted by Rowe and Henwood [1961]. They observed that higher drag forces on *isolated* spheres close to an upstream face of an assembly of spheres pull the isolated spheres strongly toward vacant sites on the assembly.

From Figure 52(a), it can be seen that the expanded zone is pronounced at a phase angle of 15°. However, dark bands present in the expanded zone reflect the fact that the air trapped in the bed from the previous vibrational cycle is still being forced out at this instant. The expanded zone at 15° is therefore a remnant from the previous cycle. A small expanded zone is seen at 42° in Figure 52(b), and is seen to be growing at 82° in Figure 52(c).

Once the bed is falling downward with respect to gravity, the drag caused by the air, which is still flowing down into the air gap, accelerates the center of gravity of the bed downward faster than do particles in the top layers. This follows because there is a greater drag in the relatively more densely packed bulk of the bed, resulting in an even more rapid expansion of the expanded zone, as is the case at 150° shown in Figure 52(d). Note the relatively uniform nature of the expanded bed, and

also that gas driven by the downward sloping vertical pressure gradient is rushing into the gap even as it closes (Figure 53 on page 194).

At 200°, the floor gauge-pressure becomes positive, and the air is forced upward out of the bed. This outward rush of air maintains and further enlarges the expanded zone. Jets of gas are seen within the zone. At 270°, when the floor pressures go through a peak, jets of particles, driven by the gas, may be seen erupting into the expanded zone as shown in Figure 52(e). At 280°, the gap beneath the bed is closed, and the floor pressure falls. However, a substantial quantity of air is still being expelled from the bed at this point as seen in Figure 52(f). This expulsion of air from within the bed continues into the next cycle, as indicated by the photograph at 15°. It is important to note that although the above sequence of events is noticed for all small-particles beds that bunker, the exact phase angles at which an event may occur is dependent on several factors, most importantly floor pressures, but also the particle density, bed depth-to-width ratio, vibrational intensity, and frequency of vibration.

Photographs and visual observations of the expanded zone using a strobe light, as well as high-speed motion photography, indicate a high degree of turbulent gas-solid mixing within this region. Also, visual observation and high-speed cinematography shows that the expanded zone provides a major path for the flow of particles from the center of the bed toward the walls of the vessel.

5.4 Particle Circulation in Vibrated Beds

Characteristic particle circulation patterns are observed in vibrated beds. This section describes different types of circulation patterns observed, and attempts to correlate experimental findings with bed dynamics.

5.4.1 Results of the Experimental Observation of Particle Circulation

Particle circulation in vibrated bed has previously been studied by Sprung *et al.* [1986], and Sprung [1987], using colored tracers and rubber markers. The colored tracers give an indication of particle circulation at the walls of the vessel, while the rubber markers are used to measure the particle circulation rates. The smallest marker used is 1.5 mm in diameter, which is considerably larger than the particle sizes used. Therefore, the measured rates at which these rubber markers circulate can at best be used to estimate the relative circulation rates among different beds.

In this study, fluorescent tracers are used to examine the particle circulation in the vibrated bed. The fluorescent tracers, illuminated by UV light, allow the movement of particles up to one-quarter of an inch within the bed to be examined if glass beads are used, as described in Chapter 4. In terms of overall circulation patterns, examination of the movement of tracers within the bed shows that in small-particle beds that bunker, particles within the bed move at the same velocity as particles at the wall; that is, circulation patterns and particle velocities observed at the front and rear walls are an accurate description of the circulation within the bed.

With large-particle beds that do not bunker, the observation of colored tracers at the wall indicates a flow of particles down at the walls [Sprung *et. al.*,1986]. By conjecture, particles within the bed have been assumed to flow upward. Observation of the circulation using fluorescent tracers shows that this is indeed the case. Particles move down at the wall only within the two particle layers that are immediately adjacent to the wall. The downward particle velocity at the particle layer in contact with the wall is greater than that of the next layer. Since the downward flow is within such a narrow band, the resulting upward flow within the bed is much slower. There is very little particle mixing in the horizontal direction, and it appears to take place by a process of particle diffusion within the bed. If a heat-transfer tube is placed within such a bed, distortions in the circulation patterns produced by the presence of the tube, cause lateral mixing of particles, particularly in the vicinity

of the tube. These distortions in the circulation patterns caused by the presence of a heat-transfer surface within the bed will be dealt with in the following chapter.

Generalized flow patterns that have been observed in vibrated beds of glass beads with particle sizes of 88, 177, and 707 μm are shown in Figure 54 on page 199, at K-values of 2 and 4. The most noticeable difference is the direction of particle circulation, which depends on whether the bed is bunkered or not.

88-μm beads show a greater tendency to move in a horizontal direction over a larger section of the bed. At the center, they move steeply upward. The return flow of particles is along the top section of the bed within the expanded zone. 177-μm particles move with an almost horizontal trajectory only in the lowest section of the bed. In the middle part of the bed, the flow is more diagonal. In the top part of the bed (but below the expanded zone), particles are drawn into the bed as shown in Figure 54 on page 199, from the return flow which is within the expanded zone on the top surface. The diagonal flow of particles is more noticeable at $K=4$ than at $K=2$.

In addition to the effect of particle size, circulation patterns also depend on solid density. Sprung [1987] has mapped circulation patterns using 177-μm particles of high- and low-density glass, and Master Beads. His results are presented in Figure 55 on page 200. The patterns indicate that the downward component of the particle velocity tends to increase as the particle density is increased.

5.4.1.1 Particle Circulation Patterns in a Vacuum

When the air pressure within the bed is reduced to a value at which viscosity effects are no longer important, all beds exhibit circulation patterns that are identical to that observed in large-particle non-bunkered beds — that is, downward in a narrow band at the wall, and upward within the bed. Bunkering is no longer present in any type of bed. With 707-μm particles, the downward particle velocity at the wall is somewhat lower than that at atmospheric pressure. The major particle mo-

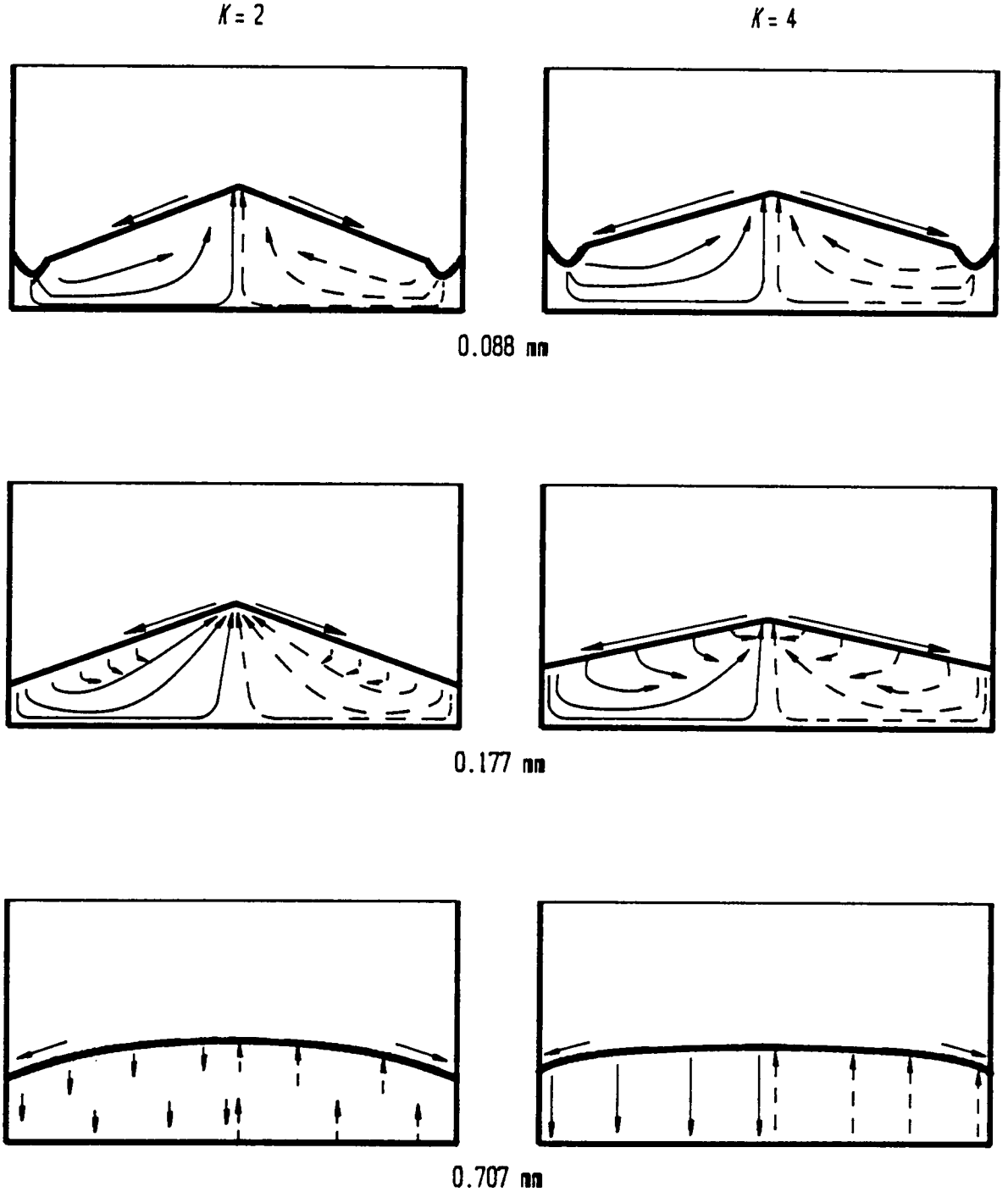

Figure 54. Generalized solid circulation patterns in vibrated beds: General circulation patterns in vibrated beds of 88-, 177- and 707-μm particles at $K = 2$ and 4. The solid arrows in the left half of each bed indicate circulation patterns seen at the wall. The dashed lines in the right half indicate circulation patterns within the bed observed by the use of fluorescent tracers. Note: With the 88- and 177-μm particle size beds, a center-high bunker configuration is used. Different circulation patterns result from other bunker configurations (see also Figure 59 on page 218).

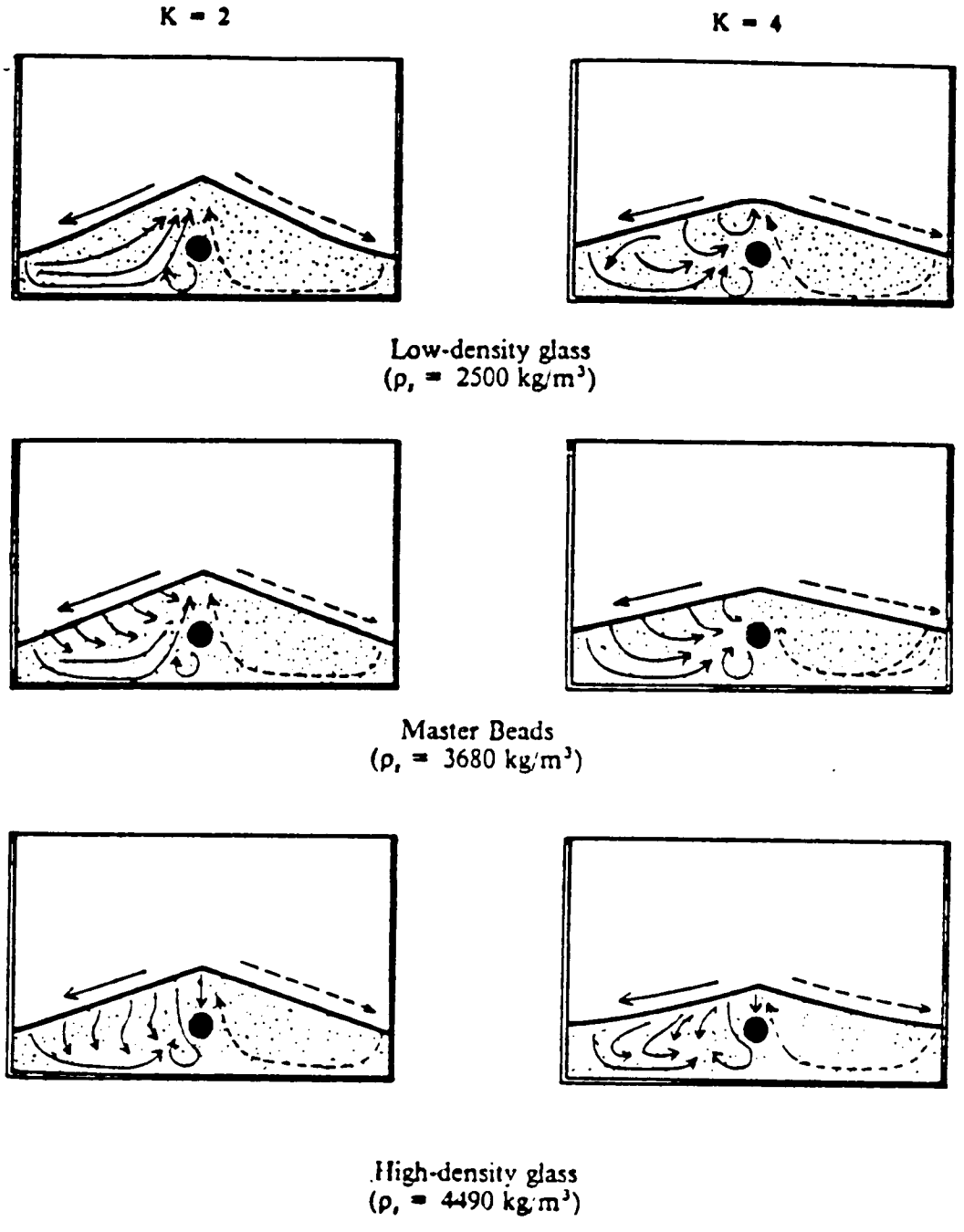

Figure 55. The effect of solid density on particle circulation patterns: Particle circulation patterns for 177-μm particles of three different solid densities at K = 2 and 4 [Sprung,1987]. Note that Sprung obtained these circulation patterns with the dummy tube placed across the bed.

tion is the vertical oscillatory motion relative to the bed due to the bed throw, which is now much larger. This agrees with earlier observations of vibrated beds at low pressures made by Sapozhnikov and Syromyatnikov [1970].

5.4.1.2 Description of Particle Motion Within a Vibrational Cycle

Periodic Particle Motion in Bunkered Beds

The motion of 177-μm Master Beads with colored tracers is observed within one cycle, with the aid of high-speed cinematography. The bed is vibrated at $K = 4$, and filmed at 2500 and 1250 frames per second (fps). The film is played back at 25 fps, slowing down the action 100 times and 50 times, respectively. The bed is bunkered, with the center of the bed being highest.

The film shot at 1250 fps shows that as the bed lifts off the vessel floor, particles within it become loose and start moving. Within the dense region of the bed, below the expanded zone, particles move from the side walls toward the center. The expanded zone can clearly be seen, and particles move from the center to the side walls in this region of the bed. Once the bed comes in contact with the vessel floor, the bed becomes compacted, and the particle motion in the bed below the expanded zone stops completely until the start of the next cycle.

The film shot at 2500 fps shows that as the bed collides with the vessel base, particle motion in any part of the bed is stopped as the compaction wave passes through that part of the bed.

The particle motion in the expanded zone takes place primarily when it is fully expanded, but as stated in Section 5.3, it never fully collapses, so some particle motion is always present in this region. During the flight period, particles are observed to be pulled down from the expanded region into the denser region of the bed.

This is the first instance, as far as can be established from the published vibrated-bed literature, that the motion of particles within a single cycle has been directly observed.

Periodic Motion of Particles in "Breathing" Beds

As described in the previous section, beds of fine aeratable powders (Geldart group A/C powders), exhibit a periodic expansion and contraction at a frequency much lower than the vibrational frequency. This phenomenon which has been termed "breathing" occurs because the bed does not completely collapse within one vibrational cycle. The periodic motion of particles in such beds is determined by the time period of the "breathing", rather than by the vibrational period.

Particles move from the wall toward the center as long as the bed is expanded, which is usually over about 23 to 24 vibrational cycles. When the bed collapses, the particle motion suddenly halts. This is similar to the periodic particle motion in bunkered beds as described above. Essentially in both "breathing" and other bunkered beds, particle motion only takes places while the bed is in a "loose" state, and layers of particles can move relative to each other.

Periodic Particle Motion in Non-Bunkered Beds

Similar observation of particle motion at the wall within one cycle is made using high-speed cinematography. Low-density glass beads with a diameter of 707 μm are used. Glass particles are colored black with a permanent dye, and the motion of these tracers are followed.

The film is viewed frame-by-frame and the movement of the colored tracers followed. At the start of the flight period, particles at the wall are accelerated downward. They reach a maximum downward velocity. Later as the bed starts to fall back toward the vessel floor, the particles are retarded, and suddenly come to a halt as the bed collides with the vessel floor. At the bottom of the bed, during the flight period, particles are drawn in from the layer adjacent to the wall into the rest of the bed.

5.4.2 Proposed Mechanism for Particle Circulation in Bunkered Beds

Because of the different types of particle circulation, mechanisms responsible for circulation depend on the bed bunkering.

Observed directions of particle circulation in small-particle beds shown in Figure 54 on page 199 and Figure 55 on page 200, are remarkably close to the directions of gas flow shown in Figure 42 on page 164, which are derived from horizontal and vertical pressure gradients within the bed. This fact suggests that the flow of gas within the bed caused by the pressure gradients is responsible for the particle motion. The disappearance of this type of solid circulation in a vacuum or when bunkering is suppressed, supports this hypothesis.

As the bed lifts off the vessel floor, both horizontal and vertical pressure gradients develop within the bed. Particles move down along the side walls, and are drawn down into the bed from the expanded zone along the top. During the flight period, the pressure at the wall is higher than at the center, so that particles move down this gradient from the wall to the center. This is particularly true in lower layers of the bed where gas flows are largely horizontal. With a solid of higher density, the vertical pressure gradient is larger than that for a low-density solid. This causes a larger vertical component in the particle velocity as observed in Figure 55 on page 200 by Sprung [1987]. As the gap closes, pressures within and beneath the bed rise above atmospheric, but as long as the bed is in flight, the horizontal pressure gradient slopes down toward the center. The vertical component of the particle velocity is now upward, but the horizontal component still remains directed toward the center of the bed. Thus, particles continue to move toward the center, although they may also move upward slightly.

The bed falls back onto the vessel floor from the side walls toward the center. A compaction wave passes through the bed as described earlier. In front of the compaction wave, the bed is loose and the horizontal pressure gradient is still downward in the direction of the center. Because of the large

vertical pressure gradients that develop, particles also start to move upward, particularly at the center, where vertical pressure gradients are largest. Behind the wave, the horizontal pressure gradient reverses direction as shown in Figure 42 on page 164, causing gas to move from behind the compaction wave to the wall. However, since the bed is compacted in this region, no particle movement is possible. The bed "freezes" from the wall toward the center as the gap closes.

Thus, particle motion is caused by gas flows that are driven by vertical and horizontal pressure gradients within the bed; and it only takes place while the bed is in flight and "loose".

5.4.2.1 Correlation of Pressure Gradients with Particle Velocities

Particle velocities are difficult to establish with any reasonable degree of accuracy by visual observation, since only single particles can be followed at a time. In Chapter 7, techniques using a digital computer will be suggested that will allow the simultaneous tracking of several particles at one time, thereby yielding far more accurate results than those obtained in this study.

The best estimate for the horizontal velocity component in a bed of 177-μm low-density glass beads (obtained by measuring the horizontal distance travelled by a tracer particle in a given amount of time) is 2 mm/s at $K=3$, and 8 mm/s at $K=4$. The value of 8 mm/s suggests a time of 10 seconds for a particle to move the 80-mm distance between the wall and center of the "two-dimensional" vessel. This compares well with the time of 11 seconds quoted by Sprung [1987] using the rubber marker, under otherwise identical conditions. However, at $K=3$, circulation velocities obtained by the two methods are different. The horizontal velocity obtained in this study suggests a time of 40 seconds for a particle to move from the wall to the center, whereas Sprung [1987] obtained a time of 17 seconds with a rubber marker. It should be noted that the time obtained in this study is for the particle to move to the dead center and emerge from the top of the bed. Particles that emerge from the top surface of the bed on either side of the dead center, have a much shorter residence time within the bed. It is possible that the rubber marker was not emerging from the dead center, and

the value quoted by Sprung [1987] is based on an average residence time within the bed. It is also possible that for some reason, the rubber marker does not move at the same rate as the particles do at lower values of K.

The general trend observed both in this study and that of Sprung [1987], is that the circulation rate for a given particle size increases with increasing vibrational intensity. This is in accordance with the observations of Suzuki *et al.* [1980b].

General observations of beds of low-density glass beads with particle sizes from 353 to 88 μm, at $K=4$, show that the rate of particle circulation first increases with decreasing particle size, then reaches a maximum for a particle size of 177 μm, after which it declines with further reductions in the particle size. This is supported by circulation rates for the rubber marker obtained by Sprung [1987]. At $K=4$, the time taken by the rubber marker to move from the wall to the center is 11 seconds in a bed of 88-μm Master Beads, and 7 seconds for 177-μm Master Beads. At lower values of K, differences between the two particle sizes becomes even more marked. Suzuki *et al.* [1980b] have reported similar trends at $K=1.21$. The circulation rate for a bed of glass beads with a size range of 177-210 μm is reported to be higher than that for a bed with a size range of 297-350 μm. When the size range is further reduced to 105-125 μm, the particle circulation rate is lowered.

Sprung [1987] has observed that circulation rates for 177-μm low-density glass beads are higher than those for high-density glass beads of the same size at both $K=3$ and 4. Circulation rates for Master Beads however, are the highest.

The discharge of solids from a fluidized bed through an orifice is often modeled as the hydraulic discharge of an inviscid fluid through the orifice [Massimilla, 1971]. The flow of solids between two adjacent fluidized beds with different levels that are connected by a pipe can be approximated by the efflux rate of solids into the atmosphere through an orifice with the same diameter as the pipe and for the same pressure difference, as the difference in "hydrostatic head" between the two beds.

These results, if applicable to a dense gas-fluidized bed, can be extended to a vibrated bed in the flight period. During the flight period, particles are in effect weightless, and a vibrated bed is therefore analogous in that respect to a gas-fluidized bed.

Since it has been established that particles only move during the flight period when the bed is in free-fall, the pressure gradients that are pertinent to particle circulation are those which exist during this period. The average horizontal pressure gradient during flight $\overline{\Delta P_x}$, is calculated from:

$$\overline{\Delta P_x} = \frac{\int_{\theta_s}^{\theta_c} \Delta P_x \, d\theta}{\int_0^{2\pi} d\theta} = \frac{1}{2\pi} \int_{\theta_s}^{\theta_c} \Delta P_x \, d\theta \qquad [5.44]$$

where ΔP_x is the horizontal pressure gradient between the wall and the center during flight, assuming that the gas is incompressible. The phase angle of lift-off is θ_s, and θ_c is the phase angle of bed-vessel collision. It is easy to determine θ_s, since all parts of the bed lift-off the vessel floor within the span of a few degrees. However, θ_c is difficult to estimate, since the gap does not close uniformly. For the purposes of calculating the average horizontal floor pressure gradient during flight, θ_c is taken to be the phase angle of bed-vessel collision at the wall. Although this is not strictly correct, the pressure gradient is not predictable beyond this phase angle, because of the compaction wave that travels through the bed. Average horizontal pressure gradients at the bottom of the bed calculated in this manner are shown graphically in Figure 56 on page 207.

Particles are accelerated from zero velocity at the start of each flight period. Because of the change in particle momentum that must be produced, the mass or density of the solid has to be taken into consideration. The average horizontal drag force per unit bed weight during the flight period as shown graphically in Figure 57 on page 208, takes both the horizontal pressure gradient and solid density into account. This quantity, which is dimensionless, is given by the ratio:

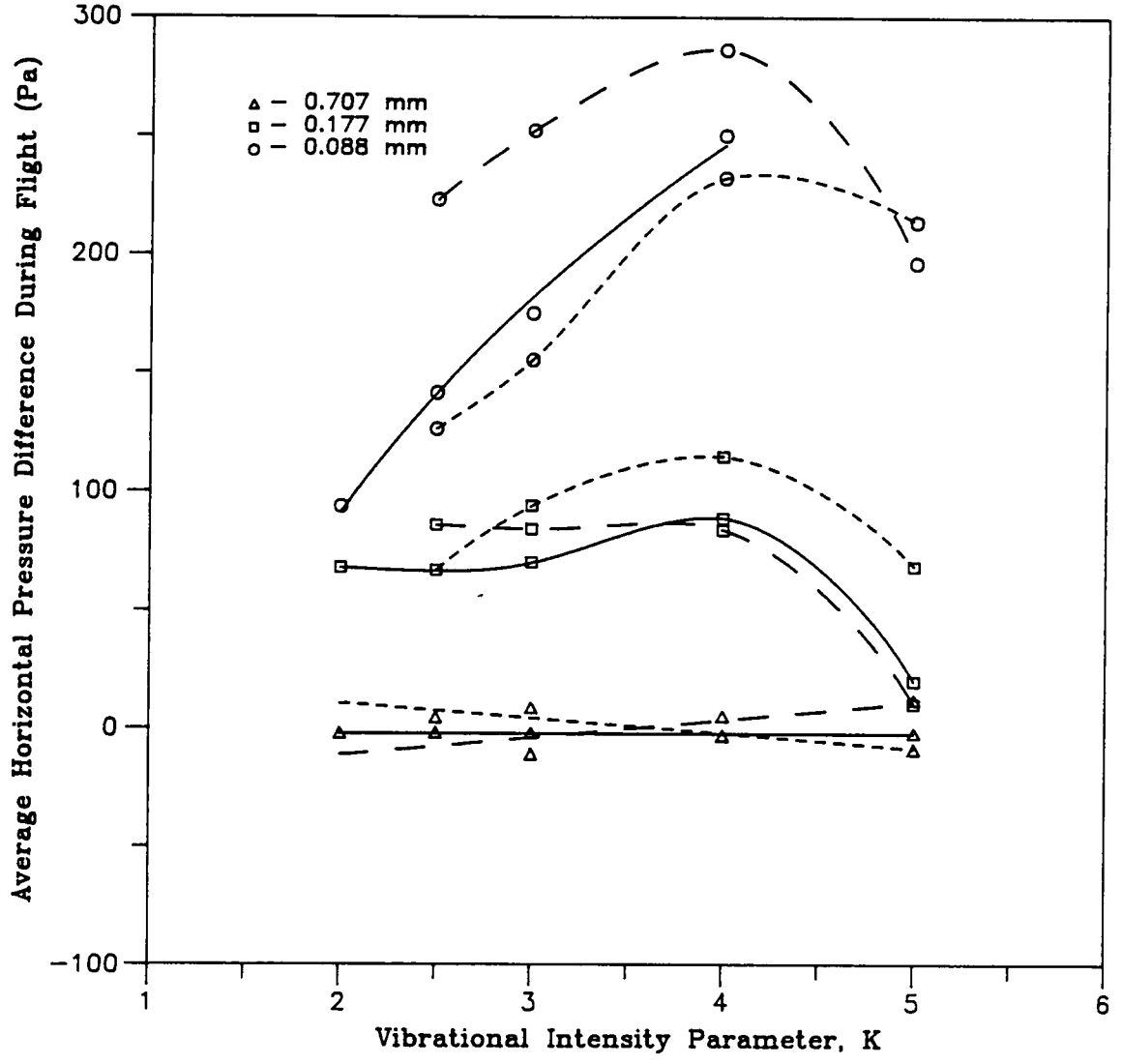

Figure 56. The average horizontal pressure difference during bed flight: The average horizontal pressure difference at the bottom of the bed during bed flight as a function of the vibrational intensity parameter *K*, for different particle sizes and solid types. ———— Master Beads; — — — — high-density glass beads; ———— low-density glass beads.

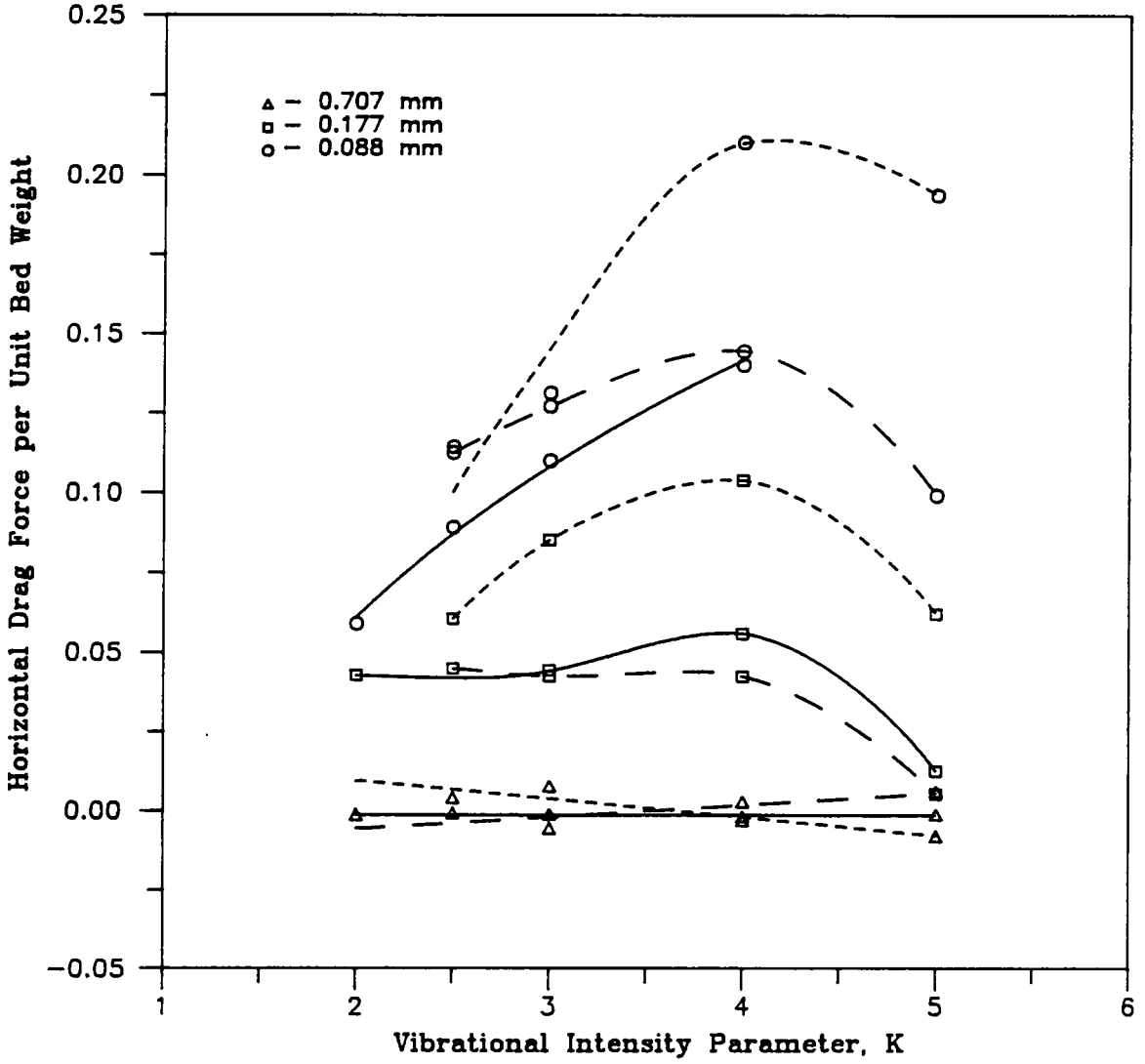

Figure 57. The average horizontal drag force per unit bed weight at the bottom of the bed: The average drag force acting on the bottom of the bed in the horizontal direction during bed flight. The direction of the force is from the walls toward the center of the bed. ———— Master Beads; — — — — high-density glass beads; ·-·-·-·- low-density glass beads.

$$\frac{\overline{\Delta P_x} A_h}{\rho_b R A_h g} = \frac{\overline{\Delta P_x}}{\rho_s (1-\varepsilon) R g}$$

where A_h is the cross-sectional area of a thin horizontal "slice" across the bed, R is the half-width of the bed (the distance between the wall and the center), and ρ_s is the solid density.

Values of this ratio for 707-μm particles are always close to zero. This is consistent with the observation of there being almost no horizontal particle motion in such beds. With smaller particle sizes, there are a couple of inconsistencies when the ratio is compared with observed trends in particle circulation rates. First, the drag in the direction of particle flow is higher for 88-μm particles than it is for 177-μm particles; whereas both this study and that of Sprung [1987] have shown that the circulation of 88-μm particles is always more sluggish at a given value of K. Secondly, the drag force per unit bed weight is larger for low-density glass beads than it is for Master Beads, which would predict that circulation rates for low-density glass beads are higher than for Master Beads. This is in conflict with the results of Sprung [1987] which state that the circulation rates are highest with Master Beads.

Massimilla *et al.* [1959] have suggested an alternative approach to describing the efflux of particles in the fluidized dense phase through an orifice, which may be adapted to describe particle circulation in a vibrated bed. The interstitial gas-percolation velocity is related to the horizontal pressure gradient by Darcy's law

$$u_i = -\frac{\kappa}{\mu\varepsilon} \frac{\partial P_x}{\partial x} \qquad [5.45]$$

However, instead of correlating the particle efflux rate with the drag force exerted by the gas flow on the bed as a whole, the particle movement is related to the drag exerted by the interstitial gas flow on individual particles. By assuming that each particle is accelerated from a velocity v to $v + dv$, in a horizontal distance x because of the drag on each particle, a force balance gives:

$$\frac{dv}{dt} = -v\frac{dv}{dx} = \frac{C'_D \rho A_p}{2\rho_s V_p}(u_i - v)^2 \qquad [5.46]$$

A_p is the projected area of the particle in the direction of the flow, and V_p is the volume of a single particle. C'_D is a drag coefficient for the particle within a packed bed. It should be noted that in a vibrated bed, u_i is time-dependent because of the periodic oscillations in gas pressures. For spherical particles:

$$\frac{dv}{dt} = -\frac{3}{4}\frac{C'_D \rho}{\rho_s d_p}\left(\frac{\kappa}{\mu\varepsilon}\frac{\partial P_x}{\partial x} - v\right)^2 \qquad [5.47]$$

The exact equation for C'_D is not known, but usually for laminar flow, $C'_D = f(Re^{-1}) = f(d_p^{-1})$. The bed permeability κ is a function of d_p^2 . Therefore, by making the appropriate substitutions, it is seen that:

$$\left(\frac{dv}{dt}\right) = f\left(d_p^2,\ \rho_s^{-1},\ \frac{\partial P_x}{\partial x}(t)\right) \qquad [5.48]$$

This shows that the acceleration of the particle (and hence its velocity) during the flight period is dependent not just on the horizontal pressure gradient, but also strongly on the particle size. If the gas flow can be assumed to be incompressible, the average value of the product $[\rho_s^{-1}(\partial P_x/\partial x)]$ is equivalent to the average drag force per unit bed weight plotted in Figure 57 on page 208.

The average horizontal interstitial velocity component during flight can be calculated from the average horizontal pressure gradients given in Figure 56 on page 207. For Master Beads, this velocity is approximately 5.6 mm/s at $K = 4$, and 3.0 mm/s at $K = 3$ for 177-μm particles. For 88-μm particles, these values are 2.4 mm/s at $K = 4$, and 1.9 mm/s at $K = 3$. Substituting these values into equation [5.46] shows that the particle acceleration, and consequently the particle velocity, will be smaller for 88-μm particles than for 177-μm particles.

With low-density glass beads, the horizontal interstitial gas velocity at the bottom of a bed of 177-μm particles is 7.3 mm/s at $K=4$, and 4.8 mm/s at $K=3$. For 88-μm particles, it is 3.3 mm/s at $K=4$, and 1.6 mm/s at $K=3$. Since the particle velocity depends on the interstitial gas velocity, these figures indicate agreement with the observed trend between particle velocity and particle size.

Interestingly, the value of 7.3 mm/s at $K=4$ for 177-μm particles is close but *lower* than the observed horizontal particle velocity of 8 mm/s for this solid. Although relative comparisons of the particle velocity obtained from equation [5.46] can be made by using average horizontal pressure gradients, absolute particle velocities can only be obtained by integrating equation [5.46]. The initial conditions for solving the differential equation are that $v=0$ and $(\partial P_x/\partial x)=0$ at the start of the flight period. By referring to Figure 34 on page 149, it is seen that the horizontal pressure gradient is initially large. Thus, particles are accelerated rapidly during the first part of the flight period. After the negative peak in the floor pressures, the horizontal pressure gradient becomes smaller, and remains at this low value for several degrees until the gap closes. If the particles have gathered sufficient momentum during the first part of the flight period, they can move faster than the gas in the later part of the flight period even if they are slightly retarded by the relatively slower flow of gas. Therefore, it is possible to have average particle velocities that are greater than the average gas velocity, although the particles are driven by the gas flow.

The analysis given above is entirely based on the point of view of fluid mechanics. It assumes inviscid or frictionless flow of particles within the bed. Although particles are "weightless" during the flight period, they are still in contact with each other. From the particle flow patterns, it is clear that layers of particles within the bed move relative to each other. Thus, shear stresses are transmitted through the bed, implying that the motion of particles cannot be modeled entirely by fluid-mechanical theory, but must include consideration of the bed as a solid continuum (requiring the consideration of soil-mechanical theory). The importance of shear stress will depend on the "looseness" of the bed. Obviously, if the bed is very loose, and particles are not in contact with each other, there will be no transmittance of shear stresses through the bed even if there is relative motion of the particle layers. A bed of 177-μm particles at $K=4$ is looser than the same bed at $K=3$. The

"looseness" of a bed can be determined by drawing a rod horizontally through the bed. It requires less force to draw a rod through a looser bed. The low particle velocity (2 mm/s) at $K=3$, when compared to the interstitial gas velocity (4. mm/s), is probably due to the interparticle shear stresses which are high in this bed. Lower circulation rates in glass-particle beds relative to beds of Master Beads [Sprung,1987] might be caused by interparticle forces in the bed. Static charges are more prevalent in beds of glass particles. The static charge in the bed causes particles within the bed to stick together, and will tend to retard the motion of the particles, since the shear stress that would be required to move one layer of particles relative to another increases. With fine Teflon powder vibrated in plastic-walled vessels, the static charge can build up sufficiently to prevent any motion of particles within the bed.

5.4.3 Proposed Mechanism of Particle Circulation in Non-Bunkered Beds

In a bed with a flat top surface, there are almost no horizontal pressure gradients and as a result, very little horizontal motion of the particles is present. The major circulation path is downward in a narrow band of two particle layers at the wall, and upward at a much slower velocity within the rest of the bed.

Since this type of circulation is still present, although to a somewhat lesser degree, at low pressures where gas-viscosity effects are negligible, it can be concluded that the motion is not induced entirely by gas flows. A mechanism that has been suggested by Muchowski [1980] involves the action of wall friction on particle layers adjacent to vessel walls. This mechanism will be elaborated on here. Suppose that wall friction is acting on the layer of particles next to the wall. As the bed lifts off the vessel floor, this layer will be retarded relative to the rest of the bed. This downward force on the layer will continue as long as the bed as a whole continues to move upward relative to the vessel. If there is also a downward flow of gas, an additional downward drag will be exerted on this layer by the down-flowing gas. However, since vertical pressure gradients are approximately the same at

all horizontal locations within the bed, the drag exerted by the down-flowing gas will be equal over the whole bed. Therefore, there is no net effect of gas drag on the particle motion at the wall, relative to the rest of the bed.

The relative downward motion of particles close to the wall produces a shear stress that propagates through the rest of the bed. This means that the center of the bed moves faster than any other part of the bed, and that there is a particle velocity gradient through the cross-section of the bed as shown in Figure 58 on page 214. This type of particle velocity gradient has also been reported by Kapustin *et al.* [1980]. It can also be deduced by observing the top surface of the bed with a strobe lamp that is triggered by a phase-delayed pulse. As the bed rises, the top surface of the bed is dome-shaped. The center moves upward the most, and the wall layers the least.

As particle layers within the bed lift higher than those adjacent to the walls, particles roll down from these layers toward the walls along the top surface of the bed. This can clearly be seen from observing the fluorescent tracers. When these particles enter the wall-adjacent layer, they immediately experience the relative downward drag due to wall friction, and are moved downward relative to the rest of the bed. At the bottom of the bed, inner layers move up higher than those layers adjacent to the wall. Particles at the wall move inward here, since there is no barrier preventing them from doing so, and because of the angular momentum imparted on them by the wall friction. Hence, a circulatory motion of particles is induced in the layers close to the wall. In practice, neither wall surfaces nor particle surfaces are perfect. As a result, the frictional force at the wall may not always be in the strictly vertical direction. This can sometimes cause a particle at the wall to be pushed into the bed before it reaches all the way to the bottom, as can be observed when viewing the movement of the fluorescent tracers.

As the gap starts to close, the bed begins to move downward relative to the vessel. The relative direction of the drag on the wall-adjacent layers due to friction is now reversed. Since the net movement of the bed relative to the vessel over one vibrational cycle is zero, there must be some factors

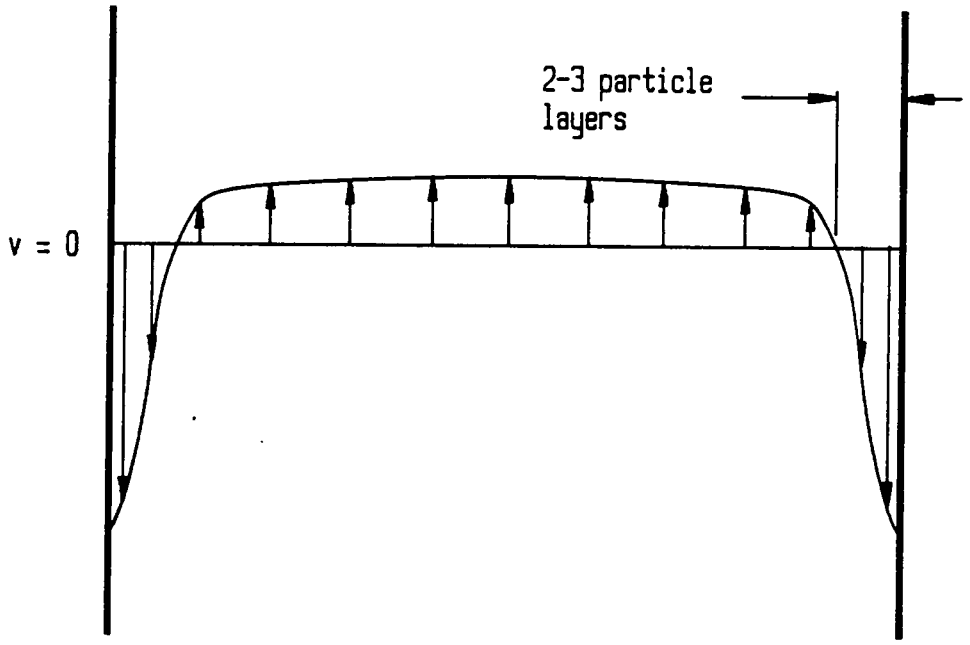

Figure 58. Particle velocity gradient in non-bunkered beds: Particles move downward in two to three particle layers at the walls (which are shown as thick lines). *v* is the particle velocity.

that prevent wall-adjacent particles from returning to the same position relative to the rest of the bed as at the start of the cycle. If this were to happen, there would be no net circulation in the bed.

It should be kept in mind that bed trajectories shown in Figure 45 on page 173indicate that the rate at which the bed reverses its direction of motion relative to the vessel (after the gap has reached its maximum thickness), is rapid when compared to the rate at which the bed moves upward relative to the vessel after lift-off. Also, particles at the wall possesses a downward momentum as the gap reaches its maximum size when the center of gravity of the bed stops moving relative to the vessel. When the bed reverses its relative direction of movement and moves downward relative to the vessel, it will drag down the wall-adjacent particles with it. Since the walls are now moving upward relative to the wall-adjacent layer, they will exert an upward frictional force on this layer. However, because particles in this layer possesses a downward momentum, and the change in direction is relatively rapid, these wall-adjacent particles will slip past the wall surface. It should be remembered that the relative motion during bed lift-off is more gentle, and that particles adjacent to the wall are initially at zero velocity, so that the degree of slip as the bed lifts will be smaller than when it falls relative to the vessel.

The downward slip relative to the wall will continue until the frictional force reaches a magnitude that is sufficient to stop it. After this point, the wall friction force will tend to pull wall-adjacent particles upward relative to the rest of the bed. However, high-speed motion photography shows that although the rate at which particles move down at the wall slows down considerably as the bed falls back toward the floor, they never reverse direction (while the bed is at atmospheric pressure). To summarize, particles at the wall which are pulled downward relative to the bed as the bed lifts, slip past the wall surface as the bed falls back, so that the net result is that wall-adjacent particles move downward relative to the rest of the bed over one vibrational cycle.

The bed trajectory at $K = 3$ (Figure 45 on page 173) indicates that under atmospheric pressure, the bed moves upward relative to the vessel for approximately 216°, whereas it moves downward for only 102° The effect of operating the bed in a vacuum is for the bed trajectory to approach that

predicted by the single-particle model. A comparison of the bed trajectory predicted either by the Kroll or the Gutman model, with that predicted by the single-particle model as shown in Figure 48 on page 177, indicates that the phase angle at which the bed reaches its maximum positive displacement relative to the vessel is not very different whether the effect of air drag is included or not. However, the time taken for the bed to fall back onto the vessel floor is longer for the single-particle model. This means that when the bed is operated under a vacuum, it spends a longer time than it would at atmospheric pressure in moving downward relative to the vessel. As a result, there is a greater chance that during the period while the bed is falling back onto the vessel floor, that the wall friction will cause the wall-adjacent particles to reverse their downward direction of motion before the bed collides with the vessel floor. Thus, the net downward motion of a wall-adjacent particle over one vibrational cycle will be less than at atmospheric pressure. This is a probable reason for the reduction in circulation rate observed in large-particle beds under vacuum.

Equations of motion for the particle motion in non-bunkered beds will depend almost entirely on the continuum mechanics of the bed. The only relevance of fluid mechanics to the situation will be in predicting the height of throw of the center of gravity of the bed. As such, a mathematical treatment of the particle motion is beyond the scope of this study.

5.5 Bunkering in Vibrated Beds

Vibrated beds particularly of fine particles, exhibit a tendency to pile up at certain locations within the containing vessel, so that the top surface of the bed is no longer flat. This phenomenon, called bunkering, has been observed in previous studies [Kroll,1955; Pakowski *et al.*,1984]. Bed bunkering has also been observed in this study. It is usually restricted to beds of small particles, but it is also present in some large-particle beds at low values of K.

5.5.1 Types of Bed Bunkering

Three types or configurations of bed bunkering are observed both within three-dimensional cylindrical and "two-dimensional" rectangular geometries. Each has a characteristic particle circulation pattern associated with it. These bed configurations, and their associated particle circulation patterns are illustrated in Figure 59 on page 218 for both types of geometry. At 25 Hz., only these three types of bed configuration result from bunkering. Attempts to create two bunkers within the width of the vessel do not succeed, because the final configuration will be one of those shown. Shapes of the bed surface shown in Figure 59 on page 218 agree in general with the observations of Pakowski *et al.* [1984]. The three types of bed bunkering are discussed in greater detail below.

Center-High Configuration

The center of the bed is the highest position, and the top surface slopes down toward each wall. In a cylindrical geometry, the high point is located along the central axis of the cylinder, and the top surface of the bed is dome- or cone-shaped. If a heat-transfer tube is placed horizontally in a cylindrical bed, the top surface of the bed will peak along the length of the tube, so that the surface configuration will resemble more that of the "two-dimensional" rectangular bed than a dome.

The particle circulation pattern associated with this configuration is one in which particles flow downward at the walls, and toward the center within the bed. At the center, they move upward.

This is the first configuration that results from an initially flat bed, once vibrations are applied. However, it is also the most unstable configuration. With a particle size of 177 μm, a small non-vertical component can cause instability. With a particle size of 88 μm, this configuration is inherently unstable, particularly at higher values of K, unless the bed is forcibly restrained from changing its configuration. Once this type of configuration becomes unstable, the high point moves toward

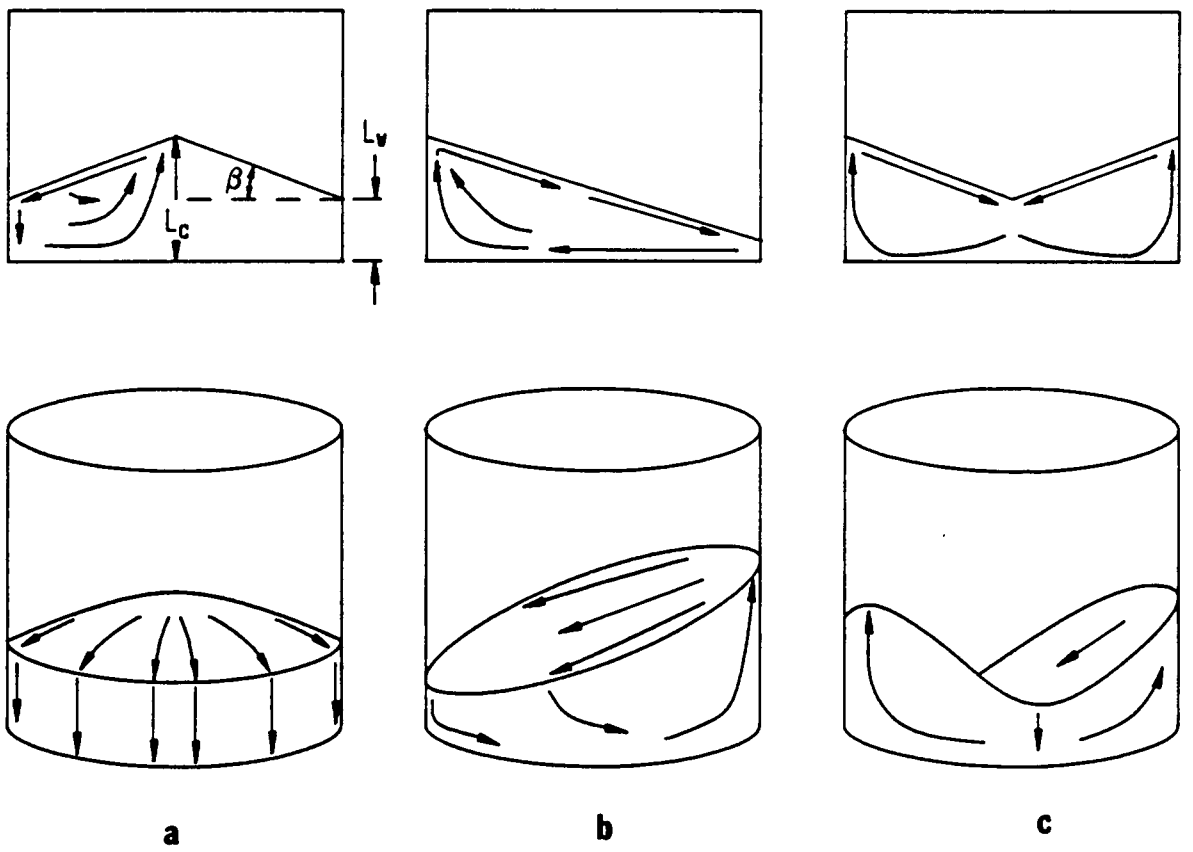

Figure 59. Configurations of bunkered beds: Configurations of bunkered vibrated beds in rectangular and cylindrical vessel geometries. Particle circulation patterns associated with each configuration are indicated by arrows. (a) Center-high configuration; (b) Wall-high configuration - the high point can be at any wall; (c) center-shallow configuration.

one of the vessel walls (one of the side walls in the two-dimensional rectangular geometry), until it reaches that wall. When this happens, the wall-high configuration results.

Wall-High Configuration

This is usually the type of configuration that results after the center-high configuration becomes unstable. The highest point on the bed surface is located against one wall; the lowest point is located at the opposite end of the vessel. In a cylindrical geometry, the top surface appears as a plane that cuts across the cross-section of the cylinder at an angle.

Particles move along the bottom from the shallow to the deep part of the bed; then they move upward at the wall, and flow back along the top surface to the shallow end. The top surface of the bed is expanded as with the center-high configuration. This configuration is very stable, because it is supported on the deep side by the wall. A detailed explanation of the stability of different types of bunkering is given in the next section.

Center-Shallow Configuration

With this type of bunkering, the center is the shallowest part of the bed. There are two high points that are located at opposite ends of the vessel, and which are at an equal height above the vessel floor. It is the inverse of the center-high configuration, and appears like a wall-high bunker at either end, meeting at the center of the vessel. Particle circulation is symmetric about the center; in each half, the circulation pattern is the same as in a wall-high bunker. Particles in the two halves do not mix.

This type of bunkering most usually results if there is a valley at the center of the bed when vibrations are initially applied. Occasionally, if the center-high configuration becomes unstable, and a horizontally placed object, such as a heat-transfer tube, is present along the center-line of the bed, a center-shallow configuration will be the result.

5.5.2 Factors Affecting Bed Bunkering

Bed bunkering is strongly affected by the particle size. With a large particle size, the top surface is almost flat. With a bed of 707-μm particles, the top surface is wavy, but overall, it is not significantly sloped when $K > 2.5$. Waves appear to travel along the top surface. By viewing the bed over the whole vibrational cycle, it becomes clear that these waves are only present as the gas is expelled from the bed as shown in Figure 29 on page 142. Crests of the wave correspond to locations at which gas is being expelled from the bed. During lift-off and the first part of the flight period while air is flowing down across the bed, the bed has minor depressions in it, through which gas preferentially flows into the gap at the bottom of the bed. The crests move toward the wall over several cycles giving the appearance of a wave-like motion along the surface. Regions of the bed closest to the wall are sloped slightly downward. This is possibly due to the wall friction effects that are responsible for the downward flow of particles at the walls. When the vibrational intensity parameter K is reduced below 2.5, the bed of 707-μm particles begins to bunker.

With a bunkered bed, the slope of the top surface can be expressed in terms of the gradient angle β as shown in Figure 59 on page 218. For the center-high configuration, this angle can be experimentally obtained by measuring the depth of the bed at the center L_c, and the depth at the wall L_w. Then, $\beta = \tan^{-1}[2(L_c - L_w)/D]$ where D is the width of the bed. This calculation for the angle assumes a straight-line slope between the center and the wall. This assumption, although almost correct for small-particle beds, is in error for a large-particle bed where only slight bunkering is observed. In such beds, the top surface is almost flat, except at locations close to the walls.

Values of gradient angle β of the top surface obtained in this manner for Master Beads are shown graphically in Figure 60 on page 221 as a function of particle size, and vibrational intensity parameter K. The angles are calculated from measurements of the bed depth at the wall and center by Warren [1986] as part of this study. There is agreement within $\pm$ 1.5° with values of β calculated from the bed-depth data of Sprung [1987]. The figure shows that the degree of bunkering increases

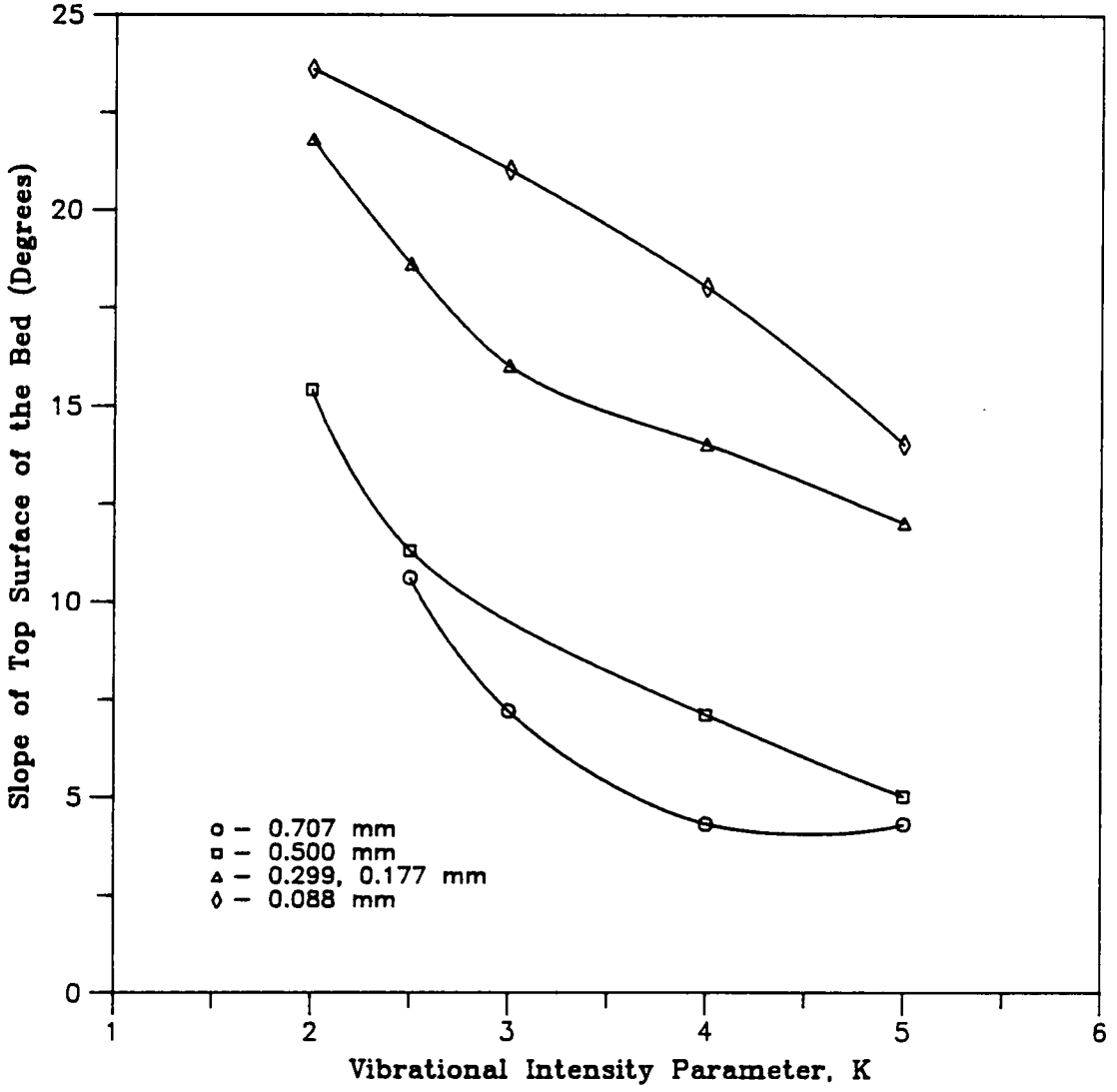

Figure 60. Slope of the top surface of the vibrated bed: The slope of the top surface of center-high vibrated beds as a function of the vibrational intensity parameter *K*, for different sizes of Master Beads.

with decreasing particle size. At a particle size of 500 μm, the slope is significant even at $K = 3$; but the bed is almost flat at $K = 4$ and above. The slopes for beds of the 329-μm and 177-μm particles are virtually identical at all values of K, and only one curve is shown for both particle sizes.

The graph shows that the angle becomes less steep as the vibrational intensity is increased. For the particles with sizes between 500 and 177 μm, the slope of the surface decreases sharply with increasing vibrational intensity, until $K = 3$. Beyond that, the slope decreases more gently, but still significantly. For 88-μm Master Beads, the reduction in β with increasing K is almost linear.

Sprung [1987] has measured L_c and L_w for 177-μm glass beads of both high and low densities, at $K = 2.5$ and 4. Calculation of β from his measurements gives values of 24.8° for low-density glass beads and 19.3° for high-density glass beads at $K = 2$. The corresponding value for Master Beads is 21.8°. At $K = 4$, the values are 16.7° for low-density glass beads and 12° for high-density glass beads, whereas the corresponding value for Master Beads is 14°. Thus, bunkering appears to be more pronounced with lower-density particles. Sprung [1987] has also noted that the top surface of the high-density glass beads appears to be curved slightly inward at $K = 4$.

5.5.3 Proposed Mechanism for Bed Bunkering

Particle circulation and bed bunkering are inter-dependent. Bunkering of the bed is responsible for the horizontal pressure gradients that cause particle movement. Since particles move from the shallow to the deep part of the bed, particle motion in turn sustains the bunkered structure of the bed.

The mechanism by which the bunker forms, can perhaps be best understood by observing the initially flat bed shortly after vibrations are applied. In the first few seconds after the start of vibration, all beds, regardless of particle size and density, exhibit particle circulation patterns that are similar to those present in large-particle non-bunkered beds. That is, particles move downward in a narrow

band close to the walls, and upward within the bed. This type of flow pattern, as explained in the previous section on particle circulation, is caused by wall-friction effects. This causes the bed to be slightly lower at the walls. If the bed is in a vacuum, no further changes take place. This type of particle circulation will persist, and no bunkering can be observed even in beds of FCC or 10-μm copper powder.

At atmospheric pressure, these depressions at the wall cause a perturbation in the horizontal pressure gradient which is initially zero. Because the bed is shallower at the wall, the pressure beneath the bed at the wall will be slightly higher (less negative) than at adjacent regions of the bed away from the walls during the flight period. With a large-particle bed that is extremely permeable to gas flows, this horizontal pressure difference will diminish by the flow of a small quantity of gas from the wall toward the center. Because the pressure gradients are small, the flow of gas will be insufficient to move any particles horizontally by a significant amount. In small-particle beds, which are less permeable to gas flow, horizontal pressure gradients are larger, and the resulting flow of gas will produce a slight movement of particles away from the walls and toward the center. This causes a further increase in the difference between the bed depth at the center and that at the wall as the next cycle starts, which in turn leads to greater horizontal pressure differences in that cycle. By the end of that cycle, differences in depth are even greater, and so on. In this manner, the process of bed bunkering escalates over several cycles until a center-high bunker is formed. It is easy to deduce from horizontal symmetry, that the center-high configuration will result from a bed that is initially flat, and subjected to a strictly vertical vibration.

Once the center-high bunker is fully formed, it will remain stable as long as the system is not perturbed, and remains perfectly symmetrical about the center line of the bed. Since horizontal pressure gradients are symmetrical about the center line, no mixing of particles will take place between the two halves of the bed. However, in practice, it is unlikely that the system will maintain this symmetry for an infinite amount of time. For example, it is possible that tensions of the leaf-springs supporting the vibrating structure will alter unequally with time. With fine powders, disturbances are always present particularly at high values of K, where vertical pressure gradients are high, and

the flow of air into the bed from above can sometimes cause depressions in the top surface. Thus, the center-high configuration is never stable in fine-particle beds at high vales of K.

Once mass is transferred across the center line from one half of the bunker to the other, one side will become deeper than the other. This causes horizontal pressure gradients in the two halves to become asymmetric. During the flight period, the pressure beneath the deeper half will be more negative than that beneath the shallower half. This will cause a movement of particles from the shallower to the deeper half, which in turn increases the horizontal pressure gradient and so on. As a result, the peak of the bunker moves in the direction of the deeper half. The process continues until finally, the peak reaches a wall which provides a physical barrier to any further movement. A wall-high bunker is created as a result of instabilities in the center-high configuration.

This mechanism also explains the results of the U-tube experiment [Gutman,1974]. The movement of fine particles from the shallower arm to the deeper arm of the U-tube follows the same rules as for bunkering.

5.5.3.1 The Degree of Bunkering

The graphs of β shown in Figure 60 on page 221 indicate that there is a characteristic angle associated with each particle size and density for a given value of K at 25 Hz. Bed bunkering will also occur in beds that are as shallow as 1 mm, if sufficiently small particles are used. Bunkers form in such ultra-shallow beds because of disturbances on the bed surface that create perturbations in pressure gradients within the bed. These disturbances may be caused by gas attempting to penetrate the surface of the bed as it lifts off the vessel floor. In fine powders, bunkering in ultra-shallow beds may be caused by the tendency of such powders to group together in an aerodynamic flow-field (see also the next section on "states" of the vibrated bed). Once these center-high bunkers form in ultra-shallow beds, they attain the characteristic gradient of the top surface. As a result, if the

bunker is sufficiently small (because the volume of particles in the bed is small), it will not extend across the whole floor.

Since bunkering is caused by a flow of particles from the shallow to the deep end of the bed, it would be intuitive to argue that any condition that results in an increased flow of particles in the desired direction would increase the gradient of the top surface. However, as Figure 60 on page 221 clearly shows, the gradient decreases with increasing K for all particle sizes, even though the horizontal particle velocity from the wall toward the center actually increases at the same time.

It is more likely that the angle of the top surface is determined by the dynamic angle of repose. The results of Jackson and Judd [1981] can perhaps be used to determine the angle. They considered the slope of the surface of a particulate material in a horizontally rotating drum, with an additional flow of air blown upward across the material. The angle that the material takes in the rotating drum is a function of the air velocity across the material. The angle reduces as the air flow across the material is increased. Jackson and Judd correlated the slope of the surface to the air velocity by considering the normal and shear stresses that act on a surface inclined at an angle β to the horizontal. Their analysis can be extended to determining the angle of the top surface of the bunker because these two situations are similar. Using their equation for the angle of the top surface one can write:

$$\beta = \upsilon - \sin^{-1}\left(\frac{\kappa u_n}{\mu}\ \frac{\sin\upsilon}{\rho_b g}\right) = \upsilon - \sin^{-1}\left(-\ \frac{\sin\upsilon}{\rho_b g}\ \frac{\partial P_n}{\partial n}\right) \qquad [5.49]$$

In this equation, υ is the angle of friction of the flowing powder, u_n is the velocity of the gas flowing out normally across the surface, and $(\partial P_n/\partial n)$ is the pressure gradient normal to the bed surface in the direction of the unit vector n which is normal to the bed surface. The normal pressure gradient is the resultant of the vertical and horizontal pressure gradients. Since these gradients change their directions during each vibrational cycle, the normal pressure gradient will be positive as the air flows into the bed, and negative when it flows out.

When the bed is in free-flight, the net component of the gravitational force acting on the bed surface will be equal to zero. This means that there will be no shear stress acting on the top surface due to gravity. In fact, there will be some shear acting on the surface due to the circulatory motion of the particles within the bed, but it will be small. The normal stress that acts on the top surface during flight is only due to the normal pressure gradient on the surface. Therefore equation [5.49] does not apply during the flight period. Examining the shape of the top surface during the flight period (Figure 52 on page 193) indicates that the angle of the top surface does not change during the flight period. It may therefore be assumed that the net instantaneous force acting at any point along the top surface is equal to that at any other point along the top surface, while the bed is in flight.

As air rushes out of the bed, the shape of the top surface is deformed, becoming convex as shown in Figure 52 on page 193, and in Figure 30 on page 143. Once the bed has come into contact with the vessel base, the bed is no longer in free flight, and the force of gravity begins to act on the top surface. Equation [5.49] is now applicable. As the vessel accelerates beyond 1g, the force acting on the top surface will also increase. This means that the gravitational acceleration term in equation [5.49] actually varies with time after the bed-vessel collision between 1g and Kg. Equation [5.49] shows that the angle β theoretically attains a minimum value when the normal pressure gradient is at its largest magnitude, and the gravitational acceleration is as small as possible (that is, 1g). Assume that the bed just comes into contact with the vessel floor as the floor pressure peaks (implying that the gravitational acceleration is equal to 1g at this instant, since the bed has not yet started accelerating at the same rate as the vessel). Then the instant at which the floor pressure peaks corresponds to the point at which the value of β is smallest. It is unlikely considering the short time scales involved, that the surface of the bed will increase in slope beyond this value after the initial instant of bed-vessel contact. Also, in practice, the compaction wave passes through the bed shortly after the collision, and particles within the bed are locked into position, so that further changes in the surface slope are prevented. This value of β therefore characterizes the degree of bunkering for a particular bed at a given set of vibrational conditions, since it is the lowest of possible maximum angles of surface stability.

According to equation [5.49], the angle of the surface β, should decrease as the normal pressure gradient ($\partial P_n/\partial n$), increases. As the vibrational intensity is increased, for a given particle size, both the horizontal and vertical pressure gradients at the instant of collision are larger. This implies a larger normal pressure gradient, and consequently a shallower bunker with increasing values of K, as shown in Figure 60 on page 221.

By recognizing that the minimum fluidization velocity, u_{mf}, is the superficial air velocity which will just support the weight of the bed, $\rho_b g = \kappa u_{mf}$. Substituting this into equation [5.49] gives:

$$\beta = \upsilon - \sin^{-1}\left(\frac{u_n}{u_{mf}} \sin \upsilon\right) \qquad [5.50]$$

When the normal velocity through the top surface of the bed, equals the minimum fluidization velocity for the bed, the value of β becomes zero, and bed bunkering disappears. This conclusion is supported by the observation of particle circulation in vibrated aerated beds by Suzuki *et al.* [1980a]. They have reported that the particle circulation within the bed drops sharply when the velocity of superimposed vertical gas flow through the bed reaches the minimum fluidization velocity. Since overall particle circulation in small-particle beds is a consequence of bunkering, the disappearance of bunkering leads to a cessation of overall solid mixing.

It should be noted, however, that the value of β as predicted by equation [5.49] is the *maximum stable* angle of bunkering that is possible. If the bunker assumes an angle that is lower than this, it will still be stable. In large-particle beds, pressure gradients are small, and equation [5.49] would predict large values of β for such beds, since $\beta \rightarrow \upsilon$ as $(\partial P_n/\partial n) \rightarrow 0$. Figure 60 on page 221 shows that the slope of the surface in such beds is actually quite small. If for example, the horizontal pressure gradient ($\partial P_x/\partial x$), which provides the driving force to initiate and *sustain* bunkering, does not develop, bunkering will be absent. This will be the case in a bed which is extremely permeable to gas flows, or in a vacuum.

With the large particle sizes used here, bunkering is present at small values of K. For example, a 500-μm bed of Master Beads is bunkered at $K=2$, with a surface slope of over 15°. The bunker forms very slowly from an initially flat bed, taking up to 3 minutes to reach steady-state, as opposed to the few seconds required for small-particle beds. Bunkering in such beds disappears if a vacuum is produced in the vibrating vessel. This implies that horizontal pressure gradients are marginally sufficient in such beds to produce bunkering. As the vibrational intensity is increased, the bunkering rapidly disappears, even though the pressure gradients do not increase by very much. In any case these gradients are not as large as in small-particle beds. This suggests that the reduction in surface slope with increasing K is not brought about by an increased flow of gas through the top surface in large-particle beds, but rather by another mechanism.

A mechanism may be postulated by examining the noise present on the accelerometer output during the bed-vessel collision. As stated previously, a collision between a large-particle bed and the vessel produces a large amount of noise on the output, particularly at high values of K. However, a small-particle bed produces no such distortion, even if the bed density is several times that of the large-particle bed (for example, if 10-μm copper powder were used). Since the small-particle bed is more impermeable to gas flow than the large-particle bed, the gas in the gap is compressed to a higher pressure as the gap closes, as is evident from the graphs of floor pressures. As the bed falls onto the vessel base, the compression of the gas within the gap and in the bed serves as a "shock-absorbing" mechanism in small-particle beds that tends to absorb the energy of impact (which is equal to the relative kinetic energy of the bed at the instant of impact). With a large-particle bed, the compression is much smaller, and the energy of impact is dispersed within particles in the bed, causing a break-up of any "structure" that might be established. This can be observed, if a 505-μm bed that is bunkered at $K=2$ is suddenly subjected to a higher vibrational intensity, say $K=4$. The bunkering that is present disappears within a fraction of a second following the increase in K. Also, if a small-particle bed which is bunkered is vibrated in a vessel from which air is continuously withdrawn, a degree of vacuum is reached when the noise of the bed-vessel collision appears, and simultaneously, bed bunkering disappears.

To summarize, bunkering in vibrated beds is caused and sustained by the presence of horizontal pressure gradients during the flight period that cause a flow of particles from the shallow to the deep regions of the bed. In small-particle beds, the maximum degree of bunkering is determined by the stresses on the top surface as the bed falls onto the vessel base. The energy of the impact is absorbed by the compression of the gas within the bed during the bed-vessel collision. Equation [5.49] qualitatively predicts the observed trends in bunkering in such beds, but it is impossible to test the quantitative agreements without a knowledge of angles of internal friction for the solids used. With large-particle beds, the energy of impact is transmitted into the bed where it causes a break-up of any bunkered bed structure that might form during the flight period. Consequently, bunkering cannot occur in such beds.

Finally it should be noted that bed bunkering is observed in beds that are 60 mm deep for all the particle sizes below 500 μm. The depths within such a bed of 177-μm Master Beads are measured to be 70 mm at the center and 50 mm at the wall for a center-high configuration. The analysis of bunkering according to Buevich *et al.* [1979] (described in Chapter 2) treats the bed as inter-connected one-dimensional systems. However, according to the data of Buevich *et al.* [1979], shown in Figure 8 on page 41, in Chapter 2, and the experimental observations of Kroll [1955] and Gutman [1974], the average pressure during the flight period beneath a 70-mm deep *one-dimensional* bed will be higher (less negative) than that beneath a 50-mm deep bed. This would imply a pressure gradient that opposes center-high bunkering if the bed at the wall and at the center were treated as inter-connected one-dimensional beds. However, since center-high bunkering is observed, this illustrates the danger of extending the predictions or experimental observations of one-dimensional systems to a multi-dimensional system.

5.6 *The Transition from a Static to Mobile Bed*

The critical value of the vibrational intensity parameter (K_{cr}) at which there is a transition from a static to a "vibrofluidized" bed depends on the type of solid and the nature of the static bed (packed or loose). This is described as follows:

1. With glass beads (both light and heavy) and alumina spheres of average particle sizes of 707 and 177 μm, which are group B according to the Geldart classification [Geldart,1973]: $K_{cr} = 1$, for both packed and loose static beds.

2. For glass beads (both light and heavy) and alumina spheres with an average particle size of 177 μm, and which lie close to the border between Geldart group A and group C: $K_{cr} = 1.15$, for both packed and loose static beds.

3. FCC: This powder is aeratable, and is a group A solid. If the static bed is initially packed (de-aerated), $K_{cr} = 1.95$; but if the static bed is loose and in an aerated state, $K_{cr} = 1.35$. Both values of K_{cr} remain constant for bed depths varying from 3 to 6 cm.

4. The 10-μm copper powder is a group C solid according to the Geldart classification, but lies on the border between groups A and C according to Grace's modification [Grace,1986] of the Geldart classification. The powder does not appear to be aeratable, but is only very mildly cohesive. $K_{cr} = 1.80$, for transition from the packed static bed, and $K_{cr} = 1.35$, for transition from the loose static bed.

5. The fine aluminum powder has a wide size range, but it is aeratable and most probably a group A powder. However, it is angular and appears to be more cohesive than the copper powder. With a packed static bed, $K_{cr} = 2.60$, and with a loose static bed, $K_{cr} = 2.20$.

6. Fine-ground wheat flour has a wide size range, and spans the group A - group C boundary of the Geldart classification. However, it is not at all aeratable, and is very cohesive, forming lumps easily. With this solid, particles in a thin band on the top of the bed start to move at $K = 2.75$, but an overall bed motion is detected only at $K_{cr} = 4.95$. Even after there is overall bed mobility, large cavities are seen to form within the bed, and occasionally, "dead" regions are seen to form temporarily within the bed. When $K > 6.6$, the appearance of this bed is indistinguishable from any of the other beds.

The results indicate that $K_{cr} = 1$ for bed with particles larger than 100 μm. This agrees with the observations of previous investigators [Herber,1970; Kapustin *et al.*,1980] who have reported increases in K_{cr} for particles below 100 μm., for a given type of solid. The increases are particularly rapid as the particle size is reduced below 50 μm. It is interesting to note that bed motion in 177-μm particles is detected once K just exceeds unity, although the bed itself cannot be observed to lift-off the vessel base at these low values of K. This is because the top of the bed, which is often looser even if the bed is static, is free to move before the rest of the bed. However, once this top layer moves, the lower layers will also gradually start to move, with sufficient air being drawn into the bed to induce bulk particle circulation. This delay in initial movement between the top and lower sections of the bed becomes more noticeable as the particle size is reduced; and with the finer particles used in this study, a delay of a few seconds can be observed between the initial motion on the top and that in the bottom of the bed.

As the particle size in the bed is reduced below 100 μm, there is an increase in K_{cr}, but the results clearly show that the actual value of K_{cr} depends on more properties of the powder than merely the average particle diameter. In addition, differences in K_{cr} between initially packed (or deaerated) and aerated beds of group A particles, coupled with the higher values of K_{cr} recorded for powders that show signs of cohesiveness, indicate that the critical acceleration for the transition is strongly dependent on the bed cohesiveness. This agrees with the results of Ur'ev [1978] who measured K_{cr} to be about 9 for sub-micron particles of calcium carbonate. When a small amount of surfactant

was added to this bed, it had the effect of breaking up some of the inter-particle bonds in the bed, and the value of K_{cr} dropped to approximately 3.

It is also clear that even with a bed of cohesive powder, the vibrational acceleration can be increased sufficiently to provide enough shear to break up the bed, giving it an appearance of a less cohesive bed at a lower value of K.

5.7 States of the Shallow Vibrated Bed.

Visual observations of the bed at equivalent bed depths of 24 μm up to 30 mm, indicate the existence of a number of different "states" of the vibrated bed. The concept of an "equivalent bed depth" is explained in Section 4.5 of Chapter 4. The transitions from one state to another are found in this study to depend on the particle size and type, vibrational intensity, and bed depth. The different states can be identified as described below.

5.7.1 The "Newtonian" State

When the bed is very shallow, usually in the order of about a single particle diameter deep, particles appear to move about in a random fashion. As described earlier, their trajectories can be determined by Newtonian mechanics, and therefore this state can be thought of as the "Newtonian" state.

Two types of Newtonian states are observed. A *Newton-I* state, in which the vertical dispersion of particles in the bed does not change within the vibrational cycle, is shown clearly in Figure 61 on page 233 of a 120-μm deep bed of 707-μm glass spheres. The vertical distribution of particles is approximately the same at a phase angle of 90° (a), and at 280° (b). In the *Newton-II* state, shown

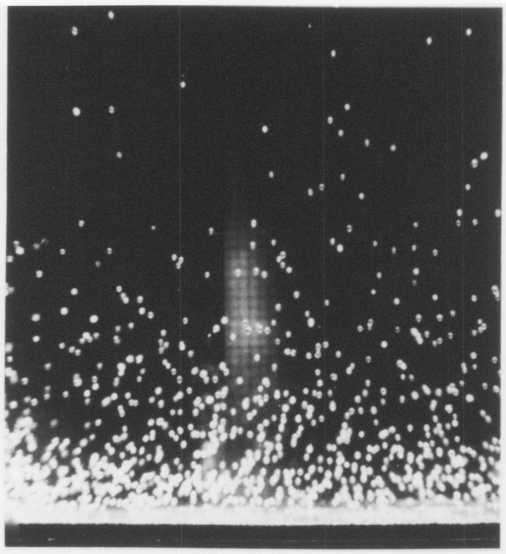

a

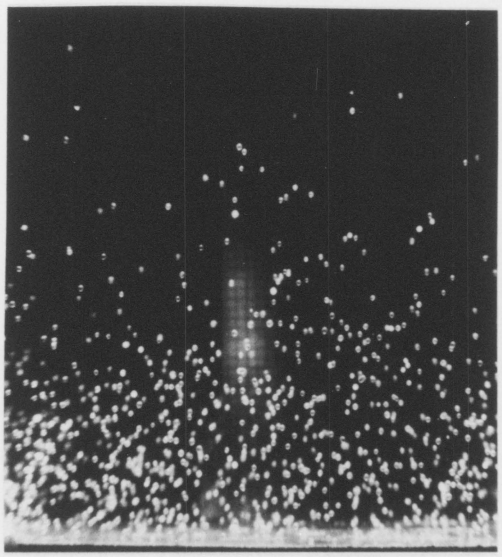

b

Figure 61. **The Newton-I state:** Top-lit photographs of a bed of 707-μm low-density glass spheres with a equivalent static bed depth of 120 μm at $K = 3.5$. The bed is in the Newton-I state. Observe that the vertical distribution of particles is approximately the same at phase angles of (a) 90° and (b) 280°.

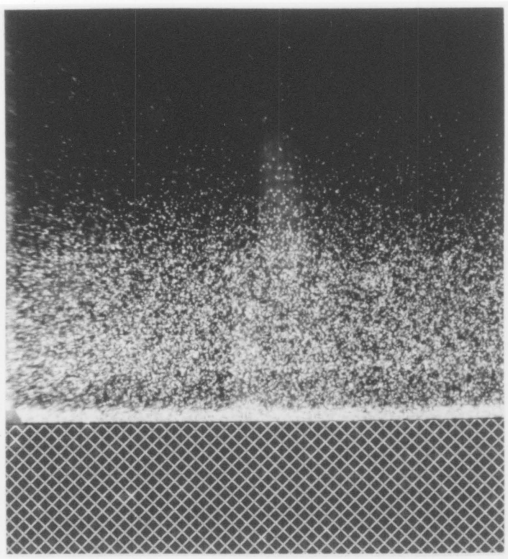

a

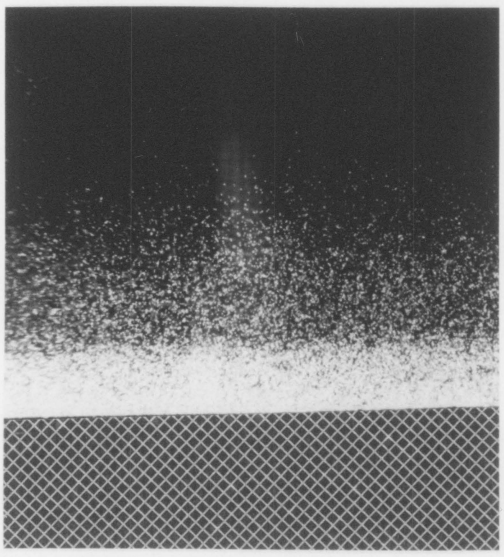

b

Figure 62. **The Newton-II state:** Top-lit photographs of a bed of 88-μm high-density glass spheres, with an equivalent static bed depth of 24 μm, at $K = 4.5$, showing the Newton-II state. (a) At a phase angle of 90°, the dispersion of particles is uniform across the bed height. (b) At 280°, some of the particles have settled to the lower part of the bed, causing a (bright) band of higher particle density.

in Figure 62 on page 234 of a 24-μm deep bed of 88-μm glass particles, particles are uniformly dispersed at a phase angle of 90° (a), but at 280° (b), a portion of the particles have lost sufficient kinetic energy that they form a dense band at the lower region of the bed. All beds that show a Newton-I state also show a Newton-II state, as the bed depth is increased at a fixed value of K.

In the Newtonian state, the kinetic energy of particles is lost through collisions between particles and in some collisions between particles and the vessel floor. Other collisions between particles and the floor result in a transfer of kinetic energy to the particles. The balance between losses and gains in kinetic energy and the effect of aerodynamic drag on the particles determines the persistence of the Newtonian state. As the number of particles in an ultra-shallow bed is increased, the collision frequency increases, and the bed tends to completely collapse at some point in the cycle. In a bed of particles with a high coefficient of restitution (highly "bouncy" particles) such as glass spheres, Newtonian states tend to persist to greater bed depths than in beds of equally sized, but less bouncy particles such as alumina beads. Fine-particle beds exhibit a strong tendency to group together even with bed depths of less than a single particle diameter. As a result, the Newtonian state for fine powders disappears at very shallow bed depths, particularly if the value of K is low. For FCC, there is no Newtonian state present for values of K less than 7, even if the bed depth is as small as 24 μm.

5.7.2 The Coherent-Expanded (CE) State

As the bed depth is increased further, aerodynamic effects become considerable, and the particles in the bed begin to act in concert, lifting off together with a gap appearing below the bed. This is illustrated in Figure 63 on page 236, (a and b) of a bed of 707-μm low-density glass spheres with an equivalent bed depth of 1200 μm at $K = 3.5$, and also in Figure 65 on page 239 — (a) to (d), showing the motion of a 960-μm deep bed of FCC through an entire vibrational cycle. The tran-

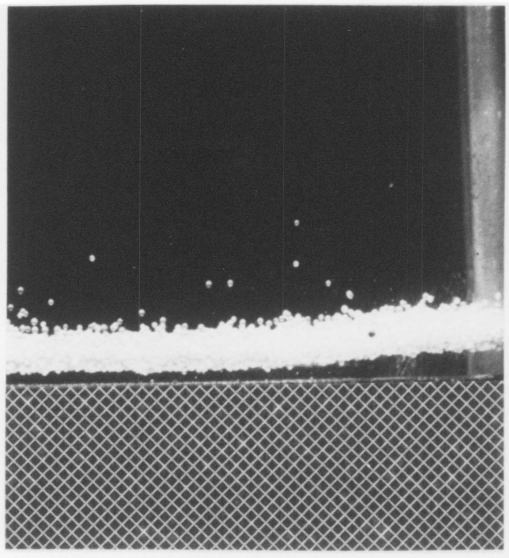

a

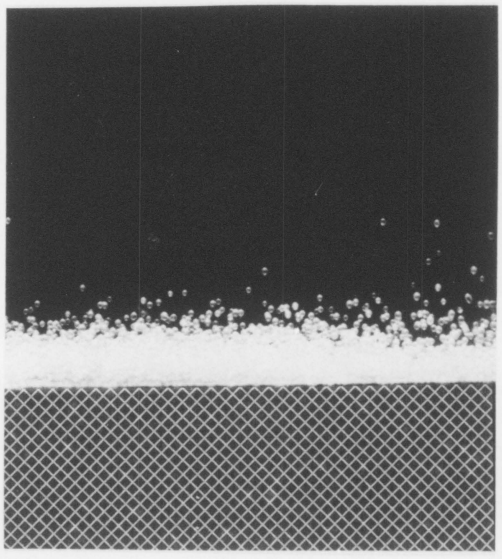

b

Figure 63. The coherent-expanded state in large-particle beds: Top-lit photographs of a bed of 707-μm low-density glass beads with an equivalent static bed depth of 1200 μm, at $K = 3.5$. The bed is in the coherent-expended state. (a) At 180°, while the bed is in flight, it is not very expanded. (b) At 312°, after the bed has collided with the floor, the gas rushing upward significantly expands the bed. Note: The white grid pattern represents the location of the vessel base in this and all subsequent photographs of vibrated bed "states".

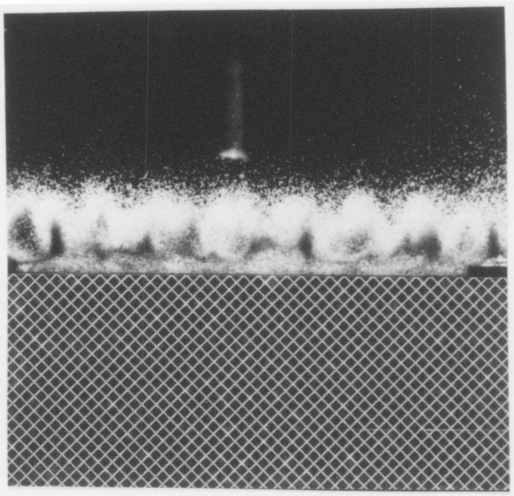

a

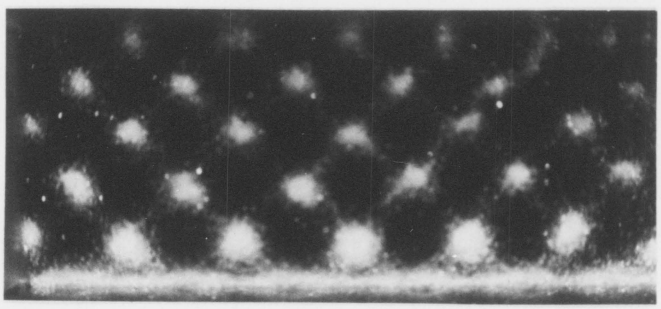

b

Figure 64. **The coherent-expanded state in small-particle beds:** Top-lit photographs of a bed of 177-μm glass spheres, with an equivalent static bed depth of 720 μm, at $K = 4$, showing the bed in the coherent-expanded state. (a) The bed tends to form "spikes" as the gas rushes out of the bed. (b) By looking directly down from above, it can be seen that the spikes (seen as bright circular spots) form a very symmetric pattern. Lighting for (b) was provided from one side source, and as a result, the photograph is brighter on one side than the other.

sition from the Newtonian-II state to this state for a given particle type occurs at slightly greater bed depths as the vibrational intensity is increased.

As shown in Figure 63 on page 236, Figure 64 on page 237, and Figure 65(a)-(d), the passage of gas through the bed, particularly the upward passage as the bed and vessel are forced together, significantly expands the bed, with the degree of expansion being greater for finer particles. Since the bed now acts as a coherent mass, but with a significant expansion, this state can best be described as a ***coherent-expanded (CE) state.***

As described in the Chapter 4 (§4.5), expanded regions in beds of glass spheres show up as very bright bands if top-lighting is used. Dark spikes can be seen in Figure 64(a) of a 720-μm deep bed of 177-μm glass spheres vibrated at $K = 4$, indicating that not all of the bed is expanded at this point in the cycle. However, later in the cycle, when the upward flow of gas is even greater, the dark regions disappear for a small fraction of the cycle. Looking down from above as shown in Figure 64(b), the bed is seen to consist almost entirely of symmetric spikes - the bright circular dots. There is no uniqueness about the symmetry shown in Figure 64(b); sometimes other symmetric patterns have also been observed. With a slightly deeper bed, the spikes join together to form bands as shown in Figure 65(e). The formation of spikes and banded structures are phenomena only found in small-particle beds, and illustrate the tendency of such particles to group together in a flow of gas.

The coherent-expanded state is also characterized by a high degree of turbulent particle motion caused by the violent expansion of the bed in one part of the vibrational cycle. This would recommend the CE state for gas-solid mixing purposes. The optimum value of bed depth for radiant drying reported by Volovik *et al.* [1975] probably represent a coherent-expanded state. The high drying rates reported must have been caused by the rapid exposure of all particles within the bed to the radiant heat source.

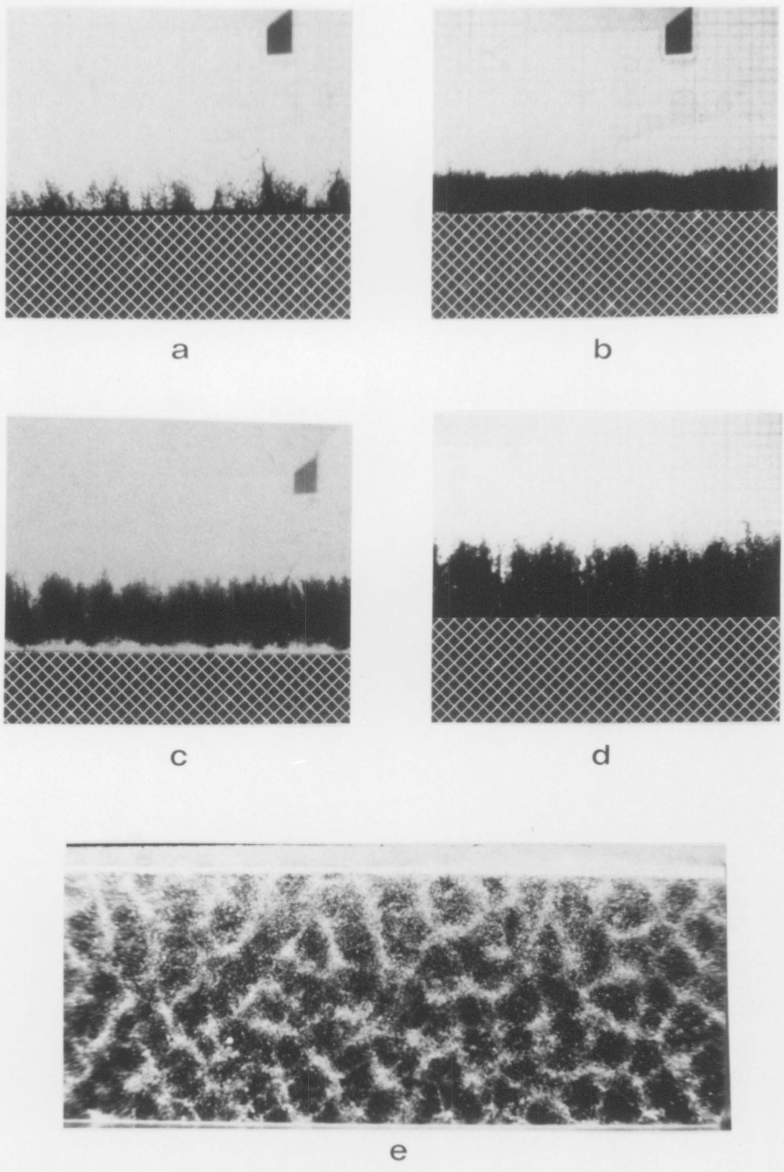

Figure 65. Evolution of a coherent-expanded bed over a vibrational cycle: (a)-(d) Back lit photographs of a bed of FCC with an equivalent bed depth of 960 μm, at $K = 5$, showing the coherent-expanded state at different phase angles in the cycle. (a) 48° - Jets of particles thrown up in the previous cycle. (b) 158° - The bed is lifting off the floor. (c) 253° - As gas rushes out of the bed, it expands it and creates a banded structure. (d) 270° - The bed expands even further and the banded structure, more pronounced. (e) Looking directly down from above at 297° the bands are clearly seen as white wavy lines.

5.7.3 The Coherent-Condensed (CC) State

As the bed depth is increased even further, the degree of bed expansion rapidly decreases. Eventually, the bed becomes largely condensed, that is, the bed porosity changes only by a minute fractional amount through the entire cycle, and the bed as a whole is in a more "packed" state. The bed continues to behave as a coherent mass, leading to a description of the state as ***coherent-condensed (CC)***.

The lower dark regions in a top-lit bed of 177-μm glass beads seen in Figure 66 on page 241 — (a and b), represent the condensed section of the bed. With large particles, the appearance on the condensed state coincides with the complete disappearance of the expanded state; but with small particles, an expanded layer continues to be seen on the top surface of the bed. Although this expanded layer appears thick, it consists of only a few particle layers at the top of the bed. As noted previously, the expanded layer is seen on top of beds of fine particles, because of differences between the drag exerted on the looser top layers and that on the more uniformly packed lower layers by the induced gas flow through the bed.

There is a bulk circulation of particles within the bed once the condensed layer forms. However, particles move much slower, but in more predictable patterns than for the CE bed.

5.7.4 Bunkering

This is not strictly a different state of the vibrated bed since it is essentially a special configuration of the vibrated bed. However, the initial occurrence of bunkering produces marked changes in the vibrated bed. The bed surface is no longer flat, and particles circulate within the bunker with patterns that are determined by the shape of the top surface. Bunkering occurs most commonly in the CC state, but for fine powders, it can also occur in the CE state. As described earlier, small-particle

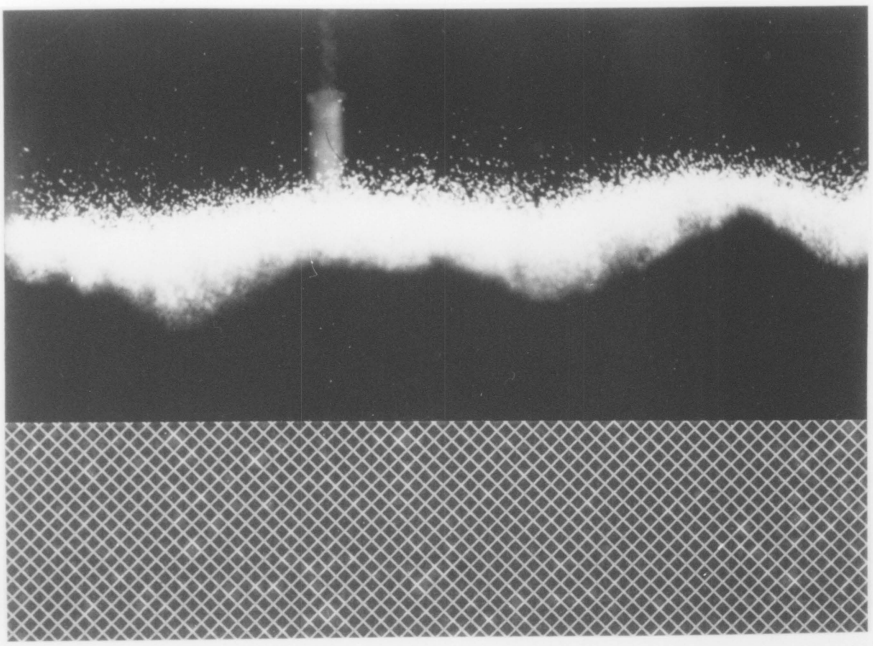

Figure 66. **The coherent-condensed state in small-particle beds:** Top-lit photographs of a coherent-condensed bed of 177-μm glass beads. The condensed bed is the dark lower region of the bed. The bright band on the top of each bed is the expanded zone. At an equivalent bed depth of 1 cm, small-scale bunkers can be seen, some of which are unstable.

beds exhibit a tendency to bunker. As seen in Figure 64 on page 237 and Figure 65 on page 239, fine particles group together to form spikes and bands, even while in the coherent-expanded state. These spikes and bands soon join together to form mounds, particularly at low values of K , and these grow to become bunkers as the bed depth is increased.

With 88-μm particles and FCC, bunkering starts even while the bed is still in the expanded state at low values of K. As will be shown later, this early occurrence of bunkering can cause such beds to prematurely undergo a transition into the coherent-condensed state. The early occurrence of bunkering in fine-particle beds could be due initially to the presence of inter-particle forces such as electrostatic forces. This causes particles in a small locality to group together, forming the "nucleus" of a bunker. Once these clumps have formed, the distortion of the aerodynamic flow field by these clumps causes more particles to enter the "wakes" of the clumps. Once a sufficient number of particles join the clump, differential pressures occur within it, and bunkering results.

When bunkers initially form, they tend to be unstable at values of K greater than 3. Unstable bunkers move about the vessel floor, and appear to be moved by sudden flows of gas that are drawn into the condensed bed close to the lower ends of the bunker. As the size of the bunker grows, it becomes relatively stable, and can either be center-high as shown in Figure 66 on page 241(b) or piled up against a side wall. With small-particle beds, the bunkering remains unstable even at bed depths of 3 cm when $K \geq 5$.

5.7.5 Quantitative Measurements of Factors Affecting State Transitions

As described earlier, observation of the bed at several different values of K while increasing the bed depth in very small increments over a wide range, permits determination of some of the critical conditions under which transitions from one state to another occur. The Newtonian state is possi-

bly only of academic interest; and the transition between Newton-I and Newton-II, although noted in the experimental study, is not discussed any further in this chapter.

Three dimensionless groups Γ, Ψ, and Λ introduced in the discussion of the Kroll and Gutman models, may be written in an alternative form. The permeability term κ, that appears in Γ and Ψ, can be replaced by the Kozeny-Carman expression for the bed permeability given by equation [5.6]. The bed density term ρ_b, in Λ can be written as $\rho_s(1-\varepsilon)$. With these substitutions, the dimensionless groups may be rewritten as:

$$\Gamma = \left[\frac{P_o \varepsilon^2}{180(1-\varepsilon)^2 \mu\omega} \right] \left(\frac{d_p}{L} \right)^2 \qquad [5.51]$$

$$\Psi = \left[\frac{P_o \varepsilon^3}{180(1-\varepsilon)^2 \mu\omega} \right] \left(\frac{d_p}{L} \right) \left(\frac{d_p}{a_o} \right) \qquad [5.52]$$

$$\Lambda = \left[\frac{P_o}{\rho_s(1-\varepsilon) d_p a_o \omega^2} \right] \left(\frac{d_p}{L} \right) \qquad [5.53]$$

Therefore, logarithmic plots of these three dimensionless groups as functions of the dimensionless bed depth, expressed as the number of particle layers (L/d_p), will be straight lines if all other factors are kept constant. In addition, if properties of the fluid and the frequency of vibration are kept constant, logarithmic plots of Ψ versus L/d_p will appear as a family of straight lines, with a_o/d_p as the parameter.

The transitions in bed behavior that are dependent on the aerodynamics of the flow of gas through the bed might possibly be expressed in terms of these three dimensionless groups. This follows because combinations of these groups govern the magnitude of the pressure fluctuations below the bed, the linearity of pressure gradients in the bed, the velocity of the gas flowing through the bed, and the drag exerted on the bed by the gas flow.

Newtonian to Coherent-Expanded

The transition between these two states is determined not just by the aerodynamics of the bed, but also by the rate at which particles within it loose kinetic energy, and tend to group together. The transition is therefore probably dependent on some particle properties. However, for glass beads, which have a high coefficient of restitution, it was found that the bed is always in a coherent-expanded state when the bed depth exceeds 1.5 for $K = 6$. The transition occurs slightly sooner at lower values of K, and for fine-particle beds.

Coherent-Expanded (CE) to Coherent-Condensed (CC)

The dimensionless group that seems to best describe this transition is Ψ . The group Γ describes the effect of gas compressibility. Since transitions from CE to CC occur at ultra-shallow bed depths, it is unlikely that gas compressibility is a factor that needs to be considered. Figure 67 on page 245 shows a logarithmic plot of Ψ as a function of the bed depth in number of particle layers (L/d_p) , at constant values of a_o/d_p . As mentioned previously, these are a family of straight lines, and are seen as dashed lines in Figure 67 on page 245. For a given particle size, each dashed line then represents a line of constant vibrational amplitude, and if the frequency is fixed, lines of constant K .

Transitions from the CE to CC state appear as a series of parallel lines with the position of the line dependent on the particle size. The data points shown in Figure 67 on page 245 for each particle size, represent the transition at values of K of 2.5, 3, 4, 5, and 6. For either particle sizes of 707 μm or 177 μm, transitions occur at exactly the same bed depth for both high- and low-density glass beads. For 88-μm beads, transitions for the two densities of glass beads are not at coincident values of bed depth when $K \geq 3$, and are represented as two closely spaced parallel lines. Note that transitions for low-density 88-μm glass beads occur in a slightly shallower bed than for 88-μm high-density glass beads at the same value of K. It is not clear if this is truly an effect of the dif-

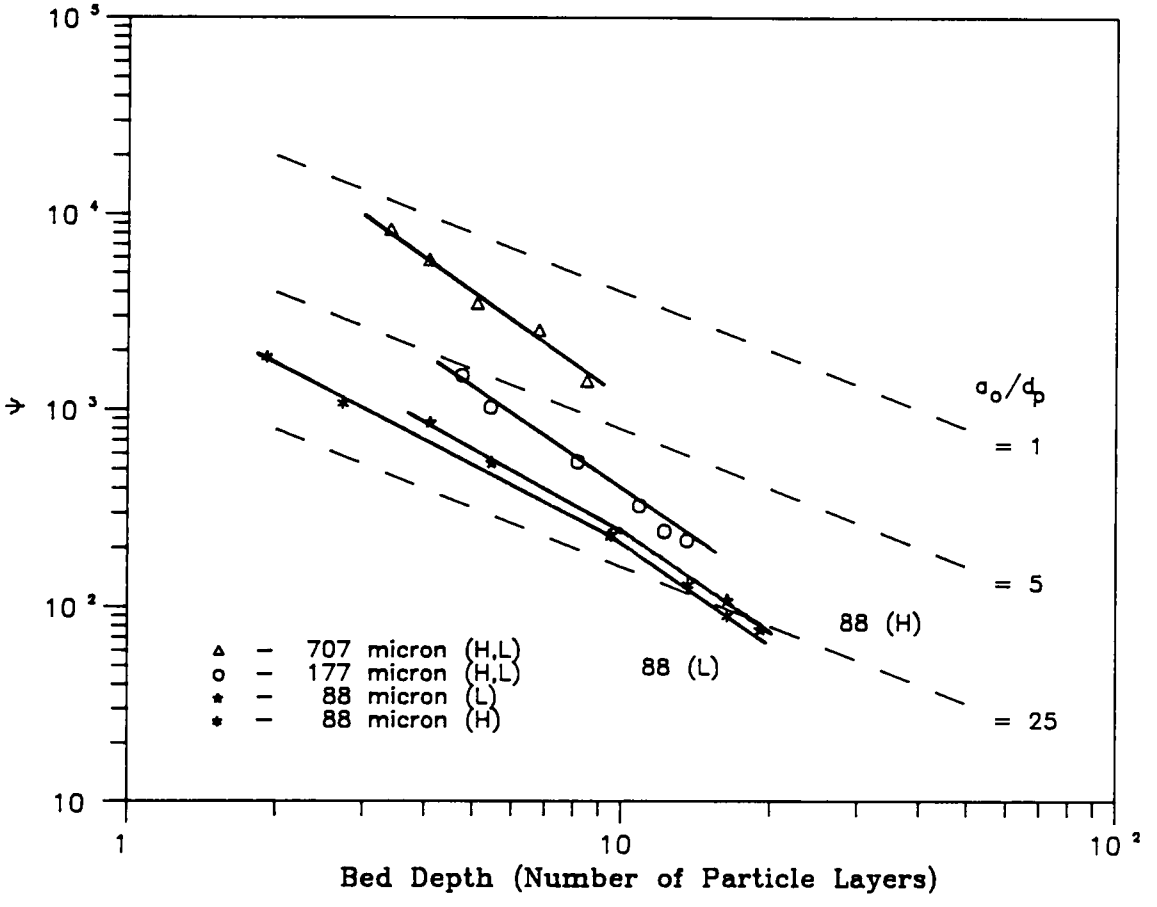

Figure 67. Transitions from the coherent-expanded to coherent-condensed state: Data representing the transition between CE and CC states for three sizes of glass beads. The solid lines represent the loci of transitions, and are fitted to the data points shown. Moving down from upper left to lower right along any transition line, represents increasing values of K. Note that the lower sections of the transition lines for 88-μm particles are parallel to the lines for 177- and 707-μm beads. (H = high-density glass beads; L = low-density glass beads).

ference in densities, but it is more likely due to the presence of electrostatic charges fine-particle beds. This is particularly a problem with low-density glass beads, causing them to stick to the walls of the vessel. As seen in Figure 67 on page 245, transitions occur prematurely at lower values of K ($K < 3$) for 88-μm beads. This premature transition can be explained in terms of the bed bunkering and will be dealt with in the next section.

The fact that transitions for a given particle size fall on the same line regardless of the density (the small difference in 88-μm beads is more probably caused by electrostatic effects than by differences in densities), suggests that the range of solid densities used in this study for determining the transitions, is not significant enough to influence the CE to CC transition. Since Λ mainly determines the effect of particle density on the transition, no useful purpose would be served by plotting the transitions as a function of this dimensionless group (at least, for the range of solid densities used in this study).

Occurrence of Bunkering in the Bed

Figure 68 on page 247, Figure 69 on page 248, and Figure 70 on page 249show both transitions from the CE to CC states (solid lines) and the onset of bunkering in the beds (thick dashed lines in Figure 68 on page 247 and Figure 69 on page 248)

With 88-μm particles (Figure 68 on page 247) bunkering is observed to occur at shallower bed depths with low-density glass beads than with high-density glass beads. If the transition to bunkering is compared with the transition from the CE to CC state, the premature transitions at lower K can be explained. Note that for simplicity, only a single solid line has been drawn in Figure 68 on page 247to represent transitions from the CE to CC state at higher values of K. This is not strictly correct, but is an average of the two closely spaced parallel lines shown in Figure 67 on page 245, and will serve to illustrate the point. The dotted line is an extension of this line, and represents the transitions from the CE to CC state that would be expected at lower values of K if transitions at higher values of K were extrapolated downward. It can be seen that if bunkering

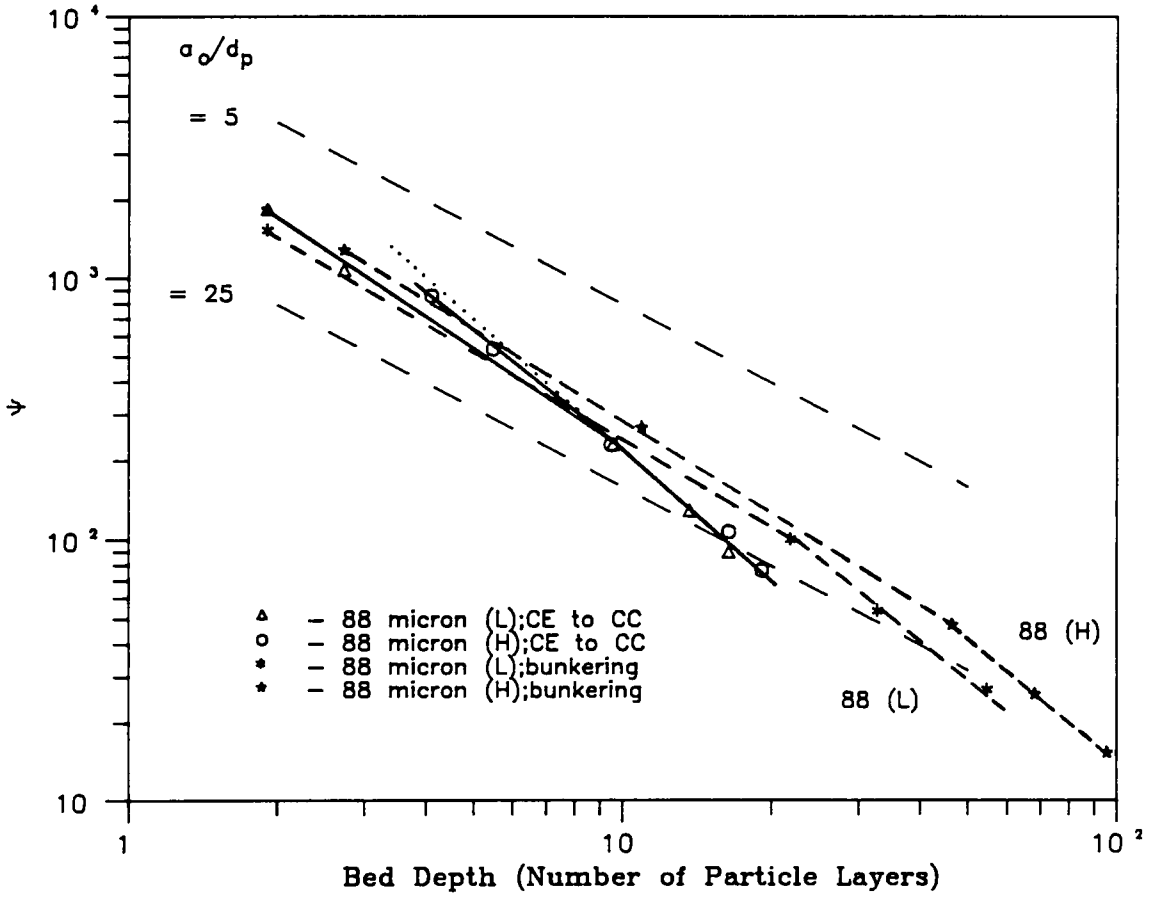

Figure 68. The CE to CC transition and the start of bunkering in 88-μm glass beads: The start of bunkering (thick dashed lines), and the transition from the CE to CC state (thick solid lines) for 88-μm glass beads. Only a single solid line which represents an "average" of the transitions for the two particle densities is shown for $K > 3$. The dotted line is an extrapolation of this solid line, and represents transitions from the CE to CC state that would be expected at lower values of K based on the data at higher K-values. (H = high-density glass beads; L = low-density glass beads).

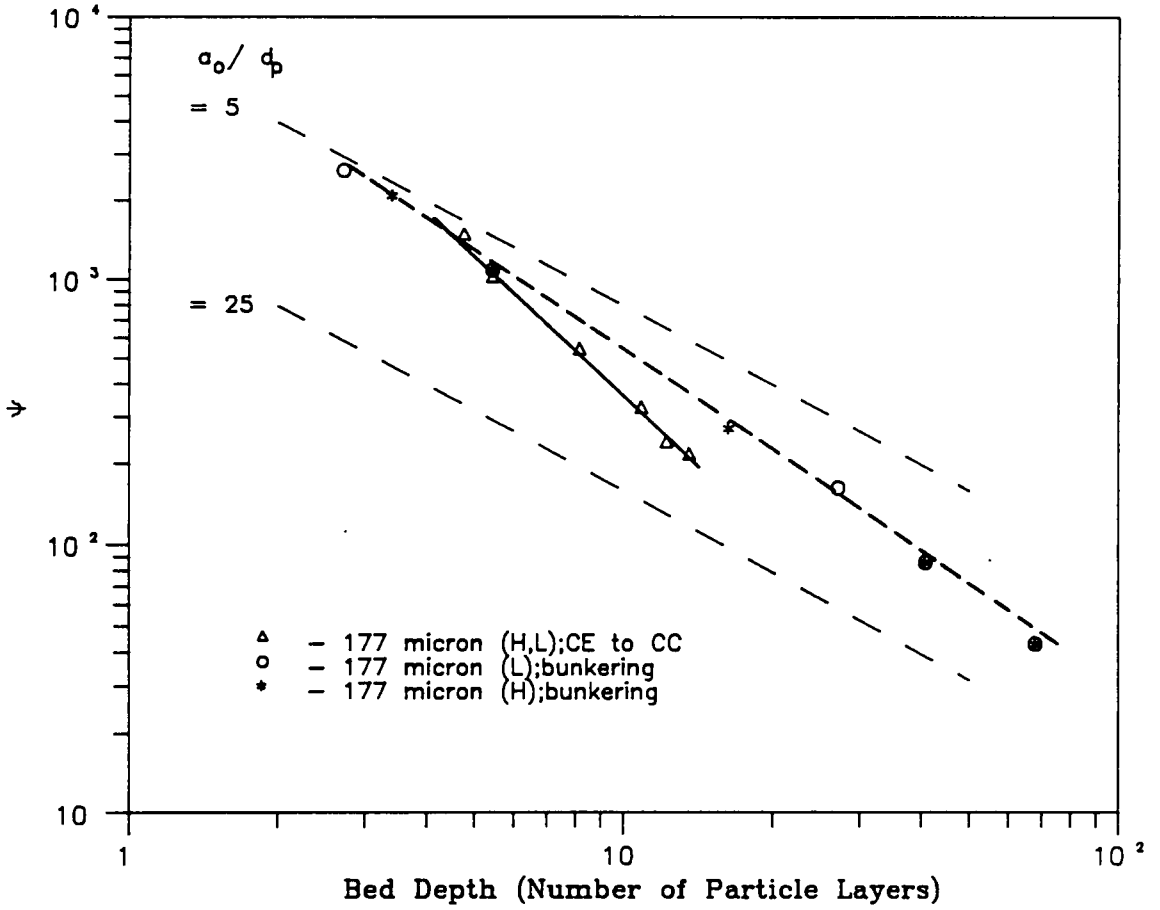

Figure 69. The CE to CC transition and the start of bunkering in 177-μm glass beads: The start of bunkering (thick dashed line), and the transition between the CE and CC state (thick solid line) for 177-μm glass beads. (H = high-density glass beads; L = low-density glass beads).

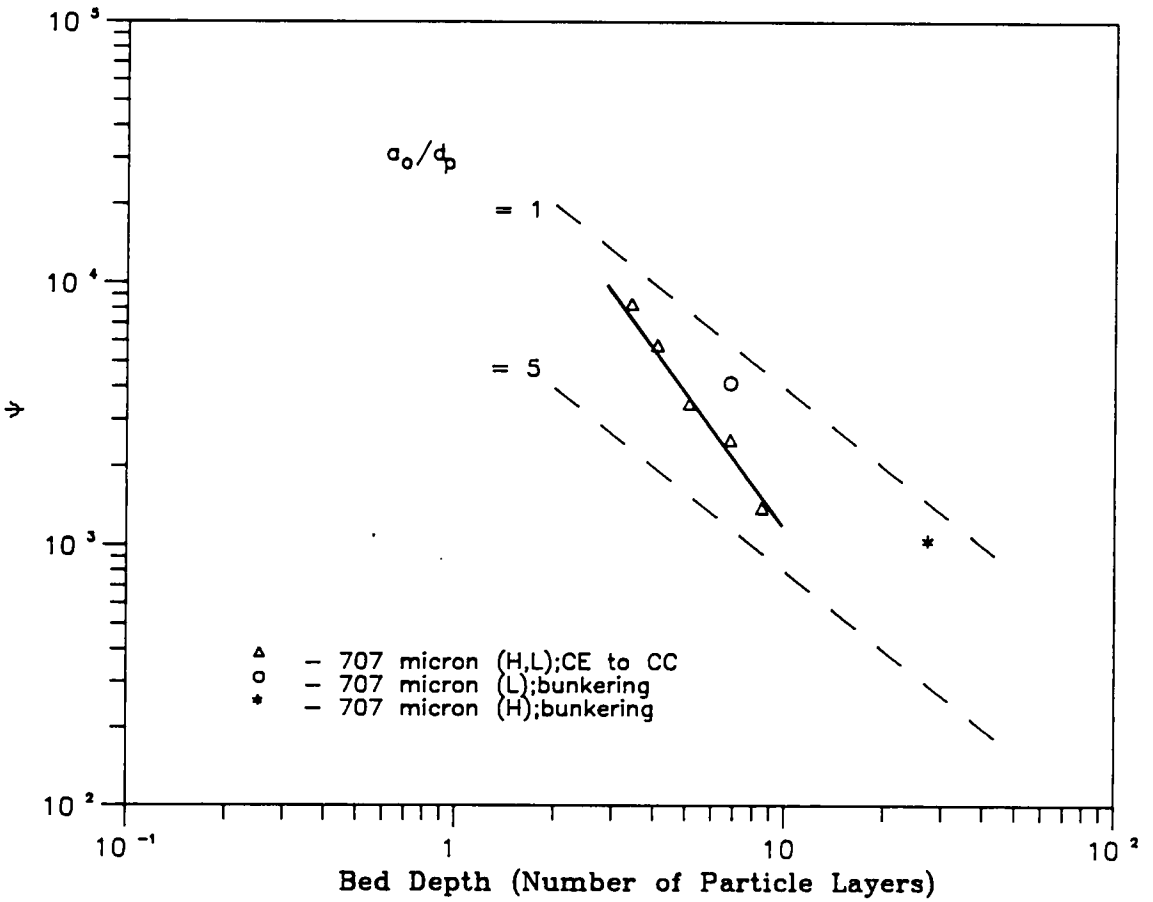

Figure 70. The CE to CC transition and the start of bunkering in 707-μm glass beads: Occurrence of bunkering and the transition between the CE and CC state (thick solid line) for 707-μm glass beads. There are only two points at which bunkering is observed for this particle size. (H = high-density glass beads; L = low-density glass beads).

occurs before the expected transition from a CE to a CC bed, the CE to CC transition will be premature. What this means in physical terms is that bunkering in these beds starts even when the bed is quite shallow, because of the tendency of fine powders to group together. Once bunkering starts, the bed under each small bunker in the bed quickly becomes condensed, thus causing a premature transition to the CC state. This set of events is also observed in practice.

As the bed passes a certain depth, bunkering becomes more rapid and almost assured for this particle size, and is represented by a transition to a steeper slope in the dashed lines representing the onset of bunkering.

For 177-μm glass beads (Figure 69 on page 248), the bunkering line and the CE to CC transition line intersect at $K = 2.5$. This means that in all probability, the CE to CC transitions at values of K lower than 2.5 will be premature for this particle size. It should be noted that the onset of bunkering at a fixed value of K does not always occur at the same value of bed depth for the two densities of glass beads used. However, at least half of the points are coincident, and it is possible that errors in judgment on the occurrence of bunkering in the bed probably account for the points that are not coincident.

With 707-μm glass beads (Figure 70 on page 249), bunkering only occurs for K values of 2.5 or less, for bed depths up to 3 cm. For the high-density glass beads, there is only mild bunkering at these low values of K, and then only in a relatively deep bed.

5.7.5.1 Further Notes on Quantitative Measurements

In this study, transitions between different states have been detected by a visual technique. This calls for some judgment in determining whether a transition in states has occurred, and is particularly a problem since some transitions occur when the bed depth is increased by only a few particle layers. Even so, the transitions are found to be interpolated satisfactorily by straight lines. However, the

accuracy and ease of determining a transition could be improved if a less subjective technique were used. A method to do this will be suggested in Chapter 7.

For the range of conditions covered in this study, the difference in densities between the two types of glass beads used does not appear to be sufficient to produce differences in transition points for a given particle size, other than for the 88-μm particles. Even for this size, the differences are slight and are probably caused by the presence of electrostatic charges, which are more problematic in 88-μm low-density glass beads. This does not mean that the solid density is unimportant. Obviously differences between light plastic and copper particles of the same size, for example, would most probably show up, even within the range of other conditions considered in this study. In that case, additional plots of Λ (which contains the solid density) as a function of bed depth would also be necessary.

It should be emphasized that the method of quantitatively representing transitions between different states adopted in this study, is only a first attempt at producing a quantitative description of the transitions, and is included primarily to show that the transitions between vibrated-bed states is quantifiable. It is possible that there are other combinations of dimensionless groups which will better describe the transitions.

5.8 The Basis of a More Comprehensive Model

In this section, requirements for a comprehensive model of the vibrated bed that include some factors left out of previous models, but which this study shows are important, will be discussed. Because of a lack of complete data, the model cannot be solved here. The mathematical treatment of the vibrated bed in this section must only be regarded as laying the ground-work for further quantitative analysis of the bed.

A more comprehensive model must include most importantly, for two additional features not included in current models.

1. The model must include more than one dimension. For most beds, symmetry will allow a treatment of two dimensions, instead of three.
2. It should include the effects of bed expansion. The porosity of the bed is a function of both time and space.

5.8.1 Mathematical Analysis

Consider an elemental volume of the bed which is sufficiently small that at any given instant, there are negligible spatial variations of the local porosity across it. The average porosity of a small volume that includes only two particles would not vary across the volume at any given instant. Let this local porosity be designated ε_v since it varies with time and spatial position within the bed. An equation of continuity for the flow of gas through this volume can be written as:

$$\frac{\partial(\varepsilon_v \rho)}{\partial t} = \nabla(\varepsilon_v \rho u_i) \qquad [5.54]$$

where u_i is the interstitial velocity of the gas in the bed. A localized form of Darcy's equation, such as that used for compressible filter cakes [Ward,1987], is:

$$u_i = -\frac{\kappa_v}{\mu \varepsilon_v} \nabla P \qquad [5.55]$$

where μ is the gas viscosity. Since the porosity is time- and space-variant, the permeability κ_v represents a localized permeability constant. κ_v varies both with time and spatial position. Substituting for the interstitial velocity in the equation of continuity gives:

$$\frac{\partial(\varepsilon_v \rho)}{\partial t} = -\frac{1}{\mu} \nabla[\rho \kappa_v \nabla P] \qquad [5.56]$$

From ideal gas theory, $\rho = (\rho_o/P_o)P$, where ρ_o is the gas density at (atmospheric) pressure P_o . Substituting in equation [5.56] for the density and expanding gives:

$$P\frac{\partial \varepsilon_v}{\partial t} + \varepsilon_v \frac{\partial P}{\partial t} = -\frac{1}{\mu}\left[\kappa_v(\nabla P)^2 + P\nabla\kappa_v\nabla P + P\nabla\kappa_v\nabla^2 P\right] \qquad [5.57]$$

Assuming small changes in P as in the one-dimensional model, $\kappa_v(\nabla P)^2 \ll P\kappa_v\nabla^2 P$ and $P \simeq P_o$. Therefore:

$$P_o\frac{\partial \varepsilon_v}{\partial t} + \varepsilon_v \frac{\partial P}{\partial t} = -\frac{P_o}{\mu}\left[\nabla\kappa_v\nabla P + \kappa_v\nabla^2 P\right] \qquad [5.58]$$

This equation cannot be solved any further without a knowledge of $\varepsilon_v = f(x,y,z,t)$. Such a function for ε_v will also determine κ_v at any location at any given instant.

Variations in Bed Porosity

If porosity variations are negligible, $(\partial\varepsilon_v/\partial t) \to 0$, $\nabla\kappa_v \to 0$, and equation [5.58] becomes a three-dimensional equivalent of the Gutman model. If the bed is not bunkered, the model reduces to the one-dimensional Gutman equation, as is the case with large-particle beds. Furthermore, with such beds, gas-compressibility effects are negligible, and the Kroll model suffices.

The phase lag between the instant of lift-off calculated from the Gutman model and the observed separation of the bed from the vessel floor suggests that the bed does not lift-off the vessel floor as soon as the sum of forces on the bed equals zero, as assumed by the rigid-mass model. Instead, the bed expands while the gas is flowing into it. It barely remains in contact with the vessel floor, so that the normal force on the bed is equal to zero during this period. When the bed has expanded by some amount $\delta\varepsilon$, it separates from the vessel floor. It is possible that this expansion is that required to permit motion of particles over one another. An estimation of $\delta\varepsilon$ using measured pressures and the one-dimensional Gutman model (§5.2.7) shows that the increase in porosity required to cause the phase lag in the observed bed-vessel separation is small (in the order of 1 to 2 percent).

If the bed expansion in the period between the instants of null force on the bed and bed-vessel separation may be assumed to be uniform over the whole bed, ε_v will be a function of time alone. Methods for experimentally determining $\varepsilon_v = f(t)$ are discussed later in this section. With a knowledge of this function, equation [5.58] can be solved in the period between the null-force instant and the instant of bed-vessel separation.

While the bed is in flight, but before it starts to collide with the vessel floor, the bed expansion is determined by the variation of drag forces on different sections of the bed. If the effect of gas compressibility is large, the pressure gradient across the bed will be highly nonlinear as shown in Figure 25 on page 128. When the bed is considered to be nonrigid, the nonlinear drag forces resulting from these pressure gradients, will cause differences in the acceleration of different spatial locations within the bed, that is, tensile stresses are set up within the bed structure. These stresses cause a relative motion of each location within the bed, resulting in bed expansion. The spatial variation in porosity will lead to further variations in drag forces across the bed, and so on.

The value of the compressibility factor Γ, at which this occurs must represent the point at which the (one-dimensional) Gutman model breaks down, since that model is based on a porous rigid-mass assumption. Gutman [1974,1976a] has suggested that his model breaks down when $\Gamma < 0.125$ based on experimental evidence. Examination of Figure 25 on page 128 shows that this value of Γ represents a considerable deviation from a linear pressure gradient. Values of Γ for the beds and vibrational conditions used in this study are larger than this value. Observation of the bed shows that when compressibility effects cause a significant deviation of the pressure gradient from linearity, the bed no longer lifts off the vessel floor through the entire vibrational cycle for vibrational intensities under which it maintains a stable configuration. Although it is always possible to increase the vessel acceleration to the point at which such a bed lifts off the floor, the bed will be extremely unstable, swinging from side-to-side within the vessel. It is possible to obtain the expansion of a bed due to the differential pressure gradients through it by performing force balances on elemental volumes within the bed and integrating over the whole bed. This is facilitated by the simplicity of the lower boundary condition ($\partial P_z / \partial z = 0$) if the bed remains in contact the vessel floor

through the entire vibrational cycle. Another approach would be to model the bed as a viscoelastic mass. However, the analysis of vibrated beds with highly nonlinear pressure gradients will not be pursued any further in this study.

There is a differential drag force acting on the expanded zone on the top surface of the bed as described earlier. However, this zone constitutes such a minute fraction of the bed mass (provided the bed is more than a few millimeters deep) that the differential motion of particles in this zone relative to the rest of the bed has only a negligible effect on the motion of the center of gravity of the bed. The dynamics of the expanded zone is affected by the dynamics of the condensed zone below it, but not vice versa. The mechanics of the expanded zone may be treated as a separate problem which depends of the solution of the model for the condensed zone.

5.8.1.1 Boundary Conditions and Equations of Motion

The three-dimensional problem can be somewhat simplified if only symmetric configurations are considered. Because of the symmetry of the bed about its center line, only one half need be considered. Figure 71 on page 256 shows the four boundaries that must be considered. Because of bunkering, each boundary is not necessarily normal to its adjacent neighbors.

At the wall, since there is no flux across the wall:

$$\left.\frac{\partial P_x}{\partial x}\right|_{x=R} = 0 \qquad [5.59]$$

where R is the half-width of the bed in the major horizontal direction. At the center of the bed, symmetry gives:

$$\left.\frac{\partial P_x}{\partial x}\right|_{x=0} = 0 \qquad [5.60]$$

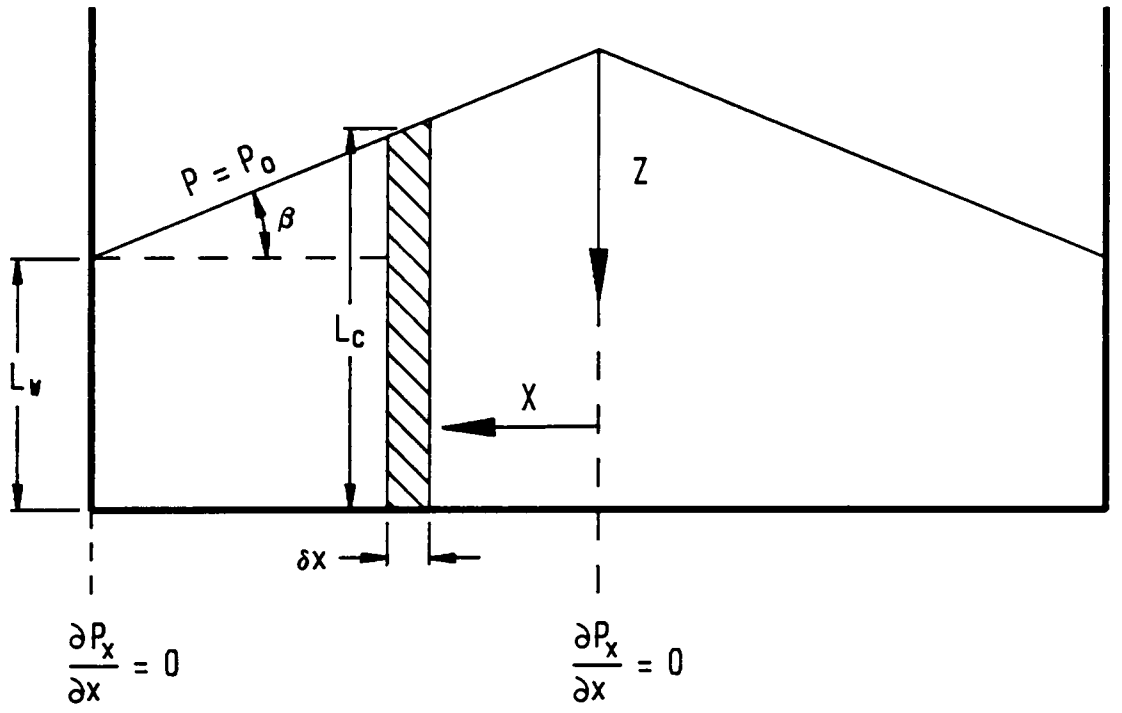

Figure 71. Schematic representation of the bed for the multi-dimensional model: The bed is symmetric in the third dimension, so only two dimensions need be considered. With center-high bunkering, only one half of the bed need be considered. Notation: P - pressure; P_o - atmospheric pressure; $(\delta P_x/\delta x)$ - horizontal pressure gradient; z - vertical ordinate; x - horizontal ordinate. The width of the bed is w_b (into the plane of the paper).

Along the (sloped) top surface:

$$P = P_o \qquad [5.61]$$

The slope of the top surface is given by:

$$\beta = \upsilon - \sin^{-1}\left(- \frac{\sin \upsilon}{\rho_b g} \frac{\partial P_n}{\partial n} \right) \qquad [5.49]$$

The normal pressure gradient at the surface ($\partial P_n/\partial n$), is the resultant of horizontal and vertical pressure gradients at the surface.

The boundary condition at the lower boundary depends on whether the bed is in flight, or is in contact with the vessel floor. If the bed is in contact with the floor, the condition that there is no flux of gas across the floor leads to:

$$\left. \frac{\partial P}{\partial z} \right|_{z = L_x} = 0 \qquad [5.62]$$

where L_x is the depth of the bed at any horizontal location x. By referring to Figure 71 on page 256, it is seen that the depth of the bed at any point is given by:

$$L_x = L_w + (R - x) \tan \beta \qquad [5.63]$$

where L_w is the depth of the bed at the wall (not including the gap).

As stated above, experimental observation shows that for all practical purposes, a gap will appear at the bottom of the bed only if the pressure gradient through the bed is linear ($\Gamma > 0.125$). Under these conditions, it can be assumed that porosity variations during the flight period are negligible, and a simplified form of equation [5.58] can be used during this period. The porosity during the flight period can be written as ε, and the permeability as κ.

Suppose that a gap of thickness s_x has formed at a given time t at a horizontal location x beneath the bed. Consider a small horizontal area along the bottom of the bed of thickness δx, as shown in Figure 71 on page 256, which is small enough that the thickness of the gap does not vary between x and $x + \delta x$. If variations in the y-coordinate can be neglected, the width of the area may be taken as w_b, the width of the bed in the y-direction. The mass flow rate of gas across this area into the gap is:

$$\delta x w_b \rho u = -\delta x w_b \rho \frac{\kappa}{\mu} \left.\frac{\partial P}{\partial z}\right|_{z=L_x} \qquad [5.64]$$

The vertical pressure gradient in the gap can be assumed to be zero. As there are no particles within the gap, the resistance to flow within it is negligible compared to that in the bed, so this is a reasonable assumption.

Consider a small volume within the gap immediately below this area, whose cross-sectional area is also $\delta x w_b$. The height of the volume is s_x The elemental volume is bound on three sides by solid walls through which there can be no flow. The top surface is bound by the bed, and the flow into this top surface equals the flow rate of gas across the bed-gap boundary. A mass balance across the volume can be written as :

$$w_b \delta x \frac{\partial (s_x \rho_x)}{\partial t} = w_b s_x \left[\rho u|_x - \rho u|_{x+\delta x}\right] - w_b \delta x \rho \frac{\kappa}{\mu} \left.\frac{\partial P}{\partial z}\right|_{z=L_x} \qquad [5.65]$$

where ρ_x is the gas density at the location x beneath the bed. Dividing through by $w_b \delta x$ and taking the limit as $\delta x \rightarrow 0$:

$$\frac{\partial (s_x \rho_x)}{\partial t} = s_x \frac{\partial (\rho_x u_x)}{\partial x} - \rho_x \frac{\kappa}{\mu} \left.\frac{\partial P}{\partial z}\right|_{z=L_x} \qquad [5.66]$$

This equation of continuity contains the horizontal velocity of the gas, u_x, within the gap. If an inviscid flow of gas is assumed, there will be no velocity gradients in either the vertical direction, or along the width of the bed (the y- direction). In addition, if pressure variations are small,

$(\partial\rho/\partial t) \ll (\partial S_x/\partial t)$ and $\rho \rightarrow \rho_o$ With these simplifications, the equation of continuity for the flow of gas in the gap becomes:

$$\rho_o \frac{\partial s_x}{\partial t} = s_x \frac{\partial(\rho u_x)}{\partial x} - \rho_o \frac{\kappa}{\mu} \left.\frac{\partial P}{\partial z}\right|_{z=L_x} \qquad [5.67]$$

The gap thickness s_x can be obtained by considering a force balance on the bed. As stated above, this analysis is restricted to beds which do not undergo significant porosity variations during the flight period. Therefore, a thin vertical slice across the bed of horizontal thickness δx can be considered as shown in Figure 71 on page 256. By making δx small enough, the horizontal pressure gradient across the strip can be neglected in comparison with the vertical pressure gradient. Although particles move in and out of this strip, the net quantity of mass within the strip remains constant with time. Thus, the motion of the center of gravity of the strip is only affected by the vertical trajectory of the strip. The trajectory of the strip at any instant is equal to the sum of the thickness s_x of the gap and the vertical displacement a of the vessel. Since only cases where the pressure gradient is not severely nonlinear are being considered, the drag force on the entire strip can be written in terms of the overall pressure gradient across it. A force balance similar to that for a one-dimensional bed can be written for the strip:

$$\frac{d^2 s_x}{dt^2} = a_o \omega^2 \sin(\omega t) - g + \frac{P_{Lx} - P_o}{\rho_b L_x} \qquad [5.68]$$

where P_{Lx} is the floor pressure at the horizontal location x . By combining equations [5.68] with equation [5.67], the lower boundary condition can be written for the bed while it is flight, and *before* the bed-vessel collision starts:

$$\frac{1}{P_o} \frac{\partial}{\partial t}\left(s_x \frac{\partial}{\partial x}(P_{Lx} u_x)\right) - \frac{\kappa}{\mu} \frac{\partial}{\partial t}\left(\left.\frac{\partial P}{\partial z}\right|_{z=L_x}\right) = a_o \omega^2 \sin(\omega t) - g + \frac{P_{Lx} - P_o}{\rho_b L_x} \qquad [5.69]$$

This is a difficult boundary condition to use, even though several simplifications are included. Note that it contains the term $(P_{Lx} u_x)$. This term cannot be directly written in terms of a horizontal pressure gradient through the use of the Hagen-Poiseuille law, because of the unsteady-state nature

of this problem. If the flow is inviscid, the Euler approximation to the equation of motion applies [Bird *et al.*,1960], and $\partial(P_{Lx}u_x)/\partial x$ can be written in terms of $(\partial u_x/\partial t)$ and $(\partial P_{Lx}/\partial x)$. Even so, the boundary condition is complex, since it is in itself an unsteady-state boundary-value differential equation. So far this analysis has not included the additional complications of the bed-vessel collision process, which can no longer be treated as an instantaneous event in the two-dimensional system. Nor has it included the effects of a highly nonlinear pressure gradient.

5.8.2 A Semi-Empirical Approach to Modeling the Bed

It is debatable whether any useful purpose will be served by solving a model as complex as the one discussed above. It is perhaps more useful to adopt a semi-empirical approach to describing the two-dimensional vibrated bed.

With such an approach, floor pressures at the bottom of the bed are directly measured at three different horizontal locations over one vibrational cycle. If the bed is symmetric about a center line, pressure measurements can be made in one half of the bed. The gas-flux conditions give $(\partial P_L/\partial x) = 0$ at the wall and center. Floor pressures can be interpolated as a function of horizontal location x at any given instant by using an cubic spline interpolating function $P_x^{(3)}$, which will be unique, given the boundary conditions and the pressures at three locations. Obviously if floor pressures are measured at more than three horizontal locations, the interpolating function will be more accurate.

Owing to its highly periodic form, the floor pressure at each horizontal location can be related to the phase angle of vibration by representing it as a Fourier series of the form:

$$P(\theta) = \frac{c_o}{2} + \sum_{j=1}^{n}(c_j \cos j\theta + d_j \sin j\theta) \qquad [5.70]$$

The Fourier coefficients c_o, c_1, ... , c_n, and d_1, ... , d_n can be determined from the experimental data.

These two interpolating functions give an empirical description of the lower boundary condition at all times during the cycle. Equation [5.58] can now be solved over the whole cycle to give the pressure at any point within the bed, and as a consequence, gas velocities. The equation of motion for each horizontal location within the bed can be solved using the measured pressures to give the gap thickness as a function of the horizontal ordinate x and time. By using the solution of the equation of motion in equation [5.67], gas velocities within the gap may also be obtained.

The semi-empirical approach requires the measurement of pressures at least at three locations along the floor, but when compared to the mathematical effort required to solve the two-dimensional model in its analytical form, even with several simplifying assumptions, it is a practical attractive engineering approach that yields all the aerodynamic information necessary. Once gas velocities have been estimated, particle circulation rates may also be obtained.

5.8.2.1 Estimating Bed Expansion by the Semi-Empirical Method.

The expansion of the bed during the process of lift-off (the period between the instant at which the net force on the bed equals zero and the actual separation of the bed and vessel floor) can be estimated by solving the model with measured pressures to obtain the instant of null-force, and calculating the net flow of gas between this instant and the experimentally observed instant of bed-vessel separation. If the bed expands at the same rate at which the gas flows into it, it barely remains in contact with the vessel floor, and the gap size may be assumed to be equal to zero during this period. By equating the rate of bed expansion to the rate at which gas flows into the bed, the total bed expansion during this period, $\delta\varepsilon$, may be calculated. Furthermore, if the bed is assumed to expand uniformly during this period, $e_\varepsilon = f(t)$ may also be obtained.

As the bed collides with the vessel floor, a compaction wave passes through the bed, The semi-empirical solution through use of the equation of motion will determine the horizontal component of the wave propagation velocity. However, the vertical propagation velocity must be experimentally determined. Since the collision process reverses the expansion of the bed during the "lift-off" period, the difference in porosity across the wave is $\delta\varepsilon$.

5.9 Summary

The most important results regarding aspects of vibrated bed dynamics covered in this study, may be briefly summarized as follows:

1. Both Kroll and Gutman models may be written in dimensionless form for easy manipulation

2. Floor pressures measured beneath the bed show the same cyclic features as those obtained in previous studies.

3. Floor pressures are found to vary with horizontal position in small-particle beds which are not very permeable to gas flows. In other words, a horizontal scale-effect on floor pressures is noted.

4. When horizontal pressure gradients develop within a bed, they give rise to bed bunkering, in which the bed piles up unevenly within the vessel. Three types of bunker configuration can occur: a center-high configuration, a wall-high configuration, and a center-shallow configuration.

5. The angle of bunkering appears to be determined by the horizontal and vertical pressure gradients that develop across the top surface of the bed, as the bed collides with the vessel base.

6. In bunkered beds, particle motion which is driven by horizontal interstitial gas flows, takes place only while the bed is in flight. The direction of particle motion is from shallow regions of the bed toward deeper regions, except for a narrow region along the bed surface where particles return to the shllow section of the bed.

7. In non-bunkered beds, particle motion is downward at the walls within two or three wall-adjacent particle layers, and upward everywhere else. Particle motion is driven by wall-friction effects.

8. The observed instant of bed-vessel separation lags the theoretical instant of bed lift-off by several degrees. This is most probably due to a slight expansion of the bed while it attempts to separate from the vessel floor.

9. The bed does not collide uniformly with the vessel floor. Instead, the bed-vessel collision occurs first at the vessel walls, and last at the center of the bed. As the bed collides with the floor a compression wave is observed to travel diagonally through the bed. Behind the compaction wave the bed enters a packed immobile state, and remains that way until the following vibrational cycle.

10. Beds of fine aeratable powders do not collapse into a packed form by the end of one vibrational cycle. As a result they continue to draw in air and expand over several cycles. Finally, a critical volume is reached when the gas within the bed is suddenly expelled with one vibrational cycle.

11. An expanded zone is observed along the top surface of small-particle bunkered beds. The expanded zone is formed by differential drag effects on the top-most particle layers which are more loosely packed than the rest of the bed.

12. Different "states" of the vibrated bed are identified. Each state has a unique set of characteristics that differentiate it from other vibrated-bed states.

13. The two-dimensional model is difficult to solve for two reasons:

    a. the unsteady-state nature of the gas flow within the air gap beneath the bed, and
    b. the expansion of the bed is largely unknown.

    Instead of solving the model in a purely analytical form, it might be easier to employ a semi-empirical technique that uses experimentally measured floor pressures at three horizontal locations beneath the bed.

6.0 Heat Transfer - Results and Discussion

6.1 Measured Surface-to-Bed Heat-Transfer Coefficients

Heat-transfer coefficients are measured for several sizes of Master Beads and some sizes of glass beads of both high and low densities. Trends in the measured values are discussed below for each type of solid.

6.1.1 Heat-Transfer Coefficients for Master Beads

Surface-to-bed heat-transfer coefficients are measured as described in Section 4.7. The immersed surface is a horizontally placed tube with a diameter of 12.7 mm (§3.3.4). The center of the tube is located 20 mm above the floor of the vessel.

All heat-transfer measurements are made with an average heater surface temperature between 80 and 90°C. As described in Section 4.7, the probe temperature is the average reading of four thermocouples located at various positions along the length and circumference of the heater tube.

The heat probe is designed to maintain a constant temperature along the entire surface. The highest and lowest temperatures read by the four thermocouples on the surface vary by at most 2.5°C, if the heat flux into the bed is high. Considering that thermocouples are only accurate to ± 1°C, the surface temperature can be considered to be uniform for all practical purposes. Assuming a steady state, an overall heat-transfer coefficient is calculated using Newton's law of cooling,

$$h = \frac{Q}{S_p(\Theta_p - \Theta_b)} \qquad [6.1]$$

In this equation, h is the overall surface-to-bed heat-transfer coefficient, Q is the heat input to the heater in Watts, S_p is the surface area of the heater tube, Θ_p is the average temperature of the heater surface, and Θ_b is the average bed temperature. The bed temperature is based on the average of the readings of six thermocouples that represent major mixing paths within the bed.

Heat-transfer coefficients measured in 3-cm deep beds of Master Beads are shown in Figure 72 on page 267 and in Table 9 on page 270, as a function of the vibrational intensity parameter K, for various particle sizes. With the exception of two values (shown as darkened squares in Figure 72 on page 267), all measurements are made with a center-high bunker configuration — if bunkering is present. Since a heat-transfer tube is present within the bed, the top of the bunkered bed is not dome-shaped, but rather peaked above the length of the heat-transfer tube. The effect of this configuration on circulation patterns in the vicinity of the heat-transfer surfaces will be discussed later. The two solid squares represent wall-high bed configurations in which the flow of solids is normal to the horizontal axis of the heater tube, as shown in Figure 59 on page 218 in Section 5.5.1.

Features of the graphs of heat-transfer coefficients to be noted are:

1. With all particle sizes, the heat-transfer coefficient increases from its value at $K = 2$, as the value of K is increased.

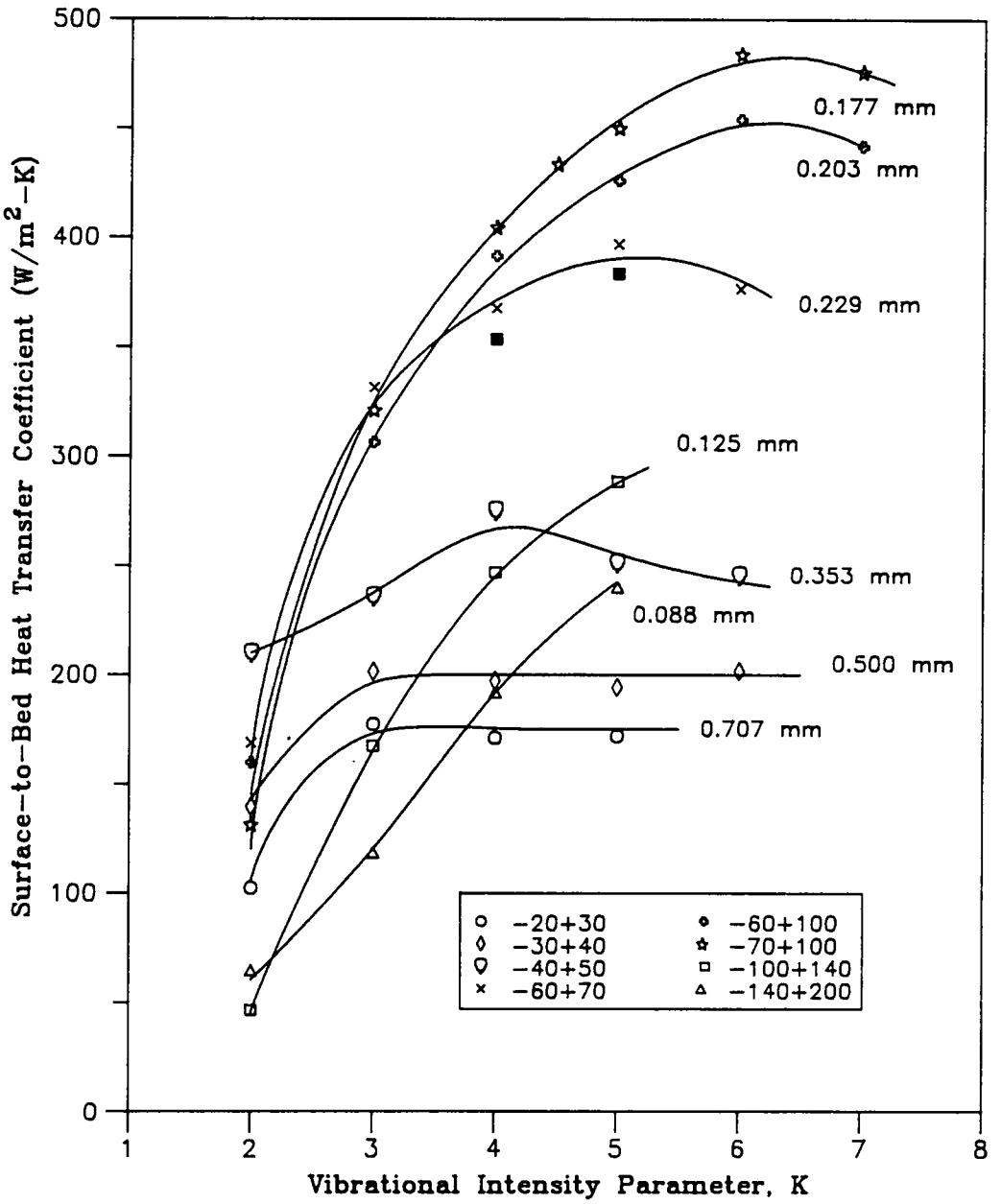

Figure 72. Surface-to-bed heat-transfer coefficients for Master Beads: Experimentally measured heat-transfer coefficients for Master Beads as a function of the vibrational intensity parameter, K, for various particle sizes. The darkened squares (■) represent values for 125-μm Master Beads with "normal" flow, i.e., with wall-high bunkering. All other values are obtained with center-high bunkering.

2. With the two largest particle sizes (707 and 500 μm), the heat-transfer coefficient reaches a maximum at $K = 3$ and then flattens out at this value.

3. The rate of increase in the heat-transfer coefficient with increasing K beyond $K = 2$ is greater as the particle size is reduced from 707 to 177 μm.

4. For particle sizes from 353 to 177 μm, heat-transfer coefficients pass through a maximum as K is increased.

5. The location of the maximum heat-transfer coefficient shifts to higher values of K as the particle size is reduced.

6. For the two smallest particle sizes (125 and 88 μm), a maximum heat-transfer coefficient is not reached within the range of K-values considered. With these two particle sizes, it is impossible to keep the bed stable (for any bed configuration) at values of K greater than 5. The bed rocks from side to side within the vessel, exposing the heat-transfer surface for several seconds at a time. This causes wild swings in the temperature of the heater, and a steady state cannot be achieved. However, the shape of the curve for the 125-μm Master Beads indicates that the heat-transfer coefficient is approaching a maximum value.

7. For any value of K greater than 2, a particle size of 177 μm always yields the highest heat-transfer coefficient. At $K = 2$, the highest heat-transfer coefficient is achieved with a particle size of 353 μm.

8. Heat-transfer coefficients obtained with a "normal" flow pattern (associated with wall-hugh bunkering) past the heat-transfer tube are each about 100 W/m^2-K higher than corresponding heat-transfer coefficients obtained with a center-high configuration.

9. The highest value of heat-transfer coefficient measured is 484 W/m^2-K for the 177-μm Master Beads at $K = 6$.

As described in Chapter 4, heat-transfer data are collected several times over a period of 30 to 40 minutes after the bed has reached a steady state. Usually, six to eight values of the heat-transfer coefficient are obtained for each particle at each value of the vibrational intensity parameter K. Average heat-transfer coefficients and 95% confidence intervals (C.I.) on the data are given in Table 9 on page 270. The 95% C.I.s give an indication of the spread of the data. The power to the heater is strictly controlled, and the ambient temperature in the laboratory varies at most by 2 to 3°C during the course of an experiment. Therefore, variations in heat-transfer coefficients for one set of operating conditions must come from "instabilities" in the heat-transfer process within the bed. Observation during data acquisition indicates instabilities in the configuration of some bunkered beds. When the center-high configuration becomes unstable during the course of a heat-transfer experiment, the circulation pattern of particles near the probe changes. The bed must be pushed back into place as it first becomes unstable.

For particle sizes of 707 and 500 μm, there are no instabilities in the bed configuration. As observed in Chapter 5, bunkering is not pronounced in large-particle beds. Since the bed remains essentially flat on top, and no horizontal pressure gradients are developed within the bed, there is little that can cause the bed to become unstable if vibrations are applied in a strictly vertical direction. This is reflected in the low values of the 95% C.I.s for these particle sizes.

As the particle size is reduced and bunkering occurs, the 95% C.I.s become larger in value. The instabilities are still not severe for 353-μm particles, but the 95% C.I.s for this particle size are on the average larger than those for bigger particle sizes. With particle sizes of 229 μm and less, the 95% C.I.s are noticeably larger. Initially the 95% C.I.s are largest at $K=2$. At this low value of K, the position of the bunker is very dependent on the direction of vibration. Over the course of one experimental run (about one hour), the direction of vibration usually deviates slightly from vertical, leading to bed instabilities. The instability can be corrected as it occurs by slightly adjusting the tensions of the leaf springs until the peak in the bunker is in the center of the bed again. Because of the low rate of heat transfer from the surface to the bed, as well as from the bed to the sur-

Table 9. Experimentally measured surface-to-bed heat-transfer coefficients for Master Beads

Particle Size Range (U.S. Standard Mesh)	Nominal Size (μm)	Vibrational Intensity Parameter, K	Heat-Transfer Coefficient, h (W/m^2-K)	95% Confidence Interval for h (W/m^2-K)
-20+30	707	2	102.1	±0.4
		3	177.1	±0.6
		4	170.9	±0.8
		5	171.7	±2.0
-30+40	500	2	139.6	±2.0
		3	201.2	±0.9
		4	196.9	±1.1
		5	194.0	±0.3
		6	201.4	±1.3
-40+50	353	2	209.6	±1.4
		3	235.5	±2.4
		4	274.7	±1.6
		5	250.8	±1.3
		6	245.0	±1.7
-60+70	229	2	168.5	±5.0
		3	331.3	±2.7
		4	367.5	±2.7
		5	396.7	±1.4
		6	376.3	±2.2
-60+100[1]	203	2	159.4	±7.0
		3	306.2	±2.0
		4	391.2	±2.7
		5	425.8	±1.8
		6	453.8	±1.9
		5	441.5	±3.0

table continued on the following page

Table 9 continued

Particle Size Range (U.S. Standard Mesh)	Nominal Size (μm)	Vibrational Intensity Parameter, K	Heat-Transfer Coefficient, h (W/m^2-K)	95% Confidence Interval for h (W/m^2-K)
-70+100	177	2	131.3	±6.0
		3	320.9	±2.5
		4	404.2	±2.9
		4.5	433.0	±4.8[2]
		5	449.9	±1.8
		6	483.7	±1.8
		7	475.6	±3.4
-100+140	125	2	46.2	±2.1
		3	167.2	±0.4
		4	246.7	±4.7
		5	288.2	±12.5
		4[3]	353.2	±3.3
		5[3]	383.2	±8.7
-140+200	88	2	64.2	±5.5
		3	118.4	±0.7
		4	191.5	±1.5
		5	239.8	±10.7

1 - 50/50 mixture by volume of -60 + 70 and -70 + 100

2 - average value based on a limited number of experimental points

3 - data obtained with "normal" flow past the heat-transfer tube

roundings at $K = 2$, the bed temperature takes a longer time to return to its original value after an instability has been corrected than at higher values of K.

For particle sizes of 203 μm and smaller, values of the 95% C.I.s also increase at higher values of K. In this case, the bunker configuration becomes unstable because of increased agitation within the bed. The two halves of the center-high bunker do not remain perfectly symmetric to each other, and this leads to instabilities. The problem is especially severe for 125- and 88-μm particles. With these particle sizes, the larger vertical pressure gradients occasionally cause depressions in the surface as the gas attempts to rush into the bed. When this happens, the symmetry of the center-high configuration is lost and the bed configuration becomes unstable. The exceptionally large values of the 95% C.I.s at $K = 5$ for 125- and 88-μm particles reflect these instabilities in bed configuration. The 95% C.I.s are smaller for the wall-high configuration (leading to normal flow past the heater), indicating as observed in Chapter 5 (§5.5.1) that this bed configuration is inherently more stable than the center-high configuration.

6.1.2 Heat-Transfer Coefficients for Glass Beads

Heat-transfer coefficients are measured for glass beads of both high and low densities using particles sizes of 88, 177, and 707 μm. These values are plotted as a function of the vibrational intensity parameter K, in Figure 73 on page 273, which also shows for comparison, the equivalent data for Master Beads. Values of the heat-transfer coefficient and corresponding 95% confidence intervals (C.I.s) are given in Table 10 on page 274.

Trends in heat-transfer coefficients for glass beads are approximately the same as for Master Beads. Heat-transfer coefficients for 707-μm glass beads also approach a limiting value; but surprisingly, it is somewhat higher than the equivalent limiting value for 707-μm Master Beads. This result is unexpected because all properties relevant to heat transfer: density ρ_s, thermal conductivity k_s, and

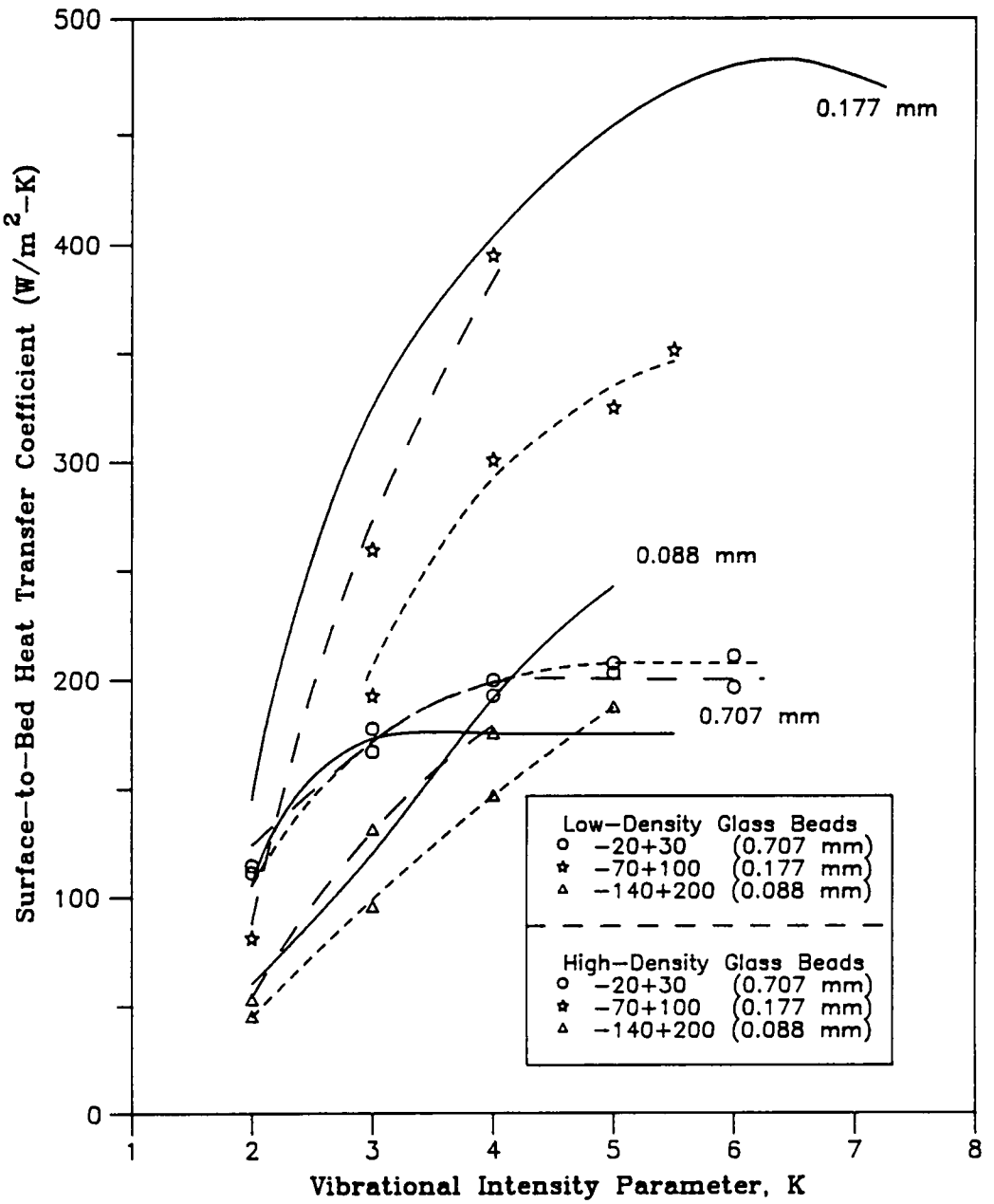

Figure 73. Surface-to-bed heat-transfer coefficients for glass beads: Experimentally measured surface-to-bed heat-transfer coefficients for glass beads, as a function of the vibrational intensity parameter, K, with particle sizes of 88, 177, and 707 μm. — — — — : high-density glass beads, ———— : Low density glass beads. For comparison, the solid lines represent the heat-transfer coefficient for Master Beads.

Table 10. Experimentally measured surface-to-bed heat-transfer coefficients for glass beads

Particle Size (microns)	Vibrational Intensity Parameter, K	Low-Density Glass		High-Density Glass	
		Heat-Transfer Coefficient (W/m^2-K)	95% CI (W/m^2-K)	Heat-Transfer Coefficient (W/m^2-K)	95% CI (W/m^2-K)
707	2	110.9	±1.09	114.2	±0.35
	3	177.3	±0.83	166.9	±1.00
	4	192.6	±0.80	199.6	±0.88
	5	207.3	±0.50	202.8	±0.82
	6	210.7	±0.55	196.3	±2.14
177	2	(a)	---	81.0	±1.76
	3	192.6	±1.47	259.5	±1.62
	4	300.9[1]	±2.16	395.2	±1.87
		308.7[2]	±7.09		
	5	325.0	±3.40	(a)	---
	5.5	351.5	±1.63	(a)	---
88	2	44.8	±1.04	52.7	±3.04
	3	95.4	±0.70	131.1	±0.75
	4	146.6	±0.63	175.2	±5.01
	5	187.2	±2.75	(a)	---

(a) - bed configuration too unstable for accurate measurement

1 - measurement made with humidified air within the bed

2 - measurement made with bone-dry air within the bed

heat capacity $c_{p,s}$, are lower for low-density glass beads than for Master Beads. The thermal diffusivity $\alpha(= k_s/\rho_s c_{p,s})$, which is the controlling transport property for transient thermal diffusion is 14.93 $\times$ 10^{-6} m^2/s for Master Beads and 0.75 $\times$ 10^{-6} m^2/s for low-density glass beads. The thermal heat capacity ($\rho_s c_{p,s}$), which determines the quantity of heat that may be transferred by a single particle from the heater surface to the bed (for a given rise in the temperature of the particle as it contacts the heater), has a value of 2.41 $\times$ 10^6 J/m^3-K for Master Beads, and a value of 1.88 $\times$ 10^6 J/m^3-K for low-density glass beads.

Heat-transfer coefficients for 177-μm low-density glass beads are lower than for equivalently sized Master Beads, whereas the values for 177-μm high-density glass beads are approximately the same as for Master Beads. With 88-μm particles, heat-transfer coefficients for Master Beads are close to those for glass beads up to $K = 4$. Beyond that, heat-transfer coefficients for Master Beads increase faster with increasing K, than do those for glass beads.

Heat-transfer coefficients are more difficult to establish in beds of glass beads because of the presence of electrostatic charges within the bed. The problem is particularly bad with particle sizes of 177 and 88 μm. The charges become more problematic as the temperature of the bed is increased and moisture is driven out of the bed. They cause particles to cling together, and to the walls, causing severe limitations in the bed mobility, and also leading to instabilities in the bed configuration. The particles also stick to the heat-transfer surface because of the charges. When this happens, the temperature of the probe rapidly increases because the heat-transfer coefficient drops sharply. For 177-μm particles, they drop by almost 100 W/m^2-K; and for 88-μm particles the heat-transfer coefficient approaches fixed-bed values (50 W/m^2-K). Removing the bed from the vessel reveals that particles form a layer coating the heat-transfer surface. With 177-μm particles, the layer is usually 1 to 2 particle layers thick; with 88-μm particles, the layer can be up to 2-3 mm thick. The layers are usually stuck sufficiently hard onto the tube surface, that a fair amount of force is required to remove them. It should be noted that the design of the heat-transfer probe and supports does not provide for an electrically grounded surface. However, running a ground wire to the surface does not help the situation either. What happens then is that the particles start to stick

together in the "dead" region of lowered particle circulation which forms below the probe. This builds up, and forms a "crust" around the heater. When the heat-transfer probe is placed within a gas-fluidized bed, glass particles can be observed to stick to the surface due to electrostatic charges. However, the frequent passage of bubbles (that reach the tube from below) washes away the build-up, except for a small cap of particles right on top of the tube. Although electrostatic forces are most severe in small-particle beds, they are not absent with 707-μm particles. The forces are strong enough to cause particles of this size to cling to the walls at low K. The electrostatic problem is eliminated to some degree by continuously passing 100-percent humidified air over the bed at low velocities.

The values of the 95% C.I.s given in Table 10 on page 274 further emphasize the configuration instabilities and electrostatic problems encountered with glass beads. The values are small for 707-μm particles where electrostatic and instability problems are small. With 177-μm particles, the 96% C.I.s are larger. Two values are shown at $K=4$ for low-density 177-μm glass beads. One is with humidified air and the other is without. Although the average values are approximately the same, the 95% C.I. is much larger on the heat-transfer obtained with no humidification. The higher degrees of agitation in the bed at $K=5$ prevents the bed from building up on the probe. Temperatures do not fluctuate as they do at lower values of K, resulting in lower values of the 95% C.I.

With the exception of the one point noted in Table 10 on page 274, all other values are collected with the use of humidified air. This eliminates static to the degree that particles no longer stick onto the heater, but it does not eliminate bed configuration instabilities. With 177-μm low-density glass beads, the maximum value of K that can be reached before the center-high configuration becomes very unstable is 5.5; for 177-μm high-density glass beads, the maximum K possible is only 4.

With 88-μm glass beads, the center-high configuration is unstable at all values of K, and the bed has to be forcibly restrained from adopting a wall-high configuration. The major path of particle movement from one half of the bed to the other as the center-high configuration becomes unstable, is below the probe supports. Placing a thin sheet of rubber below the supports provides a non-

conductive barrier to the movement, and prevents the center-high bunker from becoming unstable until $K = 4$ for high-density glass beads and $K = 5$ for low-density glass beads. Because the bed is forcibly restrained, the 95% C.I.s for the 88-μm glass beads cannot be directly compared with those for other particles.

6.1.3 Possible Sources of Error in the Measurements

There are some potential sources of experimental error involved in the measurement of heat-transfer coefficients. These are discussed individually in the following sub-sections. Methods to reduce or eliminate these sources of errors will be suggested in the Chapter 7, as recommendations for future work.

6.1.3.1 Estimating the Bed Temperature

The bed temperature, Θ_b, is the average reading of six thermocouples positioned as shown in Figure 12 on page 60. The two thermocouples closest to the heat-transfer probe (2 and 5), which are in the direct path of hot particles, usually read a few degrees higher than the others. Heat-transfer coefficients based only on these two temperatures are in general about 8-10% higher than those based on the average of six readings. When the difference in temperatures between the two closest thermocouples and others in the bed is large, the heat-transfer coefficient based on the higher readings can be up to 15% higher. Thermocouples 1,3,4, and 6 represent solid mixing longitudinal to the probe. For large particles, the horizontal mixing in the bed is poor, and the heat does not reach these thermocouples as efficiently as it does the two closest ones. Thus the error arising out of incorrectly estimating the bed temperature is greatest if the particle size is large, or if the vibrational intensity is low. If the bed were uniformly heated by a heat-transfer tube that runs along the entire diameter of the bed (which would be the case in practice, if for example, a steam heating

tube runs through the bed), heat-transfer coefficients, would be closer to those estimated by using only the two highest readings of the thermocouples within the bed.

6.1.3.2 Heat Conduction Through the Heater Supports

There are two ways in which the passage of heat directly from the heater to its supports, can lead to errors:

1. The heat from the probe conducts down the supports and is transferred into the bed. This leads to an error, since the amount of surface available for heat transfer is now greater than just the surface area of the heat-transfer probe.
2. Some of the heat conducted down the supports will reach the ends of the supports where it is lost to the surroundings. This causes an error, since the total heat flow into the bed no longer equals the power supplied to the heater, as required by equation [6.1].

To reduce these sources of error, a rubber washer is inserted between the Lexan supports and the copper probe as shown in Figure 74 on page 279. In addition, the protrusion of the copper body that fits into the Lexan support is coated with a thin layer of rubber compound. The conductivity of rubber is low (0.012 W/m-K). By comparison, the thermal conductivity of copper is 400 W/m-K, and for Lexan is 0.21 W/m-K. The rubber insulations reduce the heat loss through the supports significantly, but not completely.

Fortunately, it is possible to obtain a reasonably accurate estimate of the error introduced from conduction losses through the support, if the temperature at one end of the Lexan support is monitored. As shown in Figure 74 on page 279, 6.35 mm of the Lexan support is in intimate contact with the copper probe body, since it fits over the protrusion at the end of the probe. Since the copper is at a constant temperature, this 6.35 mm of Lexan can also be assumed to be at a constant temperature (although lower than the temperature of the copper). The rubber washer be-

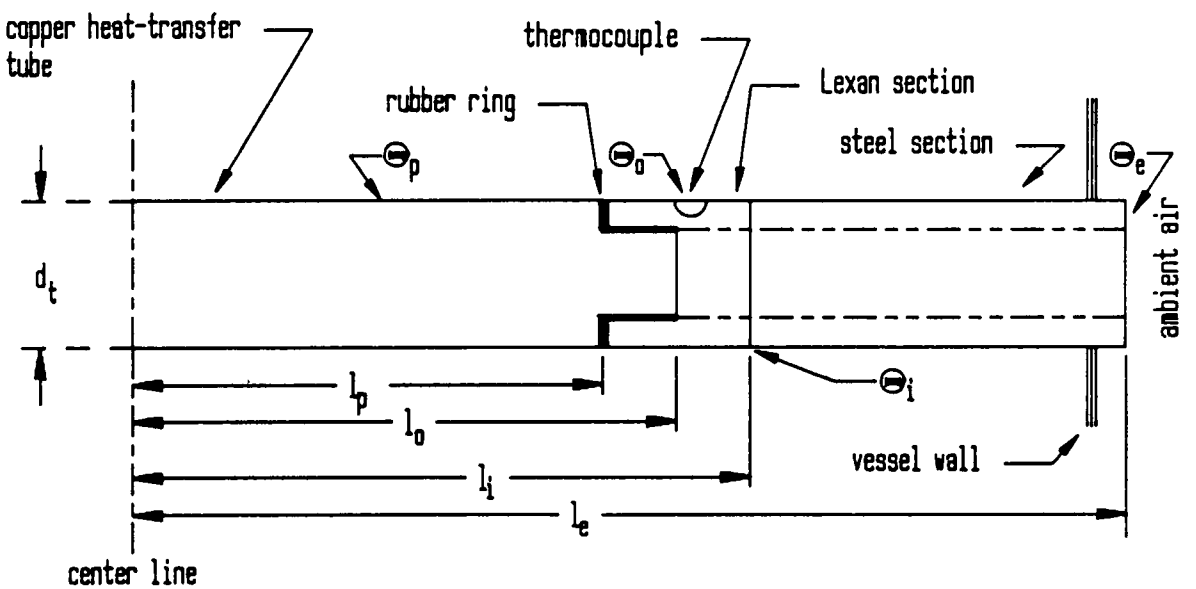

Figure 74. Schematic representation of the heat-transfer probe and its supports: Illustration of one half of the probe and its support at one end. The structure is symmetric about the center line. Notation: l_p - length of the main body of the copper heat-transfer probe; l_o - length to the end of the copper heat-transfer probe; l_i - distance from the center line to the end of the Lexan section; l_e - distance from the center line to the end of the steel section; Θ_p - temperature of the copper heat-transfer probe; Θ_o - temperature indicated by the thermocouple implanted in the Lexan section; Θ_e - temperature at the end of the steel section facing the ambient air. Note: $l_o - l_p = 6.35$ mm; $l_i - l_o = 6.35$ mm.

tween the Lexan and copper body prevents a significant amount of heat from entering the Lexan support at this end. As shown in Figure 74 on page 279, a thermocouple is implanted in the Lexan, close to the end of the copper protrusion.

By making the following assumptions, heat losses through the probe supports can be mathematically analyzed:

1. The 6.35 mm of Lexan which fits over the copper protrusion is at a uniform temperature Θ_o, which is the temperature measured by the implanted thermocouple.

2. Since the Lexan and steel sections of the support are of exactly the same diameter as the copper heat-transfer probe, the heat-transfer coefficient on the Lexan and steel surfaces are the same as for the heat-transfer probe.

3. Heat-transfer coefficients do not vary with angular position. This assumption has already been made in calculating the overall heat-transfer coefficient.

4. There are no radial or circumferential variations in the temperature within the Lexan or steel sections of the support. That is, the only temperature variation is along the length of the support. If the heat-transfer coefficient is constant with angular position, and the bed temperature is uniform, there cannot in fact be any circumferential variations in the temperature. Also, since the walls of the Lexan and steel sections are thin (the center of the support is hollow as described in Chapter 3), radial variations in temperature at any given distance along the support will be small.

5. The interconnection between the Lexan and steel sections of the support is thermally perfect. That is, there is no contact resistance in the joint, and the temperature, Θ_i, at the end of the Lexan section is equal to the temperature of the beginning of the steel section.

6. Heat losses from the end of the steel section that sticks out of the bed are only by convection to the ambient air. In reality, the heat will also be lost by conduction into the supporting structure, and down to the vibrating table assembly. To compensate for this, the area available for convective heat losses at the end of the steel section is increased by a factor of five over what is actually available. As it turns out from the solution, heat losses by convection do not in practice affect those from the probe through the support, so this assumption is irrelevant anyway.

If the total heat input to the heater is Q Watts:

$$Q = Q_p + Q_L + Q_s + Q_c \qquad [6.2]$$

where Q_p is the heat that flows into the bed across the heater surface; Q_L and Q_s are the heat that flow from the Lexan and steel sections of the support, respectively, into the bed; and Q_c is the convective heat loss to the ambient air from the ends of the supports. Heat-transfer coefficients are calculated on the basis of Q, whereas to be accurate, they must be calculated on the basis of the total heat that flows into the bed: $(Q_p + Q_L + Q_s)$.

Consider an element at a location x along the probe *or* its supports, which is small enough that the temperature gradient along it is negligible when compared to the temperature difference between its surface and the bed. If the area of the surface element is dA, the flow of heat into the bed can be written as:

$$\frac{dQ}{dA} = h\,\Delta\Theta(x) \qquad [6.3]$$

where $\Delta\Theta(x)$ is the difference between the temperature of the element Θ_x, and the bed temperature Θ_b . If the radius of the probe is r_p, and the thickness of the surface element is dx, the total heat that flows into the bed from a section of length $(l_2 - l_1)$ is given by:

$$\int_{l_2}^{l_1} dQ = 2\pi r_t h \int_{l_2}^{l_1} \Delta\Theta(x)\, dx \qquad [6.4]$$

The copper heat-transfer probe is isothermal and at a temperature Θ_p, so the total heat that flows into the bed from the probe is given by:

$$Q_p = 2\,[2\pi r_t\, h l_p(\Theta_p - \Theta_b)] \qquad [6.5]$$

where l_p is half the length of the heat-transfer probe. Similarly, the 6.35 mm of Lexan closest to the copper tube is isothermal at a temperature Θ_o. So, the heat flow into the bed from this section of the Lexan is given by:

$$Q_{Li} = 2\,[2\pi r_t\, h\,(l_o - l_p)(\Theta_o - \Theta_b)] \qquad [6.6]$$

In this equation, $(l_o - l_p)$ is the length of the isothermal section of Lexan (6.35 mm). The heat flow from the non-isothermal section of Lexan is:

$$Q_{Lv} = 2\left[2\pi r_t\, h \int_{l_o}^{l_i} \Theta_L(x)\, dx\right] \qquad [6.7]$$

where l_i is the distance of the Lexan-steel joint from the center of the heat-transfer probe. Similarly, for the steel section:

$$Q_s = 2\left[2\pi r_t\, h \int_{l_i}^{l_e} \Theta_s(x)\, dx\right] \qquad [6.8]$$

where l_e is the distance of the end of the support from the center of the heat-transfer probe. The heat lost by convection to the ambient air is given by:

$$Q_c = 2\left[2\pi r_t^2\, 5h_a\,(\Theta_e - \Theta_a)\right] \qquad [6.9]$$

Here, Θ_e is the temperature at the end of the steel section facing the ambient air, Θ_a is the ambient temperature, and h_a is the convective heat-transfer coefficient from a plane surface. A factor of 5 is introduced to account for additional conductive losses of heat from the end of the steel into the vibrating table assembly. This is one of the assumptions made in setting up the problem. However, as shown in appendix F, it turns out that the convective losses do not affect the analysis.

A knowledge of the temperature gradients in the Lexan and steel sections of the support is required to evaluate the integrals. Expressions for the temperature profiles $\Theta_L(x)$ and $\Theta_s(x)$ are developed in appendix F from heat-conduction theory. The profiles are functions of both h and x . Now equation [6.2] can be written as:

$$\frac{Q}{4\pi r_t} = h\left[l_p(\Theta_p - \Theta_b) + (l_o - l_p)(\Theta_o - \Theta_b) + \int_{l_o}^{l_i}\Theta_L(h,x)\,dx + \int_{l_i}^{l_e}\Theta_s(h,x)\,dx\right] \qquad [6.10]$$
$$- 5r_t h_a(\Theta_e - \Theta_a)$$

It is shown in appendix F (by considering heat conduction along the entire length of the probe support), that for typical values of h and Θ_o, the temperature at the joint between the steel and Lexan sections $\Theta_i \simeq \Theta_b$. This is because of the low thermal conductivity of Lexan in relation to the high surface-to-bed heat-transfer coefficients. Thus, heat is preferentially transferred into the bed rather than flowing down the Lexan supports. Furthermore, the analysis also shows that the temperature of the steel section is essentially equal to the bed temperature Θ_b, along much of its length, until the end exposed to air is approached. Thus, an isothermal barrier exists which prevents the flow of heat down the steel section of the support. Since the steel support is essentially at the bed temperature, the only heat that flows across its surface flows *into* the steel support from the bed close to the vessel walls. This heat is directly dumped into the ambient air. Therefore, heat flows into the bed only from the heat-transfer probe and Lexan supports, and no heat flows directly into the ambient air from the heater. As a result, the heat flow terms Q_t and Q_e can be neglected. Equation [6.10] for the true heat-transfer coefficient may be written as follows:

$$\frac{Q}{4\pi r_t} = h\left[l_p(\Theta_p - \Theta_b) + (l_o - l_p)(\Theta_o - \Theta_b) + \int_{l_o}^{l_i} \Theta_L(h,x)\,dx\right] \qquad [6.11]$$

The easiest way to obtain h from this equation is to use the value of h obtained by considering heat transfer only across the probe surface as an initial guess, and then to solve the equation iteratively for h .

As stated in appendix F, observation shows that two extreme practical conditions can occur:

1. A high heat-transfer coefficient which requires a large heat input to maintain a probe temperature of 85°C. This always results in a high value of Θ_o .
2. A low heat-transfer coefficient which requires a low heat input to maintain the required probe temperature. This always results in a low value of Θ_o .

It should be emphasized that (as shown in appendix F), both cases (1) and (2) lead to the condition that $\Theta_l \simeq \Theta_b$ at the Lexan-steel joint. A typical example of case (1) is 177-μm Master Beads at $K = 5$. The apparent heat-transfer coefficient is measured at 450 W/m^2-K. Temperatures measured directly are:

$$\Theta_o = 66°C = 339\ K$$

$$\Theta_a = 20°C = 293\ K$$

$$\Theta_b = 55°C = 328\ K$$

$$\Theta_p = 85°C = 358\ K$$

Using these values and the expression for $\Theta_L(h,x)$ given in appendix F, an iterative solution for the actual value of the heat-transfer coefficient h, gives 429 W/m^2-K. This means that the apparent heat-transfer coefficient of 450 W/m^2-K is 4.8% higher than the actual value.

At the other extreme, a typical example of case (2) is the heat transfer to a bed of 707-μm Master Beads at $K = 4$. The apparent heat-transfer coefficient based only on the surface area of the heat-transfer probe is 171 W/m^2-K. Measured temperatures are:

$$\Theta_o = 55°C = 328\ K$$

$$\Theta_a = 20°C = 293\ K$$

$$\Theta_b = 45°C = 318\ K$$

$$\Theta_p = 85°C = 358\ K$$

With these values, the iterative solution for h gives an actual value of 166.4 W/m^2-K. Therefore, the apparent value is only about 3% higher than the actual value of the heat-transfer coefficient.

6.1.3.3 Temperature of the Bed Directly Below the Probe

This is really a special case of an error that arises out of incorrectly estimating the bed temperature. However, unlike the previous error caused by estimating bed temperatures, it cannot be eliminated by heating the bed uniformly. This error is caused by solid circulation patterns in the locality of the heat-transfer probe, which will be described in further detail later in this chapter. Briefly, there is a "segregated" or "dead" region that exists below the probe when the bed is bunkered with a center-high configuration [Sprung *et al.*,1986]. Particles in this region either circulate very slowly within the region; or as is the case with particle sizes of 125 μm and smaller, they hardly move at all. In any case, they do not mix appreciably with particles in the rest of the bed. A thermocouple located directly below the probe (see Section 4.7) reads temperatures within this region of the bed that are about 8-10°C (and occasionally 20°C) higher than average bed temperatures for Master Beads [Thomas *et al.*,1986]. With 177-μm high-density glass beads, the temperature within this region is about 30°C higher than the average bed temperature at $K = 2$.

Observation of circulation patterns in the neighborhood of the heat-transfer probe with fluorescent tracers shows that the dead zone can cover up to one-quarter of the total heat-transfer area for 177-μm particles, and almost half of the heat-transfer area for 88-μm particles.

There are two ways in which the presence of this dead zone can lead to errors in estimating the overall surface-to-bed heat-transfer coefficient. First, higher temperatures that occur in the zones reduce the temperature gradient and hence the driving force for heat transfer at the bottom of the heat-transfer probe. This leads to a lowered heat flux across the bottom of the probe. Furthermore, since particles in this region do not mix with the rest of the bed, the flow of heat into the dead zone is mainly transmitted down into the floor of the vessel, and not into the rest of the bed where it is seen by the six thermocouples measuring the bed temperature. Secondly, with fine particles, the solid in the dead zone does not even circulate appreciably, so that the zone is essentially a packed-bed. With such particle sizes, heat-transfer coefficients along the bottom half of the heat-transfer probe surface are only of the magnitude of packed bed values (50 W/m^2-K). Because of this, temperatures in the dead zones are lowest in fine-particle beds. Most of the heat flux is therefore into the rest of the bed across only about half of the available heat-transfer area. That is to say, the over-estimation of the actual surface area over which heat transfer takes place leads to calculated heat-transfer coefficients that are lower than their true values. When a wall-high bunker configuration is used, the normal flow of solid past the tube eliminates the dead zone. The higher heat-transfer coefficients measured for 125-μm Master Beads with this bed configuration (the darkened squares in Figure 72 on page 267) must be at least in part due to the elimination of dead zones.

6.1.4 Comparison of Measured Values with Previously Published Results

The shape of the graphs of heat-transfer coefficient as a function of K shown in Figure 72 on page 267, indicates certain similarities to those obtained by Kossenko *et al.* [1975] at 20 Hz as depicted

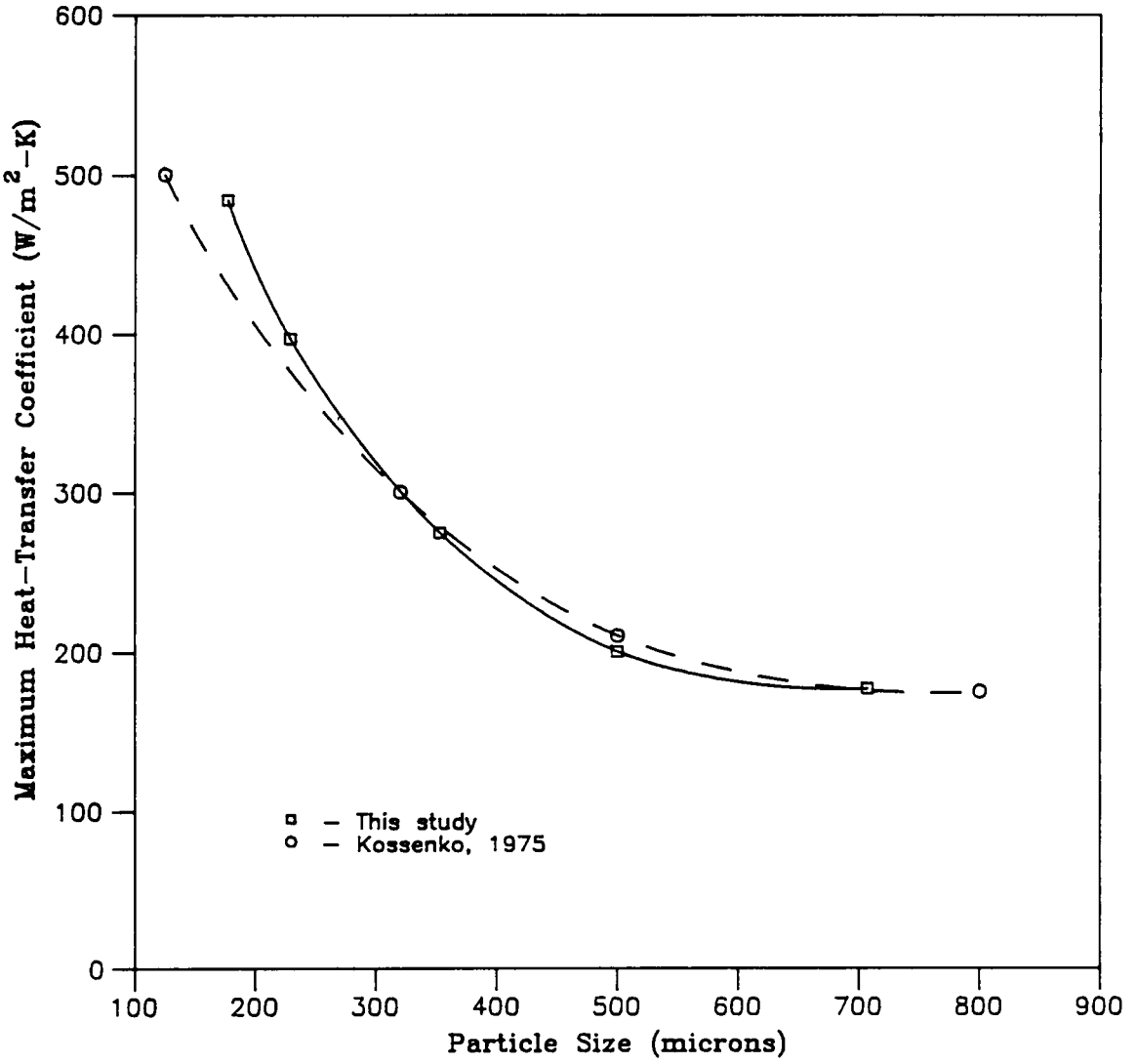

Figure 75. Comparison of heat-transfer coefficients with those obtained by Kossenko: A comparison of maximum surface-to-bed heat-transfer coefficients obtained from this study using Master Beads at a frequency of 25 Hz, with those obtained by Kossenko *et al.* [1975] using alumina spheres and a frequency of 20 Hz. The diameter of the heater tube used in this study is 12.7 mm, while a tube diameter of 38 mm was employed by Kossenko.

in Figure 4 on page 18 in Chapter 1. In that study, heat-transfer coefficients were measured for horizontal tube bundles, with a tube diameter of 38 mm (compared to the 12.5 mm used in this study). The data in Figure 4 on page 18 are for a single row of tubes. The solid used was spherical alumina, which is comparable to Master Beads. A bed depth of 160 mm was employed. Although conditions are different between the two studies, the similarity in the shape of the graphs suggests the shape is fundamental to heat transfer from immersed horizontal tubes. In fact, maximum values of the heat-transfer coefficient obtained from the two studies are virtually the same within a particle size range of 177 to 707 μm, as shown in -- Figure id 'htcompr' unknown --.

Gutman [1976b] has measured heat-transfer coefficients from a vertical heater to a bed of glass beads. His results also indicate a trend toward a limiting heat-transfer coefficient with large particles. However, with 800-μm low-density glass beads, a limiting value of 300 W/m^2-K is reported at $K=4$ with a vibrational frequency of 20 Hz. That limiting value is about 1.5 times that obtained in this study for 707-μm low-density glass beads. As will be shown later, this is most likely due to the heater geometry. Using 260 μm (a range of 210 to 325 μm) low-density glass beads, Gutman obtained a heat-transfer coefficient of 250 W/m^2-K at $K=4$, and 200 W/m^2-K at $K=3$. These values are close to those obtained in this study using 177-μm low-density glass beads at equivalent values of K. No measurements are made in this study with glass beads of the same size used by Gutman, but the variation in heat-transfer coefficients with particle size for Master Beads suggests that the values that would be obtained using a cylindrical heat-transfer surface geometry must be lower than those obtained herein with 177-μm particles. Therefore, Gutman's results do indicate some improvement in heat transfer with a flat vertical heater geometry, for smaller particle sizes as well.

6.2 *Formation of Air Gaps Surrounding the Heat-Transfer Surface*

The formation of air gaps over horizontal surfaces such as the vessel floor is well established. Gutman [1974] and Bukareva *et al.* [1969] also report air gaps above and below flat horizontal surfaces immersed in the bed. Malhotra and Mujumdar [1985] have observed air-gap formation around horizontal tubes immersed in vibrated gas-fluidized beds. Similar air gaps are also observed to form around heat-transfer tubes immersed in vibrated beds. Such gaps form because of the motion of the bed relative to the vessel to which heat-transfer tubes are normally attached.

The formation of the air gaps and their evolution through a vibrational cycle is studied using a dummy "heat-transfer" tube placed across the two-dimensional vessel as shown in Figure 13 on page 62. Direct observation is made by back-lighting the bed with a strobe lamp. The lamp can be free-run at a frequency slightly lower than the vibrational frequency of 25 Hz., or it can be triggered by a phase-delayed pulse for observation at particular phase angles. Based on these direct observations, the following general points can be made regarding the gap formation:

1. With the exception of the two smallest particle sizes (125 and 88 μm), all beds show air gap formation above and below the heat-transfer probe. The 125-μm beads show air gaps of a small size appearing intermittently around the probe for $K \geq 5$.

2. For particle sizes of 177 and 203 μm, only very small intermittent air gaps are seen for $K < 3$. At $K = 3$, small air gaps are observed.

3. For particles with sizes of 707, 500, and 353 μm, air gaps appear at the probe for $K \geq 2$. These get bigger with increasing K values, and eventually for the 707- and 500-μm particles, air gaps completely surround the heat probe for a fraction of the vibrational cycle.

4. In general, gaps appear at lower values of K as the particle size is increased.

5. As the vibrational intensity is increased, the gaps increase in size, covering a greater surface area of the heat-transfer probe. In addition, gaps are visible for a greater fraction of the vibrational cycle. With the 707- and 500-μm particles, a limiting coverage is reached when the entire probe is covered by the air gap.

6. Air gaps are formed regardless of the type of solids circulation or bunkering present in the bed.

7. No air gaps are formed around a flat vertical surface immersed in the bed.

More quantitative information is obtained by taking phase-delayed photographs of the gap formation. Typical photographs are shown in Figure 76 on page 291 for 707-μm Master Beads and in Figure 77 on page 292 for 177-μm Master Beads. Both sets of photographs are obtained at $K = 4$. Referring to Figure 76 on page 291, at 30° the gap at the bottom of the tube left over from the previous cycle is still closing. At 80°, the gap below the tube has disappeared, but a gap has fully formed over the top half of the tube. The gap is large at 180° — over 3 mm thick at the highest point. The relative downward motion of the vessel causes the tube to push down on the bed, and this results in a downward-pointing hump at the bottom of the bed as shown in the photograph. At 220°, the section of bed immediately below the tube starts to fall faster than the tube, and a gap appears below the tube. The tube is completely covered with air gaps at 270°, both on the top and bottom surfaces. Note that the section of the floor gap immediately below the tube closes prematurely, since the section of bed above it is forced downward by the tube earlier in the cycle. At 310°, the gap on top of the tube is closing, but the gap below it is large. As seen by the photographs at 30°, it persists into the following cycle.

In Figure 77 on page 292, the sequence of events for 177-μm Master Beads shows that in this case too, a small gap persists below the tube from the previous cycle at a phase angle of 10°. Gaps form above the tube by 110°. Although, it is not clear from the prints shown in the figure, the gap is

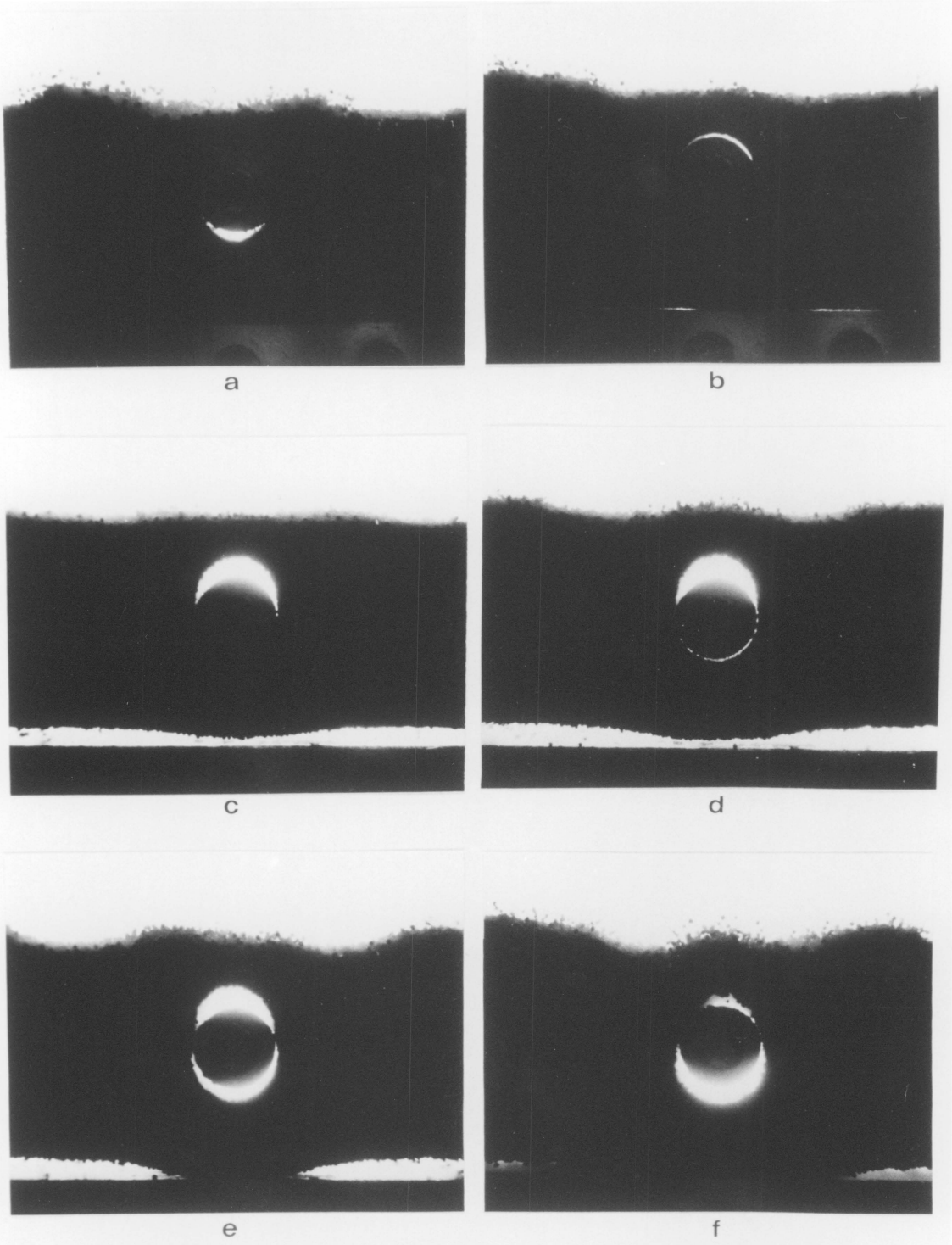

Figure 76. Air gaps surrounding the heater tube in a bed of 707-μm Master Beads: Phase-delayed photographs showing the formation and evolution of air gaps surrounding the heat-transfer surface through a vibrational cycle, at phase angles of (a) 30°, (b) 80°, (c) 180°, (d) 220°, (e) 270°, and (f) 310°.

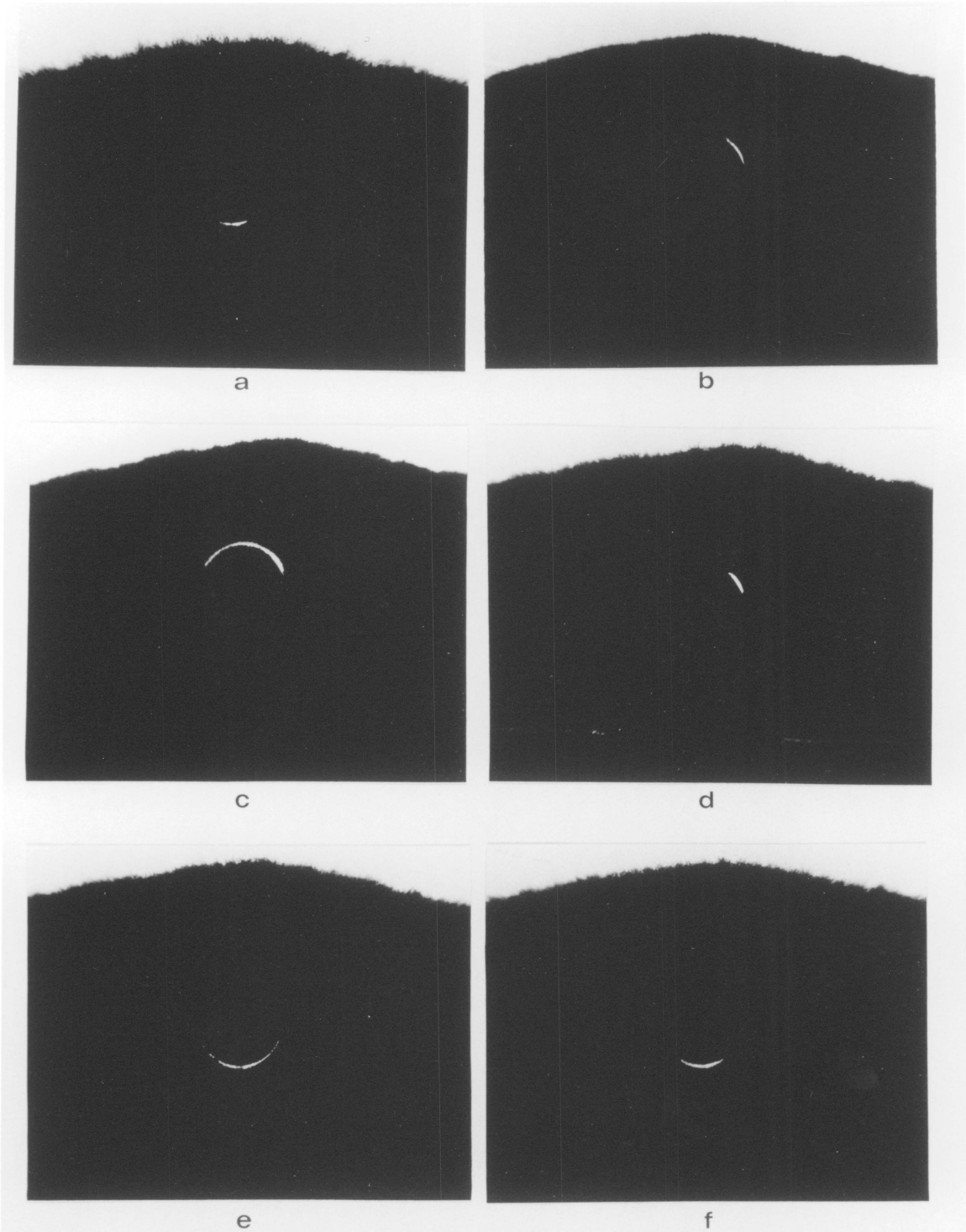

Figure 77. Air gaps surrounding the heater tube in a bed of 177-μm Master Beads: Phase-delayed photographs showing the formation and evolution of air gaps surrounding the heat-transfer surface through a vibrational cycle, at phase angles of (a) 10°, (b) 110°, (c) 160°, (d) 220°, (e) 260°, and (f) 280°. Note that the peak of the bunker does not sit exactly above the center of the tube.

formed on both sides of the tube, though more so on one side than on the other. The gap formation is not symmetric, because when a tube is present within a center-high bunker, the peak will not sit directly above the center-line of the cylinder. Instead, it locates itself slightly to one side or the other of the center-line, usually lined up with either one of the vertical tangents to the cylinder. A well-formed top gap is seen at 160°. By 220°, the gap on top of the tube is closing, and although not as clearly, a gap is forming at the bottom of the tube. Again, note the asymmetry as the gap closes on one side of the tube before the other. The bottom gap is well formed at 260°, but is already beginning to close again at 280°.

6.2.1 The Extent of Heat-Transfer Surface Coverage by Air Gaps

The extent of surface blanketing by air gaps at various phase angles is obtained by taking photographs of air gaps at regularly spaced phase angles onto 35-mm slide film. The resulting slides are projected onto a screen, forming an image as illustrated schematically in Figure 78 on page 294. The radius r_t of the heat-transfer tube, and the linear distance p between the two points of closure of an air gap on the tube surface are measured. The fraction of surface area of the heat-transfer tube blanketed by an air gap, denoted by F_{SA}, may be estimated from:

$$F_{SA}(\theta) = \frac{\sin^{-1}\left(\frac{0.5p}{r_t}\right)}{\pi} \qquad [6.12]$$

The phase angle $\theta = \omega t$. A time-averaged fraction of the area blanketed by air gaps is given by:

$$\bar{F}_{SA} = \frac{1}{2\pi}\int_0^{2\pi} F_{SA}(\theta)\, d\theta \qquad [6.13]$$

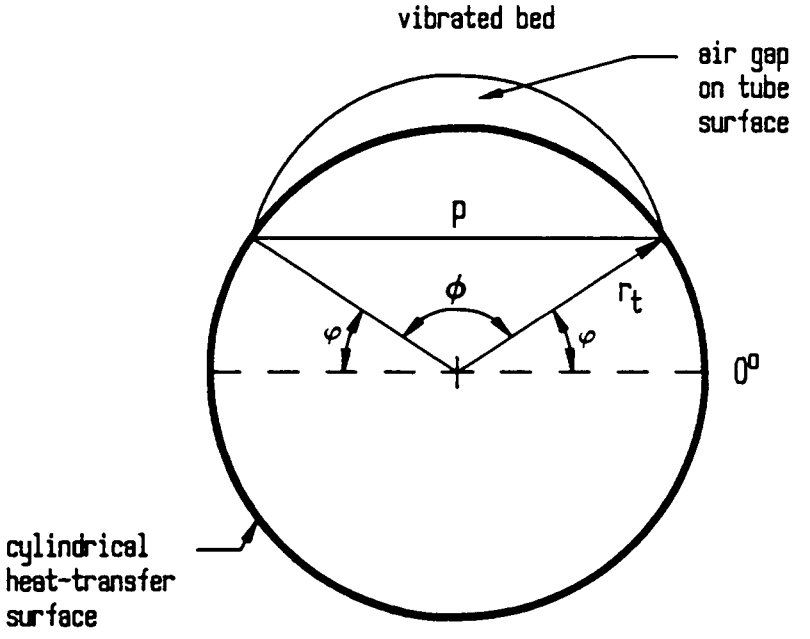

Figure 78. Illustration of an air gap on the surface of the heat-transfer tube: An air gap on the top surface of a heat-transfer tube immersed horizontally within the vibrated bed. The tube radius is r_t, and the distance between the two points of closure of the air gap on the surface is p .

F_{SA} is plotted as a function of the phase angle as shown in Figure 79 on page 296 and Figure 80 on page 297 for 707-μm and 177-μm Master Beads, respectively. With the 707-μm Master Beads, the vibrational intensity parameter K, is varied from 2 to 5, and for the 177-μm Master Beads, it is varied from 3 to 7. The plots also show features of the gap obtained by direct observation. For example, the degree of coverage is bigger for 707-μm particles than it is for 177-μm particles for any given value of K. Also the coverage is seen to increase with K.

The area under the plots of F_{SA} versus θ is obtained by numerical integration to give $\overline{F}_{SA}$. Table 11 on page 298 summarizes the variations of $\overline{F}_{SA}$ with K for the two sizes of Master Beads. The values of $\overline{F}_{SA}$ for 707-μm Master Beads are over 100% greater than those for 177-μm particles. For the large particles, the fraction of surface coverage does not increase significantly as K exceeds 3. However, for smaller particles, there is an increase in $\overline{F}_{SA}$ through the entire range of K with the most substantial increase occurring between $K = 5$ and 6.

It would be intuitive to argue that the air gaps provide a resistance to heat transfer from the surface into the bed. As seen in the photographs, the formation, growth, and closure of the air gap on the top surface is asymmetric for small-particle bunkered beds, because the peak in the bunker sits on one side of the tube. The gap appears first, grows to a larger size, and closes last on the side of the tube over which the peak is located. The resistance to heat transfer must therefore be larger on this side of the tube. Observation shows that the bed temperature read by the thermocouples numbered 2 and 5, located closest to the probe, are not identical. The bed temperature on the side on which the peak is located is always a few degrees lower than that on the other side of the tube. If the peak is physically moved over to the other side of the tube, the difference in temperatures of the two halves of the bed reverses. This suggests that the resistance provided by the larger gap and its longer duration on one side of the tube, causes a less efficient transfer of heat into the adjacent side of the bed. A fuller discussion of the effects of air gap formation on the heat transfer will be reserved until later in this chapter.

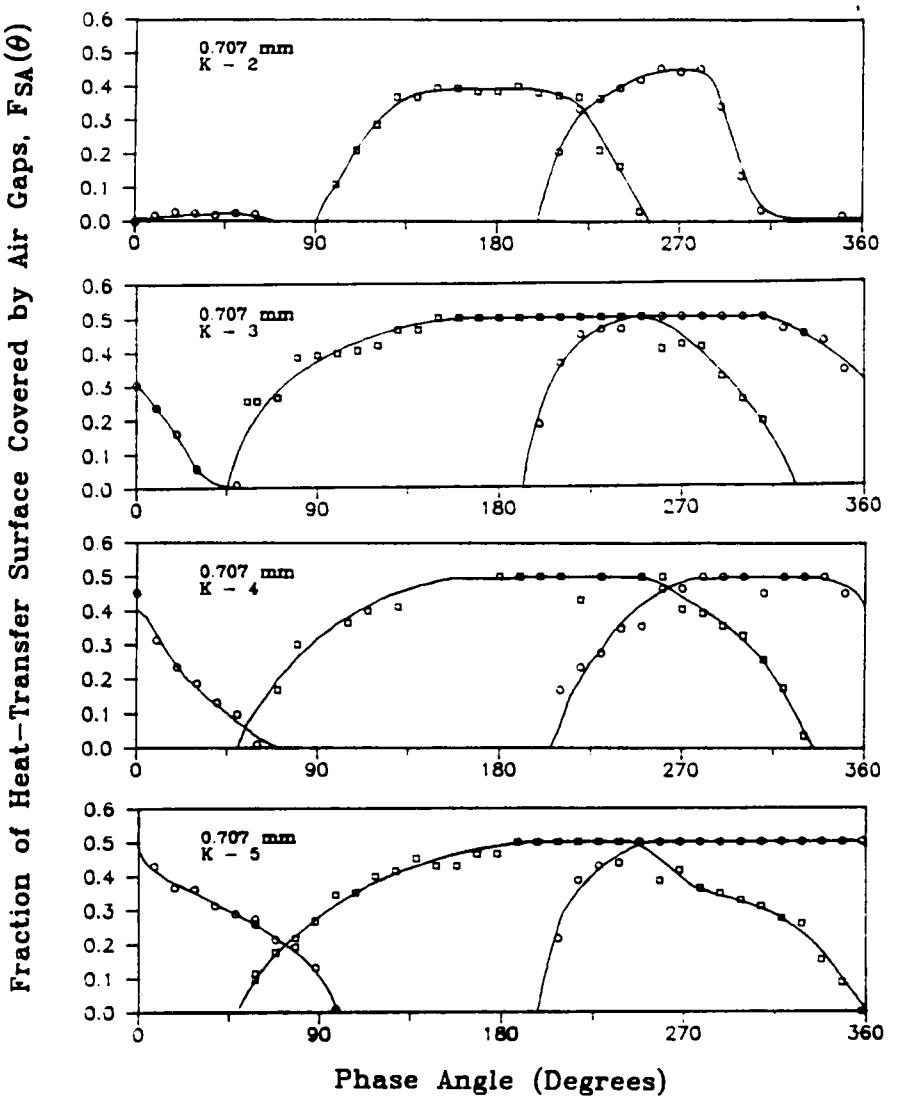

Figure 79. Fractional coverage of the heat-transfer surface by air gaps for 707-μm Master Beads: Fraction of the heat-transfer surface covered by air gaps as a function of the phase angle over one vibrational cycle at different values of K. ○ - data for gaps on the lower surface of the heater tube, □ - data for gaps on the upper surface of the heater tube.

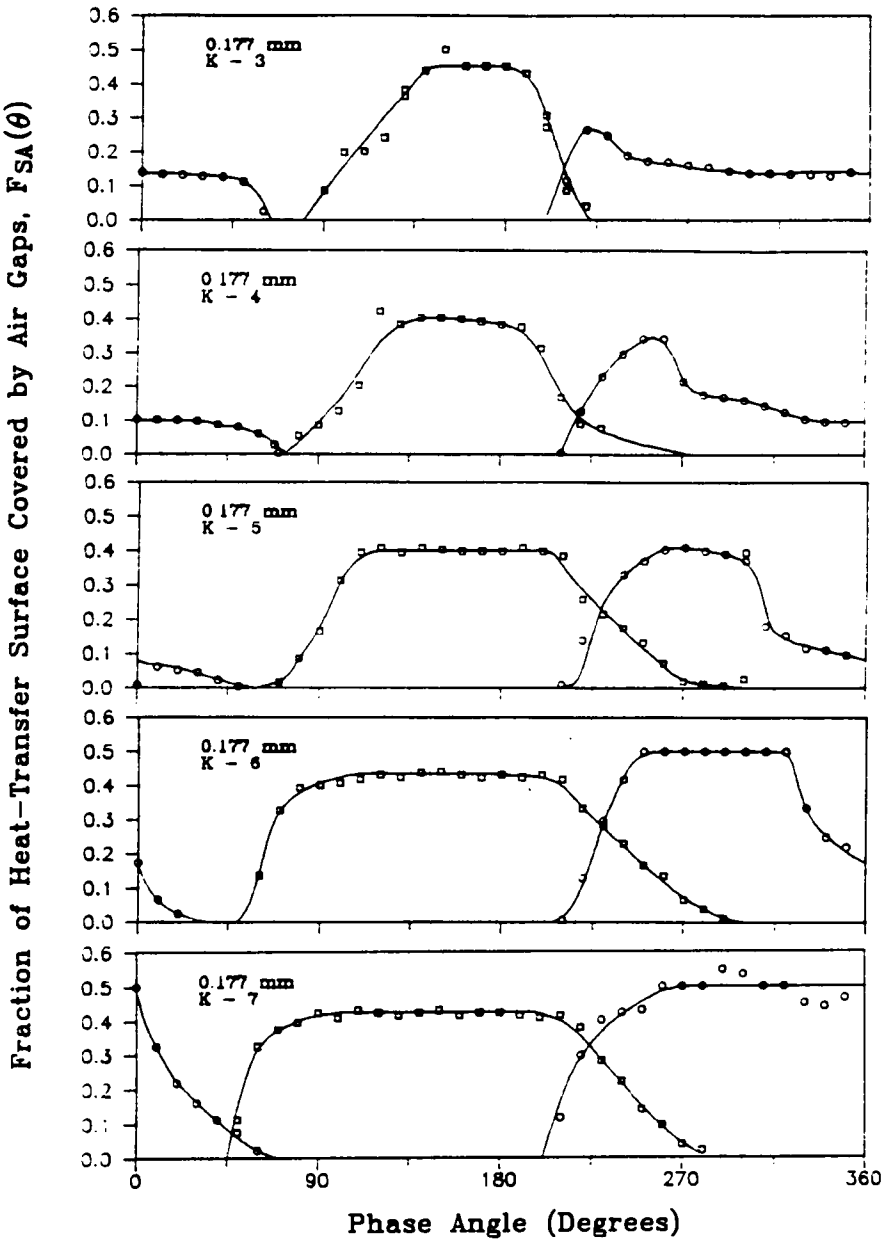

Figure 80. Fractional coverage of the heat-transfer surface by air gaps for 177-μm Master Beads: Fraction of the heat-transfer surface covered by air gaps as a function of the phase angle over one vibrational cycle at different values of K. ○ - data for gaps on the lower surface of the heater tube, □ - data for gaps on the upper surface of the heater tube.

Table 11. Average fractional coverage of the heat-transfer surface by air gaps

Vibrational Intensity Parameter, K	Particle Size (microns)	
	707	177
2	0.24	(a)
3	0.53	0.21
4	0.56	0.22
5	0.59	0.27
6	----	0.38
7	----	0.46

(a) - gaps too small and intermittent for accurate measurement

6.3 *Particle Circulation in the Vicinity of the Heat-Transfer Tube*

The presence of the heat-transfer tube causes localized distortions in the motion of the bed. This is obvious from the photographs in Figure 76 on page 291 which show the premature closure of the gap beneath the bed directly below the heat-transfer tube. Floor-pressure measurements made with the pressure sampling port located directly below the tube shows a "kink" as the gap closes prematurely at this point [Sprung *et al.*,1986]. Also, the pressure at the center does not reach the same peak value as without the tube, and it now decays much faster after the maximum pressure is reached. These direct interactions between the heat-transfer surface and the bed, as well as distortions in the pressure field in the locality of the tube, and the formation of gaps surrounding the tube alter the particle circulation patterns in the vicinity of the heat-transfer tube.

6.3.1 Description of Local Circulation Patterns

Particle circulation patterns in the locality of the tube can be studied with the use of fluorescent tracers as used in the study of overall particle circulation. Three colors of fluorescent tracers are normally used. At the start of an experiment, some tracers of one color are placed at one end of the vessel. These provide information on how particles from the rest of the bed reach the heat-transfer tube. Tracers of another color are located on top of the tube, and these give information on the movement of particles at the top of the heat-transfer tube. In view of the existence of "dead" zones below the tube, tracers of a third color are placed in a heap directly below the tube. The observed circulation patterns in beds of 707-, 177-, and 88-μm glass beads of both high and low densities are shown in Figure 81 on page 300. Key features observed for each particle size are summarized in the following sub-sections.

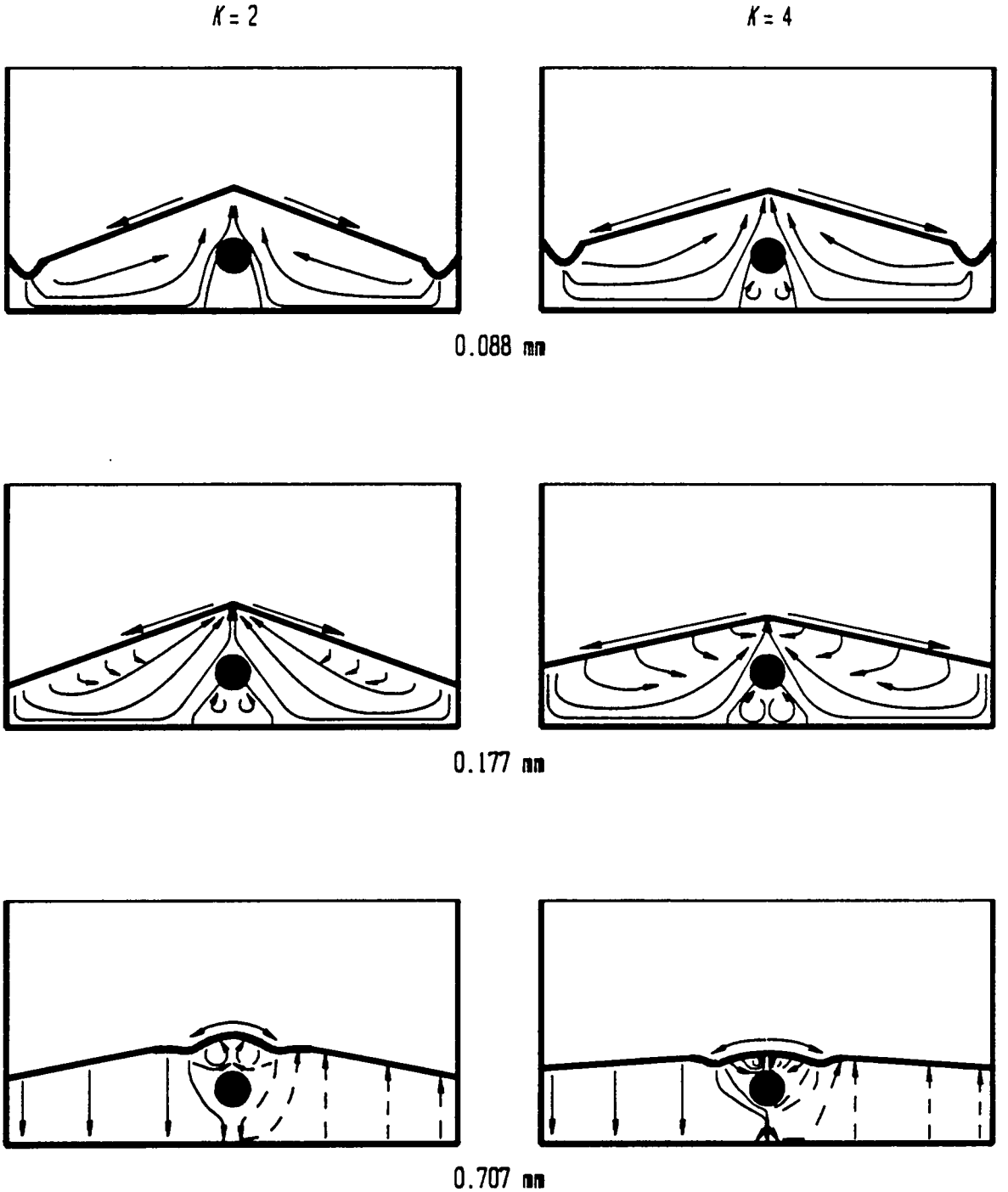

Figure 81. Solid circulation patterns in the vicinity of the heat-transfer tube: Particle circulation patterns in the bed and around the heat-transfer tube observed with the use of fluorescent tracers, for 88-, 177-, and 707-μm glass beads at $K = 2$ and 4. Note the "dead" or "segregated" zones beneath the tube with 88- and 177-μm particles. There is virtually no particle motion within the dead zone for 88-μm particles at $K = 2$. For 707-μm particles, the dashed arrows in the right half of the bed indicate the circulation patterns found within the heart of the bed.

707-μm Particles

Overall lateral particle mixing is poor in this bed, as noted previously in Section 5.4. However, close to the heat-transfer tube, particles located particularly in the interior of the bed are drawn toward the tube as indicated in Figure 81 on page 300. Most particles that are drawn in toward the tube move quickly downward past the tube. Some of them, however, end up in small-scale circulation loops that are located on top of the tube as shown in Figure 81 on page 300. From observation, the general rule appears to be that a particle drawn in to any point located on the top half of the tube, ends up in the loops; whereas if it is drawn in to a point located along the bottom half of the tube, it is immediately pulled down past the lower surface of the tube. The line dividing these two areas of the probe surface appears to be well defined. A particle stays within the loops until finally, it reaches a point slightly below the dividing line. When this happens, it is immediately pulled down past the lower surface at a high velocity, to the bottom of the bed as shown in Figure 81 on page 300. After a particle is pulled down past the tube to the bottom of the bed, it moves laterally away from the tube into the rest of the bed.

177-μm Particles

Overall particle circulation in the bed is similar to that observed without the tube. Particles still move horizontally from the shallow part of the bunker to the deeper part. As the particles travel upward at the center, they move diagonally past the tube as shown in the figure. The major effect of the tube on particle circulation is the presence of a trapezoidal "dead" or "segregated" region beneath the tube. At $K = 2$, particles barely move within this region. They circulate in loops as shown, taking several minutes to complete each loop. Since different colored tracers are placed in this region, the degree of solid mixing between this region and the rest of the bed can also be observed. At $K = 2$, there is virtually no inter-mixing between particles in this zone and the rest of the bed. Over the course of a 15-minute experiment, not a single tracer particle can be observed to move from this region into the rest of the bed.

At $K=4$, the segregated zone is still present, but now solid circulation takes place within it at a faster rate. A particle takes on the order of a few seconds to complete a loop. At the edge of the segregated region, where the loop meets the paths of upward particle motion, the shear caused by the relative motion of particles causes some exchange of particles with the rest of the bed. On the whole though, solid mixing between this region and the rest of the bed remains poor.

88-μm Particles

Circulation patterns for 88-μm particles are similar to those for 177-μm particles, except that now the size of the trapezoidal dead zone is larger as shown in Figure 81 on page 300. The lower half of the tube is in contact with the dead zone. Particle circulation rates within the dead zone are even smaller with this particle size. At $K=2$, particles within the zone are almost motionless, giving this region the appearance of a packed bed. At $K=4$, the circulation rate is slightly better, but mixing with the rest of the bed is still non-existent.

6.3.2 Residence Time of Particles Adjacent to the Heat-Transfer Surface

Johnson [1987], in work connected with this study, has measured the amount of time that particles spend in the vicinity of the heat-transfer tube. This is done by videotaping the motion of the fluorescent tracers as they move past the tube, and viewing the tape at a slower speed to record residence times.

With 707-μm glass beads, the amount of time that a particle circulating in a loop above the tube, spends adjacent to the surface is measured. Also measured is the amount of time that a particle, moving down past the lower half of the tube, spends next to the surface of the tube. This gives average surface-adjacent residence times for particles next to the top and bottom halves of the heat-transfer surface. Her results are summarized in Table 12 on page 303. The number of times

Table 12. Average residence times of 707-μm particles next to the heater surface

Type of Particle	Vibrational Intensity Parameter, K	Average Residence Time of a Particle Next to the Heat-Transfer Tube (seconds)		No. of Times Particle Loops above tube
		Top of Tube	Bottom of Tube	
-20 + 30 mesh low-density glass beads	3	---	0.868	2
	4	0.786	0.538	3
	5	0.392	0.266	5
-20 + 30 mesh high-density glass beads	3	---	0.706	-
	4	1.368	0.395	-
	5	0.469	0.296	-

that a 707-μm low-density glass bead loops above the top of the tube before it gets pulled down past the tube, is also recorded. All data in the table represent the average of 20 measured values.

The results show that the residence time of a particle next to the tube surface decreases with increasing K. The residence times are longer for high-density glass beads than for low-density glass beads on the top of the tube, but the situation is reversed at the bottom surface. These residence times should *not* be regarded as particle-surface contact times. The formation of gaps around the tube limits the contact times to only a fraction of the vibrational cycle, and a particle is touching the heater surface for only part of the time that it spends adjacent to the heater surface.

With 177-μm low-density glass beads, the amount of time that the particle spends adjacent to the heater surface is measured. For the fraction of the surface above the dead zone, the times are 0.78 seconds at $K = 3$ and 0.45 seconds at $K = 4$. Again, note that because of the formation of air gaps, these values do not represent actual contact times.

6.4 *Possible Mechanisms for Surface-to-Bed Heat Transfer*

This section will discuss a number of possible mechanisms for surface-to-bed heat transfer, including a list of factors that appear to have the greatest influence on the process. However, as will be shown later in this section, there are insufficient data at present to discriminate between different heat-transfer models.

Examining the mechanisms of heat transfer in gas-fluidized beds will help gain an understanding of which factors influence surface-to-bed heat transfer in a vibrated bed. Therefore, a brief review of some suggested heat-transfer mechanisms in gas-fluidized beds will be included here.

It may be assumed that the heat transfer from a surface to a particle in contact with it is influenced by the temperature of the particle. If the particle is at a much lower temperature than the surface (that is, the temperature gradient or driving force is high), the quantity of heat flowing into the particle will be greater than if the thermal gradient were smaller. This follows from Fourier's law of heat conduction, and is the basis for the so-called "penetration" theories of heat transfer in fluidized beds such as the packet model of Mickley and Fairbanks [1955] and the one-layer model of Zabrodsky [1963]. With a penetration mechanism, contact times of particles at the heater surface greatly influence the rate of heat transfer. Shorter contact times and frequent renewal of particles at the heater surface are beneficial, since the temperature of the particle is not raised by much, and the thermal gradient remains high.

Alternatively, the contact-resistance mechanism assigns the controlling step in surface-to-bed heat transfer to the resistance to heat transfer due to the nature of the point contact of particles at the heater surface. Spherical particles contact the heater surface at only single points. In theory, the rate of heat conduction across a single point (zero area) should be zero. Therefore, heat conduction into the particle must take place through the gas wedge enclosed between the surface of the particle and the surface of the heater. This provides a resistance to heat transfer. With larger particles, the resistance to heat transfer will be greater, since the size of the gas wedge is also larger. As the particle size is reduced, the shape of the particle layer in contact with the heater surface approaches that of a continuous solid surface, and the resistance to heat transfer drops as a consequence. The contact-resistance theory implies that the major factor influencing heat transfer is the particle dimension, and that the heat-transfer rate will be independent of solid circulation rates or the thermal properties of the particle. The one-layer model [Zabrodsky,1963] includes the effect of a contact resistance.

The penetration models suggest that as the contact time is reduced, the heat-transfer coefficient should go up accordingly. This of course means that at vanishingly small contact times, the heat-transfer coefficient should approach infinity, which is physically impossible. One way to get around this anomaly is to write the overall surface-to-bed heat-transfer coefficient h, as a combination of

a contact-resistance heat-transfer coefficient (h_c) and a penetration heat-transfer coefficient (h_p) as follows:

$$\frac{1}{h} = \frac{1}{h_c} + \frac{1}{h_p} \qquad [6.14]$$

As the contact time $t_c \rightarrow 0$, $h_p \rightarrow \infty$, and $h \rightarrow h_c$ Thus at vanishingly small contact times, the heat transfer is controlled by the contact resistance, and the heat-transfer coefficient approaches a limiting value. Schlunder [1971] argues that heat conduction across the gas wedge to the particle surface can only take place when the thickness of the wedge of gas is larger than the mean free path of the gas molecules. As such, the heat transfer is actually limited by the conduction of heat through the gas wedge, and at vanishingly small contact times, the heat-transfer coefficient will be determined by thermal properties of the gas medium.

6.4.1 Factors Influencing Heat Transfer in Vibrated Beds

The graphs of heat-transfer coefficient versus K clearly show a dependence on particle size and vibrational intensity in the manner described in Section 6.1. Similar dependence of the heat-transfer coefficient on particle size has been noted by previous investigators, as noted in Figure 2 on page 13 in Chapter 1. The heat transfer is also influenced directly by two other factors: the particle circulation, and the formation of gaps around the heat-transfer surface.

6.4.1.1 The Effect of Particle Circulation.

As noted in Chapter 5, particle circulation rates increase with increasing K. Also, residence times of particles at the heat-transfer surface decrease with increasing K (section 6.3.2) for both 707-μm (Table 12 on page 303), and 177-μm particles. Overall particle-mixing rates are poor in large-particle non-bunkered beds. In bunkered beds overall particle circulation encourages better mixing.

However, horizontal particle velocities are found to be lower for 88-μm particles than for 177-μm particles. Also, measurements made by Sprung [1987], indicate that circulation rates for glass beads of both densities are lower than for equivalently sized Master Beads.

These trends are reflected in the heat-transfer data. The initial increase in the heat-transfer coefficient with K for all particle sizes, most probably indicates an improvement in heat transfer brought about by increased circulation. As the particle-circulation rate in the neighborhood of the heat-transfer tube increases, the contact time of particles with the heater surface is reduced, resulting in an increase of the heat-transfer coefficient The overall mixing of the bed determines the rate at which heat is carried away to the rest of the bed. If the rate of mixing is high, hot particles will be removed from the locality of the heat-transfer surface, and replaced by fresh cooler particles from within the bed. This maintains a large thermal gradient between the surface and surface-adjoining particles. The lack of horizontal mixing in large-particle beds is in part responsible for the fact that heat-transfer coefficients for such beds do not increase as rapidly with increasing vibrational acceleration as they do in small-particle beds. The larger temperature gradients observed across large-particle beds support this argument.

The poor mixing of particles within the dead zone with the rest of the bed means that almost no heat is exchanged between this region and the rest of the bed. As a result, temperatures within the dead zones are always high, and the surface-bed thermal gradient low, leading to inefficient heat transfer. If particles within the dead zone circulate very slowly, as the case with 88-μm particles, the contact times of these particles with the heater surface tend to zero, and the rate of heat transfer approaches that of a packed-bed.

The higher circulation velocities noted with 177-μm Master Beads by Sprung [1987] is partly responsible for the higher heat-transfer coefficients in intermediately sized Master Beads than in equivalently sized glass beads. The electrostatic charges present in beds of glass beads can also cause a reduction in surface-to-bed heat transfer. Opalinski and Wolny [1987] report that such charges cause particles to stick to the surface as found in this study. Their theoretical evaluation of

unsteady-state heat transfer from the surface to surface-adjoining particles shows that the presence of even a single layer of particles attached to the surface by electrostatic charges, results in a considerable reduction of the heat-transfer coefficient. Furthermore, electrostatic charges increase the residence time of particles at the heater surface, since they provide an additional resistance to the flow of particles past the heat-transfer surface.

6.4.2 The Effect of Air-Gap Formation

Air gaps surrounding the heat-transfer surface provide a resistance to surface-to-bed heat transfer, which becomes more substantial as the degree of surface blanketing of the heat-transfer tube surface increases. As the gap increases in thickness, a point is reached where the heat-transfer process into the air gap when it covers a fraction of the heat-transfer surface, is no longer predominantly determined by solid properties, but rather largely by the air flow past the tube. The phase-delayed photographs of gap formation around the heater for 707-μm particles shows that there is a point in the cycle where the entire surface is blanketed by the gap. The velocity of the gas past the tube for particles of this size may be estimated from the Kroll model (which gives vertical superficial velocities across the bed). As the gas rushes downward across a bed of 707-μm Master Beads vibrated at $K=4$, the peak gas velocity is 0.28 m/s. When it rushes upward out of the bed, it reaches a peak velocity of 0.4 m/s according to the Kroll model. The heat-transfer coefficient due just to the gas flow past the tube h_g, may be estimated by a correlation for the heat-transfer coefficient for a cylinder in a normal cross-flow of air [Incropera and DeWitt,1981]:

$$Nu_t \equiv \frac{h_g d_t}{k_g} = C_t (Re_t)^m (Pr)^{1/3} \qquad [6.15]$$

with

$$C_t = 0.683, \text{ and } m = 0.466 \text{ for } 40 < Re_t \leq 4000$$

In this correlation, $Re_t \equiv (ud_t\rho/\mu)$, is the Reynolds number for the cylinder or tube, Pr is the Prandtl number for the gas, k_g is the thermal conductivity of the gas, and d_t is the tube diameter. For a peak velocity of 0.4 m/s, $Re_t = 224$, assuming a tube diameter of 12.7 mm, so that values of C_t and m listed above are valid. Using equation [6.15], the heat-transfer coefficient that would be achieved only through gas convection is 18.5 W/m^2-K. This value is much lower than typical packed-bed heat-transfer coefficients of 50 W/m^2-K. Thus, the heat-transfer coefficient in the area covered by thick air gaps, although not zero, is small, and its average value is in the order of 15-20 W/m^2-K.

Initially, higher vibrational intensities lead to higher solid-circulation rates resulting in improved heat transfer. However, as K is increased further, the thermal resistance due to air gaps surrounding the heat-transfer tube offsets further improvements in heat transfer caused by the increasing solid circulation. This results in a limiting or maximum value of the heat-transfer coefficient In fact, a peak of 484 W/m^2-K is recorded for 177-μm Master Beads at $K = 6$, and the heat-transfer coefficient falls below this value at higher values of K This trend agrees with computed values of $\overline{F}_{SA}$ given in Table 11 on page 298, where the most significant increase in $\overline{F}_{SA}$ appears between $K = 5$ and 7. By contrast, a limiting heat-transfer coefficient of 170 W/m^2-K is obtained for 707-μm Master Beads at $K = 3$, beyond which it does not increase. This value of K corresponds to that at which $\overline{F}_{SA}$ approaches a limiting value for this particle size, as indicated in Table 11 on page 298.

However, the effect of the air gaps is not solely to act as a resistance to heat transfer, but also to reduce the contact time of a particle in a surface-adjoining layer with the heater surface. If the particle is in contact with the heater surface for a fraction of the cycle, it gains heat during that contact. If it looses the heat to the rest of the bed when it is separated from the heater surface by an air gap, the particle-surface thermal contact time is the same as the fraction of the cycle in which physical particle-surface contact takes place, and will be of the same order as the period of vibration. The period of vibration is sufficiently small, that the heat-transfer coefficient must then be controlled by the gas properties or the contact resistance, since the contact time becomes vanishingly small (see also section 6.4).

Therefore, there is a balance between on the one hand, a resistance caused by the presence of the air gap which results in a reduction of the heat-transfer coefficient, and on the other hand, a reduction in the thermal contact time which tends to increase the heat-transfer coefficient to a limiting value h_c . With small particle sizes, only a small portion of the cylindrical heat-transfer surface is covered by air gaps at low values of K. At such values of K, heat transfer into small particle beds must be governed by particle circulation and mixing rates. As K is increased, the air gaps cover a greater fraction of the heat-transfer surface. Particle circulation and mixing rates simultaneously increase. Since the heat transferred into the bed is quickly removed from the vicinity of the heat-transfer surface by the circulating solid, the air gaps act mainly as a resistance to better heat transfer. Eventually, improvements in heat transfer brought about by improved circulation rates are offset by the increased resistance provided by the air gaps. In large-particle beds, the tube is engulfed in air gaps. The heat-transfer coefficient for 707-μm particles reaches a limiting value at $K = 3$ despite the decrease in residence times with increasing K noted in Table 12 on page 303. Overall particle mixing rates remain poor, so that heat is not effectively removed from the heat-transfer surface by the particles. It is therefore likely that for such beds at higher K values, the limiting heat-transfer coefficient is a balance between:

1. the reduction in time available for direct heat transfer to the solid caused by the presence of thick air gaps; and
2. a reduction of thermal contact times to the same order of magnitude as the vibrational period, so that the heat-transfer coefficient for the fraction of the cycle in which heat is transferred directly into the bed, is determined only by gas properties and particle size — the limiting case for vanishingly small thermal contact times according to Schlunder [1971].

These two effects will cause the heat-transfer coefficient for large particle sizes to reach a limiting value which is independent of the vibrational intensity parameter K.

6.4.3 Heat-Transfer Models for the Vibrated Bed

There are insufficient data at present, particularly on particle-surface contact times, to clearly differentiate between various heat-transfer models. Keeping this in mind, the treatment of models herein will be brief. It is possible to reject some models, however, simply based on the trends in the experimental results.

6.4.3.1 The Scoured-Film Model

This model is due to Gutman [1976b]. It assumes that the resistance to heat transfer is provided by a gas sub-layer composed of the wedges of gas between the particle and the heater surface as described earlier (see Figure 82 on page 312). The average surface-to-bed heat-transfer coefficient is given by:

$$h = \frac{k_g}{\delta_g} \qquad [6.16]$$

where k_g is the thermal conductivity of the gas, and δ_g, the average thickness of the gas sub-layer. The full mathematical details of the derivation of the model will not be given here. The basis of the model is that as vibrations are applied to the bed, the relative motion of the particles past the heat-transfer surface (which is fixed to the vessel) causes a reduction in the thickness of the gas sub-layer by scouring the film of gas at the heat-transfer surface, as shown in Figure 82 on page 312. Since the heat transfer in a packed bed is controlled by the contact resistance, the reduction in gas thickness caused by the vibration should lead to an increase in the heat transfer beyond that in the equivalent static or packed bed. Thus, the model suggests that the heat-transfer coefficient for a vibrated bed can be correlated with the heat-transfer coefficient of the same bed when no vibrations are applied (the equivalent packed bed), and the height of throw of the bed relative to the vessel. Mathematical analysis by Gutman [1976b] gives:

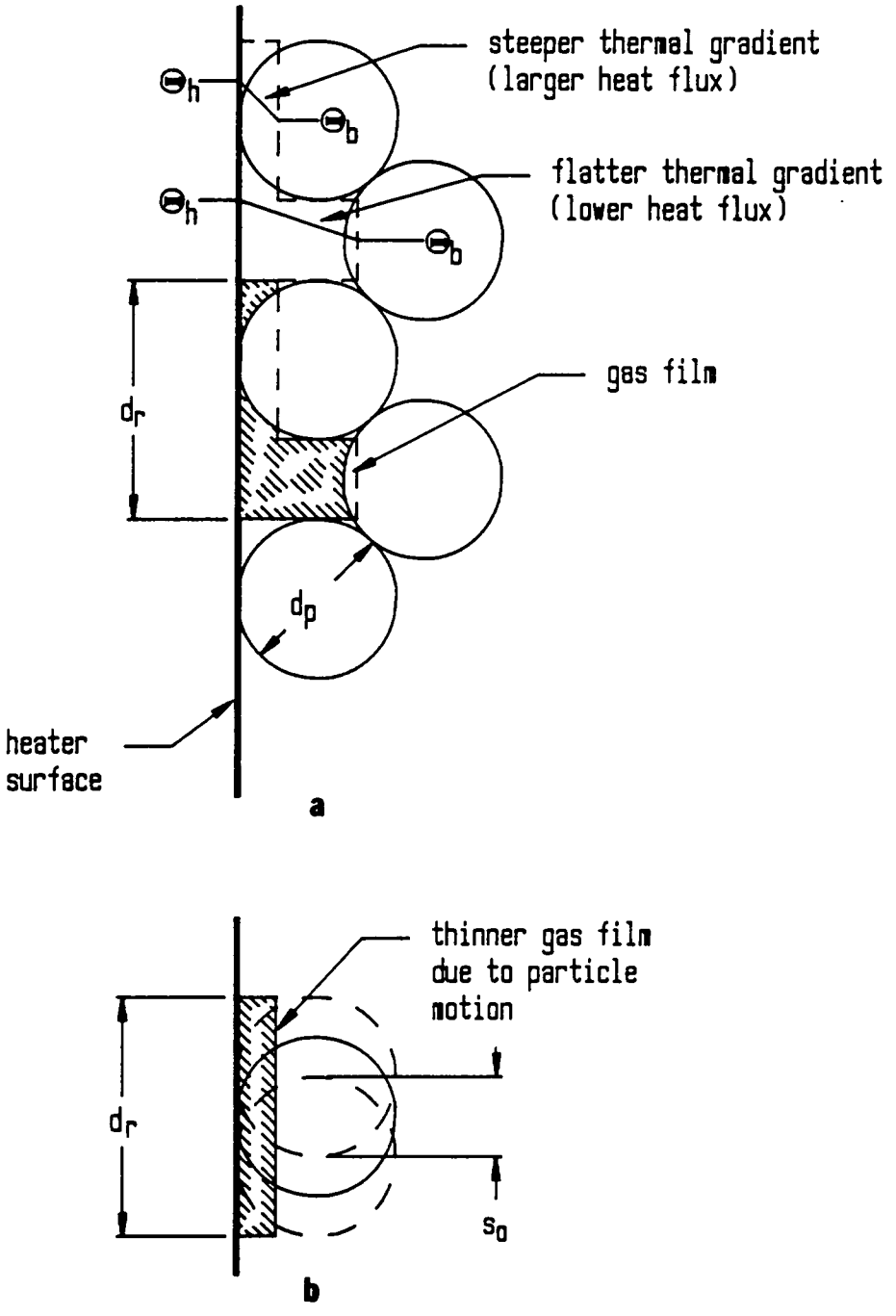

Figure 82. Schematic representation of the scoured-film model: The scoured-film model according to Gutman [1976b]. (a) In a stationary bed, particles are arranged at the heater surface in such a way that he flow of heat into particles is through a gas film which is thicker in some places. (b) As vibrations are applied, the relative motion of the particles "scours" the film, reducing its average thickness.

$$h = \frac{h_{st}(1 + d_{rp}s_o)}{1 - d_{rp}^2 s_o^2} \qquad [6.17]$$

where s_o is the maximum throw of the bed, or equivalently, the greatest thickness of the gap beneath the bed, h_{st} is the heat-transfer coefficient for an equivalent static bed. Also, $d_{rp} = d_p/(d_r^2 - d_p^2)$, where d_p is the particle size, and d_r, is a dimension of the gas sub-layer as shown in Figure 82 on page 312. Since d_{pr} and s_o are typically very small, equation [6.17] can be approximately written as:

$$h \simeq h_{st}(1 + d_{rp}s_o) \qquad [6.18]$$

suggesting a straight-line relationship between h and s_o. In addition, as the particle size is reduced, the thickness of the gas sub-layer gets smaller, leading to improved heat transfer.

This model contends that particle circulation has no direct effect on heat transfer. However, experimental evidence to the contrary is shown in this study. The higher heat-transfer coefficients obtained with normal flow past the tube — which increases particle renewal rates at the bottom of the tube — indicate that circulation rates are important.

Despite this, Gutman [1976b] obtains reasonable agreement between his experimental results and this model, particularly at low values of K. However, it should be noted that s_o is a function of K, and therefore, it is implicitly correlated to the particle circulation rate. In other words, an increase in s_o is accompanied by an increase in circulation rates. Gutman might actually have been measuring the effect of improved circulation on the heat transfer.

6.4.3.2 The One-Layer Model

The one-layer model formulated by Zabrodsky [1963] assumes that the transfer of heat is only to the first layer of particles adjoining the heat-transfer surface. Mathematical analysis by Opalinski and Wolny [1987] shows that this is the case if residence times of particles at the surface are not long

(less than 1 second). The heat transfer takes place through a layer of gas, and therefore includes the effect of a contact resistance, as shown in Figure 83 on page 315. Because of the unsteady-state nature of the problem formulation, the contact time of the particle at the surface is included.

A full mathematical analysis of the model and its applicability to vibrated beds has been attempted by Sprung [1987]. The model gives the following expression for the heat-transfer coefficient:

$$h = \rho_s c_{p_s} v_n (1-\varepsilon)\left[1 - \exp\left(\frac{-1.2\,k_g}{\delta_g \rho_s c_{p_s} v_n (1-\varepsilon)^{1/3}}\right)\right] \qquad [6.19]$$

Here, k_g is the thermal conductivity of the gas, c_{p_s} is the heat capacity of the solid, v_n which represents the rate of particle renewal at the surface, is the velocity of particles normal to the heat-transfer surface, and is related to the contact time t_c, by :

$$t_c = \frac{0.807 d_p}{v_n (1-\varepsilon)^{1/3}} \qquad [6.20]$$

The average gas-layer thickness δ_g, is given by:

$$\delta_g = b + \frac{d_p}{6} \qquad [6.21]$$

where b accounts for any additional gap existing between the heater and the surface-adjoining particles. Sprung [1987] suggests that the factor b in equation [6.21] be used to represent the thickness of the air gap surrounding the heat-transfer tube in a vibrated bed. A full treatment of the predictions of the model on vibrated-bed heat transfer has been carried out by Sprung [1987]. The problem in analyzing the model accurately is the lack of knowledge of contact times. Also, Sprung's assumption of simply including the gap thickness in the expression for δ_g , might be too simplistic, since the formation of the gap is not uniform, and it also serves to alter the contact time of particles with the heater.

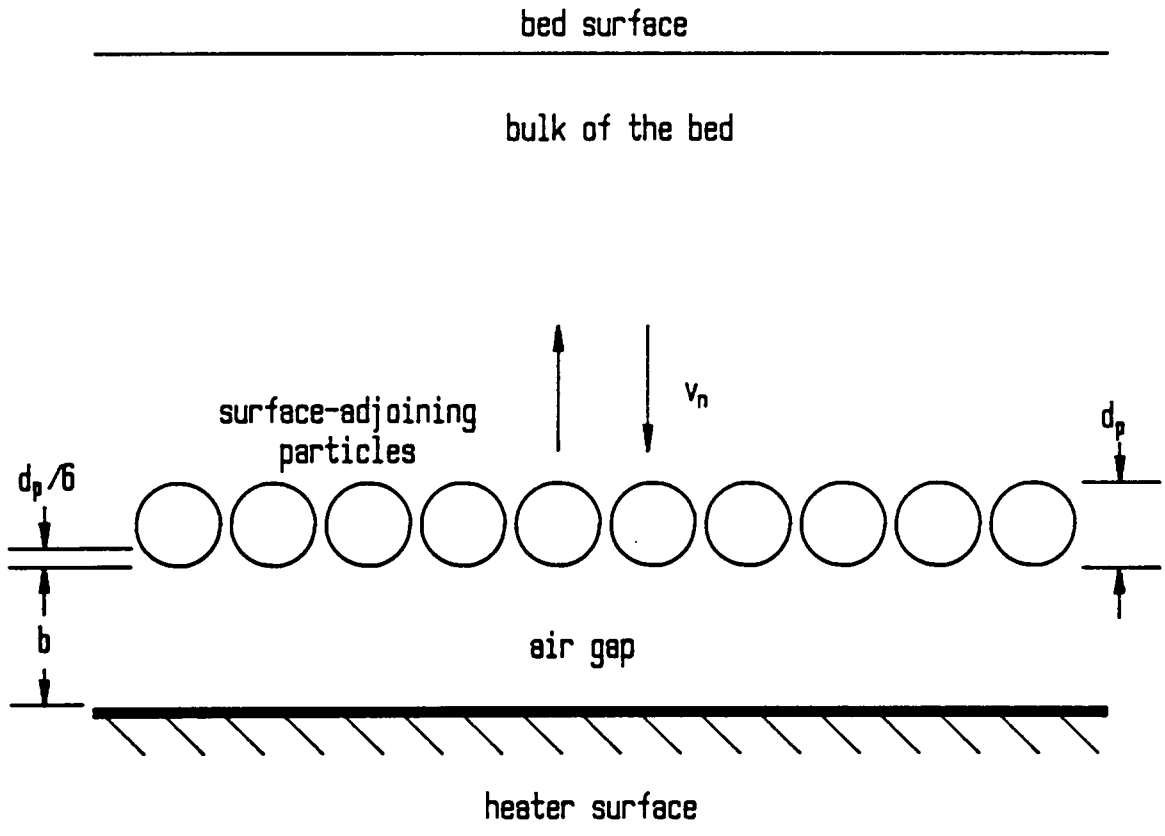

Figure 83. Schematic representation of the one-layer model: The heat-transfer process according to the one-layer model of Zabrodsky [1963]. Notation: d_p - particle size; b - thickness of an air gap separating the surface-adjoining particles from the heater surface; v_n - velocity of particle renewal at the heater surface. Particles are assumed to move into the bulk of the bed at velocity v_n , and back to the surface-adjoining layer at the same velocity. v_n therefore represents a rate of solid renewal at the surface.

Broadly speaking, the model predicts an increase in the heat-transfer coefficient with increasing particle circulation rates, and a reduction in heat transfer with increasing gap size. These trends are also observed in the experimental results. The model predicts that the effect of air gaps on reducing heat transfer is more noticeable in small-particle beds than in large-particle beds.

In the limiting case of vanishingly small contact times, the model gives for the heat-transfer coefficient:

$$h = \frac{1.2\, k_g (1-\varepsilon)^{2/3}}{\delta_g} \qquad [6.22]$$

According to this equation, under the condition of small contact times, the heat-transfer coefficient is independent of particle thermal properties and contact times. Sprung [1987] suggests that the limiting value of the heat-transfer coefficient observed with 707- and 500-μm Master Beads is a result of a very small contact time of these particles on the heater surface. If this argument were correct, heat-transfer coefficients for glass beads of the same size should approach the same limiting value, since equation [6.22] is independent of particle thermal properties. However, as seen from Figure 73 on page 273, the limiting value of the heat-transfer coefficient for 707-μm glass particles of both high and low densities is higher than for Master Beads. It is of course possible that the gap size is smaller for both types of glass beads, which would reduce the value of δ_g in equation [6.22], and lead to higher limiting heat-transfer coefficients for these solids. However, as stated earlier, the one-layer model predicts that the effect of gap thickness is small for large particles. These anomalies suggest that a straight-forward application of the one-layer model to the vibrated bed might not be suitable.

6.4.3.3 The Packet Model

Kal'tman and Tamarin [1969] use the packet model of Mickley and Fairbanks [1955] for heat transfer in gas-fluidized beds, to describe surface-to-bed heat transfer in a vibrated bed. The instantaneous heat-transfer coefficient h_{pl} is given by:

$$h_{pl} = \sqrt{\frac{k_b c_{p_s} \rho_s (1-\varepsilon)}{\pi t}} \qquad [6.23]$$

where k_b is the effective thermal conductivity of the bed, c_{p_s} is the particle heat capacity, and ρ_s, the solid density. Gutman [1974] has criticized the use of the packet model to describe surface-to-bed heat transfer in vibrated beds, because contact times calculated from the overall solid circulation velocities and the length of the heater yield heat-transfer coefficients based on equation [6.23] that are about four times lower than actual measured values (see Chapter 2, §2.1.3.2). Observation of particle circulation in the neighborhood of the heat-transfer surface shows that particle circulation rates are different at the surface. In fact, Kal'tman and Tamarin [1969] do report the existence of small-scale fast circulation loops in the vicinity of their heater. This would give smaller contact times and consequently, higher heat-transfer coefficients than if overall circulation velocities were used.

The average heat-transfer coefficient is obtained by integrating equation [6.23] over the contact time t_c, assuming continuous renewal of particles at the heater surface:

$$h_p = \frac{1}{t_c} \int_0^{t_c} h_{pl}\, dt \qquad [6.24]$$

However, this will give infinite heat-transfer coefficients as the contact time approaches zero, which is physically impossible. The solution is to combine the packet model with another model that accounts for vanishingly small contact times [Gelperin and Einstein,1971]. Schlunder [1982] proposes

the following equations to determine the heat-transfer coefficient under the condition of vanishingly small contact times:

$$h_s = (1-\varepsilon)^{2/3} h_{p_s} + \left(1-(1-\varepsilon)^{2/3}\right)\left[\frac{k_g}{(d_p/\sqrt{2}) + \lambda_{mg}}\right] \qquad [6.25]$$

Here, λ_{mg} is a modified gas mean-free path defined by Schlunder [1971]. The heat-transfer coefficient from the heater to the nearest particles, h_{p_s}, is given by:

$$h_{p_s} = \frac{4k_g}{d_p}\left[\left(1+\frac{2(\lambda_{mg}+\delta_g)}{d_p}\right)\ln\left(1+\frac{d_p}{2(\lambda_{mg}+\delta_g)}\right) - 1\right] \qquad [6.25a]$$

In this equation, δ_g is the "roughness" of the particle layer in contact with the heater, and can be considered equivalent to the thickness of the gas wedges or sub-layer defined earlier. Now the overall surface-to-bed heat-transfer coefficient may be written in a similar fashion to equation [6.14] as follows:

$$\frac{1}{h} = \frac{1}{h_p} + \frac{1}{h_s} \qquad [6.26]$$

The problem with evaluating this model is that the contact times of particles with the heat-transfer surface are not known. However, according to equation [6.14], $h \to h_s$ as $t_c \to 0$, which implies that at very small contact times, the heat-transfer coefficient is determined by gas properties. This suggests, as does the one-layer model, that heat-transfer coefficients for large particles where gaps appear around the heater tube for a large portion of the vibrational cycle, are dominated by small-contact time effects. The anomaly of higher heat-transfer coefficients for 707-μm glass beads as compared to similarly sized Master Beads still remains.

6.4.3.4 A Position-Dependent Formulation for the Heat-Transfer Coefficient

One of the problems with defining a contact time for the horizontal tube in a vibrated bed is that the presence of periodic air gaps which form on the surface reduces the actual contact time of particles at the surface, to a fraction of the time that they spend in a surface-adjoining layer. An alternative way to consider the problem is to assume that the contact time within a region of heat-transfer surface that is covered by air gaps for at least one instant within the vibrational cycle, is equal to the fraction of the cycle in which particles are in contact with the heater surface. This assumption is valid as long as the heat picked up by the particle during the fraction of the cycle in which it is in contact with the heater surface is *all* dumped into the bed during the rest of the cycle when the particle looses contact with the surface. That is, the particle returns to the bed temperature during the fraction of the vibrational cycle when an air gap separates it from the heat-transfer surface.

The probe surface can be divided into two regions: one that is covered by an air gap for at least one instant in the vibrational cycle, and another which is in contact with the bed throughout the cycle. Referring to Figure 78 on page 294, suppose that the maximum coverage of the surface by air gaps corresponds to an angle ϕ_m, such that:

$$\phi_m = 2\sin^{-1}\left(\frac{0.5p_m}{r_t}\right) \qquad [6.27]$$

The distance between points of closure of the air gap on the tube surface at maximum coverage is p_m. The maximum fractional coverage by air gaps of the whole surface area is denoted by F_m, which may be obtained from the limiting values of the plots of F_{SA} versus the phase angle θ given in Figure 79 on page 296, and Figure 80 on page 297.

The fraction of the surface never covered by air gaps is $(1 - F_m)$. Within this fraction of the surface, the contact time will be the actual time that a particle spends in a surface-adjoining layer. The av-

erage heat-transfer coefficient within this fraction of the surface, h_p, will be given by a penetration-type model, such as the packet model.

Within the fraction of the surface F_m, over which air gaps do form, a particle at any angular position φ on the surface, looses contact with the surface for a time $\theta_1(\varphi)$ to $\theta_2(\varphi)$ where $\theta_1(\varphi)$ is the phase angle at which a gap first appears at the angular location φ, and $\theta_2(\varphi)$ is the phase angle at which the gap disappears at φ. It is seen from Figure 78 on page 294, for a symmetric air gap on the top surface of the heat-transfer tube, that as the air gap appears at an angular location φ, it also simultaneously appears at $\pi - \varphi$. The angle included between these two angular positions is ϕ. On the lower surface, the gap appears at $\pi + \varphi$ and $2\pi - \varphi$, simultaneously. For either half of the tube surface, the included angle ϕ is related to the fractional coverage of the heat-transfer surface through:

$$\phi = 2\sin^{-1}\left(\frac{0.5p(\theta)}{r_t}\right) = 2\pi F_{SA}(\theta) \qquad [6.28]$$

This means that for any value of φ, values of $\theta_1(\varphi)$ and $\theta_2(\varphi)$ may be obtained from graphs of F_{SA} versus θ. The range of phase angles over which particles are in direct contact with the surface at the location φ is given by $2\pi - [\theta_2(\varphi) - \theta_1(\varphi)]$, assuming that the phase angle θ is in radians. The contact time of a particle at φ is then given by:

$$t_c(\varphi) = \frac{2\pi - [\theta_2(\varphi) - \theta_1(\varphi)]}{2\pi} \frac{1}{f} \qquad [6.29]$$

where f is the frequency of vibration. This equation states that the contact time of a particle with a region of the heat-transfer surface which is covered by air gaps for some portion of the vibrational cycle, is a fraction of the period ($1/f$). The contact times will therefore be small, and the heat-transfer coefficient for heat transfer directly to particles in these regions will approach h_t, the heat-transfer coefficient for extremely small contact times given by equation [6.25]. The heat-transfer coefficient h_t is independent of contact times and most likely of location as well. In that case, an

average contact time may be defined for the fraction of the surface F_m, which is covered by air gaps for at least one instant within the vibrational cycle, as follows:

$$\bar{t}_c = \frac{1}{\pi/2 - \varphi_m} \int_{\varphi_m}^{\pi/2} t_c \, d\varphi \qquad [6.30]$$

The angular position φ_m, corresponding to the maximum coverage of the surface by air gaps is equal to $(\pi - \phi_m)/2$. When the coverage of the surface becomes very small, $\phi_m \to 0$, and $\varphi_m \to \pi/2$. At the same time, $t_c(\varphi \to \pi/2) \to 1/f$, so $\bar{t}_c \to 1/f$, implying that the particle is in contact with the surface for the whole cycle as expected. The average fraction of the vibrational cycle during which a particle located with the area F_m is in contact with the heat-transfer surface is $\bar{t}_c f$. During this fraction of the cycle, the heat-transfer coefficient is equal to the small-contact time heat-transfer coefficient, h_s.

During the remaining fraction of the cycle $(1 - \bar{t}_c f)$, heat transfer between the surface and bed takes place through the gap by gas convection and conduction through the gas in the gap. The heat conducted through the gap is small compared to the convection term, so the heat-transfer coefficient within the gap will equal the gas convection heat-transfer coefficient h_g, as given for example, by equation [6.15]. Therefore, the average heat-transfer coefficient for the fraction F_m, of the heat-transfer surface is: $(\bar{t}_c f)h_s + (1 - \bar{t}_c f)h_g$.

For the whole surface, the heat-transfer coefficient is given by:

$$h = (1 - F_m)h_p + F_m[(\bar{t}_c f)h_s + (1 - \bar{t}_c f)h_g] \qquad [6.31]$$

where h_p is dependent on a contact time t_{ce}, (see section 6.4.3.3) that a particle spends adjacent to that fraction of the heat-transfer surface which is in contact with solids through the entire cycle (never covered by air gaps).

For a small particle size where the coverage by gaps is very small, $F_m \rightarrow 0$ and $h \rightarrow h_p$, so that the heat-transfer coefficient is determined by the particle circulation rates. This is as experimentally observed, since in small particles, the increase in heat-transfer coefficient with K is large for $K \leq 5$, where the corresponding increases in $\overline{F}_{SA}$ are small.

For large particle sizes (for example 707 μm), where the entire heat-transfer surface is covered by air gaps at some instant or another in the vibrational cycle, $F_m \rightarrow 1$. This implies that the heat-transfer coefficient for large particles is determined by h_s and h_g, both of which are only dependent on gas thermal properties and particle diameter, and will cause the heat-transfer coefficient to reach a limiting value independent of K. Also, as air gaps increasingly cover the surface for a greater fraction of the vibrational cycle, $\bar{t}_c$ becomes small, and the contribution of h_s gets correspondingly smaller. In the limiting case where the gap covers every point on the surface for the whole cycle, $\bar{t}_c \rightarrow 0$ and $h \rightarrow h_g$, which means the heat-transfer coefficient will be determined by the gas-convective heat transfer. Both these trends are also experimentally observed in large-particle beds.

The anomaly of higher heat-transfer coefficients for 707-μm glass beads remains, but if $\bar{t}_c$ for glass beads is larger than for Master Beads (the gap on average covers the surface for a shorter fraction of the cycle), then the limiting heat-transfer coefficient for 707-μm glass beads will be greater than that for equivalently sized Master Beads.

There are however two problems with this formulation for heat-transfer coefficients:

1. It is virtually impossible, short of analyzing several feet of high-speed movie film, to determine the contact time t_{cc}, of a particle with the fraction of the surface never exposed to air gaps, since theoretical predictions of particle velocities in the locality of the heat-transfer surface, and the extent of coverage by air gaps of the heat-transfer surface are not currently possible.

2. It assumes that when a particle is lifted off the heater surface, it looses all the heat which it gains while in contact with the surface.This may be true for a particle located over a point

which is covered by air gaps for at least half of the vibrational cycle. However, if the particle is located over a point which is covered for only a short fraction of the cycle, it will continue to increase in temperature from one cycle to the next, as long as it remains adjacent to the surface. To include the effects of varying temperature between one contact and the next will make the analysis far more complex, than the simple approach adopted here.

Perhaps the best way to study heat-transfer mechanisms is by using a flat vertical heat-transfer surface. Such a geometry will eliminate air-gap formation around the surface. In addition, if the vertical heat-transfer surface is joined to the floor by a non-conducting support of the same thickness, no "dead" zones can form beneath the surface. The elimination of air gaps might also lead to an increase in overall heat-transfer coefficients, so this surface geometry is of practical interest as well.

6.5 *Summary of Heat Transfer in Vibrated Beds*

The most important points pertaining to aspects of vibrated-bed heat transfer covered in this study may be summarized briefly as follows:

1. Measured heat-transfer coefficients for Master Beads and glass beads show a direct dependence on both particle size and vibrational intensity. With large particles, the heat-transfer coefficient reaches a limiting value as the vibrational intensity parameter K, is increased. With small particles the heat-transfer coefficient passes through a maximum as K is increased. Heat-transfer coefficients increase with decreasing particle size until a size of 177 μm is reached. Below this particle size, the heat-transfer coefficient drops off.

2. The greatest source of error in the method used to measure heat-transfer coefficients arises out of estimating the temperature of an unevenly heated bed. This generally leads to errors of about 10% in the measured heat-transfer coefficient, but occasionally the error can be as high as 15%.

3. Air gaps are observed to form around a horizontal heater tube placed in the bed. By taking phase-delayed photographs over a vibrational cycle, it is possible to estimate the time-averaged coverage of the heat-transfer surface by these air gaps. The average surface coverage is larger for large-particle beds than for beds of small particles.

4. In small-particle beds, "dead" or "segregated" zones which are detrimental to heat transfer form below the heat-transfer tube. Particles within these zones move at lower velocities than those within the rest of the bed, and in addition do not mix with the rest of the bed.

5. Surface-to-bed heat transfer in the vibrated bed appears to be strongly influenced by particle circulation rates in the vicinity of the heat-transfer surface. However, the formation of air gaps is detrimental to heat transfer particularly in small-particle beds. These gaps increasingly cover a greater fraction of the surface for a greater proportion of the vibrational cycle as the vibrational intensity is increased. As a result, the initial improvements in heat transfer brought about by improved particle circulation as K is increased are offset by the increased coverage of the surface by these air gaps.

6. Since the heat transfer is so strongly dependent on particle circulation rates, a penetration-type heat-transfer model is perhaps most applicable to vibrated-bed heat transfer. However, since particle contact times with the heat-transfer surface are unknown, it is impossible to quantitatively check the validity of any model.

7.0 Conclusions and Recommendations for Further Study

7.1 Conclusions of This Study

The dynamics of the shallow vibrated bed and the heat-transfer process from an immersed horizontal cylindrical surface have been investigated in this study. To reduce the number of vibrational parameters affecting the characteristics of the bed, a frequency of 25 Hz is used exclusively. Commercial mechanical vibrators usually have an upper frequency limit of 30 Hz. The frequency chosen, therefore, represents one of practical interest, and is also within the range of frequencies found to produce the best bed "quality" (10 to 40 Hz).

7.1.1 Equipment and Instrumentation

Previous experimental studies of vibrated beds have suffered from a number of drawbacks, including the following:

1. The use of inadequately designed vibration equipment, in which the mass of the vibrating table is small compared to that of the bed. This results in a severe distortion of the sinusoidal displacement-waveform of the vibrating vessel when the bed collides with the vessel floor. The distortion can be sufficiently severe to create secondary vibrations in the system.

2. Experimental work has been carried out over a range of vibrational frequencies, even though the vibration assembly has a particular resonance frequency within that range. The effect of this is that the experiment will falsely indicate a frequency dependence of some bed properties, such as the porosity.

3. Some pressure transducers used to measure the cyclic variation of floor pressures beneath the bed have had inadequate frequency responses. This causes the transducers to integrate the pressure signal, giving incorrect data on cyclic variations in floor pressures, by removing high-frequency components of the signal.

4. The use of remotely mounted pressure transducers gives false values of the average pressure beneath the bed, because of the additional volume of gas within the lines connecting the sampling port to the transducer. Particularly if pressure variations beneath the bed are large, the flux of air from this additional volume into and out of the air gap beneath the bed could be of the same magnitude as that across the bed. In one case [Chlenov and Mikhailov,1972], the average pressure beneath a 30-mm deep bed has been reported to be as low as -6 kPa, which is lower than even the lowest floor pressure obtained in this study for the same bed depth.

5. The output from transducers measuring various properties or characteristics of the bed have not been correctly phase-matched. In most cases, phase-matching the output of a transducer (for example, a pressure transducer), with the vessel displacement has been achieved by comparing both signals on an oscilloscope, which is inaccurate.

6. Some heat-transfer probe designs used previously have a number of deficient design features, including:

   a. A non-isothermal surface, leading to a transfer of heat by particles from one point on the surface to another, instead of directly into the bed.
   b. Grooves cut into the surface to carry thermocouples cause distortions in heat fluxes within the probe. In some cases, the thermocouples read temperatures that are lower than the actual surface temperature of the probe.
   c. Heating elements used in some probes have "dead" zones at either end in which no heat is generated. These dead zones lead to distortions in the thermal flux, particularly at the ends of the probe.
   d. Some probes are held in place by supports that stick vertically out of the bed. Such supports alter circulation patterns in the vicinity of the probe.

These problems have been corrected in this study as follows:

1. The vibration assembly is designed to be extremely rigid, and the mass of the vibration table is several times that of the bed. This practically eliminates any distortion of the displacement waveform due to the collision of the bed with the vessel floor. When the bed and vessel collide, some noise appears in the accelerometer signal due to the mechanical impact noise of the bed collision. However, this noise does not appear in the output of either of the displacement transducers used in this study, and therefore cannot be distorting the displacement signal.

2. The vibration system is operated close to its resonance frequency for all experiments. The resonance frequency can be changed by altering the stiffness of leaf-springs supporting the vibrating table, keeping in mind that the mass of the vibrating table must always be large enough to eliminate distortion of the displacement waveform.

3. All transducers used in this study have an adequately high frequency response. Most of the transducers used do not have any appreciable phase lag at the frequency of vibration. When the phase lag is noticeable (as is the case with the displacement transducers used in this study), it is calibrated at the frequency of operation and summed to the output signal of the transducer.

4. An electronic phase-delayed trigger circuit is devised to phase-match various cyclic phenomena and bed properties with the phase of the vessel displacement. The circuit detects the positive zero cross-over point of the displacement waveform, and then issues a trigger pulse delayed by a prespecifed number of degrees of phase lag. The trigger pulse can be used to initiate the acquisition of the output signal of a transducer used to measure some property of the bed (such as the floor pressures), at any phase angle — for example, at 0°, which is the start of the vibrational cycle. The data collected in this manner are perfectly phase-matched with the vessel displacement.

5. The phase-delayed pulse can also be used to trigger a stroboscopic light source once every cycle. Viewing the bed illuminated solely by this light source gives the bed the appearance of being "frozen" at the preset phase angle. In this manner, a periodically varying visual characteristic of the vibrated bed may be followed over a complete vibrational cycle. By illuminating the bed with an electronic flash gun triggered by the phase-delayed pulse, high-resolution 35-mm photographs of the bed may be obtained with a slow shutter speed on a camera. These techniques allow a more detailed study of cyclic phenomena within the bed than has been previously possible.

6. The heat-transfer probe used in this study is designed to maintain a constant surface temperature even if heat fluxes across the surface vary considerably with angular position. A custom-built heating element provides uniform heating along the entire length of the heat-transfer probe. It also allows for thermocouples leads to be passed radially downward from the heater surface and out through the center of the heating element, thus eliminating distortions in the heat flux across the surface caused by grooves cut in the surface for thermocouple leads.

The probe is held in place by cylindrical supports of the same diameter as the heat-transfer tube. The supports pass through the walls of the vessel, so that they do not interfere with overall circulation patterns within the bed.

7.1.2 Dynamics of the Shallow Vibrated Bed

7.1.2.1 Mechanics of the Vibrated Bed

An examination of the dynamics of the vibrated bed is carried out in relation to the one-dimensional models of Kroll [1954,1955] and Gutman [1974,1976a]. Both models can be written in a similar dimensionless form, using the same set of dimensionless groups: Ψ, Λ, and Γ . These groups are functions of the particle size and density, the gas viscosity, the bed permeability, and the vibrational frequency and intensity. Only two of these dimensionless groups (Ψ and Λ), are necessary to describe the Kroll model in a dimensionless form. The dimensionless group Ψ may be thought of as a "dimensionless bed permeability parameter", or alternatively, as a group that describes the effect of viscous drag caused by an oscillatory flow of gas through a porous bed. Λ describes the apparent weight of the bed under the influence of the vibrational acceleration. Furthermore, a ratio R_h, of these two groups may be defined, which describes the resistance of the bed per unit bed mass to gas flows at any specified vibrational frequency. The third dimensionless group Γ, used in transforming the Gutman model to its dimensionless form, describes the effect of gas compressibility on the pressure gradient across the bed.

Cyclic floor-pressure measurements made at three horizontal locations beneath the bed exhibit the same periodic nature as observed in previous studies [Kroll,1955; Gutman,1974]. As the bed lifts off the vessel floor, the gauge pressure beneath the bed become negative, causing gas to rush downward across the bed. When the bed falls back toward the vessel base, the floor gauge-pressure begins to increase again, eventually rising above zero, and causing a reversal of the direction of gas

flow across the bed. When the bed collides with the vessel base, the floor pressure goes through a sharp positive peak, after which it decays back to the level at the start of the vibrational cycle.

The positive and negative peaks in the floor pressure signals are found to be dependent on the particle size. In general, the bed becomes more resistant to gas flows as the particle size is decreased, causing peaks of greater magnitudes in the floor pressure during the cycle. As the vibrational intensity is increased, larger differences in the accelerations of the vessel and bed lead to greater cyclic swings of the floor pressures. With a 30-mm deep bed of Master Beads, the maximum positive peak floor pressure recorded is about 4.5 kPa, with a particle size of 125 μm and $K = 5$. The largest magnitude of the negative peak floor pressure recorded is about 2.6 kPa, also with a particle size of 125 μm at $K = 5$. Both positive and negative peak pressures are found to increase linearly with bed depth, up to the maximum bed depth of 60 mm used in this study. With small particles, the magnitude of the floor pressure increases with increasing solid density as predicted by theory; but for large particles, the range of solid densities used in this study has negligible effect on the magnitudes of the floor pressures.

The bed trajectory or the thickness of the air gap beneath the bed can be estimated by a semi-empirical method, by using measured pressures to solve the one-dimensional equation of motion of the bed.

Predictions of the Kroll model are reasonably close to floor pressures measured in this study for a 30-mm deep bed. The major discrepancy is the rate of decay after the bed-vessel collision. The Kroll model predicts an instantaneous decay to zero gauge-pressure after the collision, but the actual rate of decay is slower. The slower rate of decay is as a result of gas compressibility. The dimensionless group Γ, that predicts the effect of gas compressibility, is strongly dependent on the bed depth, and the agreement of the Kroll model with actual values, particularly for small particles, may not be as good as the bed depth is increased.

For large particles, the thickness of the air gap beneath the bed as predicted by the Kroll model is almost identical to that obtained from the semi-empirical method using measured floor pressures. However, the air-gap thickness or bed trajectory for large particles differs from that predicted by the single-particle model which neglects air-drag effects, indicating that although the aerodynamic drag effects are small in such beds, they are not negligible. With smaller particle sizes, differences between the predictions of the Kroll model and those obtained from the semi-empirical method become more pronounced. The Kroll model always predicts a smaller gap thickness. Also, as the particle size is reduced, the size of the air gap beneath the bed obtained by the semi-empirical method, becomes increasingly dependent on the bed porosity.

The instant at which the bed lifts off the vessel floor (the point at which the net force on the bed is equal to zero) as predicted by the Kroll model is almost the same as that obtained by the semi-empirical method, differing at most by 2 to 3° of phase lag. This means that the Kroll and Gutman models will both predict approximately the same phase angle of lift-off of a shallow vibrated bed off the vessel floor for a given set of bed and vibrational conditions.

However, the observed instant of bed-vessel separation lags the instant of lift-off predicted by theory by several degrees. With fine particles, the bed does not appear to separate from the vessel floor at any point in the cycle. It is possible that this might be caused by the method of observing bed-vessel separation (back-lighting the bed with a strobe lamp triggered by a phase-delayed pulse), which might not be accurate enough to detect an air gap with a thickness of the same order of magnitude as the particle diameter. The more likely explanation of the delay, is that the bed expands as it attempts to separate from the vessel floor. An approximate calculation shows that even a minute expansion of the bed after the instant of null-force, would account for the observed delay in the bed-vessel separation. Particles within the bed have to move apart by a certain distance in order to move relative to each other, and this will result in an overall expansion of the bed.

In addition to vertical pressure gradients that develop within the bed, horizontal pressure gradients are also observed, particularly with small particles. During the fraction of the cycle when the entire

bed is in flight, the floor pressure at the side wall is higher than at the center of the bed provided that the center of the bed is deeper than at either side wall. This gradient causes a horizontal flow of gas from the wall toward the center.

The bed does not collide uniformly with the vessel floor. Instead, if the center of the bed is deepest, the collision occurs first at the side wall, and the gap closes from the side wall toward the center of the bed. As the bed collides with the floor, a compaction wave is observed to travel diagonally upward across the bed. The horizontal propagation velocity is determined by the rate at which the gap closes toward the center of the bed, and the vertical propagation velocity is determined by the rate at which gas can be expelled from the bed. Behind the compaction wave, particles are forced together, giving that region of the bed the appearance of a packed bed. In front of the wave, the bed is still loose. After the compaction wave has passed through the whole bed, the bed remains in a packed state until the null-force point in the next cycle. As the compaction wave passes through the bed, the horizontal pressure gradient reverses behind it, so that gas flows back from behind the compaction wave-front towards the wall; but in front of the wave it continues to flow forward toward the center.

With fine aeratable powders, the gas within the bed cannot be completely expelled within one cycle, so the bed continues to draw in air and expand over a number of cycles (23 to 24 cycles at 25 Hz), until it reaches a critical volume at which micro-bubbles are formed within the bed. Once this happens, gas is suddenly expelled from the bed during a fraction of a cycle. This behavior of fine aeratable powders is termed "breathing".

The average floor pressure over a vibrational cycle is found to be negative at the center of the bed, and positive at the wall. However, average horizontal gas flows across the bed cannot be based on these time-averaged floor pressures. This is because the passage of the compaction wave through the bed during the bed-vessel collision, alters the horizontal pressure gradients considerably during that fraction of the cycle. This highlights the fact that predictions of the behavior of multi-dimensional beds cannot always be extrapolated from one-dimensional theory.

7.1.2.2 Bunkering and Particle Circulation

In small-particle beds which are resistant to gas flow, horizontal pressure gradients can develop in an initially flat bed due mainly to perturbations in the pressure fields at the walls. Once the gradients develop, the bed begins to pile up or bunker at one part of the vessel, so that the top surface of the bed is no longer flat. Three bunker configurations are possible: a center-high configuration, which is the most unstable, a wall-high configuration, and a center-shallow configuration.

Each type of bunker has a unique solid circulation pattern associated with it. In general, in a bunkered bed, particles move from a shallow part of the bed toward the deeper part of the bed, except for a narrow region on the top surface in which particles return at a high rate from the deeper section of the bed top the shallow part.

In large-particle beds, which are permeable to gas flows, no horizontal pressure gradients develop, and as a consequence, these beds do not bunker. In a vacuum, bunkering disappears in all beds, indicating that it is caused by pressure gradients within the bed.

The dependence of the angle of bunkering on the particle diameter, and the vibrational intensity appears to be qualitatively described by an equation suggested by Judd and Jackson [1980], which predicts the change produced in the dynamic angle of repose of material in a rotating drum, by a flow of gas across the surface of the material. In bunkered beds, particle motion is driven by gas flows that take place within the bed in response to pressure gradients. As the bed lifts off the vessel base, the pressure beneath a shallow region of the bed is higher (less negative) than beneath a deeper region of the bed. The resulting pressure gradient causes a horizontal flow of gas from the shallow to the deep region of the bed. Since the bed is loose during flight, particles are dragged along in the same direction by interstitial gas flows. When the bed collides with the vessel floor, it becomes packed behind the compaction wave. Even though the horizontal pressure gradient reverses its direction behind the compaction wave, particles in this region are no longer free to move, and

therefore do not reverse their direction of motion. In a vacuum, this type of solid circulation disappears, indicating that it is caused by the viscous drag of the gas on individual particles.

In non-bunkered beds, particle motion is downward in about two or three layers adjacent to the walls, and upward in the rest of the bed. The particle motion is driven by wall friction, which prevents particles at the wall from travelling upwards as fast as the rest of the bed when the bed lifts off the vessel. This sets up a downward motion of particles at the wall relative to particles within the bed, resulting in overall particle circulation. In a vacuum, this type of solid circulation persists for all particle sizes, indicating that it is driven by some factor, such as wall friction, which is independent of the pressure of air within the bed.

The presence of electrostatic forces between glass particles in the bed tends to reduce the bed mobility, and results in lowered particle circulation rates.

7.1.2.3 The Expanded Zone on the Top Surface of the Bed

An expanded zone is observed along the top surface of small-particle bunkered beds throughout the vibrational cycle. No such expanded region can be observed along the bottom surface of the bed. High-resolution phase-delayed photographs show the evolution of the expanded zone over a cycle. At the end of one cycle, the expanded zone does not collapse fully. Consequently the top layers of the bed are in a loose state at the start of the next cycle, when gas flows down across the bed. Experiencing less drag as a result of their loose packing, these layers lift off sooner and higher than the rest of the bed, which is in a packed state after the compaction wave has passed through it during the bed-vessel collision process. Thus, an expanded zone is created above the bed. Later in the cycle, gas rushing out of the bed further expands this zone, causing it not to collapse fully by the end of the cycle.

The return flow of particles from the center of the bed toward the side walls is within this region of the bed. Intense gas-solid mixing is observed within the expanded zone.

7.1.2.4 States of the Shallow Vibrated Bed

Different "states" of the shallow vibrated bed can be identified. When only a few particles are present within the vessel, they move about in a random fashion, their trajectories being determined by simple Newtonian mechanics, with superimposed air drag on each particle. This is the Newton-I state. As more particles are added, the number of particle-particle collisions increase to a point where some particles loose a significant amount of their kinetic energy during a fraction of the cycle, and tend to fall toward the floor of the vessel. In the next cycle, they are thrown upward again. The result is the appearance of a region of higher particle density close to the floor of the vessel for a fraction of the cycle. This is called a Newton-II state.

As even more particles are added, aerodynamic effects become more important, and the bed begins to act a coherent mass. It lifts off the floor at one point in the cycle, and collides with it later in the cycle. The bed is considerably expanded, particularly as it falls back toward the floor. Therefore, this state is described as coherent-expanded. The state is characterized by a high degree of particle turbulence and excellent gas-solid mixing.

When the bed depth is increased further (beyond about 10 particle layers on the average), the bed expansion during flight is considerably reduced, giving the bed a denser appearance, although particles within it continue to be mobile during the period of bed flight. Because of the nature of the bed, this is termed the coherent-condensed state. Particles move in a more orderly fashion, but particle velocities are lower than those in the coherent-expanded state. For small particles, the expanded state continues to persist along the top surface of the bed.

The tendency for small particles to group together in an aerodynamic flow field, causes bunkering to occur at very shallow bed depths for such particles. The early occurrence of bunkering also results in a premature transition from the coherent-expended to the coherent-condensed state for fine particles.

The transitions from the coherent-expanded state to the coherent-condensed state, as well as the initial occurrence of bunkering, appear as a family of straight parallel lines, with particle diameter as the parameter, on logarithmic plots of the dimensionless group Ψ (which includes the bed permeability, the bed depth, and the vibrational frequency) versus the dimensionless bed depth, expressed in terms of the number of particle layers.

7.1.2.5 A Multi-Dimensional Model

A multi-dimensional model which includes bed expansion is difficult to solve, partly because the nature of the variation in bed porosity over a vibrational cycle is not known. Some simplification can be introduced by assuming that the only significant porosity variation in a bed that lifts off the vessel floor occurs during the lift-off and collision processes, which can no longer be assumed to be instantaneous. However, the unsteady-state, two-dimensional nature of the gas flow within the gap that appears beneath the bed is still difficult to deal with mathematically.

An alternative approach suggested is to use experimentally measured pressures at three locations beneath the bed to interpolate a lower boundary condition, and thereby solve the two-dimensional problem in a semi-empirical manner.

7.1.3 Surface-to-Bed Heat Transfer

7.1.3.1 Measured Surface-to-Bed Heat-Transfer Coefficients

Surface-to-bed heat-transfer coefficients are obtained for 30-mm deep beds of Master Beads of various sizes, and both high- and low-density glass beads of three sizes (707, 177, and 88 μm). The heating surface is a cylinder of diameter 12.7 mm, immersed horizontally at the center of the bed.

Heat-transfer coefficients for Master Beads indicate a dependence on particle size. The heat-transfer coefficient increases with decreasing particle size until a particle size of 177 μm. Below this size, the heat-transfer coefficient falls again with decreasing particle size. The heat-transfer coefficient initially increases with increasing vibrational intensity. The heat-transfer coefficient reaches a limiting value with large particles, which is independent of the vibrational intensity parameter K. With smaller particles sizes, the heat-transfer coefficient increases until a maximum is reached, after which it falls off with increasing K.

Heat-transfer coefficients for glass beads follow similar trends to those for Master Beads, but the limiting value for 707-μm glass beads (of both densities) is higher than for equivalently sized Master Beads.

7.1.3.2 Possible Sources of Experimental Errors

Errors in the measurement of heat-transfer coefficients can arise out of:

1. estimating the bed temperature, since the bed is unevenly heated in this study,
2. conduction losses through the probe supports, and

3. lowered heat fluxes into the "dead" or "segregated" regions that develop beneath the heat-transfer tube.

The first source of error causes measured heat-transfer coefficients to be about 8-10% (but occasionally 15%) *lower* than actual values, whereas the second source of error causes measured heat-transfer coefficients to be about 2-4% *higher* than actual values. There is no clear way of estimating how much error is introduced by the third source. However, it should be noted that the "dead" regions are a characteristic of the manner in which the tube is placed within the bed, and the bed configuration, therefore, this factor will lead to errors, only if the current results are extrapolated to different heat-transfer coefficient surface geometries, or to different types of bunkering.

7.1.3.3 Factors Influencing Heat Transfer

Trends in the heat-transfer coefficients may be explained in terms of:

1. The particle circulation in the bed as a whole, and in the vicinity of the heat-transfer surface.
2. The formation of air gaps on the upper and lower surfaces of the heat-transfer tube.

Initially, as the vibrational intensity parameter K, is increased beyond a value of 2, the increased particle circulation brings about improved surface-to-bed heat transfer. Overall particle circulation promotes better mixing of the bed, which brings cooler particles to the heat-transfer surface, and removes hotter ones. Better local circulation decreases the contact times of particles at the heat-transfer surface.

The presence beneath the heat-transfer tube of a dead or segregated zone of reduced particle circulation and reduced mixing with the rest of the bed, limits the transfer of heat from the lower surface of the tube into the bed. Inducing a normal flow of particles past the heat-transfer tube by using a wall-high bunker configuration, destroys these dead zones. With 125-μm Master Beads, a normal

flow pattern past the heat-transfer probe results in an increase of the heat-transfer coefficient by almost 100 W/m^2-K.

The improved overall mixing in small-particle beds is responsible for the trend of increasing heat-transfer coefficients with decreasing particle size. However, as the particle size is reduced below 177 μm, the increased cohesiveness of the bed reduces bed mobility, and adversely affects heat transfer.

As the vibrational intensity is increased further, air gaps that form around the heating surface, cover a greater fraction of the surface for a longer fraction of the vibrational cycle. With 707-μm particles, the gaps completely engulf the tube for a fraction of the cycle. These gaps provide a resistance to heat transfer.

The average fractional coverage of the heat-transfer surface by air gaps, $\overline{F}_{SA}$, may be obtained from phase-delayed photographs of the gap evolution. With 707-μm particles, $\overline{F}_{SA}$ reaches a limiting value at $K = 3$, which is the same value of K at which the heat-transfer coefficient reaches a limiting value. With smaller particle sizes, $\overline{F}_{SA}$ increases considerably at higher vibrational intensities, so that the increase in heat transfer brought about by improved solid circulation is offset by the increasing coverage of the heat-transfer surface by air gaps, resulting in a maximum value of the heat-transfer coefficient at some value of K.

The air gaps also limit the amount of time a particle spends in contact with the heat-transfer surface. Particularly with large particles, where the coverage of the surface is large, contact times may be reduced to the same order of magnitude as the vibrational period, since heat can be transferred to the particle only while it is contact with the surface. The heat-transfer coefficient for such small contact times is independent of both particle thermal properties and contact time (or particle velocity), and will reach a limiting value which is dependent only on gas properties and the particle diameter, as observed.

7.1.3.4 Heat-Transfer Mechanisms

There are insufficient data at present (particularly on particle-surface contact times), to fully discriminate between different mechanisms proposed for surface-to-bed heat transfer. However, the strong influence of particle circulation on heat-transfer coefficients noted in this study suggests that a penetration model, in which the heat-transfer rate depends on the renewal rate and contact times of particles at the surface is most applicable.

A simplified position-dependent formulation for the heat-transfer coefficient may be written, which accounts for the gap formation. The heat-transfer coefficient in a region never covered by air gaps is determined by the average time that a particle spends next to this fraction of the heat-transfer surface. In the fraction of the surface covered by air gaps for at least one instant in the vibrational cycle, the heat-transfer coefficient during the period of particle-surface contact is determined by gas properties and the particle diameter. When some point on the surface is covered by an air gap, the heat-transfer coefficient is determined by the gas-convective heat transfer caused by the gas flow past the tube.

This formulation predicts that the heat-transfer coefficient for small particles, where air-gap formation is small, is determined largely by particle circulation rates (and consequently, by thermal properties of the solid). For larger particles, where the coverage of the heat-transfer surface by air gaps is greater, the heat-transfer coefficient is determined by a combination of the fraction of the heat-transfer surface covered by air gaps, and the fraction of the cycle during which a particular point on the surface is covered by air gaps. These trends are as experimentally observed.

7.2 Recommendations for Further Study

The following points are suggested for further study:

1. This study has concentrated on a vibrational frequency of 25 Hz. The effect of vibrational frequency on some of the phenomena reported herein, could be further investigated. A vibrational frequency of 15 Hz appears to be in commercial use. Higher frequencies should also be investigated, keeping in mind that accurate phase-correlation becomes more difficult, and demands on the frequency response of transducers become greater, as the vibrational frequency is increased.

2. A greater range of particle densities should be used to fully understand the effect of particle density on floor pressures, particle circulation, bed bunkering, and the transitions between states of the vibrated bed. Metals such as copper or iron in spherical form could provide an upper limit to the density, and plastic particles, a lower limit. Alternatively, the gas density can be altered by operating the bed in varying degrees of vacuum, or by using different gas atmospheres within the vibrating vessel. Also, gases with varying viscosities could be used to vary the amount of drag exerted on the bed by gas flows.

3. Unambiguous explanations for several features observed, as well as mathematical formulations for the bed dynamics require a reasonably accurate knowledge of the bed porosity. An instrument to measure bed-porosity variations within a vibrational cycle is required. Because of the large pressure fluctuations induced by the vertical motion of the bed, a technique that depends on the pressure drop of a gas flow across the bed will be unsuitable. A non-intrusive device, for example, one which obtains the bed porosity by measuring the capacitance of the bed, is suggested.

4. The movement of fluorescent tracers within the bed can be filmed on videotape, and the resulting images digitized and recorded by a computer. By digitally detecting differences in brightness between tracers and the rest of the bed in the image, the motion of several tracers can be followed simultaneously by the computer. This will increase the accuracy in determining particle circulation patterns and velocities.

5. Estimate the horizontal and vertical propagation velocities of the compaction wave using different beds and vibrational conditions. The vertical propagation velocity will give information on the rate at which gas can be expelled from the bed.

6. Determine if the delay between the null-force point and the observed instant of bed-vessel separation is caused by an expansion of the bed during lift-off. This can be done by:

   a. measuring the variation of bed porosity over the vibrational cycle, and
   b. developing a more accurate method for determining the instant of bed-vessel separation than used in this study.

7. Continue the study of the two-dimensional model, and its semi-empirical solution using measured pressures.

8. Use the two-dimensional model to determine the pressure gradients at the bed surface. This will be useful in checking the validity of extending the results of Judd and Jackson [1980] to predict the angle of bunkering in vibrated beds.

9. Develop a more reliable method for determining the transition between the coherent-expanded state and the coherent-condensed state. Since the major difference between the two states is the degree of bed expansion during part of the cycle, a measurement of floor pressures might be useful. When the bed is in a highly expanded state, the pressure drop across it will be small, compared to when the bed is in a more packed state. The pressures to be measured will all be very low in magnitude, so some method is required to eliminate random electrical noise from

the output of the pressure transducer, without introducing significant phase lag into the signal. A post-collection digital filtering technique, such as ensemble averaging, might be suitable if the floor pressure can be sampled over a large number of cycles (500 cycles for example).

10. Examine the correlation of transitions between the coherent-expanded and coherent-condensed state with other dimensionless groups. The Kroll model is applicable to the small bed depths at which the transition takes place. Because the Kroll model is based on an almost constant bed porosity, the transition between the two states must represent the lower limit of applicability of the model. Therefore, it is possible that the dimensionless ratio R_k (bed resistance per unit bed weight), might be relevant.

11. Use different heat-transfer surface geometries, particularly a flat vertical geometry, to study the effect of surface geometry on the heat-transfer process. A flat vertical geometry will have the added advantage of eliminating air gaps that surround cylindrical surfaces, and may lead to higher heat-transfer coefficients, especially for small particles.

12. Determine the particle-surface contact times, and the renewal rates of particles at the heat-transfer surface. This will be much easier if a flat vertical surface geometry is used, since the alteration of contact times by air gaps is eliminated.

13. Obtain surface-to-bed heat-transfer coefficients using other particle types, which have different thermal properties from those used in this study, to examine the effects of these properties on heat transfer. A knowledge of thermal properties of the solid (the heat capacity and thermal conductivity) will be required, and methods to measure them must be devised.

14. The errors in estimating the heat-transfer coefficient arising out of both conduction losses through the probe supports, and from the estimation of the bed temperature in an unevenly heated bed, can be eliminated by using guard heaters in the supports. The guard heaters heat the probe supports (except for a small insulating section next to the heat-transfer probe) using

a separate power supply from that used for heating the probe. The supports are heated to the same temperature as the probe, and thereby provide an isothermal barrier to heat losses through them. At the same time, the bed is evenly heated. With rectangular vessel geometries, the lateral bed mixing parallel to the probe may not be as good as with cylindrical vessel geometries. Therefore, the use of guard heaters mainly to eliminate uneven heating of the bed, is strongly recommended.

Bibliography

Abu-Baker, M.Y., *"Heat Transfer Between a Horizontal Tube and a Shallow Fluidized Bed"*, Ph.D. Thesis, University of Western Ontario, London, Canada, (1981).

Akiyama, T. and Naito, T., *Chem. Eng. Sci.*, **42**,(1987),1305.

Allen, M.L., *Trans. Inst. Chem. Engr.*, **58**,(1980),187.

Bachmann, D., *Verfahrenstechnik Z.V.D.I. Beiheft*, **No.2**,(1940),43.

Bagnold, P.A., *The Physics of Blown Sand and Desert Dunes*, Mcthuen and Co.,Ltd., London, United Kingdom, (1954).

Bird, R.B., Stewart, W.E., and Lightfoot, E.N., *Transport Phenomena*, John Wiley Inc., New York, USA, (1960).

Botterill, J.S.M., *Fluid-Bed Heat Transfer*, Academic Press, New Tork, USA, (1975).

Buevich, Yu.A., and Galontsev, V.L., *Inzh. Fiz. Zh.*, **34**,(1978),394.

Buevich, Yu.A., and Kharisova, N.M., *Inzh. Fiz. Zh.*, **34**,(1978),604.

Buevich, Yu.A., Ryzhkov, A.F., and Kharisova, N.M., *Inzh. Fiz. Zh.*, **37**,(1979),626.

Bukareva, M.F., Chlenov, V.A., and Mikhailov, N.V., *Int. Chem. Eng.*, **9**,(1969),119.

Bukareva, M.F., Chlenov, V.A., and Mikhailov, N.V., *Int. Chem. Eng.*, **10**,(1970),384.

Cheah, C.W., *"Heat Transfer Between a Supernatant Gas and a Flowing Vibrofluidized Bed of Solid Particles"*, M.S. Thesis, Virginia Polytechnic Institute and State University, Blacksburg, Virginia, (1986).

Chen, J.C., and Withers, J.G., *A.I.Ch.E Symp. Series*, **74**,(1978),327.

Chlenov, V.A., and Mikhailov, N.V., *Khim. Prom.*, **No.12**,(1964),910.

Chlenov, V.A., and Mikhailov, N.V., *Inzh. Fiz. Zh.*, **9**,(1965),196.

Chlenov, V.A., and Mikhailov, N.V., *Drying of Granular Materials in a Vibrated Bed*, Stroizdat, Moscow, USSR, (1967).

Chlenov, V.A., and Mikhailov, N.V., *Vibrofluidized Beds*, Nauka, Moscow, USSR, (1972).

Erdesz, K., and Halasz, G., *Hung. J. Ind. Chem. Veszprem*, **12**,(1984),441.

Franke, J.M., Clemmons, Jr., J.J., and Jones, S.E., *NASA Tech. Briefs*, **9**,(1985),44.

Geldart, D. *Powder Technol.*, **7**,(1973),285.

Gelperin, N.I., and Einstein, V.G. in *Fluidization*, Eds. Davidson, J.F., and Harrison, D., Academic Press, London, United Kingdom, (1971),471

Genetti, W.E., Schmall, R.A., and Grimett, E.S., *A.I.Ch.E. Symp. Series*,**67**,(1971),90.

Ginzburg, A.S., and Syroedov, V.I., *Inzh. Fiz. Zh.*, **9**,(1965),744.

Grace, J.R., *Can. J. Chem. Eng.*, **64**,(1986),353.

Gray, W.A., and Rhodes, G.T., *Powder Technol.*, **6**,(1972),271.

Gutman, R.G., and Davidson J.F., *Chem. Eng. Sci.*, **30**,(1979),89.

Gutman, R.G., *"Vibrated Beds of Powders"*, Ph.D. Thesis, University of Cambridge, Cambridge, United Kingdom, (1974).

Gutman, R.G., *Trans. Inst. Chem. Engrs.*, **54**,(1976a),174.

Gutman, R.G., *Trans. Inst. Chem. Engrs.*, **54**,(1976b),251.

O'Hanlon, J.F., *A User's Guide to Vacuum Technology*, John Wiley Inc., New York, USA, (1980).

Herber, R., *Maschinenbautechnik*, **19**,(1970),231 cited in Gutman [1974].

Hirt, D.E., *"Heat Transfer Between a Supernatant Gas and a Flowing Vibrofluidized Bed of Solid Particles"*, M.S. Thesis, Virginia Polytechnic Institute and State University, Blacksburg, Virginia, (1984).

Incropera, F.P., and DeWitt, D.P., *Fundamentals of Heat Transfer*, John Wiley, New York, USA, (1981).

Jacson, R., and Judd M.R., *Trans. Inst. Chem. Engrs.*, **59**,(1981),119.

Johnson, A., *"Particle Circulation in Vibrated Beds"*, Undergraduate Senior Research Report, VPI&SU, (1987), Unpublished.

Kal'tman, I.I., and Tamarin, A.I., *Inzh. Fiz. Zh.*, **16**,(1969),630.

Kapustin, E.A., Prosvirnin, V.I., and Butorina, I.V., *Teor. Osny. Khim. Tekh*, **14**,(1980),720.

Konyakhin, A.P., Uchitel, A.D., Ostapenko, V.N., Dorokhin, A.P., and Sabadash, V.V., *Koks i Khimiya*, **No.5**,(1976),30.

Kossenko, G.D., Reshetnikov, E.G., Syromyatnikov, N.I., and Sapozhnikov, B.G., *Inst. Fuel Symp. Series No.1: Fluidised Combustion*, **1**,(1975),B4-1.

Kroll, W., *Forschung auf der Gebiete des Ingenieurwesen*, **20**,(1954),2.

Kroll, W., *Chemie-Ing.-Techn.*, **27**,(1955),33.

Laikovskaya, E., Sapozhnikov, B.G., and Syromyatnikov, N.I., *Teplo i Massoperenos*, **5** Nauka i Tekhnika, Minsk, USSR, (1968), 153, cited in Gutman [1974].

Liu, Y.A., and Squires, A.M., *"Countercurrent Heat Exchange Between a Gas and a Vibrofluidized Solid"* Final technical report, U.S. Department of Energy, Idaho Operations Office, Grant No. DE-FG07-83ID12428, May 1986.

Malhotra, M., and Mujumdar, A.S., *Can. J. Chem. Eng.*, **63**,(1985),22.

Massimilla, L., Betta, V., and Della Rocca, C., *Rend. Acc. Sci. Fis. e Mat. Napoli.*, **XXVI**,(1959),81. cited in Massimilla [1971].

Massimilla, L., in *Fluidization*, Eds. Davidson, J.F., and Harrison, D., Academic Press, London, United Kingdom, (1971), 651.

Mickley, H.S., and Fairbanks, D.F., *A.I.Ch.E. J.*, **1**,(1955),374.

Muchowski, E., *Int. Chem. Eng.*, **20**,(1980),564.

Muckowski, E., and Mannchen, E., *Int. Chem. Eng.*, **20**,(1980),577.

Opalinski and Wolny *Int. J. Heat and Mass Trans.*, **30**,(1987),589.

Pakowski, Z., Mujumdar, A.S., and Strumillo, C., in *Advances in Drying Vol. 3*, Ed. Mujumdar, A.S., Hemisphere Publishing Co., Washington D.C., USA, (1984), 245.

Powell, J.A., Strazisar, A.J., and Seashotz, R.G., *J. Eng. Power*, **103**,(1984),424.

Ringer, D.U., in *Drying '80, Vol. 2 : Proceedings of the Second International Symposium on Drying*, Ed. Mujumdar, A.S., Hemisphere Publishing Co. Washington D.C., (1980), 144.

Rippie, E.G., Kriesel, D.C., and Rettig, H., *J. Pharm. Sci.*, **67**,(1978),1121.

Ripple, C.D., James, R.V., and Rubin, J., *Powder Technol.*, **8**,(1973),165.

Rowe, P.N., and Henwood, G.A., *Trans. Inst. Chem. Engrs.*, **39**,(1961),43.

Ryzhkov, A.F., and Baskakov, A.P., *Inzh. Fiz. Zh.*, **27**,(1974),15.

Ryzhkov, A.F., Baskakov, A.P., and Munts, V.A., *Heat Transfer - Soviet Research*, **8**,(1976),136.

Sapozhnikov, B.G., and Syromyatnikov, N.I., *Inzh. Fiz. Zh.*, **16**,(1969),1039.

Sapozhnikov, B.G., and Syromyatnikov, N.I., *The Soviet Chem. Ind.*, **No.2**,(1970),81.

Sapozhnikov, B.G., Reshetkov, Ye.G., Kossenko, G.D., and Kharisova, N.M., *Heat Transfer - Soviet Research*, **8**,(1976),141.

Schlunder, E.U., *Chemie-Ing.-Tech.*, **43**,(1971),651.

Schlunder, E.U., in *Heat Transfer 1982 - Proceedings of the Seventh International Heat Transfer Conference*, Eds. Grigull, U., Hahne, E., Stephan.K, and Straub, J., Hemisphere Publishing Co., Washington D.C., USA, 1982.

Sprung R., Thomas, B., Liu, Y.A., and Squires, A.M., in *Fluidization V - Proceedings of the Fifth Engineering Foundation Conference on Fluidization*, Eds. Ostergaard, K., and Sorensen, A., Engineering Foundation, New York, USA, (1986), 409.

Sprung R., *"Studies in Vibrofluidized Beds and Synthesis of Silica Catalysts"*, Ph.D. Thesis, Virginia Polytechnic Institute and State University, Blacksburg, Virginia, (1987).

Strumillo, C., and Pakowski, Z., in *Drying '80, Vol. 1 : Developments in Drying*, Ed. Mujumdar, A.S., Hemisphere Publishing Co., Washington D.C., USA, (1980), 211.

Suzuki, K., Housaka, H., Yamazaki, R., and Jimbo, G., *J. Chem. Eng. Japan*, **13**,(1980a),117.

Suzuki, K., Fujiyami, A., Yamazaki, R., and Jimbo, G., *J. Chem. Eng. Japan*, **13**,(1980b),493.

Takahashi, H., Suzuki, A., and Tanaka, T., *Powder Technol.*, **2**,(1968-69),65.

Tamarin, A.I., and Kal'tman, I.I., *Inzh. Fiz. Zh.*, **20**,(1971),274.

Thomas, B., Sprung, R., Liu, Y.A., and Squires, A.M., *"Heat Transfer from a Heated Tube in Shallow Vibrated Beds"*, Manuscript No.4497, A.I.Ch.E. National Meeting, Miami, Florida, Nov. 1986.

Thomas, B., Liu, Y.A., Chan, R.T., and Squires, A.M., *Powder Technol.*, **52**,(1987),77.

Tung, Y., and Kwauk, M., in *Fluidization Science and technology - Conference Papers China-Japan Symposium*, Eds. Kwauk, M., and Kunii, D., Science Press, Beijing, China, (1982), 155.

Ur'ev, N.B., *Kolloid. Zh.*, **40**,(1978),915.

Vinogradov, E.L., Makar'ev, M.A., Ur'ev, N.B., and Yamschikov, V.M., *Kolloid. Zh.*, **42**,(1980),1170.

Volovik, Yu.I., Moseychuk, G.G., and Isayev, N.A., *Heat Transfer - Soviet Research*, **7**,(1975),146.

Ward, A.S., in *Filtration*, Ed. Matteson, M.J., and Orr, C., Marcel Dekker, Inc., New York, USA, (1987), 133.

Warren, R. *"Measurement of Floor Pressures Beneath Vibrated Beds"*, Undergraduate Senior Research Report, VPI&SU, (1986), Unpublished.

Whiting G.K., *"Development of a Microreactor System for Unstaedy-State Fischer-Tropsch Synthesis"*, Ph.D. Thesis, Virginia Polytechnic Institute and State University, Blacksburg, Virginia, (1985).

Williams, J.C., and Shields, G., *Powder Technol.*, **1**,(1967),134.

Yoshida, T., and Kousaka, Y., *Kagaku Kogaku*, **5**,(1967),159.

Zabrodsky, S.S., *Hydrodynamics and Heat Transfer in Fluidized Beds* (English Translation), The M.I.T. Press, Cambridge, Mass., USA, (1963).

Zabrodsy, S.S., Zamnius, I.L., Malyukovich, S.A., and Tamarin, A.I., *Inzh. Fiz. Zh.*, **14**,(1968),448.

Zaitsev, E.D., Redekop, V.I., and Shetsov, V.V., *Khim. Farmat. Zh.*, **10**,(1976),81.

Appendix A. Calibration of the Pressure Transducers

Linear fits were used to describe the calibration curves of the pressure transducers used to measure the cyclic floor pressures below the bed. The fit for each transducer at positions W, H, and C as shown in Figure 13 is given below.

Transducer at position W:

$$P_m = 2725.226\, V_t + 11.949 \qquad [A.1a]$$

Transducer at position H:

$$P_m = 2757.349\, V_t + 88.323 \qquad [A.1b]$$

Transducer at position C:

$$P_m = 2742.616\, V_t + 157.233 \qquad [A.1c]$$

where P_m = Measured Pressure in Pascals

V_t = Transducer Output in Volts

The correlation coefficients are 0.999976, 0.999991, and 0.999981 for the transducers at positions W, H, and C respectively.

Appendix B. The Electronic Circuit for Phase-Delayed Triggering

A block diagram of the circuit used to obtain a phase-delayed trigger output with an angular resolution of one degree is given in Figure 84. The circuit essentially consists of four blocks:

1. the input signal conditioning and zero-crossover detection block,
2. the phase-locked-loop (PLL) frequency tracking and synthesis block,
3. the counter and trigger output block, and
4. the phase-angle display block.

The vertical displacement of the vessel is directly measured by a LVDT or photoelectric displacement transducer as described above. The sinusoidal output from the transducer is inverted and amplified (with a gain of approximately 5) by an operational amplifier (op amp). The inverted amplified signal is passed to a second op amp which is configured as a comparator. This op amp compares the inverted signal against a reference null-position voltage which is set using a null-position-adjust potentiometer. The null-position voltage is adjusted to equal the output voltage of the displacement transducer at the null or rest position of the vibrating table.

As the inverted signal passes below this null-position voltage, the output of the comparator switches from low to high as shown in Figure 84 on page 355. Later in the vibrational cycle, as the inverted displacement signal again crosses up past the reference voltage level, the output of the comparator switches back from high to low. A small amount of hysteresis is added to the comparator so as to eliminate errors in detecting the downward zero-crossover point, that may be caused by small amounts of electrical noise that are present on the output signals of the displacement transducers. The comparator output remains at a low level, until the start of the next vibrational cycle, when the inverted displacement input signal again passes below the null-position voltage. The output of the comparator is therefore, a square wave which has complete phase integrity with respect to the input from the displacement transducer as shown in Figure 84.

The square wave is then fed to the PLL frequency tracking and synthesis block. As shown in Figure 84, this block is configured so that the output frequency synthesized is a multiple N, of the input frequency, and is in phase with the input signal. Using a multiplication factor of 360 will give a resolution of one degree of phase delay for triggering. The maximum resolution of the circuit is limited by the maximum frequency of the PLL voltage-controlled oscillator (VCO). The CD4046 PLL VCO used has an upper frequency limit of 1.3 MHz, which restricts the input frequency to about 3 KHz if a resolution of one degree of phase lag is required.

The counters are grouped into programming counters and coincidence counters. The former are clocked by a slow-pulse (2 Hz) oscillator, and when activated by an up- or down-counter button (Figure 84), proceed to count up or down respectively in modulo 360. This presets the required angle into the circuit. The data outputs of the programming counters are read into the coincidence counters at the start of each phase-degree counting sequence, which is initiated by the leading edge of the square-wave output from the signal conditioning and zero-crossover detection block. The coincidence counters are clocked by the synthesized (multiplied) frequency from the PLL VCO, and they count down from the value preset in them (the desired phase angle) until zero is reached. At this instant a trigger pulse is issued which will be lagged after the zero-crossover point by the desired phase angle, and the cycle repeats.

The delayed trigger pulses are routed to a switch that allows selection of either a continuous stream of triggering pulses, or a single pulse on demand to initiate a single event such as firing an electronic flash.

A digital display is used to show the data in the programming counters, giving a visual indication of the phase angle selected.

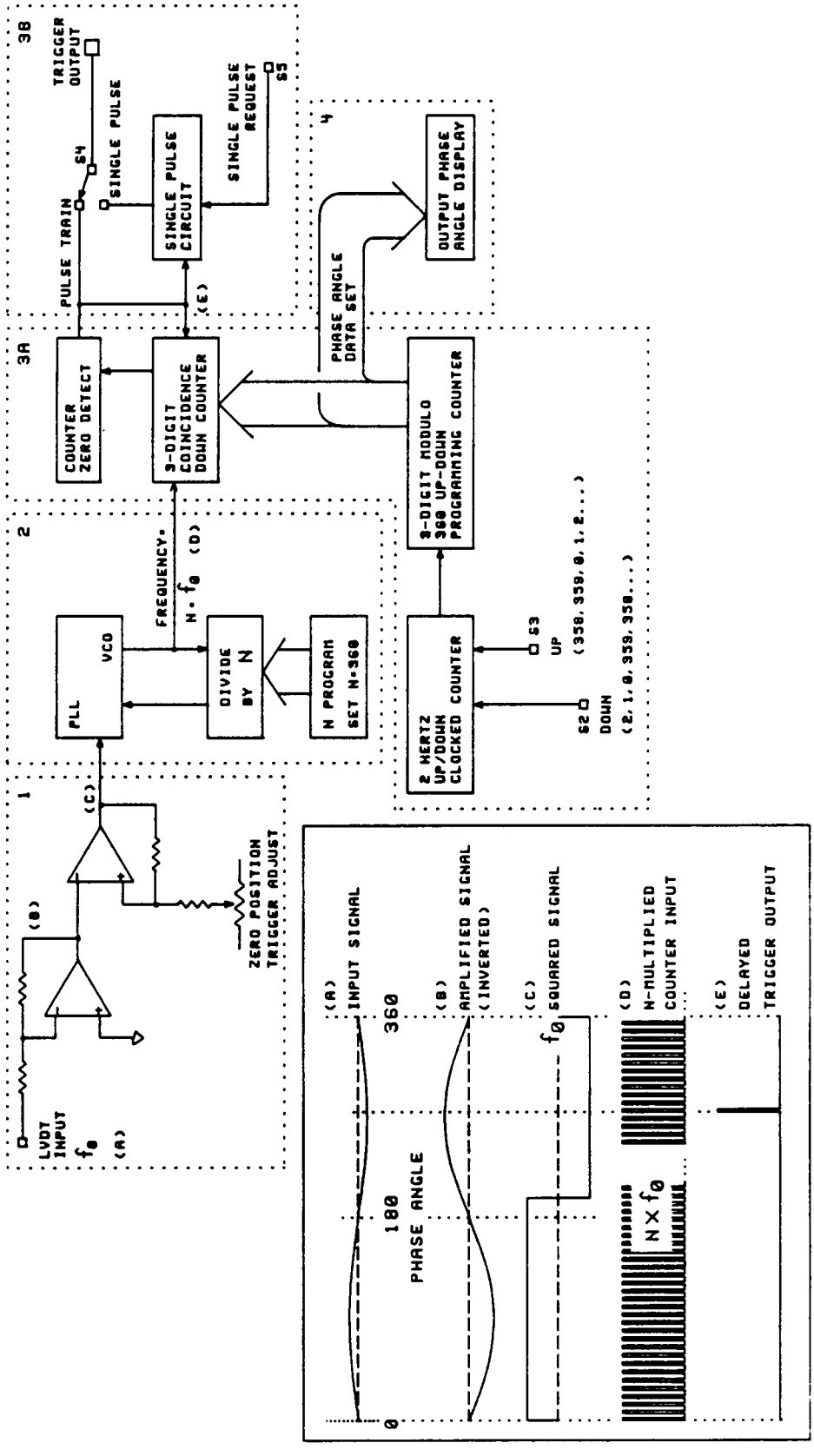

Figure 84. Block diagram of the phase-delayed trigger circuit: Signal waveforms at points A, B, C, D, and E are shown within the inset.

Appendix C. Analysis of Temperature Distributions Within the Heat-Transfer Probe

As explained in Section 3.3.4 of Chapter 3, the design of the heat-transfer probe requires an isothermal surface. However, since local heat-transfer coefficients vary with angular position, the surface temperature of the probe may vary with the angular position, if the probe design will permit large thermal gradients along its surface. Surface thermal gradients may be minimized by permitting large thermal fluxes within the body of the probe, below the surface. This may be achieved by constructing the probe body out of a material with a high thermal conductivity, and making its radial thickness as large as possible. Copper is chosen as the material of construction owing to its high thermal conductivity (400 W/m-K). The outer probe diameter is fixed at 12.7 mm. Because of construction considerations, the outer diameter of the heating element that fits into the center of the heat-transfer probe is 6.16 mm (see Figure 20 on page 84). Therefore, the thickness of the copper shell of the probe is 3.27 mm thick. The following analysis determines if a thickness of 3 mm is sufficient to produce a uniform surface temperature.

The analysis yields the maximum temperature difference across the probe (both with radial and angular position). However, since some approximations are made in defining the heat-conduction problem, the solutions will indicate only an order of magnitude, rather than exact results.

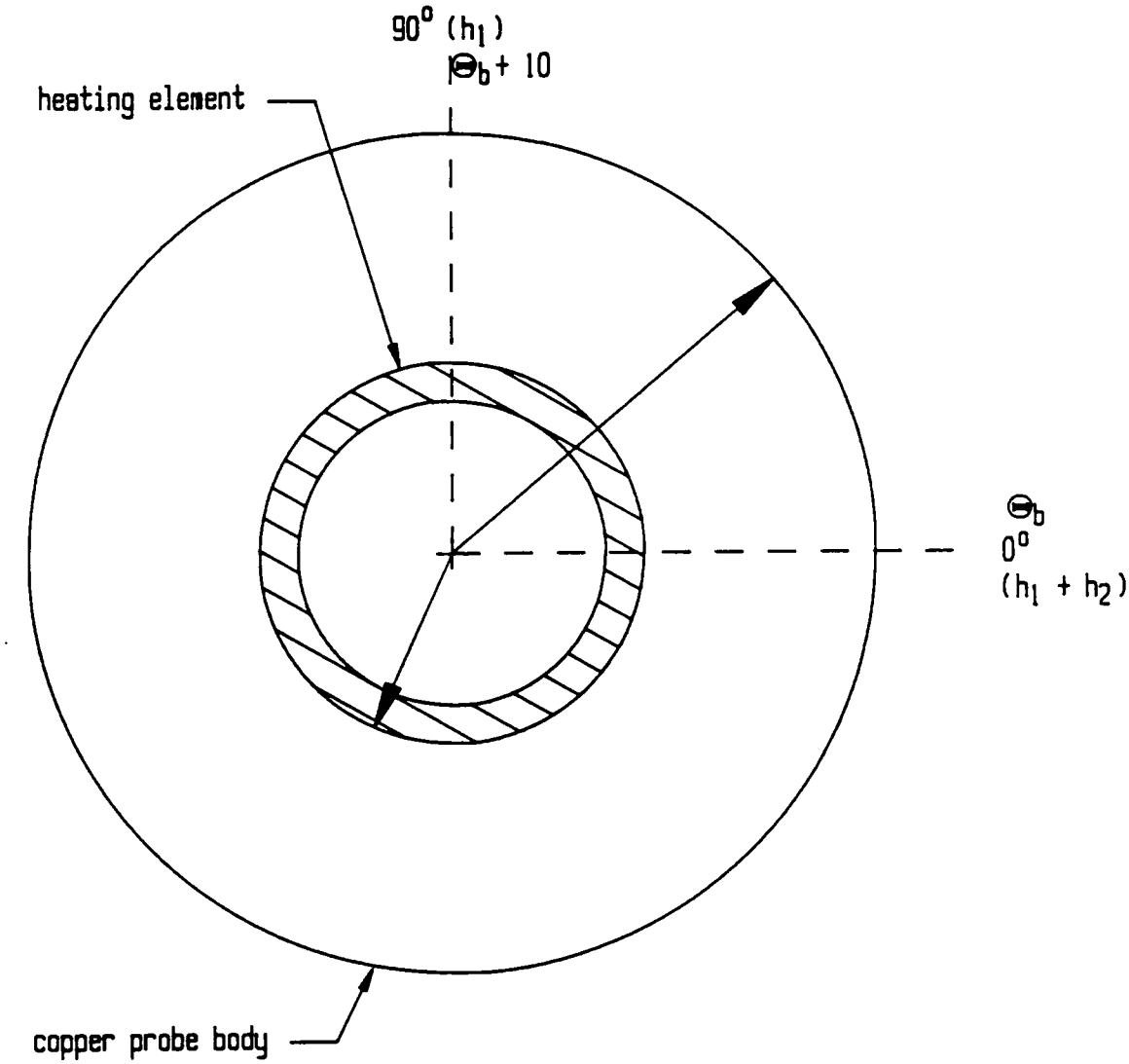

Figure 85. Cross-sectional view of the heat-transfer probe: Surface-to-bed heat-transfer coefficients vary from h_1 at the 90° position, to $h_1 + h_2$ at the 0° position. the bed temperature is Θ_b°C at the 0° position, and Θ_b + 10°C at the 90° position.

Two unknown factors have to be accounted for:

1. the angular distribution of heat-transfer coefficients, and
2. the distribution of bed temperatures around the periphery of the heat-transfer surface.

By referring to the cross-sectional view of the heat-transfer probe in Figure 85 on page 357, it is seen that the heat-transfer coefficient varies from its highest value at the "vertical" sides of the probe (the 0° position), to its lowest at the top and bottom (the 90° positions). Most of the data in the literature indicate that for both gas-fluidized and vibrated beds, the heat-transfer coefficient at the 0° position is roughly 1.5 to 2 times greater than at the 90° position. A large variation in the heat-transfer coefficient with angular position, will tend to adversely affect the distribution of surface temperatures. For the purposes of this analysis, an arbitrary function is chosen to describe the distribution of heat-transfer coefficients. A cosine distribution function is used, since it is angular in nature. The heat-transfer coefficient at any angular position φ, along the surface is given by:

$$h(\varphi) = h_1 + h_2 \cos \varphi \qquad [C.1]$$

where h_1 is the heat-transfer coefficient at the 90° position, and $(h_1 + h_2)$ is the heat-transfer coefficient at the 0° position.

Bed temperatures around the probe are similarly assumed to vary according to a sine function, with the bed temperature at the 90° position being 10°C higher than at the 0° position. The bed temperature at any angular position next to the heat-transfer surface is given by:

$$\Theta_b(\varphi) = \Theta_{b,0} + 10 \sin \varphi \qquad [C.2]$$

where $\Theta_{b,0}$ is the bed temperature next to the 0° position.

The general two-dimensional heat conduction equation in cylindrical coordinates, assuming uniform thermal conductivity, is:

$$\frac{1}{r}\frac{\partial}{\partial r}\left(r\frac{\partial\Theta_p(r,\varphi)}{\partial r}\right)+\frac{1}{r^2}\frac{\partial}{\partial\varphi}\left(\frac{\partial\Theta^p(r,\varphi)}{\partial\varphi)}\right)=\frac{\rho_c c_{p,c}}{k_c}\frac{\partial\Theta_p(r,\varphi)}{\partial t} \qquad [C.3]$$

Here, ρ_c is the density of copper (the material that the heat-transfer probe is constructed from), $c^{p,c}$ is its heat capacity, and k_c, its thermal conductivity. Equation [C.3] is solved subject to the following boundary conditions:

$$\begin{aligned}
-k_c\frac{\partial\Theta_p(r,\varphi)}{\partial r} &= q \quad \text{at} \quad r=r_i \\
-k_c\frac{\partial\Theta_p(r,\varphi)}{\partial r} &= (h_1+h_2\cos\varphi)(\Theta_p|_{r=r_i}-\Theta_b(\varphi)) \quad \text{at} \quad r=r_i \\
\frac{\partial\Theta_p(r,\varphi)}{\partial\varphi} &= 0 \quad \text{at} \quad \varphi=0 \\
\frac{\partial\Theta_p(r,\varphi)}{\partial\varphi} &= 0 \quad \text{at} \quad \varphi=\pi/2
\end{aligned} \qquad [C.4]$$

The first boundary condition describes the flux across the inner boundary (of radius r_i) of the copper annulus. All heat that flows across this boundary must be generated in the heating element. If the total heat generated by the heating element is Q Watts, the heat flux across the inner boundary is given by:

$$q=\frac{Q}{4\pi r_i l_p} \qquad [C.5]$$

where l_p is half the length of the heat-transfer probe.

The analysis of heat conduction within the heat-transfer probe is only necessary at steady state, implying that $(\partial\Theta(r,\varphi)/\partial t=0)$. However, given the form of the boundary conditions, the two-dimensional problem is best solved numerically. The computer program (PDETWO) chosen to solve equation [C.3] — mainly for its ease of use in handling complex boundary conditions — is one that obtains a numerical solution to the general unsteady-state two-dimensional partial differential

equation. A dummy initial condition may be specified, and the solution allowed to reach a steady state. The easiest initial condition to specify is that the temperature everywhere within the probe is equal to the bed temperature at the start. In other words:

$$\Theta_p(r,\varphi) = \Theta_{b,0} \quad \text{at} \quad t = 0 \qquad [C.6]$$

A typical solution assuming an average heat-transfer coefficient of 460 W-m^2-K, and heat-transfer coefficients of about 120 W/m^2-K and 503 W/m^2-K at the 90° and 0° positions respectively, is given in Table 13 on page 362. The results indicate that given this distribution of the heat-transfer coefficient, and a power input of 30 Watts, the maximum variation in surface temperatures is in the order of 0.02°C.

With an average heat-transfer coefficient of 155 W/m^2-K, and heat-transfer coefficients of about 40.5 W/m^2-K and 170 W/m^2-K at the 90° and 0° positions respectively, the maximum variation in surface temperatures is in the order of 0.05°C, when the input power is 20 Watts.

The maximum difference in bed temperatures around the probe is assumed to be 10°C in this analysis, whereas the results in Chapter 6, show that bed temperatures beneath the probe can sometimes reach 20, or occasionally 30°C over the average bed temperature. In that case, the variation in the probe surface temperature will be higher than those derived above. Another possible cause of surface temperature variation not accounted for in this analysis is the uneven distribution of the heat flux entering the inner surface of the copper annulus. The heating element is fixed within the copper body with a high-conductivity epoxy, so that thermal contact is not poor, but it is possible that the thickness of the epoxy might vary slightly with angular position. However, the effects of such factors must be small when compared with those caused by the angular variation in heat-transfer coefficient and bed temperatures. The variation in surface temperatures should certainly be less than 1°C, which is sufficiently isothermal for this study, and is about the smallest change in temperature that may be reliably detected by a thermocouple. Therefore, this analysis

shows that a copper body with a thickness of 3 mm or greater surrounding the heating element, is sufficient to produce an uniform heat-transfer surface temperature.

Table 13. Typical solution of the heat-conduction equation indicating the temperature distribution within the heat-transfer probe

Solution parameters: Probe diameter = 12.7×10^{-3} m

Thickness of copper annulus = 3.44×10^{-3} m

Heat input = 30 Watts

Average heat-transfer coefficient = 460 W/m^2-K

Temperatures in °C										
Radial Position	Angular Position (degrees) 0	10	20	30	40	50	60	70	80	90
inside perimeter	0.80784D+02	0.80784D+02	0.80785D+02	0.80786D+02	0.80788D+02	0.80789D+02	0.80791D+02	0.80793D+02	0.80794D+02	0.80794D+02
	0.80764D+02	0.80764D+02	0.80765D+02	0.80766D+02	0.80768D+02	0.80770D+02	0.80772D+02	0.80773D+02	0.80774D+02	0.80775D+02
	0.80745D+02	0.80746D+02	0.80746D+02	0.80748D+02	0.80750D+02	0.80752D+02	0.80753D+02	0.80755D+02	0.80756D+02	0.80757D+02
	0.80728D+02	0.80729D+02	0.80729D+02	0.80731D+02	0.80733D+02	0.80735D+02	0.80737D+02	0.80739D+02	0.80740D+02	0.80740D+02
	0.80712D+02	0.80713D+02	0.80714D+02	0.80715D+02	0.80717D+02	0.80719D+02	0.80721D+02	0.80723D+02	0.80725D+02	0.80725D+02
	0.80697D+02	0.80698D+02	0.80699D+02	0.80700D+02	0.80702D+02	0.80705D+02	0.80707D+02	0.80709D+02	0.80711D+02	0.80711D+02
	0.80683D+02	0.80683D+02	0.80684D+02	0.80686D+02	0.80688D+02	0.80691D+02	0.80694D+02	0.80696D+02	0.80698D+02	0.80698D+02
	0.80670D+02	0.80670D+02	0.80671D+02	0.80673D+02	0.80675D+02	0.80678D+02	0.80681D+02	0.80684D+02	0.80686D+02	0.80686D+02
	0.80657D+02	0.80657D+02	0.80658D+02	0.80660D+02	0.80663D+02	0.80666D+02	0.80669D+02	0.80672D+02	0.80674D+02	0.80675D+02
surface	0.80645D+02	0.80645D+02	0.80646D+02	0.80648D+02	0.80651D+02	0.80654D+02	0.80658D+02	0.80661D+02	0.80664D+02	0.80665D+02

Note: An angular position of 0° corresponds to the horizontal plane, and 90° corresponds to the vertical plane. Only results for one quadrant are shown, since the temperature distribution is identical between each quadrant.

Appendix D. Cyclic Floor Pressures for Vibrated Beds of Master Beads

Experimentally measured floor pressures beneath vibrated beds of Master Beads are shown graphically on the following pages. Floor pressures are measured at three locations beneath the bed (see Figure 13 on page 62), and for four different vibrational intensities, indicated within each figure. The plots show the variation of floor pressures at all three locations usually over one vibrational cycle; but if the bed trajectory is unstable, the pressure variation is shown over two cycles instead. The floor pressure beneath the center of the bed is shown as a solid curve, the floor pressure at the location halfway between the side-wall and the center is shown as a dashed curve, and the floor pressure at the side-wall is shown as a dotted (or short-dashed) curve.

Figure 86 on page 365 to Figure 91 on page 370 give floor pressure variations beneath a 30-mm deep bed of Master Beads of various particle sizes. Figure 92 on page 371 and Figure 93 on page 372 give floor pressure variations beneath 43.2-mm deep beds of 177- and 125-μm Master Beads respectively. Figure 94 on page 373 and Figure 95 on page 374 give floor pressure variations beneath 60-mm deep beds of 177- and 125-μm Master Beads respectively.

Note that the scale of the floor-pressure axis is constant over the range of vibrational intensities for a given particle size, but the scale varies between one particle size and another.

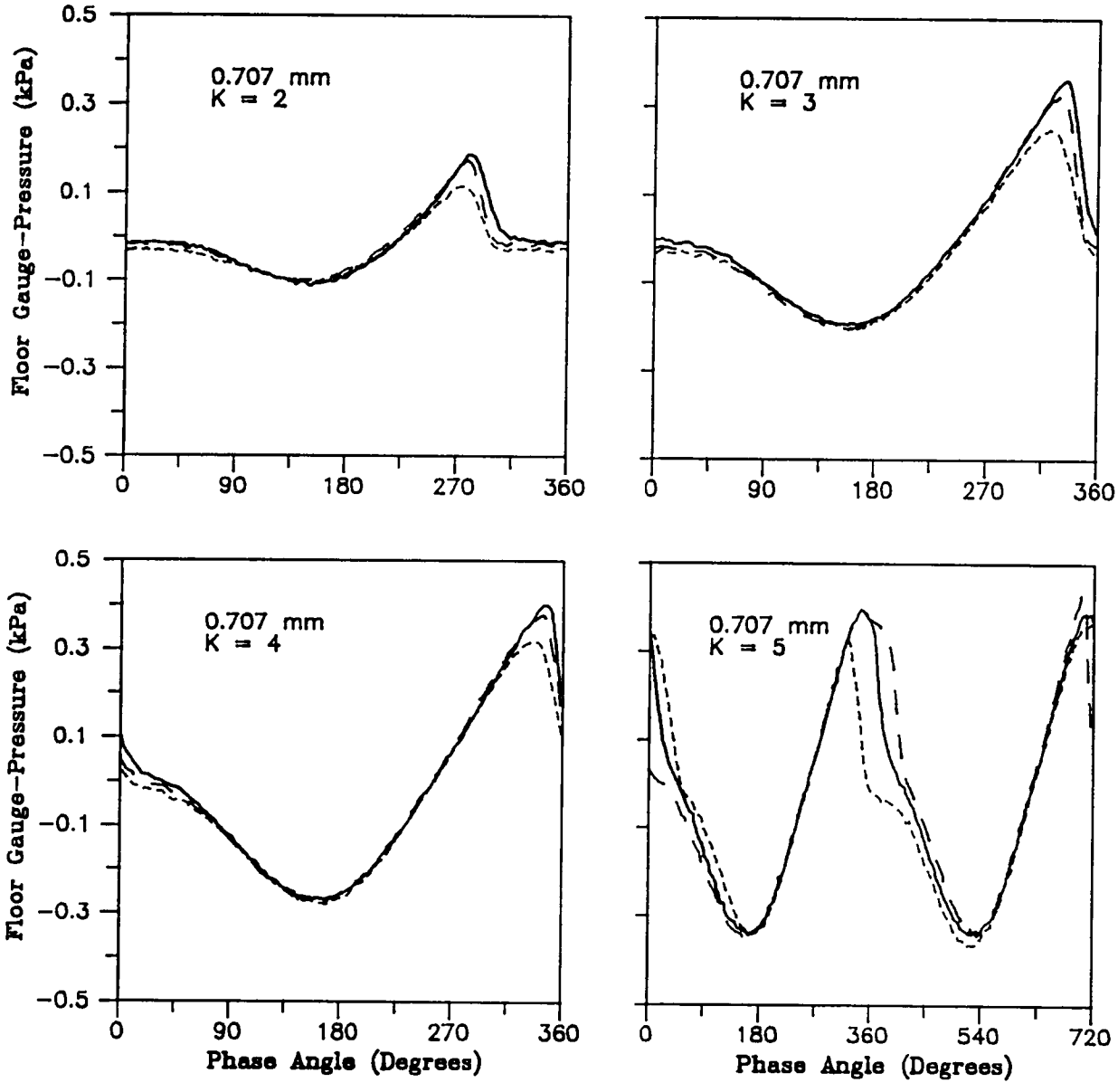

Figure 86. Cyclic floor pressures beneath a 30-mm deep bed of 707-μm Master Beads: The variation over one vibrational cycle of floor gauge-pressures at three horizontal locations beneath the vibrated bed. The vibrational frequency is 25 Hz, and $K = 2$, 3, 4, and 5. The particle size range is -20 +30 U.S. Standard Mesh. Note: At $K = 5$, the bed trajectory is unstable causing the pressure waveform in one cycle to be different from the next, therefore, two cycles are shown in this case. ———— floor pressure at the center of the bed, ---------- floor pressure at the vessel wall, and — — — — floor pressure halfway between the side-wall and the center.

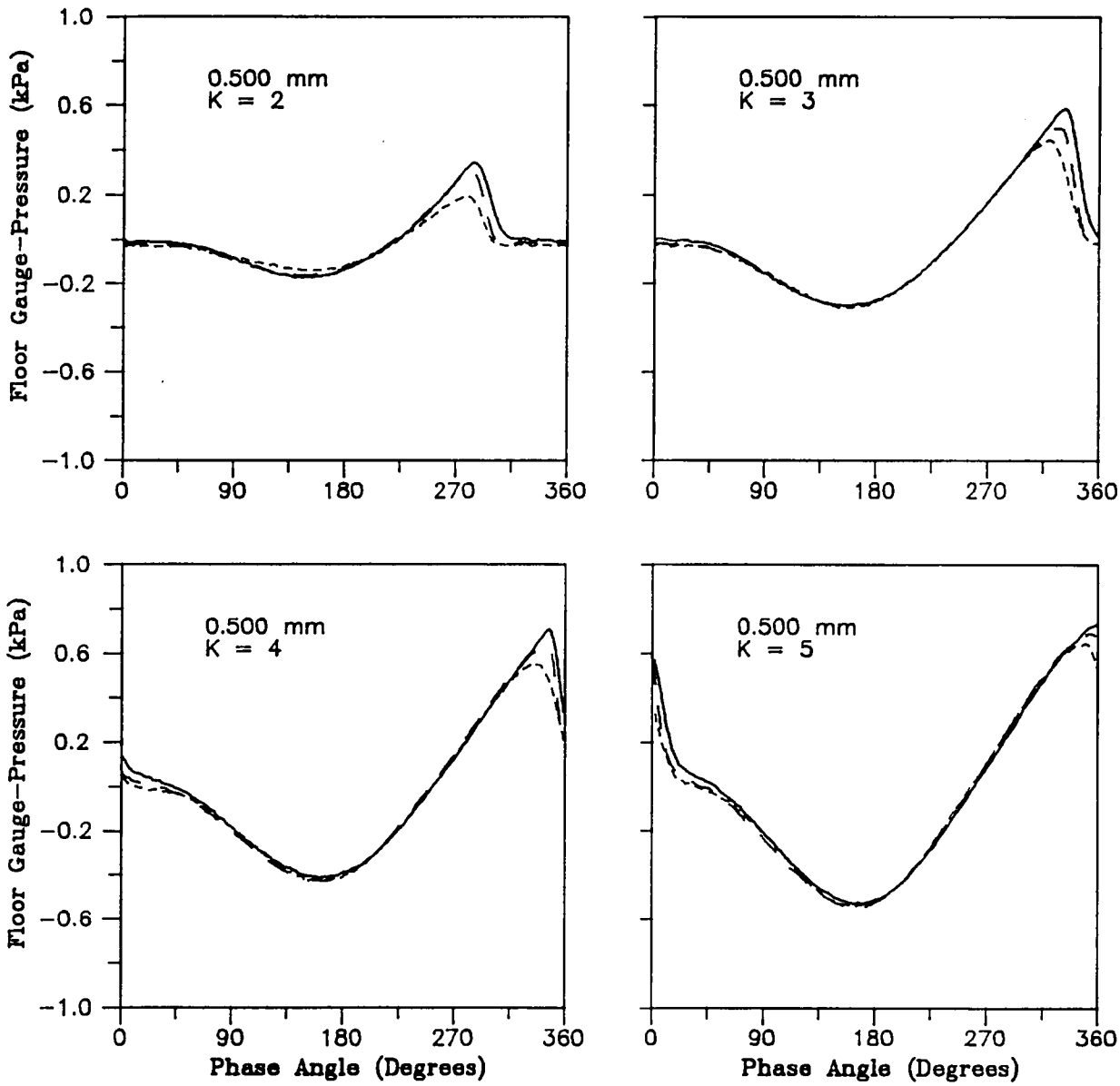

Figure 87. Cyclic floor pressures beneath a 30-mm deep bed of 500-μm Master Beads: The variation over one vibrational cycle of floor gauge-pressures at three horizontal locations beneath the vibrated bed. The vibrational frequency is 25 Hz, and $K = 2$, 3, 4, and 5. The particle size range is -30 +40 U.S. Standard Mesh. ———— floor pressure at the center of the bed, ------ floor pressure at the vessel wall, and — — — — floor pressure halfway between the side-wall and the center.

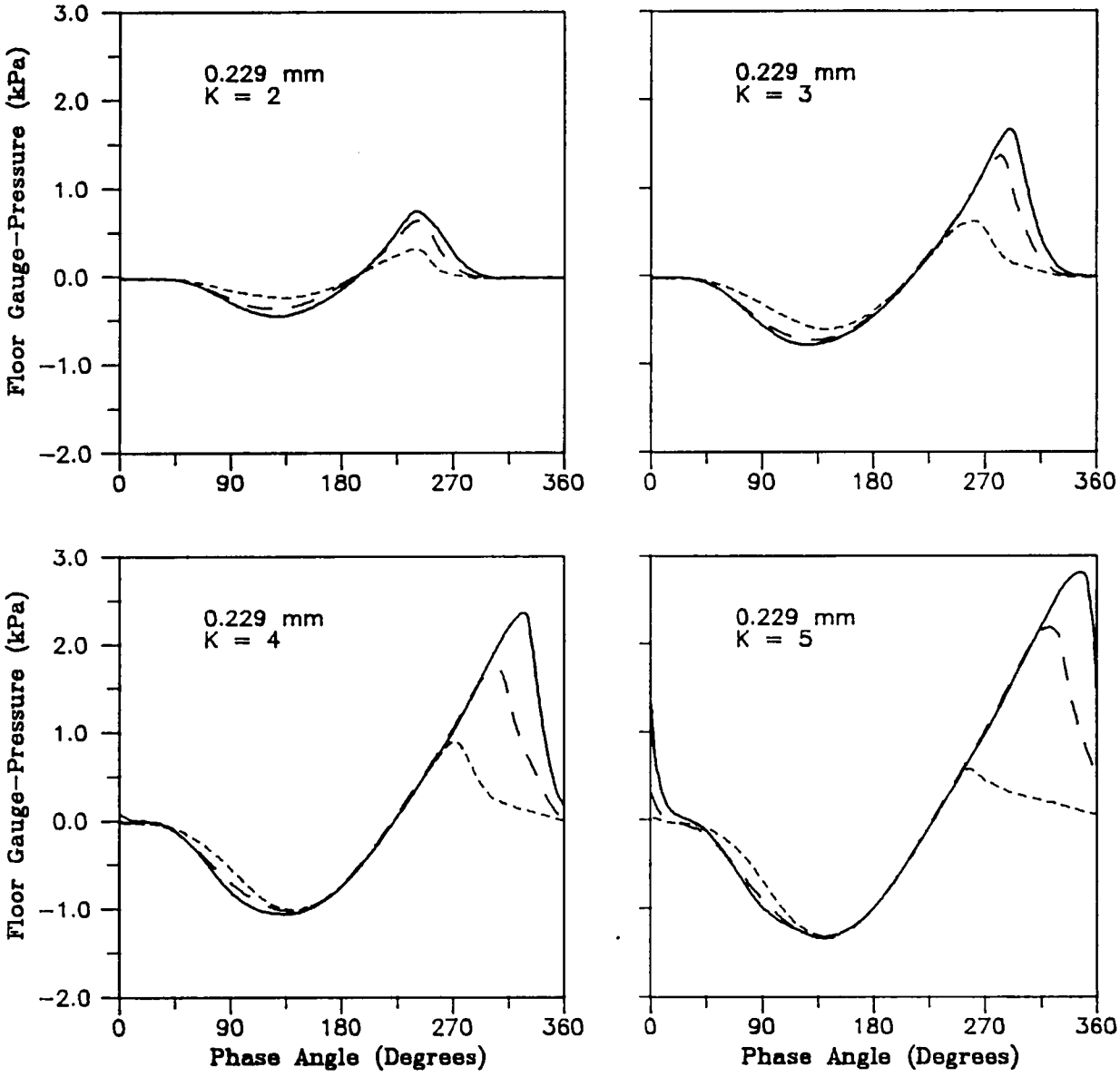

Figure 88. Cyclic floor pressures beneath a 30-mm deep bed of 229-μm Master Beads: The variation over one vibrational cycle of floor gauge-pressures at three horizontal locations beneath the vibrated bed. The vibrational frequency is 25 Hz, and $K = 2$, 3, 4, and 5. The particle size range is -60 +70 U.S. Standard Mesh. ———— floor pressure at the center of the bed, ———— floor pressure at the vessel wall, and — — — — floor pressure halfway between the side-wall and the center.

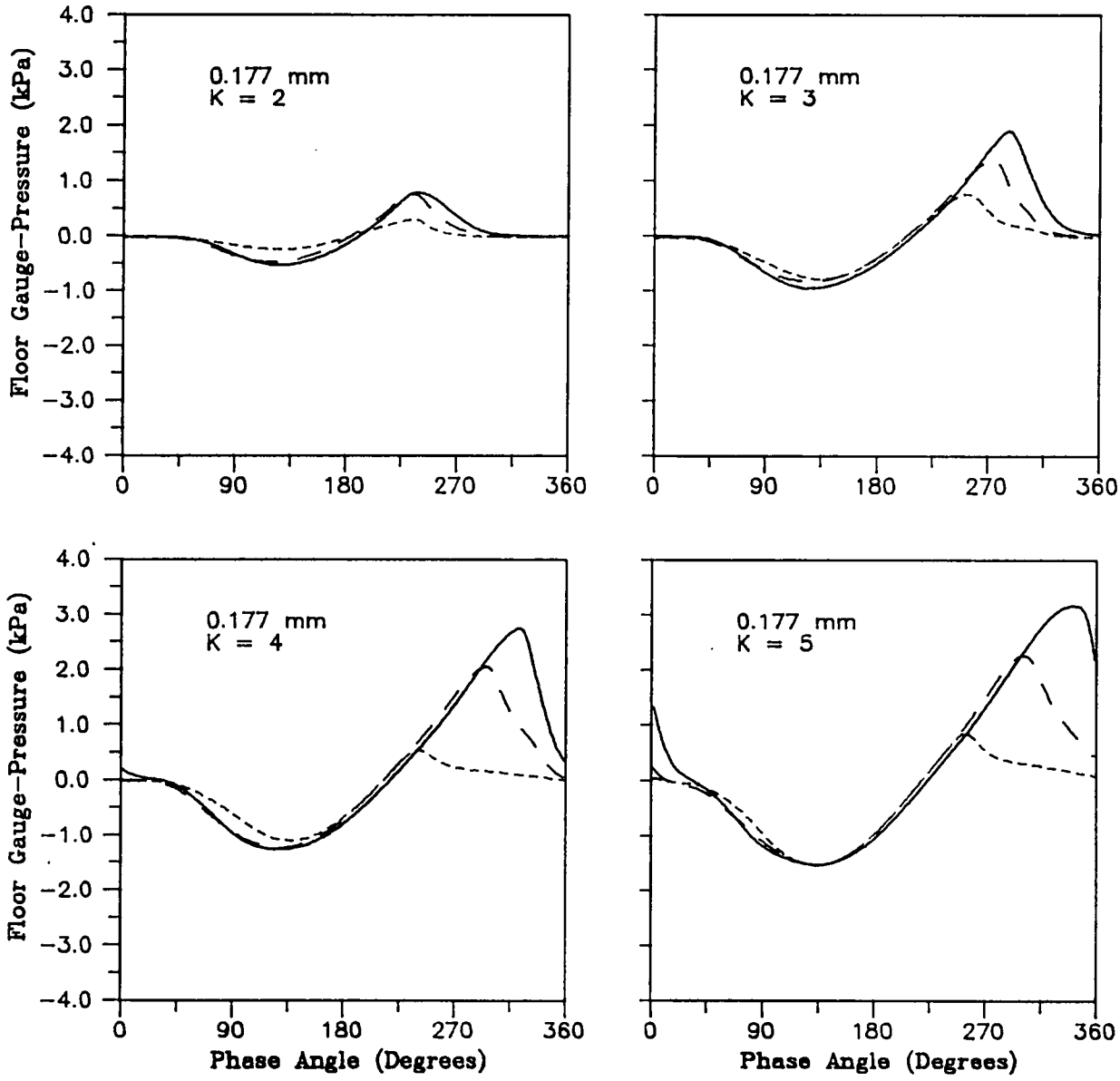

Figure 89. Cyclic floor pressures beneath a 30-mm deep bed of 177-μm Master Beads: The variation over one vibrational cycle of floor gauge-pressures at three horizontal locations beneath the vibrated bed. The vibrational frequency is 25 Hz, and $K = 2$, 3, 4, and 5. The particle size range is -70 +100 U.S. Standard Mesh. ———— floor pressure at the center of the bed, ——— floor pressure at the vessel wall, and — — — — floor pressure halfway between the side-wall and the center.

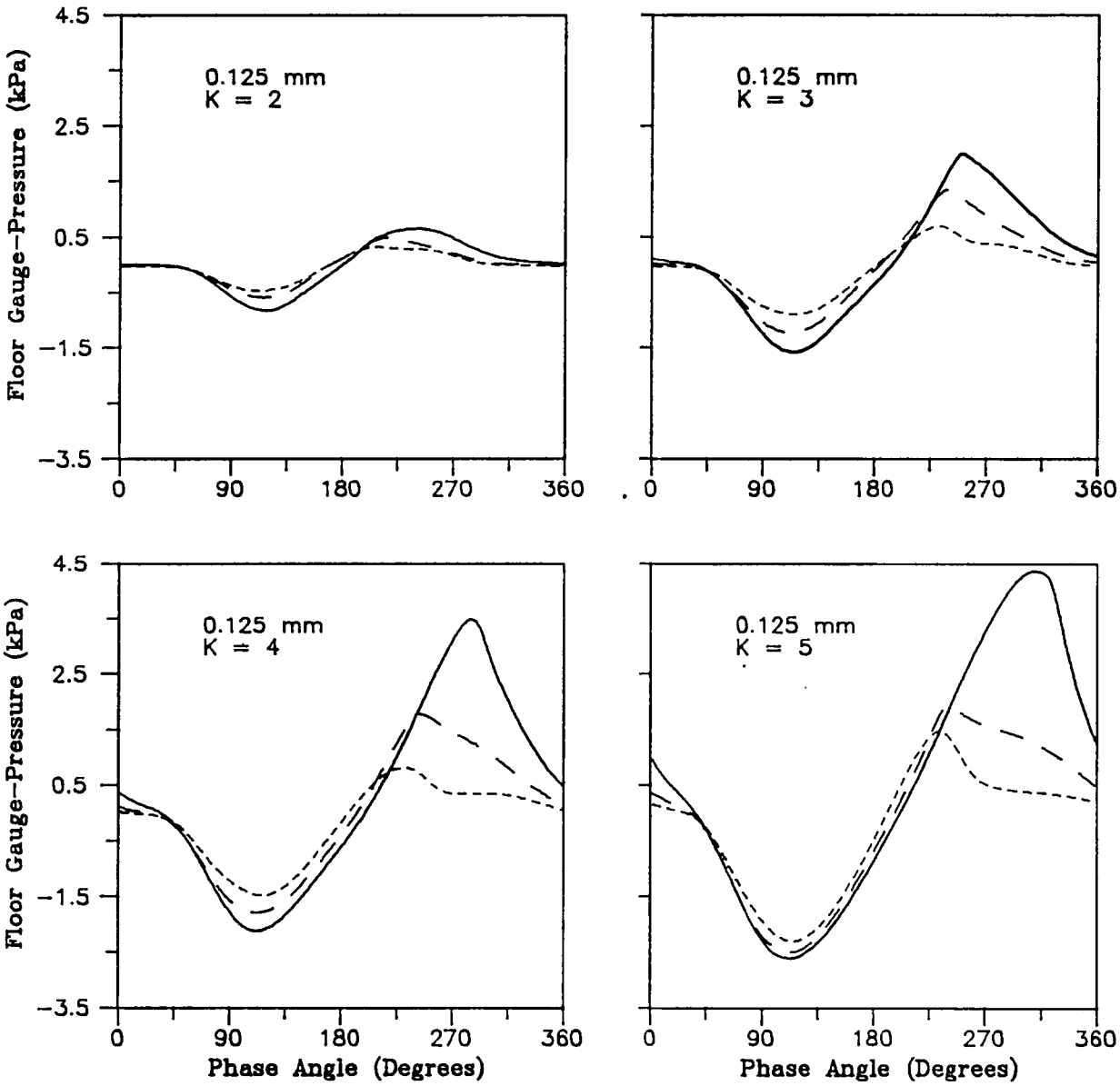

Figure 90. **Cyclic floor pressures beneath a 30-mm deep bed of 125-μm Master Beads:** The variation over one vibrational cycle of floor gauge-pressures at three horizontal locations beneath the vibrated bed. The vibrational frequency is 25 Hz, and $K = 2$, 3, 4, and 5. The particle size range is -100 +140 U.S. Standard Mesh. ———— floor pressure at the center of the bed, - - - - floor pressure at the vessel wall, and — — — — floor pressure halfway between the side-wall and the center.

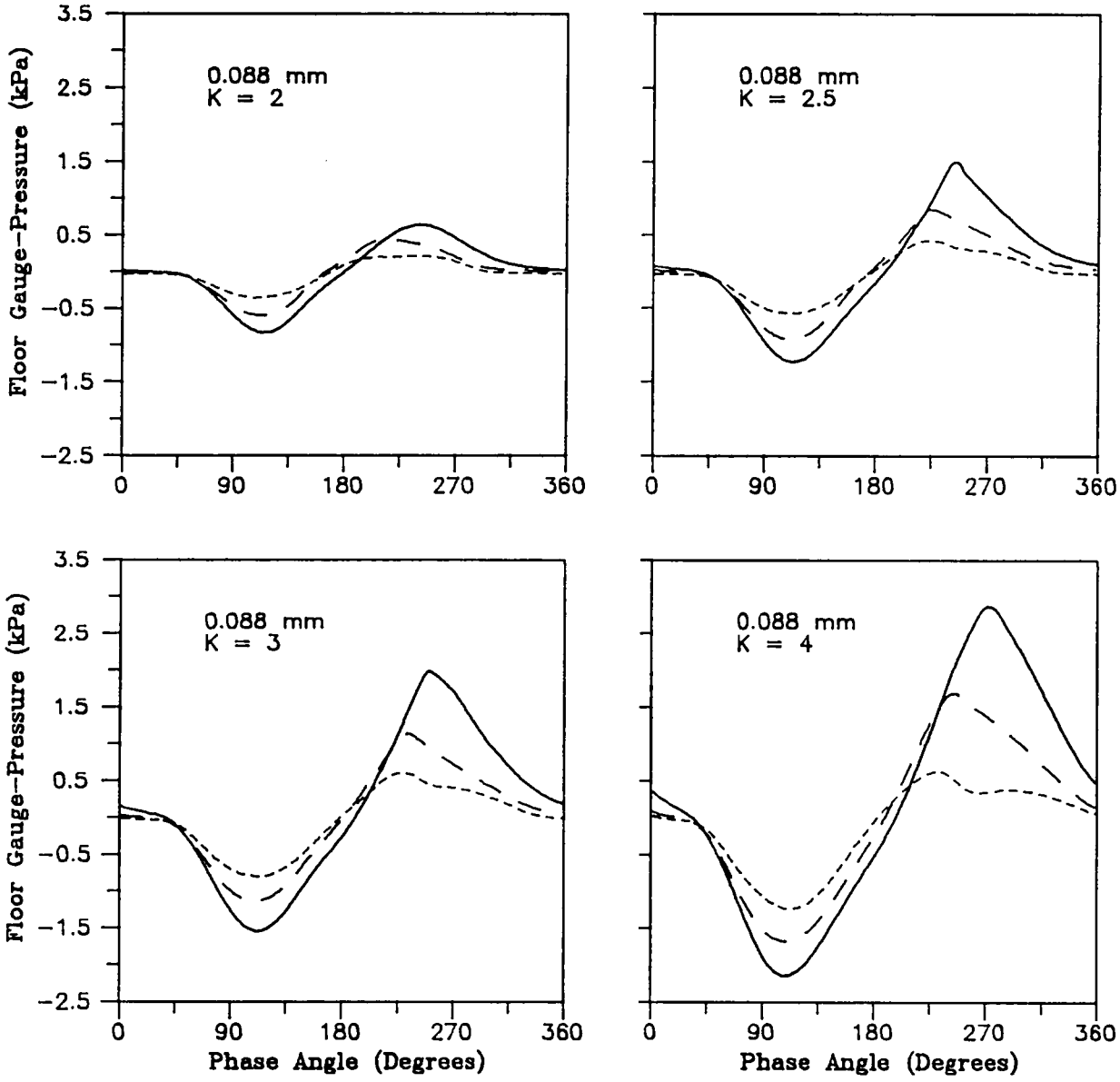

Figure 91. Cyclic floor pressures beneath a 30-mm deep bed of 88-μm Master Beads: The variation over one vibrational cycle of floor gauge-pressures at three horizontal locations beneath the vibrated bed. The vibrational frequency is 25 Hz, and $K = 2$, 2.5, 3, and 4. The particle size range is -140 +200 U.S. Standard Mesh. Note: For this particle size, the bed configuration is too unstable at $K = 5$ to obtain any reliable data. ———— floor pressure at the center of the bed, ——— floor pressure at the vessel wall, and — — — — floor pressure halfway between the side-wall and the center.

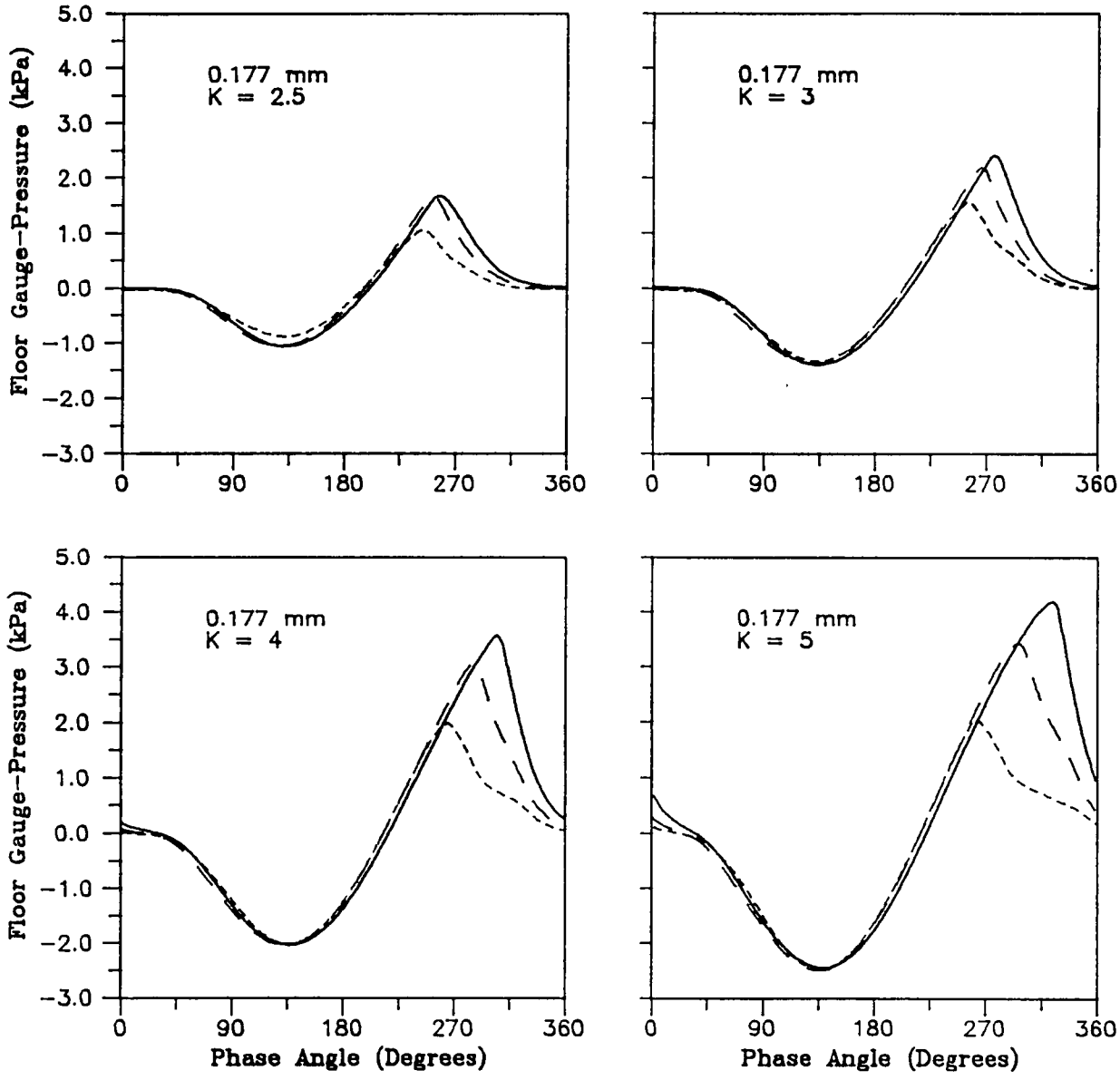

Figure 92. **Cyclic floor pressures beneath a 43.2-mm deep bed of 177-μm Master Beads:** The variation over one vibrational cycle of floor gauge-pressures at three horizontal locations beneath the vibrated bed. The vibrational frequency is 25 Hz, and $K = 2.5$, 3, 4, and 5. The particle size range is -70 +100 U.S. Standard Mesh. ———— floor pressure at the center of the bed, ---------- floor pressure at the vessel wall, and — — — — floor pressure halfway between the side-wall and the center.

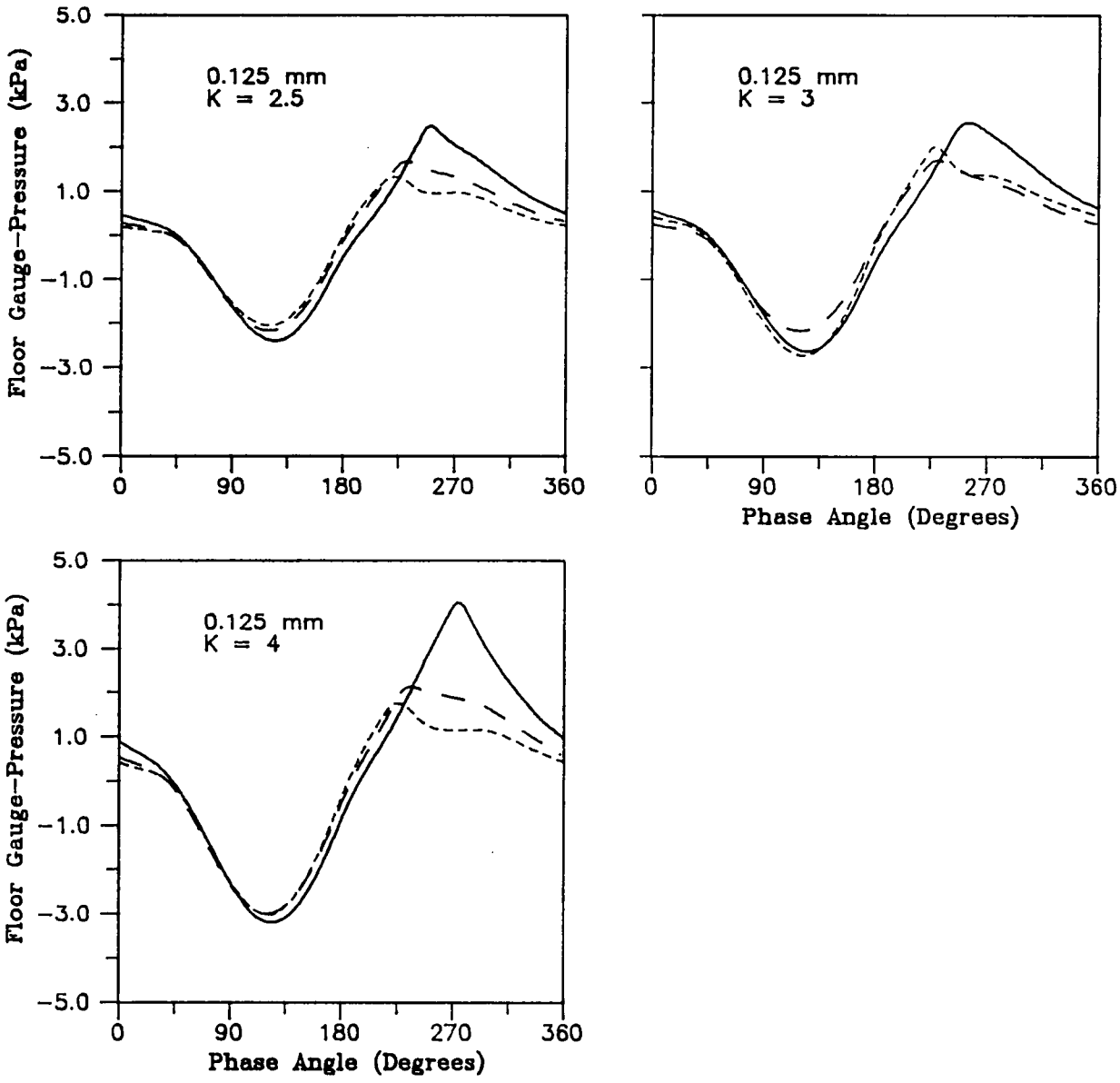

Figure 93. Cyclic floor pressures beneath a 43.2-mm deep bed of 125-μm Master Beads: The variation over one vibrational cycle of floor gauge-pressures at three horizontal locations beneath the vibrated bed. The vibrational frequency is 25 Hz, and $K = 2.5$, 3, and 4. The particle size range is -100 +140 U.S. Standard Mesh. Note: At $K = 5$, the bed configuration is too unstable to obtain any reliable data ———— floor pressure at the center of the bed, ———— floor pressure at the vessel wall, and — — — — floor pressure halfway between the side-wall and the center.

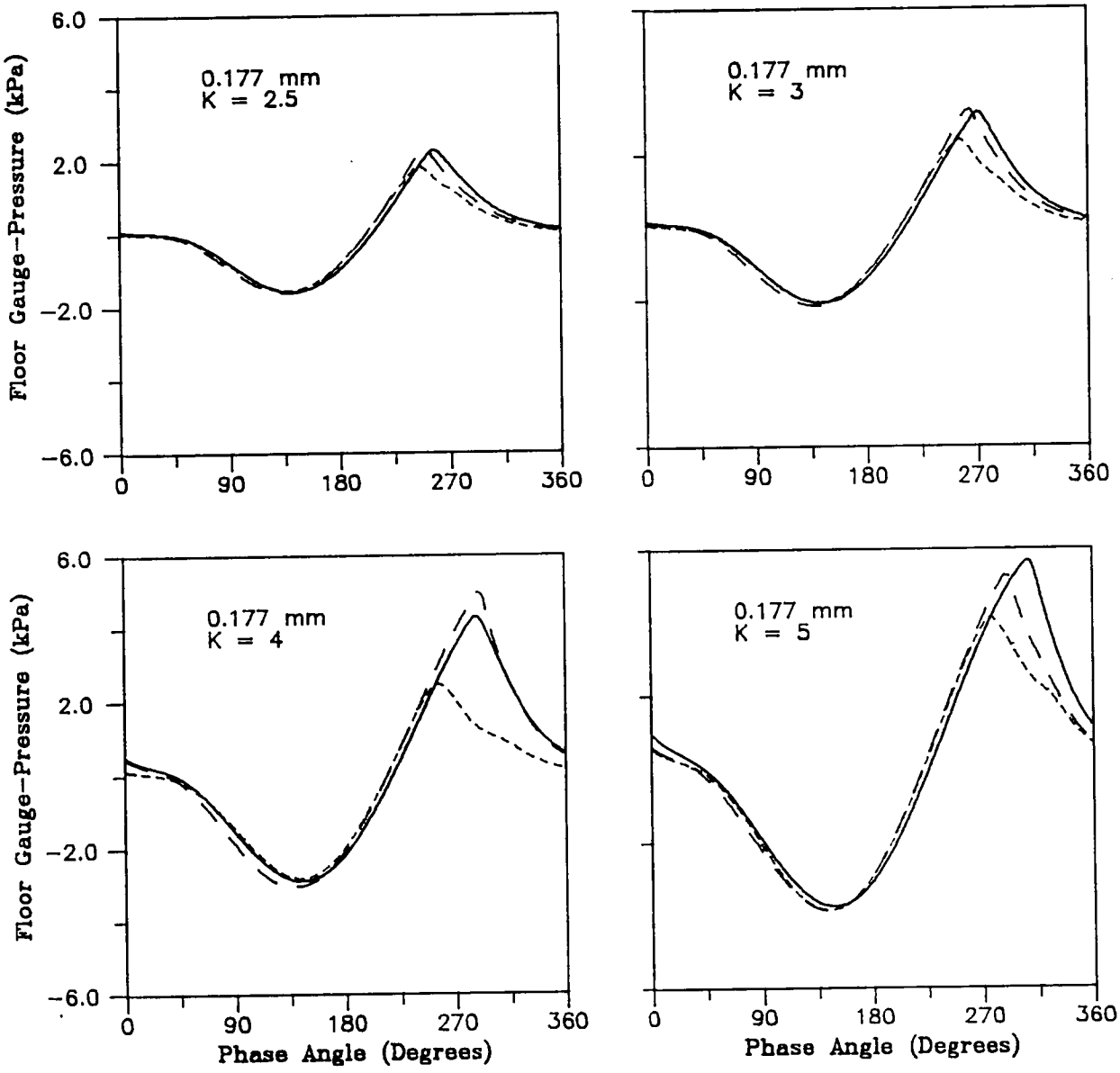

Figure 94. Cyclic floor pressures beneath a 60-mm deep bed of 177-μm Master Beads: The variation over one vibrational cycle of floor gauge-pressures at three horizontal locations beneath the vibrated bed. The vibrational frequency is 25 Hz, and $K = 2.5$, 3, 4, and 5. The particle size range is -70 +100 U.S. Standard Mesh. ———— floor pressure at the center of the bed, ------- floor pressure at the vessel wall, and — — — — floor pressure halfway between the side-wall and the center.

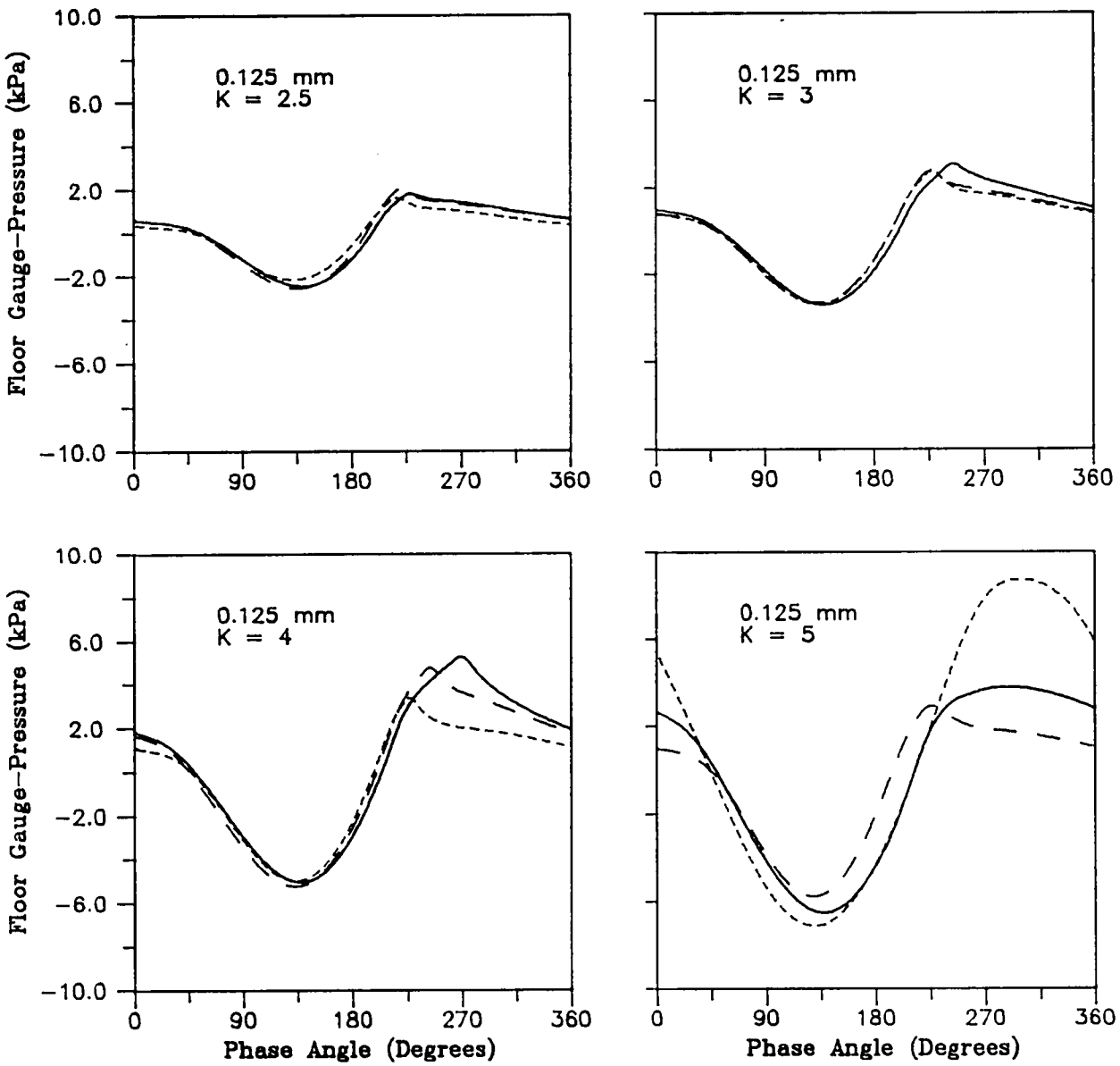

Figure 95. Cyclic floor pressures beneath a 60-mm deep bed of 125-μm Master Beads: The variation over one vibrational cycle of floor gauge-pressures at three horizontal locations beneath the vibrated bed. The vibrational frequency is 25 Hz, and $K = 2.5$, 3, 4, and 5. The particle size range is -100 +140 U.S. Standard Mesh. Note: At $K = 5$, the center-high configuration is unstable, and floor pressures are shown for a wall-high bunker configuration instead. ———— floor pressure at the center of the bed, ---------- floor pressure at the vessel wall, and — — — — floor pressure halfway between the side-wall and the center.

Appendix E. Cyclic Floor Pressures for Vibrated Beds of Glass Beads

Experimentally measured floor pressures beneath vibrated beds of glass beads of both high and low densities are shown graphically on the following pages. Floor pressures are measured at three locations beneath the bed (see Figure 13 on page 62), and for four different vibrational intensities indicated within each figure. The plots show the variation of floor pressures at all three locations usually over one vibrational cycle; but if the bed trajectory is unstable, the pressure variation is shown over two cycles instead. The floor pressure beneath the center of the bed is shown as a solid curve, the floor pressure at the location halfway between the side-wall and the center is shown as a dashed curve, and the floor pressure at the side-wall is shown as a dotted (or short-dashed) curve.

Figure 96 on page 376 to Figure 98 on page 378 give floor pressures beneath 30-mm deep beds of low-density glass beads. Figure 99 on page 379 to Figure 101 on page 381 give floor pressures beneath 30-mm deep beds of high-density glass beads.

Note that the scale of the floor-pressure axis is constant over the range of vibrational intensities for a given particle size, but the scale varies between one particle size and another.

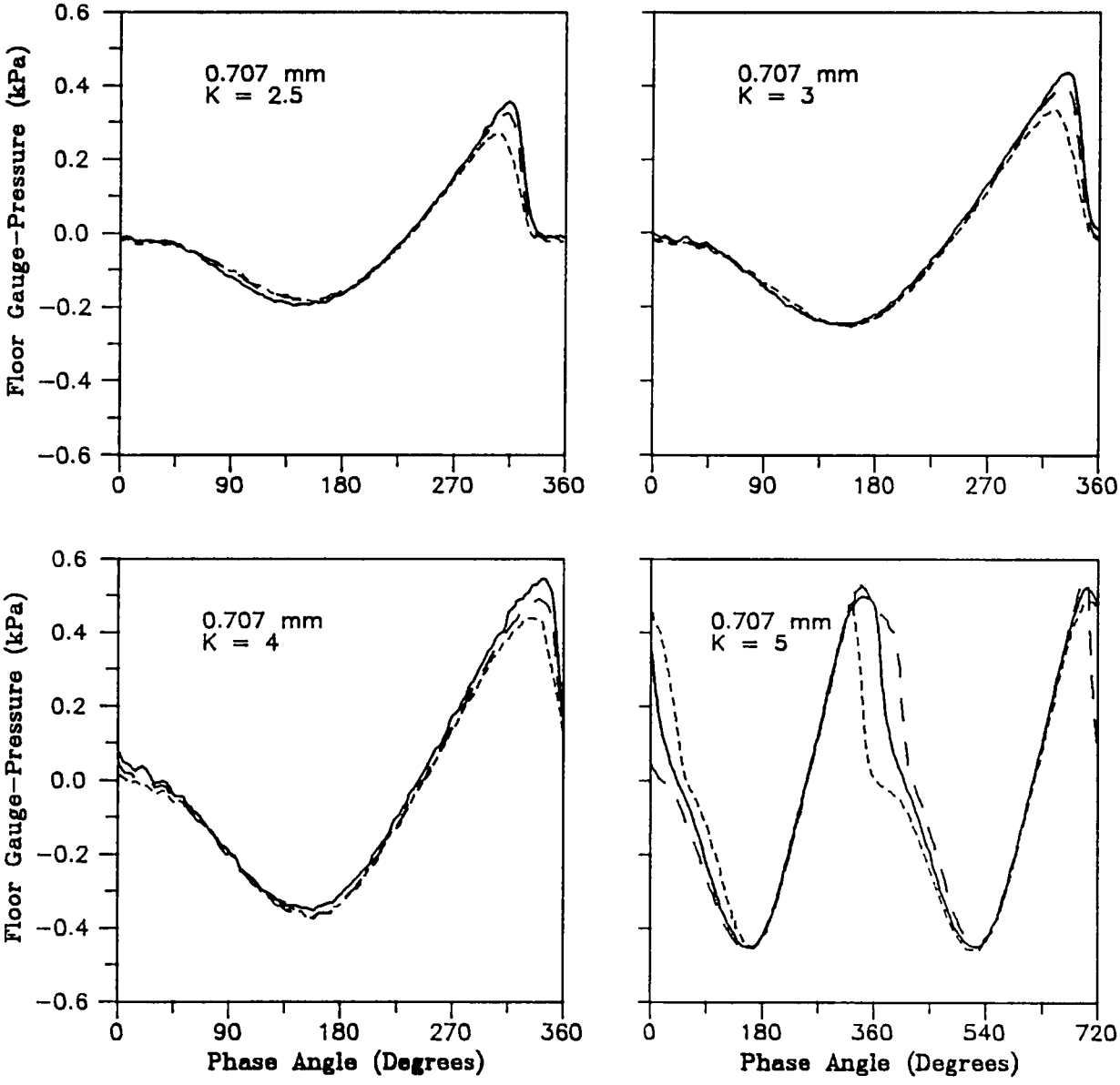

Figure 96. Cyclic floor pressures beneath a 30-mm deep bed of 707-μm low-density glass beads: The variation over one vibrational cycle of floor gauge-pressures at three horizontal locations beneath the vibrated bed. The vibrational frequency is 25 Hz, and $K = 2.5$, 3, 4, and 5. The particle size range is -20 +30 U.S. Standard Mesh. Note: At $K = 5$, the bed trajectory is unstable causing the pressure waveform in one cycle to be different from the next, therefore, two cycles are shown in this case. ———— floor pressure at the center of the bed, ---------- floor pressure at the vessel wall, and — — — — floor pressure halfway between the side-wall and the center.

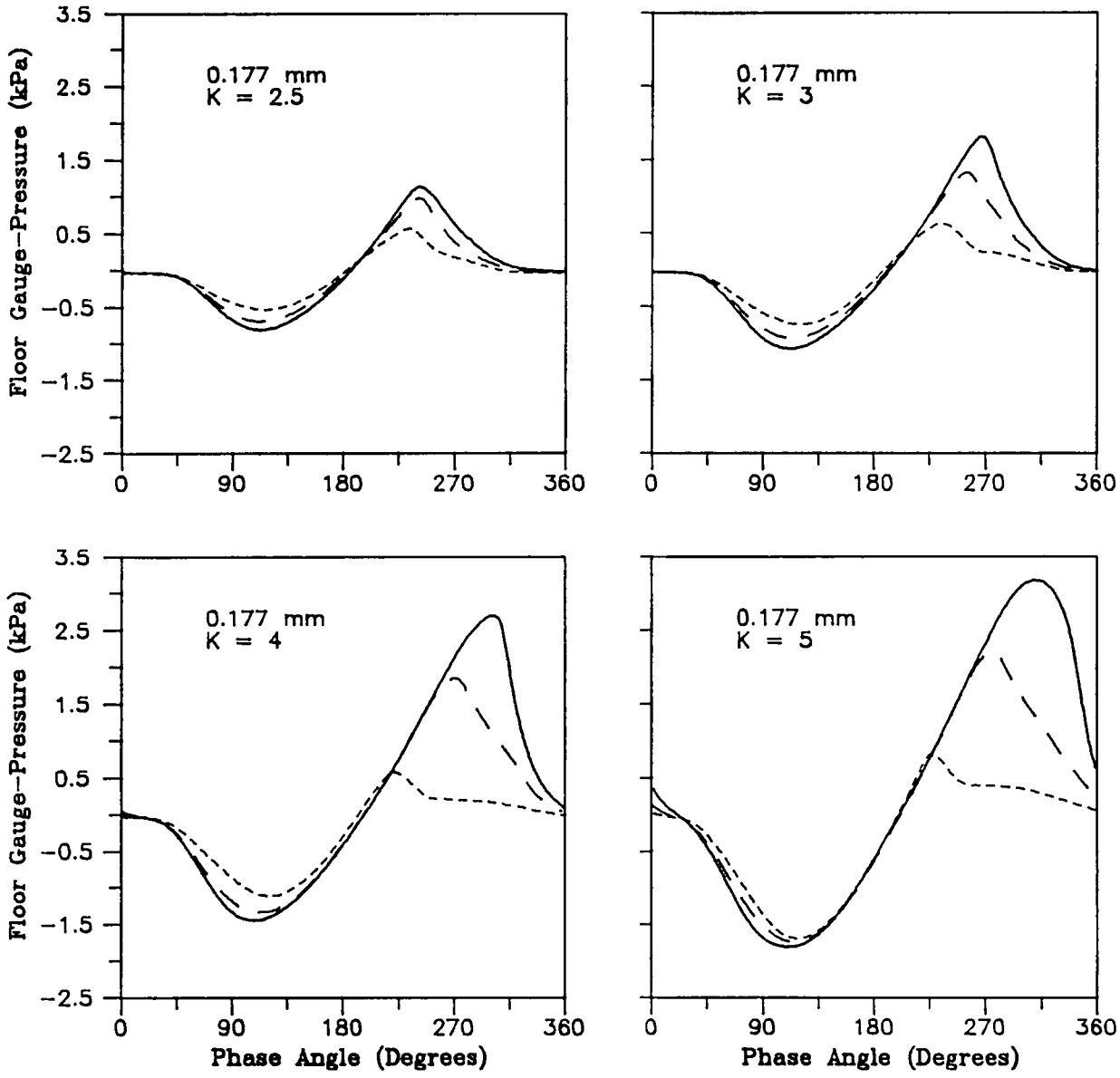

Figure 97. Cyclic floor pressures beneath a 30-mm deep bed of 177-μm low-density glass beads: The variation over one vibrational cycle of floor gauge-pressures at three horizontal locations beneath the vibrated bed. The vibrational frequency is 25 Hz, and $K = 2.5$, 3, 4, and 5. The particle size range is -70 +100 U.S. Standard Mesh. ———— floor pressure at the center of the bed, ---------- floor pressure at the vessel wall, and — — — — floor pressure halfway between the side-wall and the center.

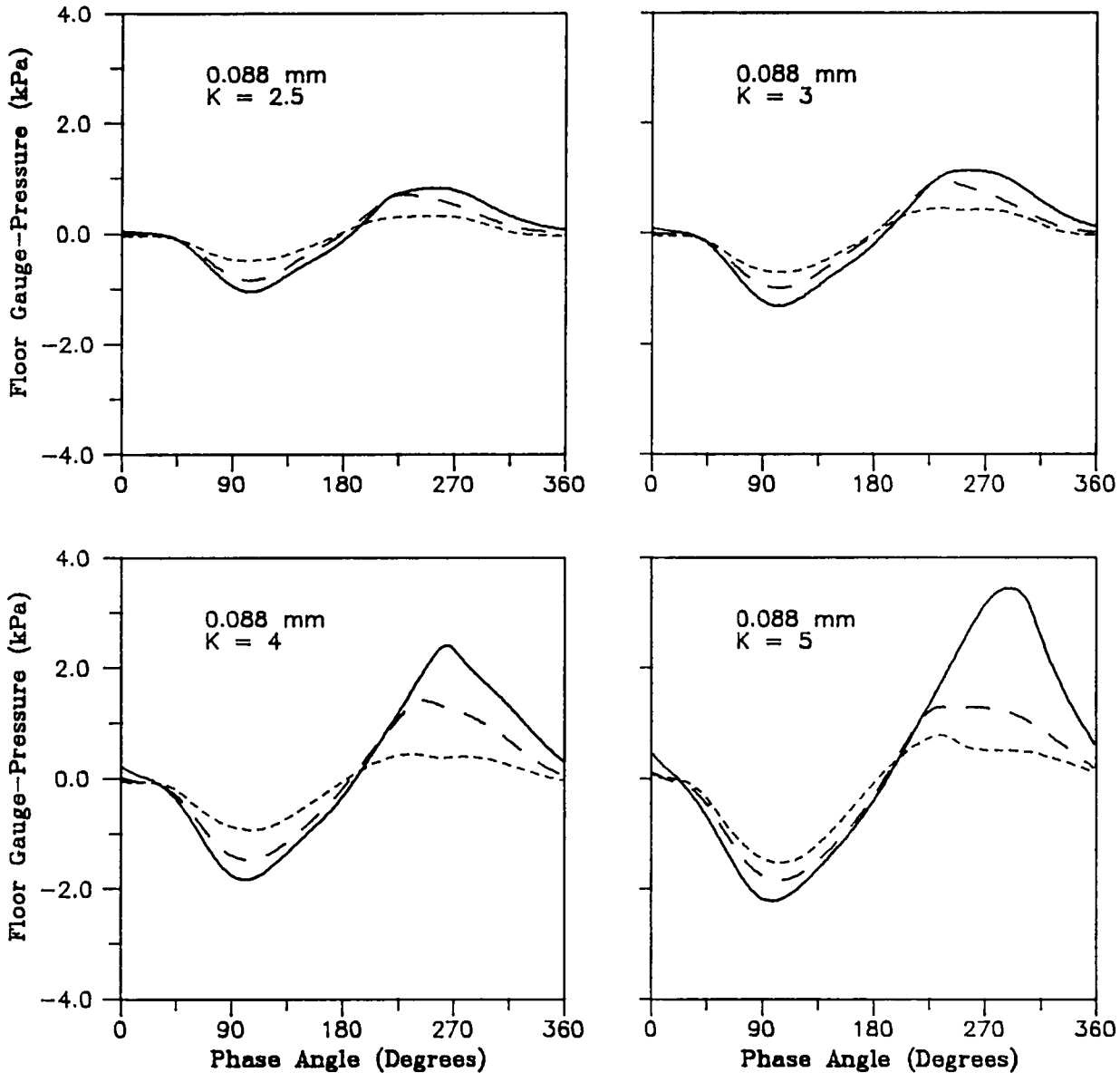

Figure 98. Cyclic floor pressures beneath a 30-mm deep bed of 88-μm low-density glass beads: The variation over one vibrational cycle of floor gauge-pressures at three horizontal locations beneath the vibrated bed. The vibrational frequency is 25 Hz, and $K = 2.5$, 3, 4, and 5. The particle size range is -140 +200 U.S. Standard Mesh. ———— floor pressure at the center of the bed, ——— floor pressure at the vessel wall, and — — — — floor pressure halfway between the side-wall and the center.

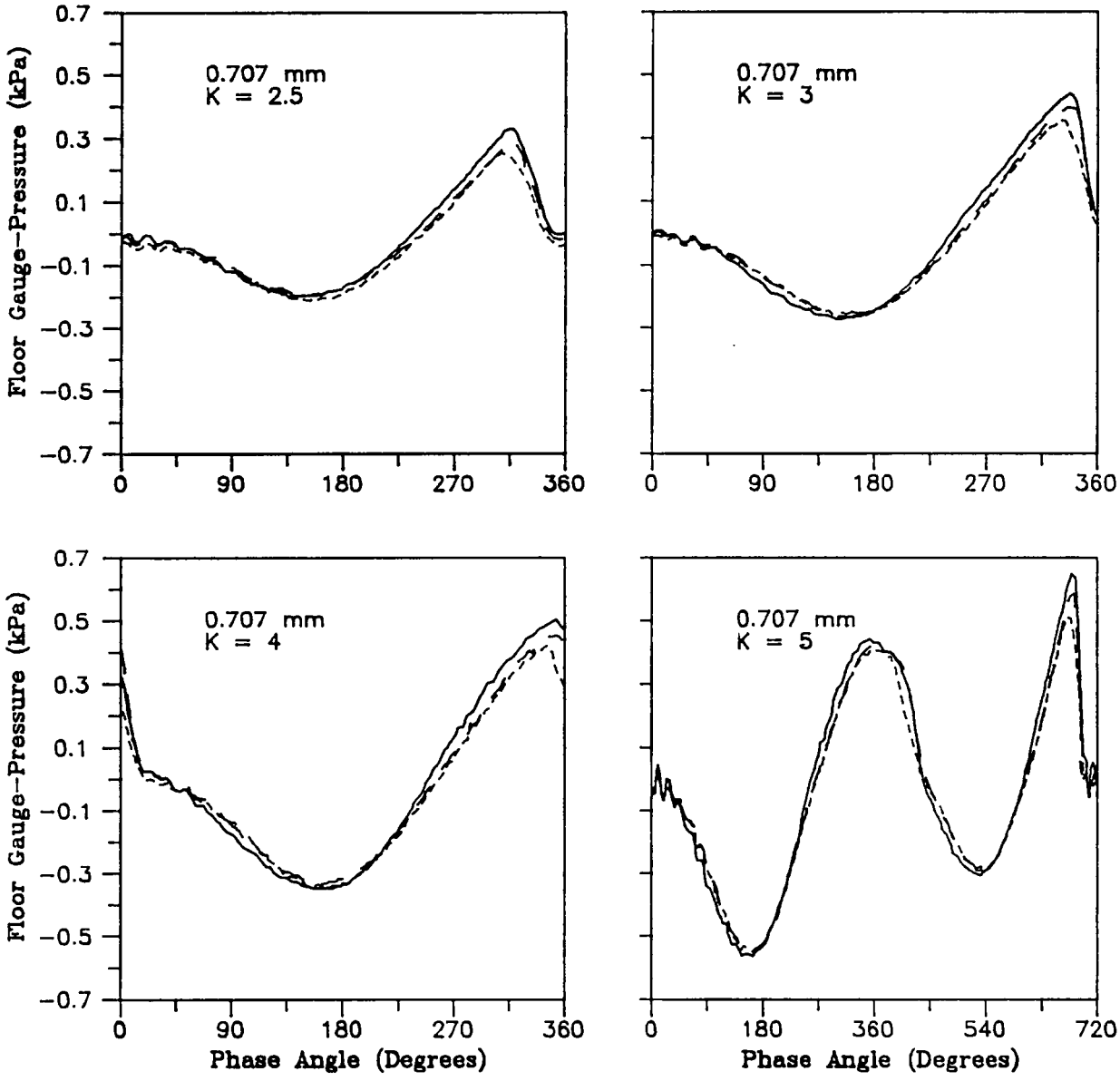

Figure 99. Cyclic floor pressures beneath a 30-mm deep bed of 707-μm high-density glass beads: The variation over one vibrational cycle of floor gauge-pressures at three horizontal locations beneath the vibrated bed. The vibrational frequency is 25 Hz, and $K = 2.5$, 3, 4, and 5. The particle size range is -20 +30 U.S. Standard Mesh. Note: At $K = 5$, the bed trajectory is unstable causing the pressure waveform in one cycle to be different from the next, therefore, two cycles are shown in this case. ———— floor pressure at the center of the bed, ---------- floor pressure at the vessel wall, and — — — — floor pressure halfway between the side-wall and the center.

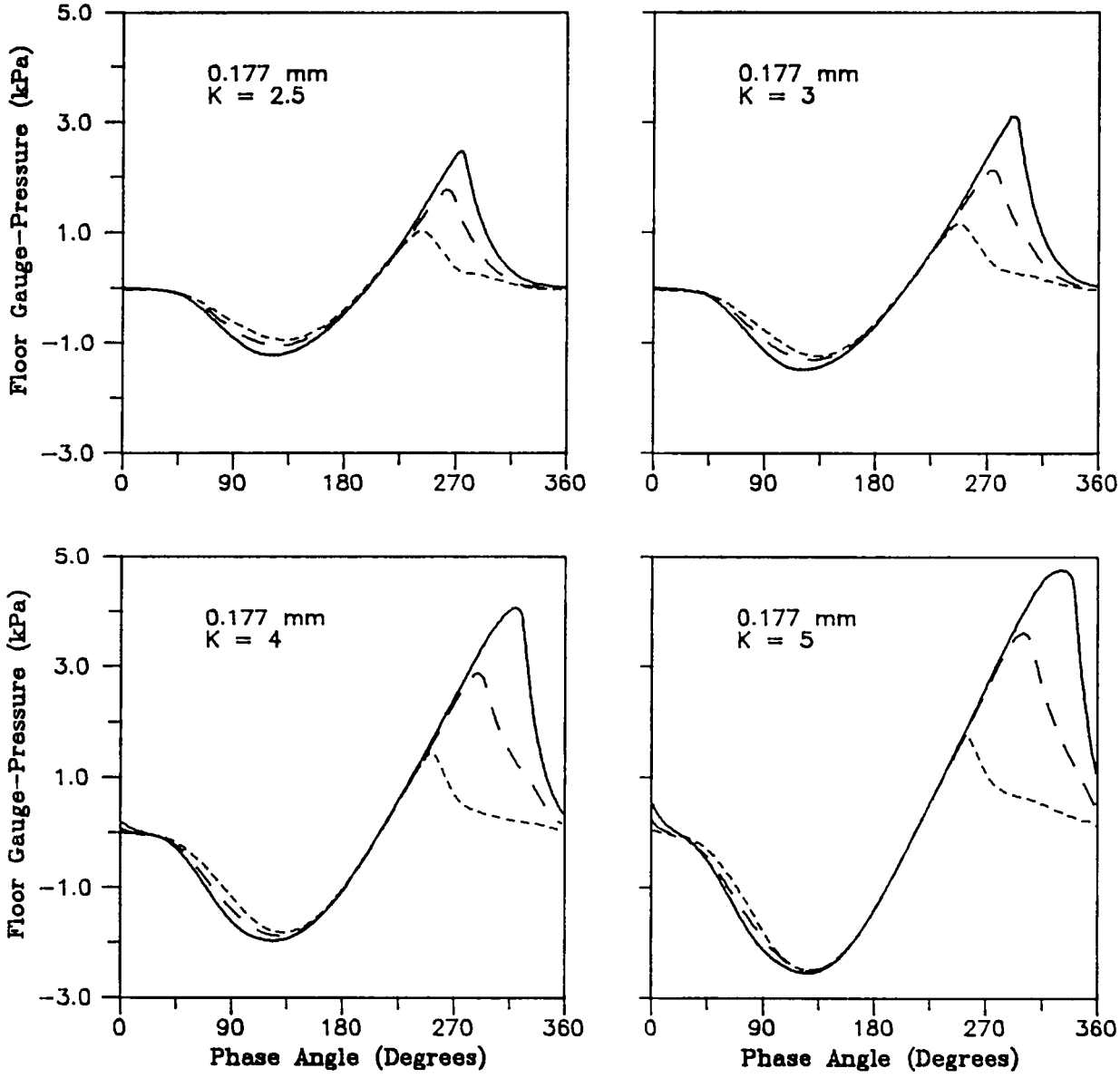

Figure 100. Cyclic floor pressures beneath a 30-mm deep bed of 177-μm high-density glass beads: The variation over one vibrational cycle of floor gauge-pressures at three horizontal locations beneath the vibrated bed. The vibrational frequency is 25 Hz, and $K = 2.5$, 3, 4, and 5. The particle size range is -70 +100 U.S. Standard Mesh. ———— floor pressure at the center of the bed, ---------- floor pressure at the vessel wall, and — — — — floor pressure halfway between the side-wall and the center.

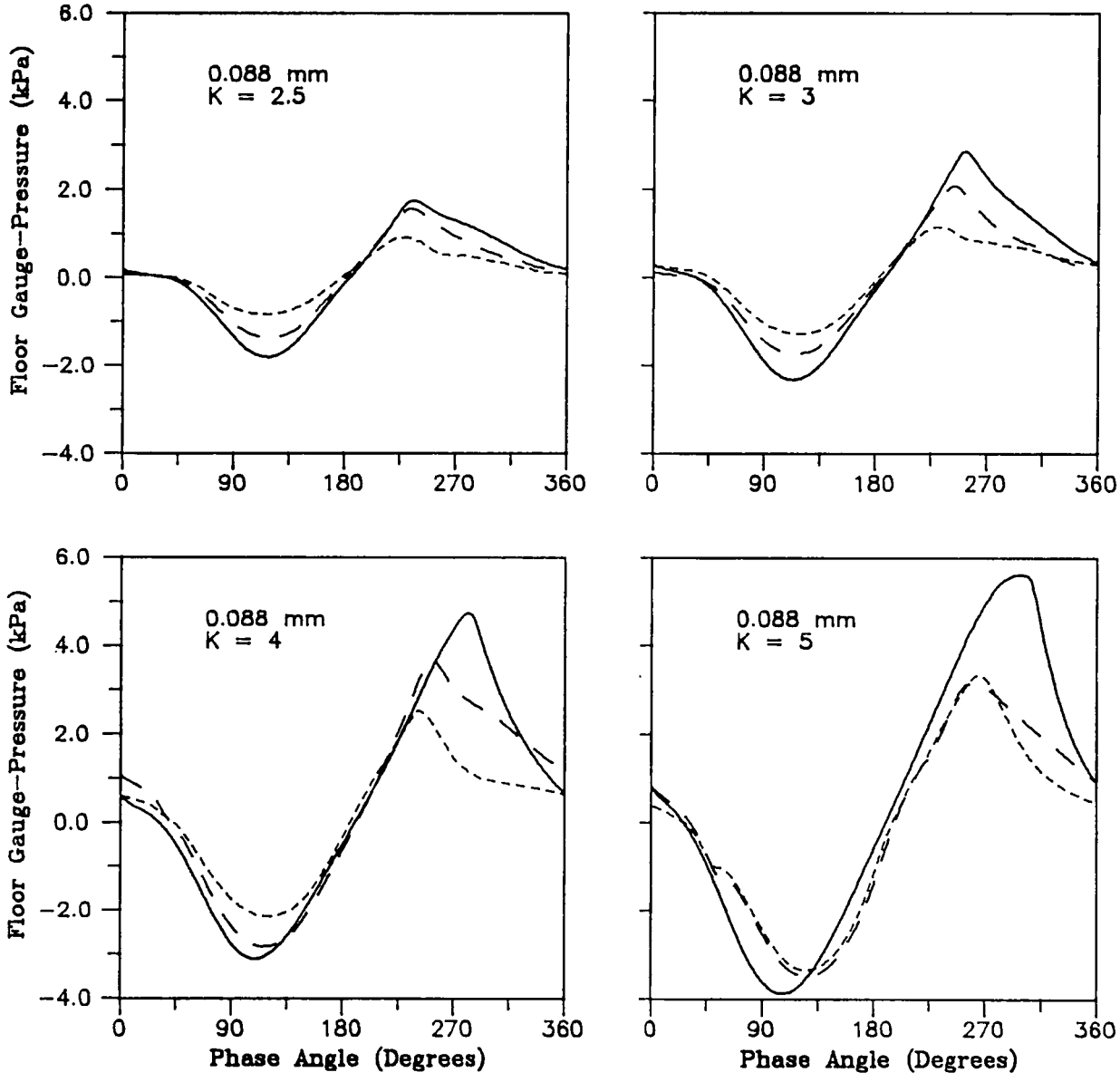

Figure 101. Cyclic floor pressures beneath a 30-mm deep bed of 88-μm high-density glass beads: The variation over one vibrational cycle of floor gauge-pressures at three horizontal locations beneath the vibrated bed. The vibrational frequency is 25 Hz, and $K = 2.5$, 3, 4, and 5. The particle size range is -140 +200 U.S. Standard Mesh. ———— floor pressure at the center of the bed, ——— floor pressure at the vessel wall, and — — — — floor pressure halfway between the side-wall and the center.

Appendix F. Temperature Profiles in the Heat-Transfer Probe Supports

An analysis of the heat conduction through a probe support to obtain a temperature profile over the length of the support is possible by making the assumptions listed in section 6.1.3.2 of chapter 6. Since the first 6.35 mm of the Lexan section of the support is at a temperature Θ_o, because of its intimate contact with the copper body of the heat-transfer probe (see also Figure 74 on page 279), only the temperature in the second 6.35 mm varies with position. The temperature will also vary along the entire length of the steel section of the support.

Only the section of the Lexan which is not isothermal, and the steel section of the support will be considered. As shown in Figure 102 on page 383, the support is an annular structure with an inner radius of r_i, and an outer radius equal to the heat-transfer probe radius, r_t. The cross-sectional area of the annulus is $\pi(r_t^2 - r_i^2)$.

Consider a surface element of thickness Δx, along the length of this section of the support, which is small enough, that the temperature is approximately Θ_x along its width. If the heat flux into the element is q_x, and the heat flux out of the element is $q_{x+\Delta x}$, a heat balance may be written over the element as follows:

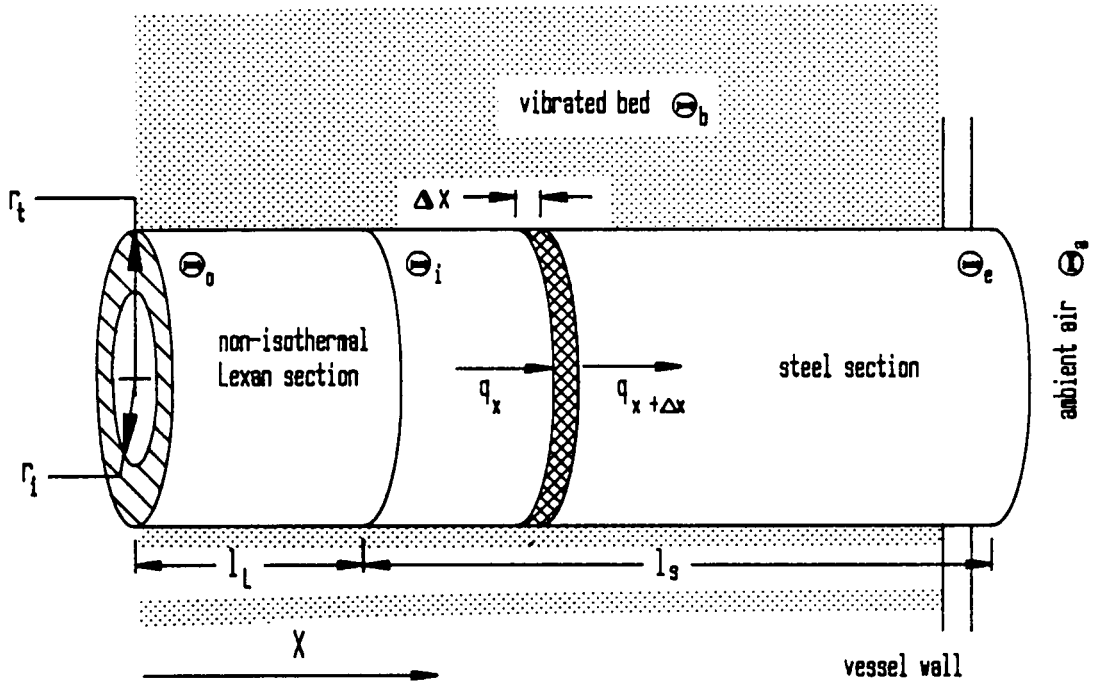

Figure 102. Heat conduction within the heat-transfer probe supports: Illustration of the non-isothermal Lexan and steel sections of a probe support. A typical surface element is shown. The heat flux into the left side of the element is q_x, and that out of the right side is $q_x + q_{\Delta x}$. Notation: Θ_0 - temperature at the beginning of the non-isothermal Lexan section; Θ_i - temperature at the Lexan-steel joint; Θ_e - temperature at the end of the steel section facing the ambient air; Θ_a - temperature of the ambient air; Θ_b - average bed temperature; x - horizontal distance ordinate.

$$\pi(r_t^2 - r_i^2)\,[q_x - q_{x+\Delta x}] - h\,(2\pi r_t)\,\Delta x\,(\Theta_x - \Theta_b) = 0 \qquad [F.1]$$

Here, h is the overall surface-to-bed heat-transfer coefficient, and Θ_b is the bed temperature. Rearranging this equation gives:

$$-\frac{\Delta q}{\Delta x} - \frac{2hr_t\,(\Theta_x - \Theta_b)}{r_t^2 - r_i^2} = 0 \qquad [F.2]$$

where $\Delta q = (q_{x+\Delta x} - q_x)$. Fourier's law of heat conduction can be written as:

$$q = -k\,\frac{d\Theta_x}{dx} \qquad [F.3]$$

where k is the thermal conductivity of the material. Substituting for q using Fourier's law in equation [F.2], and taking the limit as $\Delta x \to 0$, gives:

$$k\,\frac{d^2\Theta_x}{dx^2} - \frac{2hr_t}{r_t^2 - r_i^2}\,(\Theta_x - \Theta_b) = 0 \qquad [F.4]$$

This is a general equation for the temperature gradient in any section of the support. The following dimensionless variables may be introduced:

$$\vartheta = \frac{\Theta_x - \Theta_b}{\Theta_o - \Theta_b}; \quad \chi = \frac{x}{l}$$

Θ_o, as defined in section 6.1.3.2 of chapter 6, is the temperature of the isothermal section of the Lexan support, and is the temperature read by the implanted thermocouple. The length of any section of the support is l, so the length of the non-isothermal section of the Lexan is $l_L = (l_i - l_o)$, and that of the steel section is $l_s = (l_e - l_i)$. The distances l_o, l_i, and l_e are defined in Figure 74 on page 279. Using these dimensionless variables, equation [F.4] for the temperature profile along the support may be written in the following dimensionless form:

$$\frac{d^2\vartheta}{d\chi^2} - \lambda^2\vartheta = 0 \qquad [F.5]$$

where

$$\lambda^2 \equiv \frac{2hr_t l}{k(r_t^2 - r_i^2)}$$

For the non-isothermal Lexan section, the solution to equation [F.5] is:

$$\vartheta_L = c_1 \exp(\lambda_L \chi_L) + c_2 \exp(-\lambda_L \chi_L) \qquad [F.6]$$

where

$$\lambda_L^2 \equiv \frac{2l_L^2 h r_t}{k_L(r_t^2 - r_i^2)}, \qquad \chi_L = \frac{x_L}{l_L},$$

and k_L is the thermal conductivity of Lexan. Equation [F.6] describes the variation of the dimensionless temperature ϑ_L, of the non-isothermal section of the Lexan support, along its length l_L. The constants c_1 and c_2, can be evaluated using the following boundary conditions for this section of the support:

$$\begin{aligned} \vartheta_L &= 1 \text{ at } \chi_L = 0 \\ \vartheta_L &= \vartheta_i \text{ at } \chi_L = 1 \end{aligned} \qquad [F.7]$$

The dimensionless temperature ϑ_i, at the joint between the Lexan and steel sections of the support is given by:

$$\vartheta_i \equiv \frac{\Theta_i - \Theta_b}{\Theta_o - \Theta_b}$$

where Θ_i is the temperature at the Lexan-steel joint, as shown in Figure 74 on page 279. Solving for c_1 and c_2 using these boundary conditions gives:

$$c_1 = \frac{\vartheta_l - \exp(-\lambda_L)}{2\sinh\lambda_L} \quad \text{and} \quad c_2 = \frac{\exp(\lambda_L) - \vartheta_l}{2\sinh\lambda_L}$$

Substituting these expressions for c_1 and c_2 into equation [F.6] gives the following expression for the dimensionless temperature profile along the length of the non-isothermal Lexan section of the support:

$$\vartheta_L = \frac{\vartheta_l \sinh(\lambda_L \chi_L) + \sinh(\lambda_L[1 - \chi_L])}{\sinh\lambda_L} \qquad [F.8]$$

Similarly, the general solution for the temperature profile within the steel section may be written as follows:

$$\vartheta_s = c_3 \exp(\lambda_s \chi_s) + c_4 \exp(-\lambda_s \chi_s) \qquad [F.9]$$

Here,

$$\lambda_s = \frac{2l_s^2 h r_t}{k_s(r_t^2 - r_i^2)}, \qquad \chi_s = \frac{x}{l_s},$$

and k_s is the thermal conductivity of steel. The constants c_3 and c_4, can be evaluated by considering the boundary conditions for the steel section. At the beginning of the steel section ($x_s = 0$), the temperature is equal to that of the Lexan-steel joint, i.e. Θ_l. At the other end of the steel section, heat is lost to the ambient air by convection, so

$$-k_s \left.\frac{d\Theta_s}{dx_s}\right|_{x_s = l_s} = h_a(\Theta_e - \Theta_a)$$

Θ_e is the temperature at the end of the steel section facing the ambient air, Θ_a is the temperature of the ambient air, and h_a is the heat-transfer coefficient for convective heat transfer from a flat plate to air. These boundary conditions can be expressed in dimensionless form as follows:

$$\vartheta_s = \vartheta_l \quad \text{at} \quad \chi_s = 0$$

$$\frac{d\vartheta}{d\chi_s} = -\left(\frac{h_a l_s}{k_s}\right)(\vartheta_e - \vartheta_a) \quad \text{at} \quad \chi_s = 1 \qquad [F.10]$$

where

$$\vartheta_e = \frac{\Theta_e - \Theta_b}{\Theta_o - \Theta_b} \quad \text{and} \quad \vartheta_a = \frac{\Theta_a - \Theta_b}{\Theta_o - \Theta_b}$$

The group $(h_a l_s/k_s)$ is dimensionless. Using these boundary conditions, the following expressions are obtained for the constants in equation [F.10]:

$$c_3 = \frac{\vartheta_l \exp(-\lambda_s) - \vartheta_l \eta_s \exp(-\lambda_s) + \eta_s \vartheta_a}{2\cosh\lambda_s + 2\eta_s \sinh\lambda_s}$$

and

$$c_4 = \frac{\vartheta_l \exp(\lambda_s) + \vartheta_l \eta_s \exp(\lambda_s) - \eta_s \vartheta_a}{2\cosh\lambda_s + 2\eta_s \sinh\lambda_s}$$

The dimensionless group η_s is defined as follows:

$$\eta_s \equiv \frac{h_a l_s}{k_s \lambda_s}$$

Substituting these expressions for c_3 and c_4 in equation [F.9] gives the following expression for the temperature profile within the steel section:

$$\vartheta_s = \frac{\vartheta_l \cosh(\lambda_s[1-\chi_s]) + \vartheta_l \eta_s \sinh(\lambda_s[1-\chi_s]) + \vartheta_a \eta_s \sinh(\lambda_s \chi_s)}{\cosh\lambda_s + \eta_s \sinh\lambda_s} \qquad [F.11]$$

The interface temperature ϑ_i, can be evaluated by assuming that the Lexan-steel joint is of zero thickness. If that is the case, the heat flux from the end of the Lexan section at the joint, must equal the heat flux into the adjoining end of the steel section. In mathematical terms:

$$k_l \frac{d\vartheta_L}{d\chi_L}\bigg|_{\chi_L=1} = k_s \frac{d\vartheta_s}{d\chi_s}\bigg|_{\chi_s=0} \qquad [F.12]$$

For the Lexan section,

$$\frac{d\vartheta_L}{d\chi_L}\bigg|_{\chi_L=1} = \frac{\vartheta_i \lambda_L \cosh \lambda_L - \lambda_L}{\sinh \lambda_L} \qquad [F.13]$$

For the steel section,

$$\frac{d\vartheta_s}{d\chi_s}\bigg|_{\chi_s=0} = \frac{\eta_s \vartheta_a - \vartheta_i \lambda_s \sinh \lambda_s - \vartheta_i \eta_s \cosh \lambda_s}{\cosh \lambda_s + \eta_s \sinh \lambda_s} \qquad [F.14]$$

Substituting equations [F.13] and [F.14] for the thermal gradient at the joint in the Lexan and steel respectively, into equation [F.12], and solving for ϑ_i gives:

$$\vartheta_i = \frac{F\eta_a \vartheta_a + 1}{\cosh \lambda_L + F \sinh \lambda_s + F\eta_s \cosh \lambda_s} \qquad [F.15]$$

The dimensionless factor F is given by:

$$F = \left(\frac{\lambda_s k_s}{\lambda_L k_L} \right) \left[\frac{\sinh \lambda_L}{\cosh \lambda_s + \eta_s \sinh \lambda_s} \right]$$

The dimensionless joint temperature ϑ_i, may be evaluated by substituting actual values into the temperature profiles. The radial dimensions of the support are:

$$r_t = 6.35 \times 10^{-3} \text{ m}$$

$$r_l = 3 \times 10^{-3} \text{ m}$$

For the non-isothermal Lexan section,

$$l_L = 6.35 \times 10^{-3}\ \text{m}$$

$$k_L = 0.21\ \text{W/m-K}$$

Substituting these values into the expression for λ_L gives:

$$\lambda_L^2 = 0.07785\, h \qquad [F.16]$$

For the steel section,

$$l_s = 31.9 \times 10^{-3}\ \text{m}$$

$$k_s = 60.5\ \text{W/m-K}$$

Substituting these values into the expression for Λ_s gives:

$$\lambda_s = 0.00682\, h \qquad [F.17]$$

The surface-to-air heat-transfer coefficient at the end of the steel section, may be estimated from a correlation for convective heat transfer from a flat vertical surface into air which is flowing past the surface, such as the following [Incropera and DeWitt,1981]:

$$Nu_z \equiv \frac{h_a d_t}{k_g} = 0.664\, Re_z^{1/2} Pr^{1/3} \qquad (Pr \geq 0.6) \qquad [F.18]$$

It is assumed here, that heat transfer is taking place from a flat vertical plate with the same dimensions as the heat-transfer probe diameter, d_t. $Re_z \equiv (u_g d_t \rho/\mu)$ and k_g is the thermal conductivity of air. The air density and viscosity are ρ and μ respectively. The velocity of gas relative to the end of the steel support, u_g, is equal to the average vibrational velocity of the vessel, which the heat-transfer probe is fixed to. At any value of the vibrational intensity parameter K, the maximum velocity of the vessel is given by $(Kg/2\pi f)$, where f is the vibrational frequency. Since the motion of the vessel is sinusoidal, the average relative velocity of the end of the steel support, past the still air

is $\sqrt{2}\,(Kg/2\pi f)$. At $K = 5$, and a vibrational frequency of 25 Hz, the average relative velocity u_g, is 0.22 m/s. Using this value of u_g in equation [F.18] gives $h_o \simeq 20$ W/m²-K.

Experimental observation shows that when the heat-transfer coefficient is high, the temperature Θ_o, indicated by the thermocouple implanted in the Lexan is always high. On the other hand, when the heat-transfer coefficient is low, the temperature Θ_o is always low. These observations are only valid if a constant probe surface temperature (of 85°C in this study) is maintained for all experiments.

An example of a bed that yields a high heat-transfer coefficient is 177-μm Master Beads at $K = 5$. The apparent value of the heat-transfer coefficient h, (obtained by neglecting heat losses through the probe supports) is 450 W/m²-K in this case. The temperature profiles require a knowledge of h, but for a first approximation, the apparent value of h may be used. Using this value of h,

$$\lambda_L = 5.919$$

$$\lambda_s = 1.752$$

Experimentally measured temperatures, taken after the bed reaches a steady state are:

$$\Theta_o = 66°C = 339\ K$$

$$\Theta_a = 20°C = 293\ K$$

$$\Theta_b = 55°C = 328\ K$$

$$\Theta_p = 85°C = 358\ K$$

Using these values in equation [F.15] gives $\vartheta_t = -0.0067$. Therefore, the actual joint temperature Θ_t, is 327.9 K, which is so close to the bed temperature (given the assumptions made herein), that it may be assumed equal to the bed temperature, Θ_b.

The analysis for the heat loss into the ambient air from the end of the steel support, does not include conduction losses into the vibrating table assembly. For the sake of argument, assume that

the total heat losses from that end of the steel support are 5 times that estimated above directly into the ambient air. This will give a surface-to-air heat-transfer coefficient h_a, of 100 W/m^2-K. With this value of h_a, the dimensionless joint temperature $\vartheta_j = -0.03$, giving a value of the actual joint temperature Θ_j, of 327.7 K. This temperature is still so close to the bed temperature, given the assumptions made, that $\Theta_j = \Theta_b$. This shows that the convection and conduction losses from the end of the steel support into the ambient surroundings have almost no effect on the temperature at the Lexan-steel joint.

A typical example of a bed yielding a low heat-transfer coefficient is 707-μ Master Beads vibrated at $K = 4$. The value of h in this case is 171 W/m^2-K, which gives:

$$\lambda_L = 3.649$$

$$\lambda_s = 1.080$$

Experimentally measured temperatures are as follows:

$$\Theta_o = 55°C = 328\ K$$

$$\Theta_a = 20°C = 293\ K$$

$$\Theta_b = 45°C = 318\ K$$

$$\Theta_p = 85°C = 358\ K$$

Using these values in equation [F.15] for the dimensionless joint temperature gives $\vartheta = -0.175$. The actual joint temperature Θ_j, therefore, is 317.8 K, which is so close to the bed temperature Θ_b, that it may be assumed that $\Theta_j = \Theta_b$.

These results show that despite the value of the surface-to-bed heat-transfer coefficient, the temperature at the Lexan-steel joint is always almost equal to the bed temperature. Equation [F.11] for the temperature profile within the steel section shows that since η_s is small, $\vartheta_s \to \vartheta_j$, for small values of χ_s. In other words, the temperature of at least a short section of the steel section close to the joint

is equal to the bed temperature. Therefore, an isothermal barrier exists that prevents the flow of heat down the steel section. The analysis shows that:

1. Only the Lexan section of the support need be considered when estimating the surface area through which heat flows into the bed.
2. No heat flows directly from the heat-transfer probe to the ambient surroundings through the probe supports.

Since $\vartheta_t \simeq 0$, equation [F.8] for the temperature profile within the non-isothermal Lexan section becomes:

$$\vartheta_L = \frac{\sinh(\lambda_L[1-\chi_L])}{\sinh \lambda_L} \qquad [F.19]$$

Alternatively, this equation may be written in fully-dimensioned form for $\Theta_L(h,x)$ as follows:

$$\Theta_L(h,x) = \Theta_b + (\Theta_o - \Theta_b) \frac{\sinh\left[(l_L - x)\sqrt{\frac{2hr_t}{k_L(r_t^2 - r_l^2)}}\right]}{\sinh\left[l_L\sqrt{\frac{2hr_t}{k_L(r_t^2 - r_l^2)}}\right]} \qquad [F.20]$$

This equation for $\Theta_L(h,x)$ can be used in equation [6.11] to determine the actual heat-transfer coefficient.

The vita has been removed from the scanned document